Energy Yield Comparison of Spar & Monopile Offshore Wind Turbines using BEM & OLAF Models

Iasonas Filippidis

Master Thesis Report

Sustainable Energy Technology

23/06/2023

Ørsted

TU Delft

[This page is left intentionally blank]

Acknowledgements

I would like to express my deepest appreciation and gratitude to the following individuals who have supported and guided me throughout my research and the completion of this thesis.

First and foremost, I am immensely grateful to both of my supervisors. Firstly, to my Ørsted supervisor, Hsiu Eik Lee, for his unwavering support, invaluable guidance, and continuous encouragement. His expertise, insightful feedback, and dedication to my academic development have been instrumental in shaping this thesis. Secondly, to my TU Delft supervisor, Professor Axelle Viré, I am grateful for your support and assistance during the project and sharing your vast experience and knowledge to the world of research.

I am deeply indebted to Gabriele Bedon and René Lindeboom for kick starting this project, inviting me into an amazing company, providing me with the necessary resources, facilities, and opportunities to pursue my academic aspirations within Ørsted. Specifically, Numerical Competence Center's commitment to excellence in project delivery and research has been pivotal in shaping my academic journey. Furthermore, I am expressing my sincere gratitude to Emre Barlas for dedicating time and resources to offer guidance and valuable feedback on various unfamiliar aspects of this project. Lastly, thank you again Gabriele for all the heartwarming meetings we had during this period, you were truly amazing in uplifting me and lowering my stress levels.

I am blessed to have a loving and supportive family who has always believed in me. Their unconditional love, encouragement, and understanding have been the pillars of strength always. I am forever grateful to my parents, my brother and our dog for their unwavering support.

I would like to express my heartfelt appreciation to my dear friends for their encouragement, understanding, and companionship. Their presence and uplifting spirits have made this challenging journey more enjoyable and memorable. There are too many people to name, but special thanks to my best friends Maria, Despina and Dóróthea for making me laugh, living in the present and giving me strength.

Lastly, I could not have done all of these without the support and care of my boyfriend Nikos, who has been there for me, in my successes and failures, throughout this entire time! Thank you for your love and compassion.

In conclusion, this thesis would not have been possible without the support and contributions of these remarkable individuals and institutions. Their belief in my abilities and their continuous support have been pivotal in my academic growth. I am truly grateful for their presence in my life.

Abstract

Energy transition is imperative to effectively address the pressing issue of climate change resulting from global warming. In this transition, offshore wind power assumes a pivotal role as a crucial and indispensable source of clean and renewable energy. Offshore benefits become more pronounced as the offshore locations progress far offshore. In deep-water areas, where 80% of the worldwide offshore wind energy can be potentially harnessed, the utilization of floating foundations becomes essential instead of traditional bottom fixed ones. The present study seeks to investigate the disparities in power generation and energy production that arise from the replacement of bottom fixed wind turbines with floating counterparts. The former is represented by the monopile foundation, while the latter by the spar buoy. The power performance difference lies in the ability of floating structures to move, which can lead to suboptimal positioning of the rotor relative to the incoming wind inflow, mainly due to spar's pitch and surge motions. The investigation is conducted using two distinct aerodynamic model of lower and higher fidelities, BEM and OLAF, respectively, to assess their effects on the outcomes.

In the field of offshore wind turbine design, engineers rely on aero-hydro-servo-elastic software codes to simulate the dynamic behavior of floating offshore wind turbine systems in offshore environments. OpenFAST, an open-source software, has been extensively developed and validated for conducting such investigations. In this study, OpenFAST is employed to develop both floating and bottom fixed wind turbine models. Specifically, a coupled aero-hydro-servo-elastic model of a floating spar wind turbine is created, and the simulated motion of the spar is compared with measurements obtained from an actual floating turbine deployed in the Hywind Scotland floating offshore wind farm. Metocean data, spar measurement data, and spar system descriptions are provided by Equinor to facilitate this benchmarking process. Additionally, an equivalent monopile wind turbine model is developed for energy yield comparison purposes.

The simulated spar motion results of the developed OpenFAST model exhibit reasonable realism when benchmarked with the measured data for all load cases and modal analysis, despite assumptions and uncertainties influencing the model's accuracy. Model discrepancies primarily stem from undisclosed wind turbine parameters and controller strategy as well as some modeling simplifications inherent in OpenFAST. Nevertheless, through statistical, time series and power spectral density comparisons against full-scale Hywind measurements encompassing various wind speeds (below-rated, rated, and above cut-out), the developed floating model is validated, thereby ensuring the reliability of its energy production outcomes.

It is observed that the spar's pitch and surge mean offset is mostly affected by the current speeds while varying wave conditions (height and period) influence their oscillation amplitudes. Power is slightly affected by the ocean conditions, primarily the wave effects, while it is more strongly influenced by the spar nacelle's velocity and direction relative to the incoming wind, especially when subjected to lower wind speed fields. Finally, for both BEM and OLAF simulations, monopile bottom fixed structures produce higher amounts of energy annually compared to the floating spar counterparts. The implementation of alternative controllers specifically designed for FOWT, with optimization objectives focused on either maximizing power performance or ensuring structural integrity and longevity, results in estimated AEP reductions when utilizing a spar floater instead of a monopile foundation. For the BEM model, the estimated AEP decrease ranges from 3.46% to 8.62%, depending on the specific controller optimization objective. On the other hand, when employing the VPM-OLAF model, the estimated AEP reduction for a spar floater compared to a monopile substructure ranges from 4.50% to 9.58%, under similar conditions as previously mentioned. By employing OLAF instead of BEM, the computed annual energy yield for both Bottom Fixed and Floating offshore wind turbines increases by approximately 25%.

In conclusion, it is recommended that future research prioritizes resolving identified discrepancies in the model setup, addressing phenomena not adequately captured by the current OpenFAST model, and conducting additional validation of the spar model using a wider range of measured parameters.

Table of Contents

Nomenclature

Latin Symbols

$\boldsymbol{A}$	Added Mass Matrix	[kg]
a	Induction Factor	[-]
$\vec{a}_f$	Fluid Acceleration Vector	[m/s²]
$A_{frontal}$	Tower Frontal Surface Area	[m²]
$\vec{a}_{spar}$	Spar Acceleration Vector	[m/s²]
$\boldsymbol{C}$	Damping Matrix	[Ns/m]
C_A	Hydrodynamic Added Mass Coefficient	[-]
C_D	Hydrodynamic Drag Coefficient	[-]
C_d	Aerodynamic Drag Coefficient	[-]
C_l	Aerodynamic Lift Coefficient	[-]
C_P	Power Coefficient	[-]
C_t	Thrust Coefficient	[-]
$C_{tower,D}$	Tower Drag Coefficient	[-]
C	Blade Chord	[m]
D	Aerodynamic Drag Force	[N]
d	Local Water Depth	[m]
D_{mon}	Monopile Diameter	[m]
d_{total}	Total Water Depth	[m]
E_{WT}	Wind Turbine Energy Yield	[Wh]
$\vec{F}_D$	Drag Morison Force Vector	[N]
$\vec{F}_{ext}$	External Force Vector	[N]
$\vec{F}_{FK}$	Froude–Krylov Force Vector	[N]
$\vec{F}_{HD}$	Hydrodynamic Force Vector	[N]
F_{heave}	Hydrodynamic Heave Force	[N]
$\vec{F}_{HS}$	Hydrostatic Force Vector	[N]
$\vec{F}_I$	Inertial Morison Force Vector	[N]
$\vec{F}_{moor}$	Restoring Mooring Force Vector	[N]

F_n	Normal Force	[N]
F_v	Regularization Parameter	[-]
$\vec{F}_{tower}$	Tower Drag Force Vector	[N]
$\vec{F}_{wind}$	Aerodynamic Force Vector	[N]
g	Gravitational Acceleration	[m/s^2]
H	Wind Turbine Height	[m]
H_j	Occurrence Probability	[-]
h_{ref}	Reference Water Depth	[m]
H_s	Significant Wave Height	[m]
$\boldsymbol{K}$	Stiffness Matrix	[N/m]
k	Generator Torque Gain Constant	[Nm/(s^{-1})^2]
$\boldsymbol{K_{HS}}$	Hydrostatic Stiffness Matrix	[N/m]
$\boldsymbol{K_{moor}}$	Restoring Stiffness Matrix	[N/m]
L	Aerodynamic Lift Force	[N]
$L_{mon,driv}$	Monopile Driving Length	[m]
$L_{mon,total}$	Total Monopile Length	[m]
L_{spar}	Spar Length	[m]
$\boldsymbol{M}$	Mass Matrix	[kg]
M_{mon}	Monopile Mass	[ton]
$m_{n,i}$	Mode Shape Coefficient Constant n	[-]
N	Rotor Number of Blades	[-]
P	Generated Power	[W]
P_{el}	Electrical Power	[W]
P_{mech}	Mechanical Power	[W]
P_{wind}	Wind Kinetic Power	[W]
$P_{WT,j}$	Wind Turbine Power per Metocean Condition j	[W]
Q_{rated}	Rated Torque	[Nm]
R	Rotor Radius	[m]
r_{gear}	Gearbox Transmission Ratio	[-]
R_{spar}	Spar Radius	[m]
S	Stiffness	[N/m]

S_j	JONSWAP/Pierson-Moskowitz Spectrum	[-]
T	Rotor Thrust	[N]
t_{mon}	Monopile Thickness	[mm]
T_p	Peak Wave Period	[s]
$\vec{V}$	Incoming Wind Speed/Current Speed Vector	[m/s]
V_0	Primary Wind Flow Speed	[m/s]
$V_{0_{NS}}$	Reference Near-Surface Current Speed	[m/s]
$V_{0_{SS}}$	Reference Sub-Surface Current Speed	[m/s]
$\vec{V}_f$	Fluid Velocity Vector	[m/s]
V_k	Induced Wind Velocity at Point k	[m/s]
V_{NS}	Near-Surface Current Speed	[m/s]
V_{rated}	Rated Wind Speed	[m/s]
V_{res}	Resulting Wind Speed	[m/s]
V_{spar}	Spar Velocity	[m/s]
V_{SS}	Sub-Surface Current Speed	[m/s]
V_{sub}	Spar Submerged Volume	[m^3]
V_{tilt}	Wind Velocity Experienced in Titled Rotor Conditions	[m/s]
$\vec{V}_{tower}$	Tower Velocity Vector	[m/s]
$\boldsymbol{x}$	DOF Motion Matrix	[-]
X	Surge	[m]
Y	Sway	[m]
z	Height	[m]
Z	Heave	[m]

Greek Symbols

β	Blade Pitch Angle	[^{o}]
Γ	Vorticity Strength	[s^{-1}]
η_{gen}	Generator Efficiency	[-]
θ_{curr}	Current Directional Angle	[^{o}]
θ_{rotor}	Rotor Tilt	[^{o}]
θ_{twist}	Blade Twist Angle	[^{o}]

θ_{wave}	Wave Directional Angle	[°]
θ_{wind}	Wind Directional Angle	[°]
θ_x	Roll	[°]
θ_y	Pitch	[°]
θ_z	Yaw	[°]
λ	Tip Speed Ratio	[-]
ρ_{air}	Air Density	[kg/m^3]
ρ_w	Water Density	[kg/m^3]
φ	Inflow Angle	[°]
Ω	Rotor Rotational Speed	[s^{-1}]
Ω_{LSS}	Low Speed Shaft Rotational Speed	[s^{-1}]
Ω_{HSS}	High Speed Shaft Rotational Speed	[s^{-1}]
ω	Frequency	[Hz]
$\vec{\omega}$	Vorticity	[s^{-1}]

Abbreviations

AEP	Annual Energy Yield
BEM	Blade Element Momentum
BOWT	Bottom Fixed Offshore Wind Turbine
CFD	Computational Fluid Dynamics
DBEM	Dynamic Blade Element Momentum
DOF	Degree of Freedom
FOWT	Floating Offshore Wind Turbine
FVW	Free Vortex Wake
LL	Lifting Line
MSL	Mean Sea Level
NREL	National Renewable Energy Lab
OLAF	cOnvecting LAgrangian Filaments
PSD	Power Spectral Density
STD	Standard Deviation
TSR	Tip-Speed Ratio
VPM	Vortex Panel Method

Chapter 1. Introduction

In Chapter 1, the current environmental status, energy infrastructure and wind turbine background are briefly introduced. Following, the scope and objectives of this thesis project are analysed and finally, the report layout is presented.

1.1 Background

Every year, due to air pollution, approximately seven million people die prematurely while hundreds of millions more fall ill causing tremendous amount of unnecessary suffering as a zero-emission energy system could potentially alleviate these problems (WHO, 2014). Air-pollution is merely a part of the serious phenomenon known as climate crisis, which additionally entails global warming, environmental degradation, natural disasters, weather extremes, food and water insecurity (UN75, 2019). The science clearly shows that to avert the worst impacts of climate change and preserve a livable planet, global temperature increase needs to be limited to 1.5°C above pre-industrial levels. Compared to the pre-industrialised era, Earth is currently 1.1°C warmer. Hence, to restrain global warming to no more than 1.5°C – as called for in the Paris Agreement – emissions need to be reduced by 45% by 2030 and reach net zero by 2050 (United Nations, 2015). The energy-security problems worldwide require an immense, immediate transformation of the world's current fossil fuel-based energy infrastructure to a non-carbon emitting, 100% clean, sustainable and renewable power generating one (Jacobson et al., 2017).

The new energy infrastructure will include sources of power generation that neither contribute to pollution nor require non-renewable consumption. Some of the most prominent forms of sustainable energy are wind energy, solar energy, geothermal energy, wave energy and bioenergy. Wind energy, specifically, has the potential to constitute an essential piece in future national energy scenarios as its electricity generation use expands worldwide in an accelerating rate with multiple countries planning for its future deployment (Ezio & Claudio, 1998). As of 2022, the global cumulative wind power capacity has reached 837 GW, including both onshore and offshore installations. In 2021, a total of 93.6 GW of new installations was achieved, out of which, the onshore wind market added 72.5 GW worldwide while the offshore market commissioned 21.1 GW (Lee et al., 2022). Although the wind energy sector is rapidly growing, for the 2030 Paris Agreement goals to be met, the installations growth rate needs to quadruple, as showcased in Figure 1.1 (IEA, 2021).

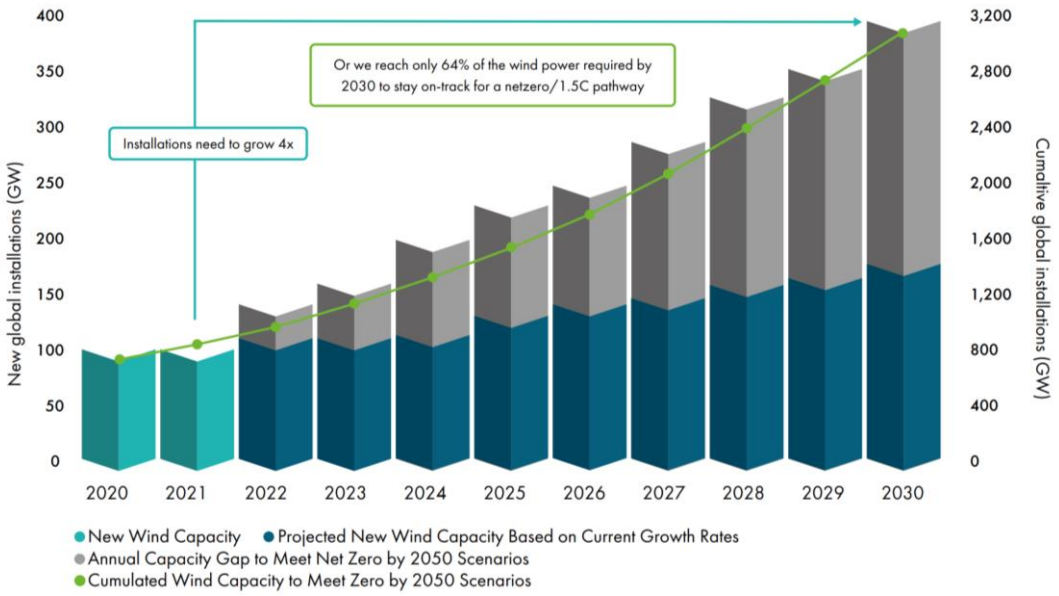

Figure 1.1 Projected wind capacity for 2022-2030 (IEA, 2021).

Wind power has additional benefits to fossil fuels and even other renewable sources of energy. Firstly, electricity generated by wind turbines does not cause water or air pollution, so wind energy does not

contribute to smog, acid rain or greenhouse gas emissions. Secondly, wind power does not require water to operate as it has a purely inexhaustible renewable energy source (US Department of Energy, 2015). It is estimated that, in 2013, wind power generation resulted in a reduced power sector water consumption by 36.5 billion gallons (Koulouri et al., 2014). Thirdly, wind energy systems have low operating expenses as there are no associated fuel costs. Lastly, wind energy is cost competitive as utility-scale wind turbines provide, currently, one of the lowest-priced energy sources available (US Department of Energy, 2015).

This type of energy is generated by wind turbines, which convert the kinetic energy (present in the wind) into mechanical energy in the form of shaft rotation and is, afterwards, converted into electrical energy via a generator. The power capacity of wind turbines is directly linked to their respectively installed location's wind field characteristics. As wind speeds are increased and become steadier over sea compared to on land, the debate of onshore versus offshore wind turbines ensues.

The upcoming growth of wind farms heavily relies on offshore development as onshore wind is currently considered fully realized in some countries due to visual and noise impact constraints (Bussemakers, 2020). These constraints have a direct impact on the future of onshore wind farms, as they impose limitations on the available locations for potential installations. In contrast, these constraints are less restrictive in the offshore wind sector, thereby enabling the deployment of wind turbines with larger rotor diameters, increased numbers of turbines, and higher rotor speeds, resulting in greater power generation capacity. Furthermore, onshore wind farms are predominantly located in rural areas where land availability is abundant. However, this poses a significant challenge as the same land is utilized for various essential purposes, including agriculture, livestock operations, and human habitation. As a result, the development of onshore wind farms must carefully consider and balance the competing land-use demands to ensure sustainable coexistence and minimal disruption to these vital activities (Bussemakers, 2020). Oceans are considered ideal locations to build wind farms with regards to scale due to their vastness. Additional advantages of offshore power plants include great cost reduction since there is an increased number of full-load hours per year, longer structure lifetimes and higher annual electricity production. Specifically, due to steadier and higher wind speeds, offshore installations can generate 50% more electricity than their onshore counterparts with an extra advantage being that construction and transportation of offshore wind turbines is scalable as large offshore turbines can be transported by barges or ships. The capacity of land-based wind farms is limited in scale while offshore farms with more than 100 MW production are feasible (Dinh & McKeogh, 2018). Finally, the offshore possibility introduces an additional option for tower foundation, floating platforms supporting the wind turbines instead of the classic bottom-fixed ones.

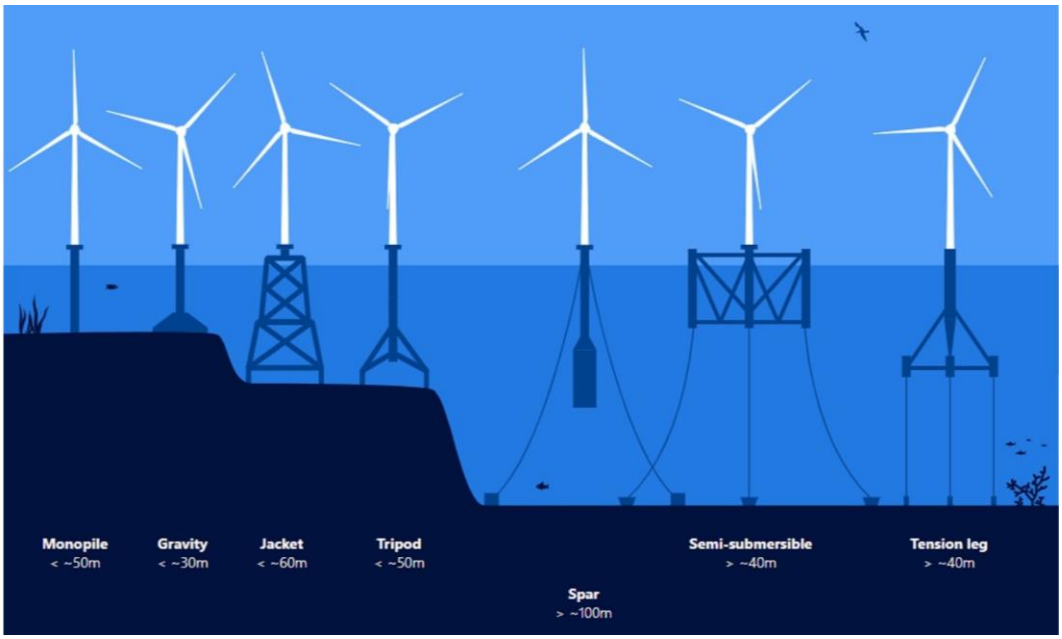

Figure 1.2 Example of typical offshore WT foundation types and applicable water depths (DHI, 2021).

In recent years, there has been a notable surge in the interest surrounding floating substructures for offshore wind turbines. This can be primarily attributed to the necessity of adapting to more demanding locations in deeper waters as the offshore wind industry continues to expand and develop wind farms further offshore. The deployment of floating wind turbines provides a viable solution for these challenging sites where the current technology based on bottom-fixed substructures is not technically or economically feasible (Lerch et al., 2019). As observed by Figure 1.2, the inclusion of floating foundations immensely increases the threshold of maximum water depth and consequently, available locations for wind power harvesting. Furthermore, the deployment of wind energy projects is typically focused on locations characterized by high and consistent wind speeds. It is noteworthy that approximately 75% of these favorable locations in Europe are situated in waters with depths of at least 60 meters. Moreover, on a global scale, around 80% of the total potential for offshore wind production is located in waters that exceed this depth threshold (Bussemakers, 2020). Consequently, floating foundations are anticipated to heavily assist in the energy transition and increase the renewable energy production in the upcoming years. The increase in wind turbine tower, rotor and generator sizes results in the traditional monopile and corresponding installation technologies to become obsolete as assembling a floating wind system can take place onshore, where later the floater-turbine structure can be towed to its final location with inferior expenses (Bussemakers, 2020). Subsequently, the floating structure is securely anchored to the seabed using mooring lines, which are specifically designed to provide stability and ensure controlled motion.

The floating motion of wind turbines, influenced by current, wave, and wind conditions, presents a new challenge in the design and operation of such systems. It is essential to consider the additional degrees of freedom (DOF) resulting from the platform's displacement when designing the turbine. These motions not only impact the power production of the floating wind turbine but also introduce complexities in accurately simulating the dynamic behavior of the floater-wind turbine structure (Bashetty & Ozcelik, 2021).

The complexity of modeling the dynamic behavior of floating wind turbines can be effectively addressed through computer simulations, as it enables the analysis of various configurations with minimal reliance on laboratory testing and on-site data measurement. To accurately capture the effects of both ocean and wind on the movement, energy generation, aerodynamic loads, and moments of the wind turbine structure, a combination of fluid dynamics and solid dynamics equations is necessary (Viré, 2012). In this study, OpenFAST is utilized as a multi-fidelity and multi-physics tool to simulate the coupled dynamic response of wind turbines. OpenFAST integrates computational modules for aerodynamics, hydrodynamics for offshore structures, control and electrical system servodynamics, and structural dynamics. This enables the simulation of coupled nonlinear aero-hydro-servo-elastic behavior in the time domain, providing a comprehensive model for analyzing the performance and response of floating wind turbines. This software was developed by Jason Jonkman, Mike Sprague and colleagues of the National Renewable Energy Lab (NREL, 2021).

1.2 Research Objectives & Scope

The main objective of this report is to investigate the power performance between bottom fixed and floating wind turbines for two aerodynamic models, namely Blade Element Momentum (BEM) and Vortex Panel Method (VPM-OLAF). In support of this, the following two broad research scopes are defined in their order of execution:

1. This study uses the spar platform as the reference floater. The first scope hence involves modelling a 6MW spar type floating wind turbine which is modelled as closely as practicably possible on the spar design deployed for Hywind Scotland. This model is to be benchmarked against the provided Hywind measured data (Equinor, 2018) to provide commentary on the realism provided by the results. Moreover, there is interest in exploring the differences between the two varying fidelity aerodynamic models on the floating spar platform responses.

2. The second scope entails power performance and energy yield comparisons between Bottom Fixed and Floating Offshore Wind Turbines (BOWT and FOWT, respectively). The energy production comparative analysis also employs both aforementioned aerodynamic models.

In relation to the scopes outlined above, the objectives of this work specifically pertain to:

1. Developing an aero-hydro-elasto-servo coupled OpenFAST model that approximates the deployed Hywind Scotland floating spar wind turbines.

2. Investigating the response and spar motion data recreation accuracy differences for the two aerodynamic models, BEM and VPM-OLAF.

3. Comparing the performance and annual energy production of a spar floating to a bottom fixed monopile wind turbine.

To add another dimension in framing this research, the main research objective was decomposed into the following sub-questions as follows:

- How can the Hywind FOWT be modelled in OpenFAST and what assumptions must be made with regards to unknown-uncertain parameters e.g., controller and airfoil distribution?

- Where do the developed Hywind OpenFAST model discrepancies stem from?

- How do the spar's motion degrees of freedom (DOF) influence the power generation?

- How do the ocean conditions affect the spar motion and the power production of the FOWT?

- Which of the two aerodynamic OpenFAST models, BEM and VPM-OLAF, produces higher precision results?

1.3 Report Layout

The layout of the report follows a certain structure. Specifically, in Chapter 1 the knowledge background along with the scope and research questions of the thesis are presented. Following, offshore wind background theory, retrieved metocean Hywind data and an OpenFAST introduction compose Chapter 2. Then, an extensive literature review of multiple reports and investigations on topics similar to the scope of the thesis are discussed in Chapter 3. In Chapter 4, the methodology behind the development of the OpenFAST models is analyzed. Chapter 5 displays the simulated results against the measured Hywind data. Chapter 6 investigates the spar motion effects on power and compares the power performance of monopile supported wind turbines to their floating spar counterparts. Lastly, conclusions and recommendations for future project continuation are included in Chapter 7.

Chapter 2. OpenFAST & Hywind Background

This chapter attempts to present majority of the theories that are used in this work. The opensource software OpenFAST along with the necessary theoretical background to achieve a strong understanding on its most enmeshed modules are discussed. Then, the acquired Hywind measured metocean data along with additional information on the first floating wind farm are presented.

2.1 Theoretical Background

2.1.1 Motion Response

Structural dynamics entail multiple types of dynamic loading, where the general system response is initially predicted by rigid body dynamics. Utilising rigid instead of flexible body dynamics allows for a simplified prediction of interconnected bodies' movement under external force application. Moreover, a lower number of response degrees of freedom (DOF) is employed to describe the translational and rotational displacement. The spar supported FOWT structure is physically freely floating and has six motion DOFs in total, three translational and three rotational divided in pairs per axis, as seen in Figure 2.1. These DOFs are:

- Surge and Roll for the x axis,
- Sway and Pitch for the y axis,
- Heave and Yaw for the z axis.

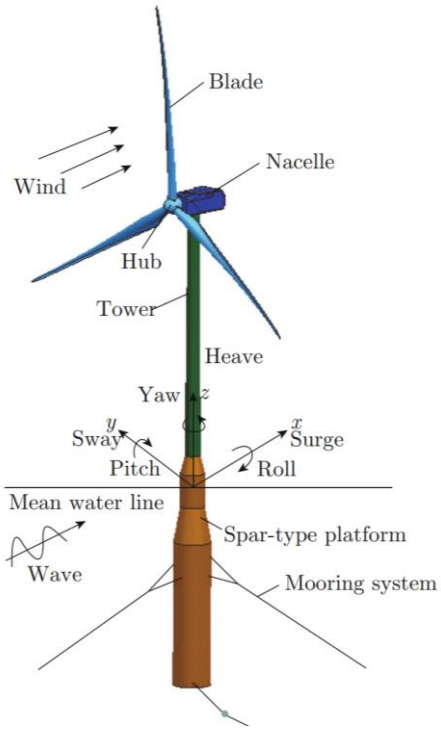

Figure 2.1 Spar type FOWT components, coordinates and platform motion DOFs definition (Long et al., 2018).

For the motion response of the spar FOWT to be calculated based on rigid body dynamics, the stiffness, damping and mass structure values are used through Equation 2.1. The spar-mooring lines-wind turbine system is portrayed as a spring-mass-damper system. There, $\vec{x}$ is the DOF motion vector as seen in Equation 2.2, and it is time-varying (t). It should be mentioned that units in bold refer to matrices.

$$(\boldsymbol{M}+\boldsymbol{A})\cdot\ddot{\vec{x}}(t)+\boldsymbol{C}\cdot\dot{\vec{x}}(t)+\boldsymbol{K}\cdot\vec{x}(t)=\vec{F}_{ext}(t) \tag{2.1}$$

$$\vec{x} = \begin{bmatrix} X \\ Y \\ Z \\ \theta_x \\ \theta_y \\ \theta_z \end{bmatrix} \tag{2.2}$$

Where X is surge, Y is sway, Z is heave, θ_x is roll, θ_y is pitch and θ_z is yaw. As for the parameters in Equation 2.1, $\boldsymbol{M}$ is the mass matrix, $\boldsymbol{A}$ is the added mass matrix, $\boldsymbol{C}$ is the hydrodynamic damping matrix and $\boldsymbol{K}$ is the stiffness matrix. All the aforementioned matrices have 6x6 dimensions and non-diagonal terms give information about coupling between the DOFs. The external loads applied on the FOWT structure are represented by the $\vec{F}_{ext}$ vector, as calculated by Equation 2.3. All the vector loads acting on the body including the wind loads $\vec{F}_{wind}$, the restoring mooring loads $\vec{F}_{moor}$, the hydrostatic loads $\vec{F}_{HS}$ and hydrodynamic loads $\vec{F}_{HD}$, are illustrated in Figure 2.2. The last one is represented mainly through the incoming wave and current loads.

$$\vec{F}_{ext} = \vec{F}_{wind} + \vec{F}_{moor} + \vec{F}_{HS} + \vec{F}_{HD} \tag{2.3}$$

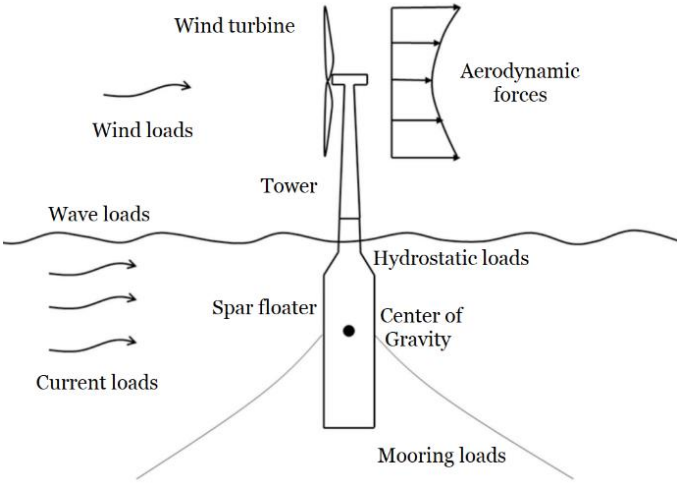

Figure 2.2 Load schematic on a spar FOWT (Huang & Wan, 2019).

The wind force is composed by the rotor thrust vector, $\vec{T}$ and the tower drag force vector, $\vec{F}_{tower}$, as presented in Equation 2.4, with the two entailed loads being calculated by Equation 2.5 and Equation 2.6, respectively.

$$\vec{F}_{wind} = \vec{T} + \vec{F}_{tower} \tag{2.4}$$

$$\vec{T} = \frac{1}{2} \cdot \rho_{air} \cdot \pi \cdot R^2 \cdot C_t(\lambda, \beta) \cdot \vec{V}_{rel}^2 \tag{2.5}$$

$$\vec{F}_{tower} = \frac{1}{2} \cdot \rho_{air} \cdot A_{frontal} \cdot C_{tower,D} \cdot \vec{V}_{t,rel}^2 \tag{2.6}$$

Where, ρ_{air} is the air density, R is the rotor radius, C_t is the wind turbine's thrust coefficient which depends on tip speed ratio (TSR) λ and blade pitch angle β, $A_{frontal}$ is the surface area and $C_{tower,D}$ is the tower's drag coefficient. Lastly, $\vec{V}_{rel}$ is the relative wind velocity vector as experienced by the moving rotor at hub height while $\vec{V}_{t,rel}$ is the relative wind speed vector as seen by the oscillating tower. They are obtained via

Equation 2.7 and Equation 2.8, respectively, by using the incoming wind speed vector, $\vec{V}$, the hub and tower velocity vectors due to the motions of the substructure, $\vec{V}_{hub}$ and $\vec{V}_{tower}$ (Lerch et al., 2019).

$$\vec{V}_{rel} = \vec{V} - \vec{V}_{hub} \tag{2.7}$$

$$\vec{V}_{t,rel} = \vec{V} - \vec{V}_{tower} \tag{2.8}$$

The wave and current loads for a moving body in an oscillating flow compose the hydrodynamic Morison equations for inertial, $\vec{F}_I$, and drag forces, $\vec{F}_D$, as well as the Froude–Krylov force, $\vec{F}_{FK}$. These forces are entailed within Equations 2.9-2.12 (Mutlu & Fredsoe, 2006). In conjunction with strip theory, the spar platform's length, L_{spar}, is divided in discrete length elements of dz.

$$\vec{F}_{HD} = \vec{F}_I + \vec{F}_D + \vec{F}_{FK} \tag{2.9}$$

$$\vec{F}_I = C_A \cdot \rho_w \cdot \vec{a}_{f,rel} \cdot \int_0^{L_{spar}} \pi \cdot R_{spar}^2(z)\, dz \tag{2.10}$$

$$\vec{F}_D = \rho_w \cdot C_D \cdot \left|\vec{V}_{f,rel}\right| \cdot \vec{V}_{f,rel} \cdot \int_0^{L_{spar}} 2 \cdot R_{spar}(z)\, dz \tag{2.11}$$

$$\vec{F}_{FK} = \rho_w \cdot \vec{a}_f \cdot \int_0^{L_{spar}} \pi \cdot R_{spar}^2(z)\, dz \tag{2.12}$$

Where, C_A is the hydrodynamic added mass coefficient, ρ_w is the water density, $\vec{a}_{f,rel}$ is the relative accelaration between the fluid's and spar's acceleration vectors, $\vec{a}_f$ and $\vec{a}_{spar}$, respectively, as seen in Equation 2.13. R_{spar} is the spar's radius that varies with its height z, C_D is the hydrodynamic drag coefficient and $\vec{V}_{f,rel}$ is the relative fluid velocity vector as experienced by the platform and as obtained in Equation 2.14 based on the fluid's and spar's velocity vectors, $\vec{V}_f$ and $\vec{V}_{spar}$, respectively.

$$\vec{a}_{f,rel} = \vec{a}_f - \vec{a}_{spar} \tag{2.13}$$

$$\vec{V}_{f,rel} = \vec{V}_f - \vec{V}_{spar} \tag{2.14}$$

For the case of no additional linear stiffness matrix, an additional equation is required for the hydrodynamic heave force, F_{heave}, as approximated by the change of the hydrostatic pressure in Equation 2.15, where g is the gravitational acceleration.

$$F_{heave} = \rho_w \cdot g \cdot 2 \cdot \pi \cdot R_{spar} \cdot \frac{\partial R_{spar}}{\partial z} \cdot Z \tag{2.15}$$

The effects of having an underwater body compose the hydrostatic platform loads, the buoyancy and gravitational-restoring force that counteract each other are presented in Equation 2.16.

$$\vec{F}_{HS} = \rho_w \cdot g \cdot \vec{V}_{sub} - \boldsymbol{K_{HS}} \cdot \vec{x} \tag{2.16}$$

Where, $\vec{V}_{sub}$ is the fluid's displaced volume when the support platform is in its undisplaced position and $\boldsymbol{K_{HS}}$ is the component of the linear hydrostatic-restoring matrix from the water-plane area effects and the center of buoyancy (Jonkman et al., 2015). The spar platform's motion is restrained by the mooring system. The mooring loads are counteracting the incoming wind, wave and current loads as well as establishing extra stability in addition to the floating platform's innate inertia and stability restoring capabilities. The mooring loads are estimated based on Equation 2.17, where $\boldsymbol{K_{moor}}$ is the restoring stiffness matrix from all mooring lines.

$$\vec{F}_{moor} = -\boldsymbol{K_{moor}} \cdot \vec{x} \tag{2.17}$$

The aforementioned formulas concern the time series motion response of the FOWT, as for the frequency domain motion response, the result will consist of a frequency and amplitude-dependent oscillating part and a constant part. This oscillating frequency domain response, in a harmonic case, is expressed through Equation 2.18. The amplitude vector $\vec{A}$ is calculated by using Equation 2.1 and replacing the time-varying terms with their frequency-dependent counterparts. This is presented in Equation 2.19, for a specific reference frequency ω.

$$\vec{x} = \vec{A}(\omega) \cdot e^{i\omega t} \tag{2.18}$$

$$\vec{A}(\omega) = \frac{\vec{F}_{ext}(\omega)}{\left[\left(\boldsymbol{M} + \boldsymbol{A}(\omega)\right) \cdot \omega^2 + \boldsymbol{B}(\omega) \cdot i \cdot \omega + \boldsymbol{C}\right]} \tag{2.19}$$

An important aspect of the frequency domain analysis is the estimation of the system's natural frequencies or eigenfrequencies. When the system DOFs oscillate at their respective eigenfrequencies a resonance occurs and the oscillation amplitude maximizes. This event can have catastrophic consequences for the FOWT, hence it is essential to acknowledge and record these specific values. In order for the system to perform a free decay, no external loads should be present and restrict-encourage its motion. Mathematically, the eigenfrequency of a DOF is calculated based on Equation 2.20.

$$det\left[-\left(\boldsymbol{M} + \boldsymbol{A}(\omega)\right) \cdot \omega^2 + \boldsymbol{B}(\omega) \cdot i \cdot \omega + \boldsymbol{C}\right] = 0 \tag{2.20}$$

However due to the complexity and coupling conditions between multiple aspects of a real FOWT, such as in the case of Hywind, Scotland, the system responses cannot be described solely by a simple harmonic oscillation. In order for multiple external and coupled effects to be properly represented simultaneously, a computational software is deemed necessary. It is highlighted that in the subsequent sections, the usage of matrix and vector notations has been intentionally omitted.

2.1.2 Power & Energy Generation

Wind turbines harvest the kinetic power of the wind, P_{wind}, as expressed in Equation 2.21. For a bottom fixed offshore wind turbine (BOWT), the generated power, P_{BOWT}, is calculated via Equation 2.22 .

$$P_{wind} = \frac{1}{2} \cdot \rho_{air} \cdot A \cdot V^3 \tag{2.21}$$

$$P_{BOWT} = \frac{1}{2} \cdot \rho_{air} \cdot \pi \cdot R^2 \cdot C_P(\lambda, \beta) \cdot V^3 \tag{2.22}$$

Where, C_p is the wind turbine's power coefficient which depends on tip speed ratio (TSR) λ and blade pitch angle β (Bianchi et al., 2007). Contrasting to the bottom fixed case, in order for the floating and moving wind turbine's generated power, P_{FOWT}, to be computed by Equation 2.23, two additional considerations have to be implemented. Firstly, the platform's lateral and rotational displacements induce an oscillating rotor tilt θ_{rotor} which annuls the rotor initial perpendicular positioning to the incoming wind field. The effect is taken into account via Equation 2.24 (Matha et al., 2016). No specific formula connecting the three rotational DOF angles to the rotor tilt is presented as multiple different parameters influence the rotor's tilt, mainly the controller's servodynamic response. Secondly, the computation of wind force, F_{wind}, takes into consideration the relative wind speed as experienced by the translationally and rotationally moving rotor, as shown in Equations 2.5 and 2.7 (Lerch et al., 2019).

$$P_{FOWT} = \frac{1}{2} \cdot \rho_{air} \cdot \pi \cdot R^2 \cdot C_P(\lambda, \beta) \cdot V_{tilt}^3 \tag{2.23}$$

$$V_{tilt} = V_{rel} \cdot cos(\theta_{rotor}) \tag{2.24}$$

As the main scope of this project, Equation 2.25 is used to estimate both the BOWT and FOWT annual energy yield, E_{WT}.

$$E_{WT} = 8760 \cdot \sum_{j=1}^{N} P_{WT,j} \cdot H_j \tag{2.25}$$

Where, $P_{WT,j}$ is the power generation of either a bottom-fixed or floating WT under certain metocean conditions j with an occurrence propabibilty of H_j. The specific metocean conditions that affect the power generation of the wind turbine types for the case of Hywind, Scotland will be assessed and specifically decided in Section 6.1.

2.2 The Hywind Floating Wind Farm

In order to achieve one of the primary goals of this project, which involves the development of an OpenFAST spar FOWT model inspired by existing structures in Hywind, Scotland, it is essential to provide an introduction to the wind farm itself. Additionally, this section presents the measured data obtained from the Hywind Scotland floating wind farm, which serve as benchmarks and validation sources for the developed model.

2.2.1 Background Information

The world's first commercialised floating wind farm was commissioned 25km off the East-coast of Scotland, offshore of Peterhead in 2017. It has been supporting the Scottish grid by generating renewable electricity to cover approximately 20.000 households in UK. It consists of five spar-supported 6 MW FOWT for a total installed capacity of 30 MW. An overview of the wind farm, information on the structure's parameters and a side view of the electric cables, spar platform and wind turbine are displayed in the schematic configurations of Figure 2.3 (Statoil, 2015). The turbine type for Hywind Scotland is SWT-6.0-154 supplied by Siemens Gamesa with the floating platform being based on Statoil's Hywind spar-buoy concept.

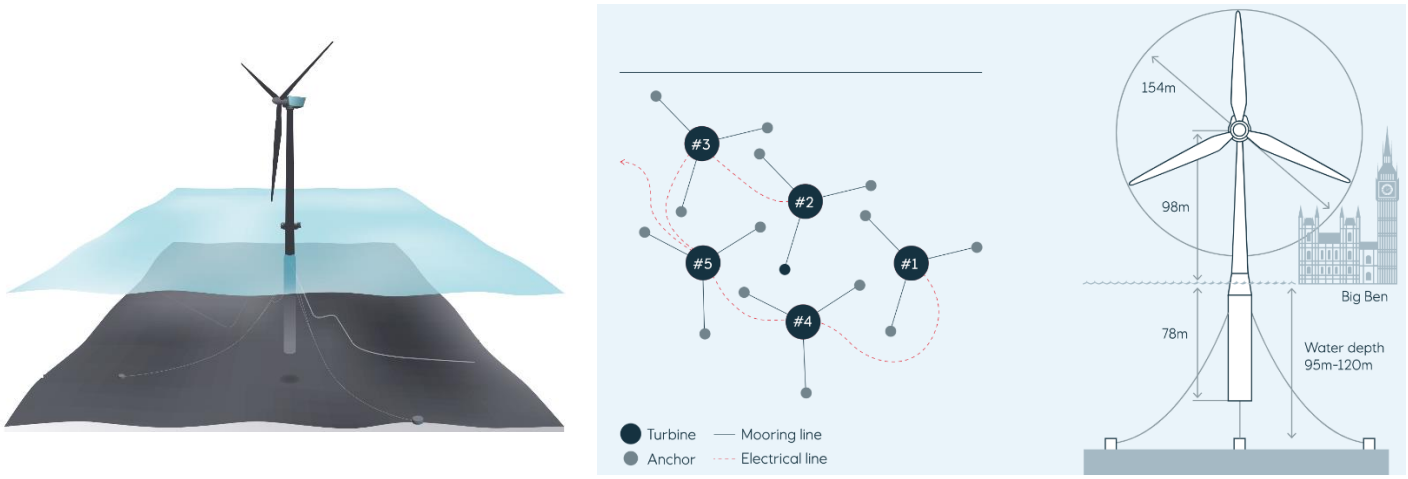

Figure 2.3 Overview of Hywind wind farm, front-view and side-view of a singular FOWT (Selas, 2018).

2.2.2 Hywind Metocean Measurements

ORE Catapult and Equinor ASA shared data of eleven different cases for 30-minute periods each. The data pertain to environmental conditions, nacelle yaw, roll and pitch motions, mooring line tensions along with platform measurements on surge, sway, roll, pitch and yaw motions. The data are set in time intervals of 0.1s for the incoming wind speed measurements or 0.2s for the motion measurements. Pertinent motion measurements are included and discussed in Section 5.2, where they are compared to the simulated model results.

Specifically, the measured environmental conditions include additional statistic data on wind speed, wind direction, significant wave height, peak wave period, wave direction, current speed and current direction. The wave and current values are recorded by a wave buoy, while the wind ones are recorded by a anemometer located at the wind turbine's nacelle. Therefore, the wind velocities are measured at roughly 99m above sea level, around the hub height.

The documented data from Hywind utilize a formal definition of wind direction, specifying it as the direction from which the wind is originating. Thus, wind coming from North is defined as 0^{o}, whilst wind coming from East is defined as 90^{o}. Similarly, the same principle applies to waves, while the opposite is true for current direction. According to Hywind documentation, current direction is defined as the direction toward which the current is flowing. For instance, currents flowing from the South to the North are assigned a current direction of 0°, whereas currents propagating from the West to the East are assigned a current direction of 90° (Equinor, 2018).

In this report, it is crucial to acknowledge that the wave buoy utilized for wave and current measurements is positioned 2.5 km from the turbine, specifically situated in the South-East direction of the wind farm site. It is assumed that the measured environmental condition values remain constant across the entire site. Consequently, no considerations are made for wave scattering or radiation effects, and there is no extrapolation of data to the turbine location. Furthermore, given the relatively remote nature of the site, it is improbable that these conditions would be substantially influenced by external factors (Equinor, 2018).

The mean values of wave and wind related parameters over the 30 min measured period per case are presented in Figure 2.4. Due to the current measurements occurring in four different water depths, the mean current speed and direction values are included, separately, in Figure 2.5. The numbering of the measured Hywind case wind, wave and current data is in chronological order instead of the order suggested in the data documents. The numbering remains consistent throughout this project. The explicit measurements are provided for completeness, in the form of tables in Appendix A, Figure A.1.

The first graph of Figure 2.4 provides an overview of wind speeds and their variations. Turbulence intensity is indicated by standard deviation bars, while the SWT6.0-154 turbine's cut-in, rated, and cut-out velocities are displayed by horizontal dashed lines. The results show that cases 8 and 9 operate below the rated regime with a constant blade pitch angle, whereas cases 1, 2, 6, 7, 10 and 11 operate around or above the rated wind speed with an expected influence of active blade pitch control. Furthermore, cases 4 and 5 indicate idling of the turbine due to being above the cut-out velocity. The turbulence intensity increases as the wind speed increases, and cases 4 and 5 indicate highly fluctuating wind speeds with potential gust or storm conditions occurring during their measurements. Wind conditions were estimated using the turbine's wind anemometer, with data from moments when the blade covered the anemometer being excluded from the statistics calculations for the idling cases (Equinor, 2018).

In relation to the wave-related graphs depicted in Figure 2.4, no clear pattern emerges regarding the correlation between wind speed and wave conditions. However, it is observed that lower wind speeds are typically associated with smaller wave heights, as demonstrated by the measured cases 8 and 9. Furthermore, an increase in wave height relative to the peak period becomes apparent as the wind speed rises.

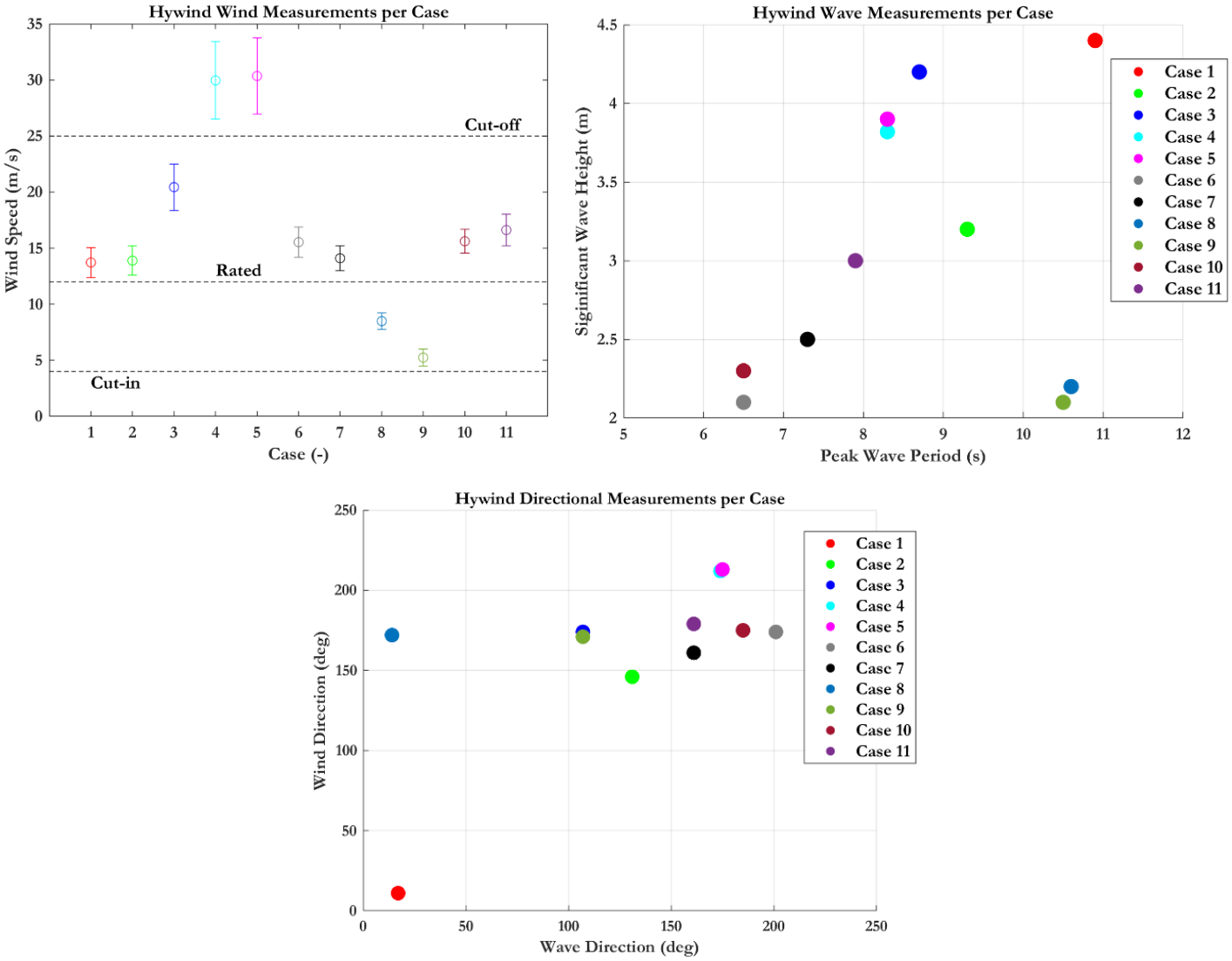

Figure 2.4 Summary of available Hywind wind and wave measurements (Equinor, 2018).

Finally, Figure 2.5 presents the distribution of current profiles across different water depths for each scenario. It is evident that the shape of the current velocity profile exhibits substantial variation among the cases and lacks consistent characterization. However, at lower current speeds, the profile remains

relatively constant throughout the measured water depths. Notably, certain current velocities are relatively high for the North Sea region, reaching a maximum of 0.6 m/s near the floater's bottom depth. This can be attributed to the deep-water nature of the location, situated in the northern part of the United Kingdom, with limited protection from the Atlantic Ocean. These findings suggest the presence of deep-water currents that are not directly influenced by local winds. Although no direct correlation between wind speed and total current velocity is observed, cases 4 and 5, characterized by high wind speeds, exhibit a notable increase in current velocity near the sea surface. Furthermore, the analysis of current directions reveals significant variability across different depths in some cases, with opposing current directions observed at certain depths (Bussemakers, 2020).

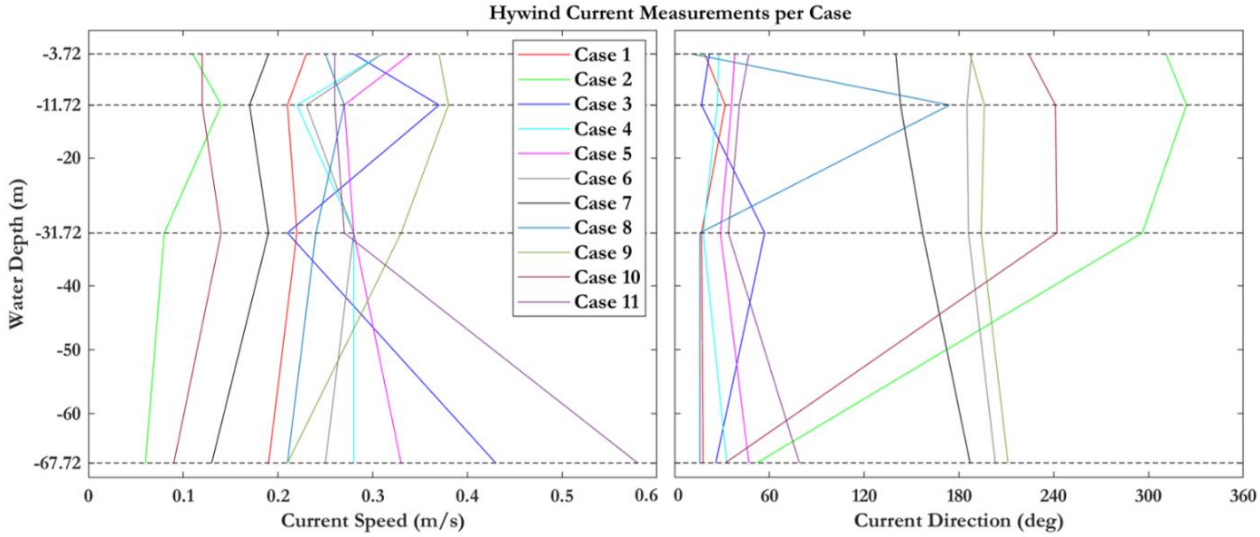

Figure 2.5 Hywind current speed and direction measurements
at four water depths (3.72m, 11.72m, 31.72m, 62.72m below MSL) (Equinor, 2018).

2.3 Introduction to OpenFAST

The computation of time series results for the six-motion response degrees of freedom (DOFs) is achieved by solving Equation 2.1. However, given the complexity of the problem, a dedicated software modelling solver is necessary. OpenFAST, the chosen software for this study, utilizes numerous intricate formulas that are beyond the scope of this report to comprehensively cover. In a realistic scenario, the governing equations that describe the response of a mechanically multidimensional structure, such as a floating offshore wind turbine (FOWT), are considerably more intricate than those previously presented. A profound understanding of hydrodynamics, aerodynamics, servodynamics, as well as rigid and flexible body dynamics is essential. Hence, it is important to acknowledge that the individual modules comprising the OpenFAST modelling software build upon the foundational equations discussed in Section 2.1.

2.3.1 OpenFAST Modules

Throughout this project, to recreate and benchmark against the Hywind measured data, in total 8 OpenFAST modules were operated and interconnected to provide satisfactory results. Specifically, the used modules are:

- AeroDyn, which predicts the aerodynamic loads on both the blades and tower based on the principles of actuator lines. AeroDyn provides several types of wake/induction model to choose between BEM, dynamic BEM (DBEM) or cOnvecting LAgrangian Filaments (OLAF). The latter is individually incorporated in a separate module. Environment conditions, airfoil information, blade properties and tower aerodynamic influence are also included in the input file (NREL, 2021).

- HydroDyn, which offers the possibility of hydrodynamic load calculation based on potential flow theory, strip theory or a combination. For the purpose of this project, strip theory modelling was used, where loads are applied across multiple interconnected members and are derived directly from the undisturbed wave and current kinematics at the undisplaced position of the substructure. The strip-theory loads include the relative form of Morison's equation for the distributed fluid-inertia, added-mass, and viscous-drag components (NREL, 2021). The module, additionally, simulates the Ocean conditions as discussed in Section 2.3.2.

- ElastoDyn, which uses Newton's laws of motion, Kane's equations of motion for a holonomic system to compute the time variation of 17 DOFs for the entire coupled system. The DOFs pertain to tower, rotor, platform, nacelle, generator and drivetrain dynamics. The module sets the initial conditions, and incorporates the turbine configuration, mass distribution and stiffness for tower and blades along with many more input data (Jonkman & Buhl Jr, 2005a).

- ServoDyn, which defines the modeling options for the controller. Both dynamic link libraries (DLL) and structural control options (typically a tuned mass damper system) can be combined to simulate the controller. A multitude of different control strategies can be manually included; pitch control, torque control, nacelle-yaw control and high-speed shaft brakes (Moriarty & Hansen, 2005).

- Inflow Wind, which receives from the driver code (wrapper .fst file) the coordinate position of various points and returns the undisturbed wind-inflow velocities at these positions. The recreation process can be achieved via multiple wind types. The ones that have been selected and simulated for this project include; steady wind, uniform wind and binary TurbSim generated wind field (Platt et al., 2016).

- MoorDyn, which predicts the dynamics of typical mooring systems, specifically the mooring restoring matrix for HydroDyn, fairlead kinematics, nodes loads, accelerations and positions. It operates based on a lumped-mass approach to discretize the cable dynamics over the length of the mooring line. It is coupled with floating platform models for an interconnected simulation of a moored floating structure (Hall, 2015).

- SubDyn, which estimates the dynamic loading on multimember substructures. The substructure is considered to be connected by springs at the seabed, to simulate soil-structure-interaction and rigidly connected to the transition piece (TP). It relies on two main engineering schematizations; a linear frame finite-element beam model and a dynamics system reduction via the Craig-Bampton method (NREL, 2021).For the purposes of this work, SubDyn is only utilised in the development of the Monopile model.

- OLAF, which is thoroughly discussed in Section 2.3.4.

Loads and responses are transferred between the modules above via the FAST driver program (glue code) to enable hydro-aero-servo-elastic interaction at each coupling time step. All the modules are presented in the schematic floating illustration of Figure 2.6, except for OLAF and SubDyn. The former is included within the AeroDyn while the latter is specifically used for substructure bottom fixed dynamics.

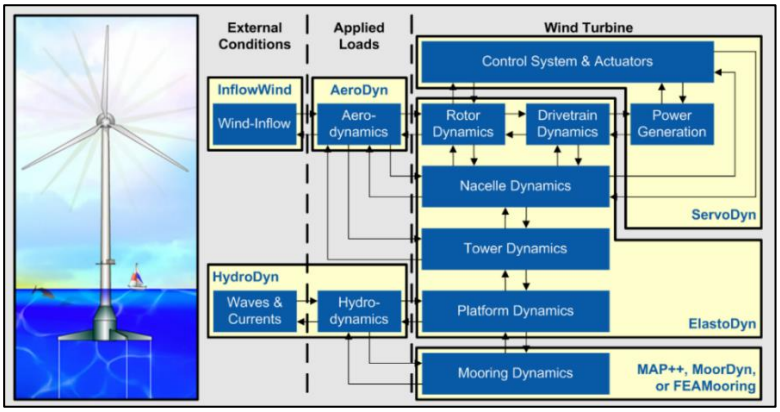

Figure 2.6 Full System Floating OpenFAST module interconnections (Jonkman, 2017).

2.3.2 Metocean Conditions

The ocean conditions include the current and wave kinematics which are incorporated in the OpenFAST model via the HydroDyn module. Firstly, the wave kinematics include regular (periodic) and irregular (stochastic), long-crested (unidirectional) or short-crested (with wave energy spread across a range of directions). For regular waves, the wave elevation, ζ, is represented as a sinusoid with a single amplitude and frequency, based on the input wave height ζ_α and wave period T. Due to their simplistic physical basis, regular waves prove inadequate for measured data recreation. Irregular or random waves are effectively used for that purpose, where multiple wave components are summed and superpositioned together to recreate the irregular sea state. They are described by an appropriate wave spectrum and for the scope of this project, the JONSWAP/Pierson-Moskowitz spectrum, S_J, is selected as defined in Equation 2.26 (peak shape parameter equals unity case). Additionally, it is highlighted that no second order wave kinematic phenomena are included for the scope of this work (Jonkman et al., 2015).

$$S_J(\omega) = \frac{5}{32\cdot\pi}\cdot H_s^2\cdot T_p\cdot\left(\frac{\omega\cdot T_p}{2\cdot\pi}\right)^{-5}\cdot exp\left[\frac{-5}{4}\cdot\left(\frac{\omega\cdot T_p}{2\cdot\pi}\right)^{-4}\right] \tag{2.26}$$

Where, H_s is the significant wave height and T_p is the peak wave period. Figure 2.7 illustrates a regular wave time history and an irregular wave superposition.

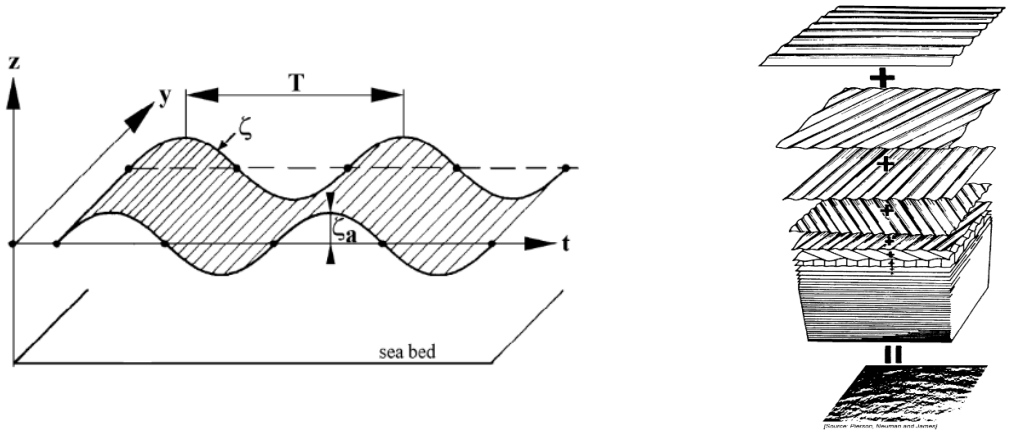

Figure 2.7 Regular wave time history (Left) & Irregular wave superposition (Right) (Journee & Massie, 2021).

The current model is also included within the HydroDyn module. It is composed of three sub-models, each one representing a different current form as defined by the offshore wind standards. Firstly, the sub-surface model recreates currents that are generated by tides, storm surge, atmospheric pressure

variations and the sub-surface current speed, V_{SS} is obtained via Equation 2.27. Secondly, the wind-induced near-surface currents are modelled by a linear distribution of the velocity with water depth, ending at zero. The corresponding current speed V_{NS} is obtained by Equation 2.28. The third model is a depth-independent model, which equates the current velocity to the constant inputted value across the water depth as set by the user. All three current sub-models are displayed in Figure 2.8 (Jonkman et al., 2015).

$$V_{SS}(d) = V_{0_{SS}} \cdot \left(\frac{d + d_{total}}{d_{total}}\right)^{\frac{1}{7}} \tag{2.27}$$

$$V_{NS}(d) = V_{0_{NS}} \cdot \left(\frac{d + h_{ref}}{h_{ref}}\right), \qquad d \in [-h_{ref}, 0] \tag{2.28}$$

Where, d is the local water depth parametric value, d_{total} is the total water depth, $V_{0_{SS}}$ is the reference current velocity for the sub-surface current model, $V_{0_{NS}}$ is the reference current velocity for the near-surface current model and h_{ref} is the reference water depth.

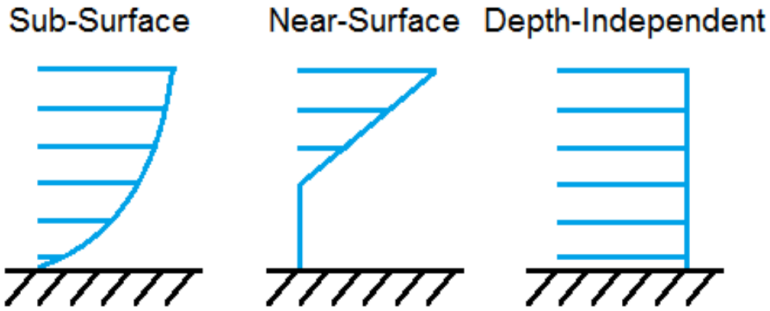

Figure 2.8 HydroDyn standard current sub-models (Jonkman et al., 2015).

As mentioned earlier, the wind field is generated by InflowWind in the cases of steady and uniform incoming wind and by TurbSim in the case of turbulent winds. Vertical shear is introduced in the wind profile via the power law as displayed in Equation 2.29, where z is the height and z_{ref} is the reference height above MSL. Horizontal shear and wind upflow angles are disregarded. Wind turbulence is added in the simulation through the von Karman model (Platt et al., 2016; Jonkman & Buhl Jr, 2005b).

$$V(z) = V(z_{ref}) \cdot \left(\frac{z}{z_{ref}}\right)^{0.14} \tag{2.29}$$

The directional definitions of metocean conditions in OpenFAST differ significantly from those used in the Hywind framework. In OpenFAST, the directional definitions are as follows: for wind, a direction from West to East is considered as 0°, while wind blowing towards the South is defined as 90°. Similarly, for waves and currents, a direction of propagation towards the East corresponds to 0°, while a direction of propagation towards the North is defined as 90°. It is important to note that in OpenFAST, the directional values represent the direction of propagation rather than the incoming direction. The relationship between the directional interpretations in OpenFAST and Hywind is extensively analyzed in Section 4.1 (NREL, 2021).

2.3.3 BEM Theory

The two aerodynamic models used to recreate the Hywind floating farm data are based on Blade Element Momentum (BEM) and Vortex Panel Method - Free Vortex Wake (VPM-FVW). Figure 2.9 illustrates the coupling mechanism of AeroDyn with both ElastoDyn and InflowWind modules. AeroDyn can utilise either BEM or FVW codes to achieve its objectives. The difference, however, lies in the desired precision level.

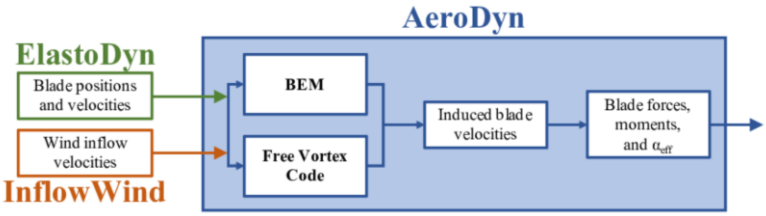

Figure 2.9 FVW and BEM integration within AeroDyn (NREL, 2021).

BEM is one of the most widely used aerodynamic solvers and is built upon the actuator disk theory. This method is the amalgamation of two separate premises, the blade element and momentum theories. The former introduces the blade division into incremental elements that act independently of surrounding elements. The incremental applied loads on these airfoils include lift, dL as obtained in Equation 2.30, drag, dD as obtained in Equation 2.31 and the normal force, dF_n distributed along the dr wide annulus as calculated in Equation 2.32. These forces are summed along the span of the blade to calculate the total forces and moments exerted on the turbine (Moriarty & Hansen, 2005; Zaaijer & Viré, 2022).

$$dL = \frac{1}{2} \cdot C_l \cdot \rho_{air} \cdot V_{res}^2 \cdot c \cdot dr \tag{2.30}$$

$$dD = \frac{1}{2} \cdot C_d \cdot \rho_{air} \cdot V_{res}^2 \cdot c \cdot dr \tag{2.31}$$

$$dF_n = dL \cdot \cos\varphi + dD \cdot \sin\varphi = N \cdot \frac{1}{2} \cdot \rho_{air} \cdot V_{res}^2 \cdot (C_l \cdot \cos\varphi + C_d \cdot \sin\varphi) \cdot c \cdot dr \tag{2.32}$$

$$V_{res} = \sqrt{\left(V \cdot (1-\alpha)\right)^2 + (\Omega \cdot r)^2} \tag{2.33}$$

$$\varphi = tan^{-1}\left(\frac{V \cdot (1-\alpha)}{\Omega \cdot r}\right) \tag{2.34}$$

The other half of BEM, the momentum theory, supports that the loss of pressure or momentum in the rotor plane is attributed to the airflow passing through the rotor disk on the blade elements. The thrust extracted by each rotor annulus is computed in Equation 2.35. Based on the flow's axial and tangential momentum loss, the induced velocities can be estimated. These induced velocities affect the inflow in the rotor plane and therefore also affect the forces calculated by blade element with Equation 2.36 connecting the two theories together. As a system of equations for dFn and dT is set and dependent on the induction factor, it can be iteratively solved for the induced velocities and the forces on each blade element. Figure 2.10 contains schematic configurations that represent the main parameters of BEM theory on an airfoil as well as the two even aerodynamic loads acting on the annulus (Moriarty & Hansen, 2005; Zaaijer & Viré, 2022).

$$dT = 4 \cdot \pi \cdot r \cdot \rho_{air} \cdot V^2 \cdot (1-\alpha) \cdot \alpha \cdot dr \tag{2.35}$$

$$dF_n = dT \tag{2.36}$$

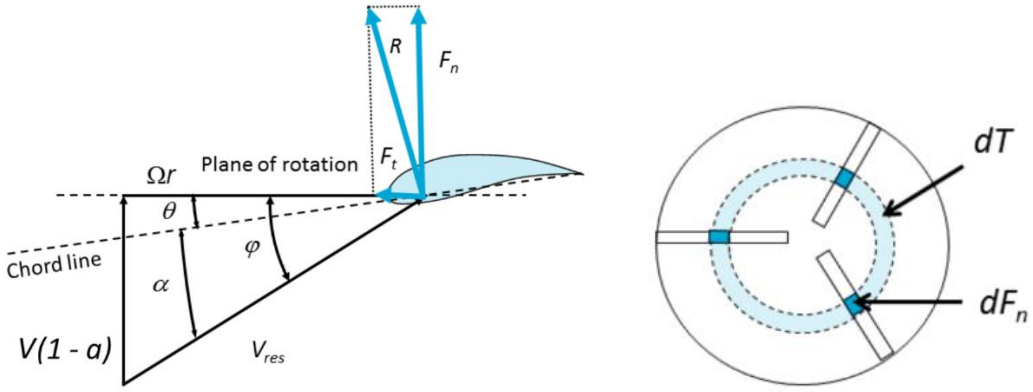

Figure 2.10 Main aerodynamic parameters on an airfoil (Left) & BEM principle configuration (Right) (Zaaijer & Viré, 2022).

Prior to initiating the solving process, it is important to acknowledge the limitations associated with the BEM despite its simplicity. Firstly, in reality, the airflow field around the airfoil is not steady and the changes in wake's vorticity have a delayed effect on the airfoil response. Contrasting, in BEM, two main simplifications are the constant airflow field's equilibrium around the airfoil and the downstream wind flow's instantaneous acceleration which accounts for the wake vorticity shift. Secondly, BEM does not model either hub and blade tip vortex (which affects the estimated induced velocities) or skewed inflow. Thirdly, due to BEM's blade element theory two-dimensional basis, it assumes little to none spanwise flow and spanwise pressure variation. An assumption that severely decreases BEM's simulating precision in rotors with large pressure gradients. Fourthly, as momentum equilibrium is hypothesised for a plane parallel to the rotor, any blade deflections that disrupt this plane configuration result in grave aerodynamic parameters errors. Finally, it does not consider the tangential component of the force, as it only equates the normal component to the thrust force (Moriarty & Hansen, 2005; Zaaijer & Viré, 2022).

OpenFAST offers multiple corrections that can be incorporated to increase the precision and realistic output of the BEM solution. These corrections include; tip and hub loss models to account for vortices shed at these locations, the Glauert correction to account for largely induced velocities, and the skewed wake correction to model the effects of incoming flow that is not perpendicular to the rotor plane. The corrections are employed in this project's OpenFAST model in order to increase the precision of its outcomes. Lastly, these corrections are presented thoroughly in the AeroDyn manual, where they are extensively discussed (Moriarty & Hansen, 2005).

2.3.4 OLAF Theory

A bound circulation lifting-line representation of the blades is used in OLAF. The spatial and time variation of the bound circulation results in free vorticity being emitted in the wake. The turbine wake is simulated in a time-accurate manner, therefore realistic phenomena are introduced in the model as vortices can convect, stretch, and diffuse. As illustrated in Figure 2.11, OLAF's turbine wake is discretized into Lagrangian position markers $\vec{r}$(defined by wake age, ζ and azimuthal position, ψ in polar coordinates) and a hybrid lattice/filament method is utilised (Shaler et al., 2020). The wake is initially simulated as helical, and due to being modelled in a time-accurate manner, realistic phenomena are introduced in the model. After this initial helical discretization, the wake is allowed to move and distort, thus changing the wake structure as the markers are convected downstream (Shaler et al., 2020).

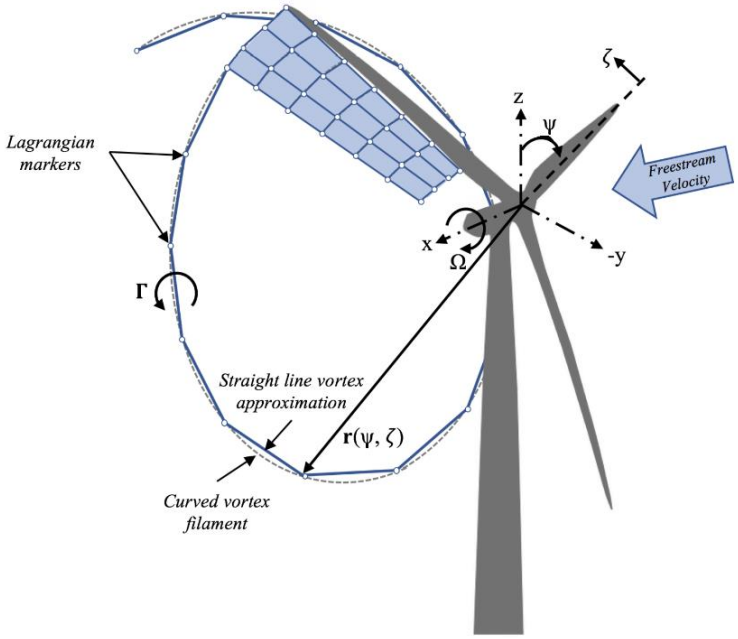

Figure 2.11 Development of Lagrangian markers, near-wake lattice and vortex approximation (Shaler et al., 2020).

A governing theorem supporting OLAF's background is the vorticity formula which represents the evolution of the wake vorticity as depicted in Equation 2.37. It is originally derived from the Navier-Stokes equations when assuming incompressible homogeneous flow in the absence of non-conservative forces. The forces exerted by the blades onto the flow are expressed through creation of vorticity, which is bound to the blade.

$$\frac{d\vec{\omega}}{dt} = \frac{\partial\vec{\omega}}{\partial t} + \underbrace{\left(\vec{V}\cdot\nabla\right)}_{convection}\cdot\vec{\omega} = \underbrace{(\vec{\omega}\cdot\nabla)\cdot\vec{V}}_{strain} + \underbrace{\nu\cdot\Delta\vec{\omega}}_{diffusion} \tag{2.37}$$

Where, $\vec{\omega}$ is the vorticity (velocity's curl) and ν is the kinematic viscosity. Vortex filaments are used to model the continuous vorticity distribution using a finite number of elements. These vortex filaments are delimited by two points, thus a vorticity tube with cross-section dS is developed between these limits. The total vorticity of the tube and the vortex filament are equal as shown in Equation 2.38, where $\vec{\Gamma}$ is the circulation strength of the vortex filament.

$$\vec{\omega}\cdot dS = \vec{\Gamma} \tag{2.38}$$

In OLAF, a lifting-line formulation represents the blades, where basically the loads are applied at each cross-section of the blade onto the mean line of the blade. Hence, this method neglects the geometrical effects of each cross section. The blade lifting-line and wake are discretized into a finite number of panels, each of them forming a four-sided vortex ring, as seen in Figure 2.12. The sides of the panels coincide with the lifting-line and the trailing edge of the blade. In Figure 2.13, it is illustrated that for each panel, a control point characterises the specific panel, a vortex ring follows its borders, the vortices rotate around this ring. The circulation of each panel is determined according to one of the three methods:

- Cl-Based iterative method, where the circulation is determined within a nonlinear iterative solver that utilizes the polar data at each control point on the lifting line.
- No-flow-through method, where the circulation is solved by satisfying a no-flow through condition at the 1/4-chord points.
- Prescribed circulation, where a constant user specified spanwise distribution of circulation is prescribed onto the blades (Shaler et al., 2020).

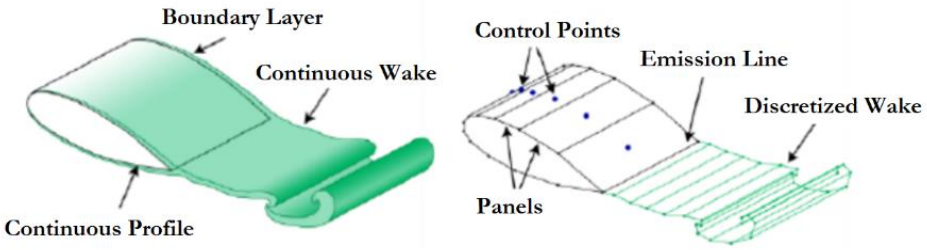

Figure 2.12 Actual continuous wake (Left) & OLAF simulated wake (Right) (Thibierge, 2020).

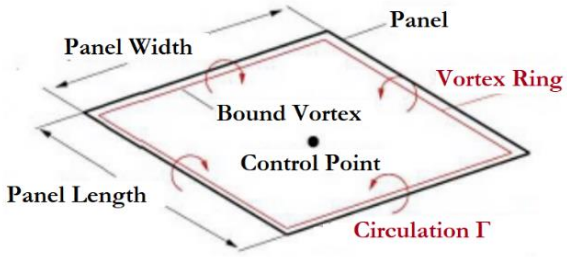

Figure 2.13 Schematic of vortex panel including vortex ring and circulation (Thibierge, 2020).

Equation 2.39 constitutes the governing equation of motion for a vortex filament. The velocity term is a nonlinear function of the vortex position, representing a combination of the freestream and induced velocities. The induced velocities at point k, caused by each straight-line filament, are computed using the Biot-Savart law, as seen in Equation 2.40 (Shaler et al., 2020). By substituting known parameters in the aforementioned formula, Equation 2.41 is produced.

$$\frac{d\vec{r}}{dt} = \vec{V}[\vec{r}, t] \tag{2.39}$$

$$d\overrightarrow{V_k} = F_v \cdot \frac{\Gamma}{4\pi} \cdot \frac{d\vec{l} \times \vec{r}}{|\vec{r}|^3} \tag{2.40}$$

$$\vec{V}(\vec{x}) = F_v \cdot \frac{\Gamma}{4\pi} \cdot \frac{(r_1 + r_2)}{r_1 \cdot r_2 \cdot (r_1 \cdot r_2 + \overrightarrow{r_1} + \overrightarrow{r_2})} \cdot (\overrightarrow{r_1} \times \overrightarrow{r_2}), \qquad with\ \overrightarrow{r_N} = \vec{x} - \overrightarrow{x_N} \tag{2.41}$$

Where, F_v is a regularization parameter, $d\vec{l}$ is an elementary length vector along the filament, $\vec{x}$ is the control point, $\vec{x}_1$ and $\vec{x}_2$ are the two edges-limits across the filament's length. Lastly, $\vec{r}$ is the vector between a point on the filament and $\vec{x}$. At last, the velocity at any point of the domain can be computed once all vortex filament induced velocities are summed and added with the primary flow vector, $\overrightarrow{V_0}$, as Equation 2.42 describes.

$$\vec{V}(\vec{x}) = \overrightarrow{V_0}(\vec{x}) + \sum_k \overrightarrow{V_k}(\vec{x}) \tag{2.42}$$

Chapter 3. Literature Review

In this chapter, the summaries of findings from past projects with relevancy to this work are discussed. Firstly, the FOWT energy yield reviews along with the metocean conditions effects on FOWT motion response and performance parameters are presented. Secondly, discrepancies that accumulate over FAST – OpenFAST model simulations against other validated codes that perform similar computations, smaller scale tank tests and real measurements comparisons are analysed. Lastly, comparative analysis results between BEM theory, VPM, Free Vortex Wake and other higher fidelity methods are discussed.

3.1 FOWT Energy Yield

In 2010, Karimirad & Moan conducted research to identify the effects of aerodynamic and hydrodynamic damping on a spar supported FOWT responses. The research was simulated in DeepC and HAWC2. They identified the two main platform DOFs influencing the system's motion response and performance to be surge and pitch. For the wind turbine's power performance to be of good quality (steady, non-oscillating and non-decreasing) the surge and pitch resonant responses as well as the wave frequency responses should remain low. The power performance is governed by the pitch oscillation and resonant responses. Overall, the quality of generated power increases as pitch resonant responses decreases.

In 2015, Farrugia et al. researched the aerodynamic characteristics of a FOWT using advanced vortex methods. Based on their outcomes, the existence of fluctuations in aerodynamic torque was verified during platform surge motions. Tip speed ratio directly influences the aerodynamic load response fluctuations, specifically, they increase simultaneously. The response amplitude linearly increases with surge velocity amplitude. As tip speed ratio increases, so does the difference between mean and steady power coefficient under surge conditions. A realisation which would not be noticeable by BEM simulations since full momentum equilibrium at all time instances is assumed. Additionally, the mean power and thrust coefficients vary with surge frequency with that variation depending on the rotor operating condition. Lastly, the mean power coefficient decreases with surge frequency at low tip speed ratios and increases at high tip speed ratios.

Tumewu et al., 2017 numerically simulated the power production influence of platform pitch motion in OpenFAST for multiple floating platforms, however a spar type was not included. Based on their outcomes, the power generation fluctuation depends heavily on the platform type while large oscillating pitch motions result in recurring power drops, basically directly affecting the power output's steadiness. Again, surge and pitch platform motion DOFs are considered critical influences on the FOWT performance.

Specifically, the effects of surge and pitch motion on both power and thrust of a spar FOWT were researched in Qblade by Wen et al., 2017 and Wen et al., 2018, respectively. They conducted a series of BEM, FVW and CFD investigations where the entire operating range was covered, including tip speed ratios, surge and pitch frequencies and amplitudes. Firstly, the outcomes for power-surge investigation are discussed. The surge motion causes applicable fluctuations in both power and thrust that are heavily attributed to varying angle of attack along the blade radius. Moreover, at low tip speed ratios, the mean power generation drops when the surge amplitude or frequency increase while the opposite is true for high tip speed ratios. Then, as surge amplitude or frequency increase, the mean power generation also increases. Regardless of the tip speed ratio value, surge motion causes the mean thrust to moderately decrease while both thrust and power variations are more prominent. These outcomes are displayed in Figure 3.1, where normalised power and thrust time series at different surge frequencies for high TSR are presented.

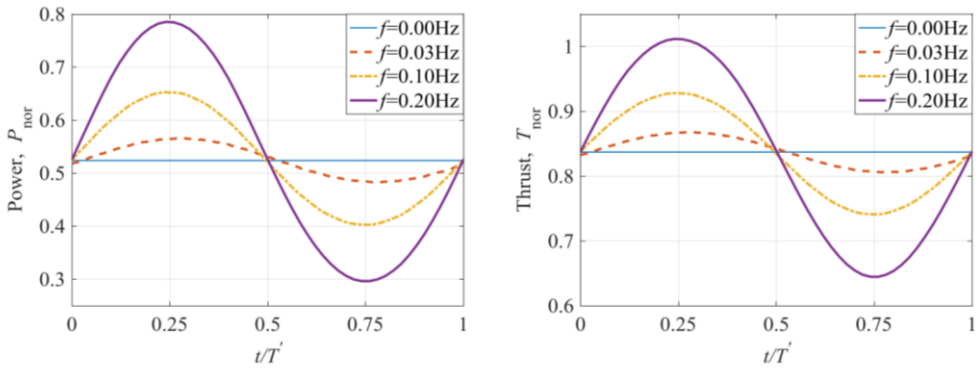

Figure 3.1 Normalised power (Left) and thrust (Right) time series for different surge frequencies at TSR = 8 and A =1.5 m (Wen et al., 2017).

Secondly, the power-pitch investigation outcomes are highlighted. The pitching motion on the spar introduces a time-dependent linear wind shear to the rotor which increases the FOWT power generation compared to a fixed foundation case. That is also the case for the design tip speed ratio of the simulated wind turbine under pitching condition. Although the mean power output increases, an increase in pitch frequency and amplitude leads to lower mean power coefficient and higher power fluctuation, an outcome that can be observed in Figure 3.2. As tip speed ratio increases so does the generated power variation, which is harmful to both power quality and FOWT components safety. For these reasons, a platform optimisation to minimise excessive pitching motion is recommended.

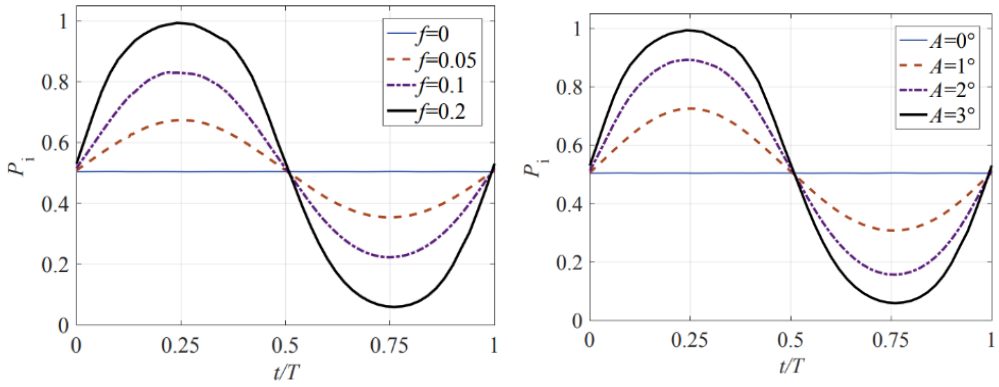

Figure 3.2 Instantaneous power output at different pitching frequencies for TSR = 7 and A = 3° (Left) and at different pitching amplitudes for TSR = 7 and f = 0.2 Hz (Right) (Wen et al., 2018).

Comparable results are presented by Johlas et al., 2020 in their research of spar floating platform effects for below rated wind speed and extreme wave height conditions on power generation. The simulations were performed in OpenFAST with the NREL 5 MW reference wind turbine. The power production gains and losses are primarily attributed to surge and pitch. Under the conditions described above, the platform pitch angle causes a rotor pitch angle increase which briefly reduces power. However, the pitch and surge effects combined lead to upwind-downwind dynamic rotor motion which momentarily increase the power output. This is caused by relatively higher wind speeds experienced by the rotor. Although the remaining platform DOFs (sway, heave, roll and yaw) also result in rotor displacement, the average power is negligibly influenced. Due to the characteristic structure of spar itself, the low center of mass leads to large pitch dominated rotor motions that eventually surpass the rotor pitch angle. These large pitch oscillations tend to take place throughout the FOWT process to find its converged quasi-static equilibrium position. Due to that, an overall power gain of 3.1% to 4.5% compared to fixed bottom wind turbine is achieved.

With regards to the converged quasi-equilibrium position of a spar type floating wind turbine, it is determined by Yu et al., 2015 that it stems mainly from combined wind and wave action as well as mooring dynamic loads. Specifically, the distance between initial position and new equilibrium position is affected mainly by the wind load while the oscillation around that position results from wave load excitation.

Different wind and wave direction effects on a dynamic floating spar's motion and displacement are reported by Luy et al., 2019 in OpenFAST. For a wind stream constantly blowing in the incident surge direction, the DOFs of surge and motion are most significantly coupled with wind and wave effects. This is mainly attributed to the characteristics of the Spar-type floating structure. The six DOFs have direct relation to the incoming wind and wave directions. Pitch experiences a maximum rotational displacement when incident wind and waves are codirectional, while surge, sway, heave, roll and yaw peak when they are perpendicular. Based on frequency domain analysis, it is found that the motion modes of sway, roll and yaw are predominantly simulated by wave loads while surge, pitch and heave are largely affected by both.

Continuing with dynamic wind and wave effects, Li et al., 2020 investigated them along with the influence of nacelle's yaw error on floating wind turbine power generation, motion and structure load in OpenFAST for a semi-sub platform. When metocean conditions and yaw are observed separately, power efficiency and stability are directly affected by yaw error as the output drops while power fluctuation becomes more prominent. Additionally, yaw error has negligible effects on structure load and wind turbine motion, wind-wave misalignment strongly affects both. This misalignment does not affect the wind turbine's performance. Once wind-wave misalignment and yaw error are combined, the FOWT's performance is affected so a combined approach is suggested.

Huang & Wan studied the interference effects of spar platform and wind turbine under wind-wave excitation in 2019. The NREL 5 MW wind turbine and OC3 Hywind spar platform are CFD simulated in order for the effects on surge, heave, pitch and yaw to be analysed. The local angle of attack seen by the rotating blades are affected by both the platform's pitch angle, pitch angular velocity and surge velocity. The first two DOFs additionally affect the local relative wind speed at the blades. Under the same wind-wave conditions, platform pitching results in five times greater aerodynamic load fluctuation compared to surge platform motion induced. Additionally, the platform motion results in double fluctuation of power compared to thrust, thus making power more sensitive. Yaw and heave do not result in aerodynamic load fluctuation. The three aforesaid comments can be also drawn from Figure 3.3's bar graphs. Once the shaft tilt and prone-cone angle are also included in the model, large platform pitching causes a drop in the mean power production. Lastly, uncoupling the platform motion DOFs generates greater FOWT motion responses compared to coupled platform motions. The heave DOF is an exception, as in coupled simulations the heave displacement is larger.

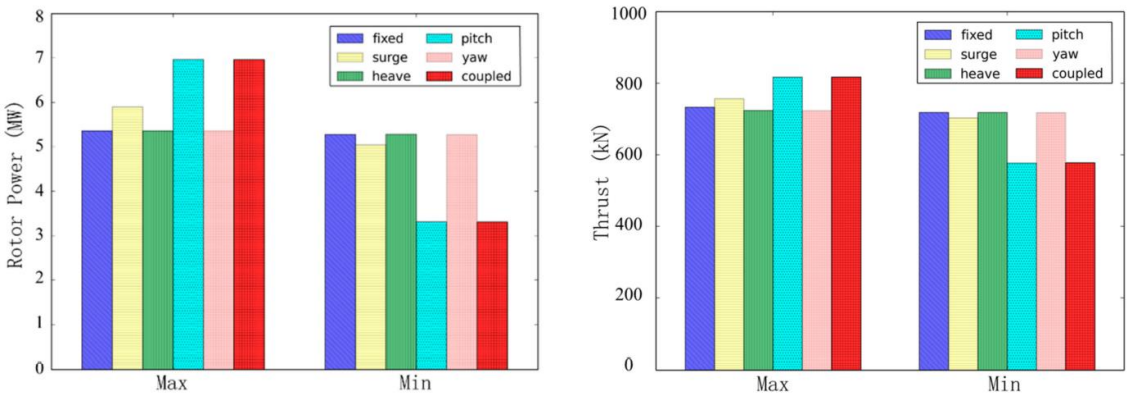

Figure 3.3 Comparisons of maximum and minimum values of power and thrust under different DOF platform motions (Huang & Wan, 2019).

Identical outcomes were observed by Lee & Lee, 2019 in their investigation of FOWT platform motion effects on aerodynamic performance for the NREL 5 MW wind turbine using the Vortex Panel Method (VPM). In single DOF motion simulations, it is shown that the DOFs of surge and pitch influence the power and thrust outputs. These platform motions induce variations in the blade angle of attack seen by the streamwise - incoming wind velocity. The aerodynamic and performance results experienced severe oscillation from the aforementioned platform DOFs oscillations. The two oscillation frequencies were consistently interrelated. Lastly, from multi-DOF floating platform comparative simulations, the barge-type platform yielded severe fluctuations in its wind turbine performance. The results for bottom fixed as well as floating type (spar, barge and TLP) power and thrust results are included in Figure 3.4.

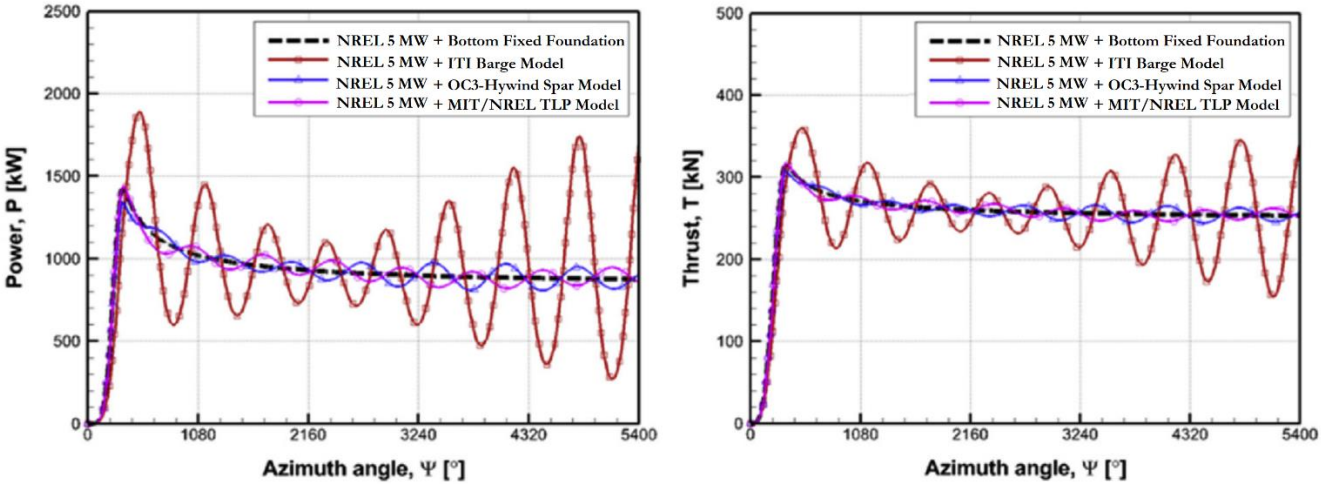

Figure 3.4 Thrust and power fluctuation for BOWT and different FOWT platform types (Lee & Lee, 2019).

Lerch et al, 2019 investigated the environmental effects, mainly waves, on the energy yield of a spar floating wind turbine with focus on surge, pitch and heave motions. An OpenFAST inspired and validated simplified MATLAB model was used for the simulations. The aerodynamic solver does not consider vortex ring states, time varying rotor induction, skewed inflow or blade-vortex interactions. Based on the findings, even an extreme wave and wind combination does not cause a power loss higher than 1.1% compared to a BOWT. The original power curve obtained by the BOWT and the curves of FOWT for multiple (significant) wave heights are compared in Figure 3.5 for the cases of regular and irregular waves. As for the governing motion influences, surge and pitch are affected by the mean wind speed, while heave remains mainly unaffected despite the metocean conditions. The heave behaviour is attributed to the balancing nature of the spar-buoy. Lastly, the aforementioned DOFs display peak responses at rated wind speed, when all the effects acting on the wind turbine are amplified.

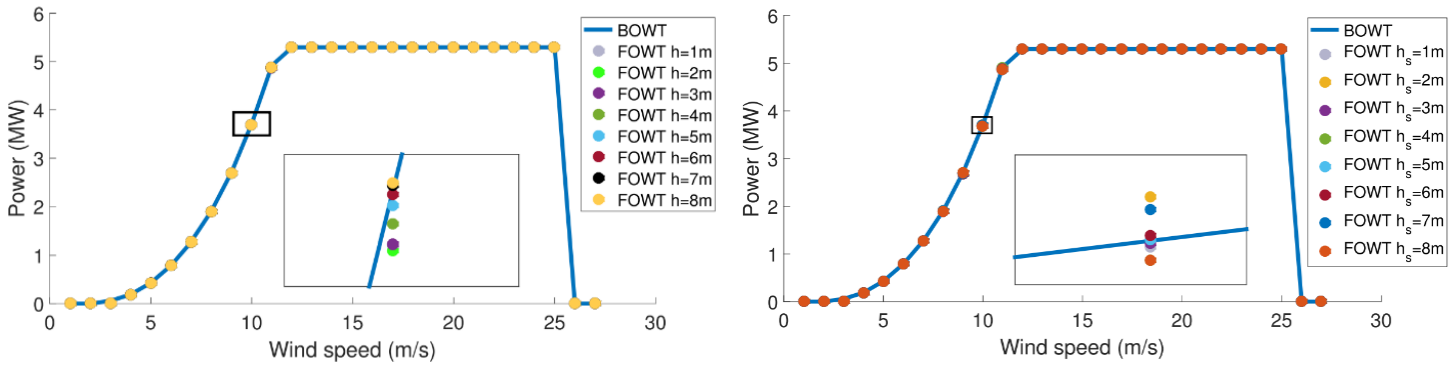

Figure 3.5 BOWT and FOWT power curve comparison for regular waves with wave height (Left) & irregular waves with significant wave height (Right) (Lerch et al, 2019).

In the energy yield computing scope of the project, Martini et al., 2015 researched the metocean conditions influencing the FOWT energy production. Their evaluating methodology entails, other than dynamic FOWT modelling, interpolation techniques for scattered data, selection methods and meteorological reanalysis databases. In this research numerical limits in the values of hub acceleration and tower tilt are incorporated to assess the WT operation. Once the limits are exceeded, to eliminate the chance of unwanted mechanical or electrical component damage, the wind turbine seizes operation and no power generation occurs, thus the energy yield is affected. Specifically, for the location of coast of Santander, Spain, the capacity factor over the span of 20 years under the condition of no shutdowns is 39%. The capacity factor severely drops once the limits are surpassed and / or harshen. Moreover, these restrictions directly affect the platform motions, effectively reducing the amplitudes of motion DOFs.

The power generation increments of a floating 15 MW reference wind turbine were investigated by Ramponi, 2022 for the coupling combinations of pitch-surge and pitch-yaw. Based on the outcomes, for a BEM aerodynamic model, the platform yaw DOF does not affect the mean power output, while the pitch and surge effects are dominating. The mean power outputs experience oscillations, attributed to the platform's varying pitch and surge responses, as observed in Figure 3.6 for both rated and above rated conditions. The introduction of a controller in the wind turbines servo-dynamic response results in a power loss due to operational transfer between below and above rated wind speeds.

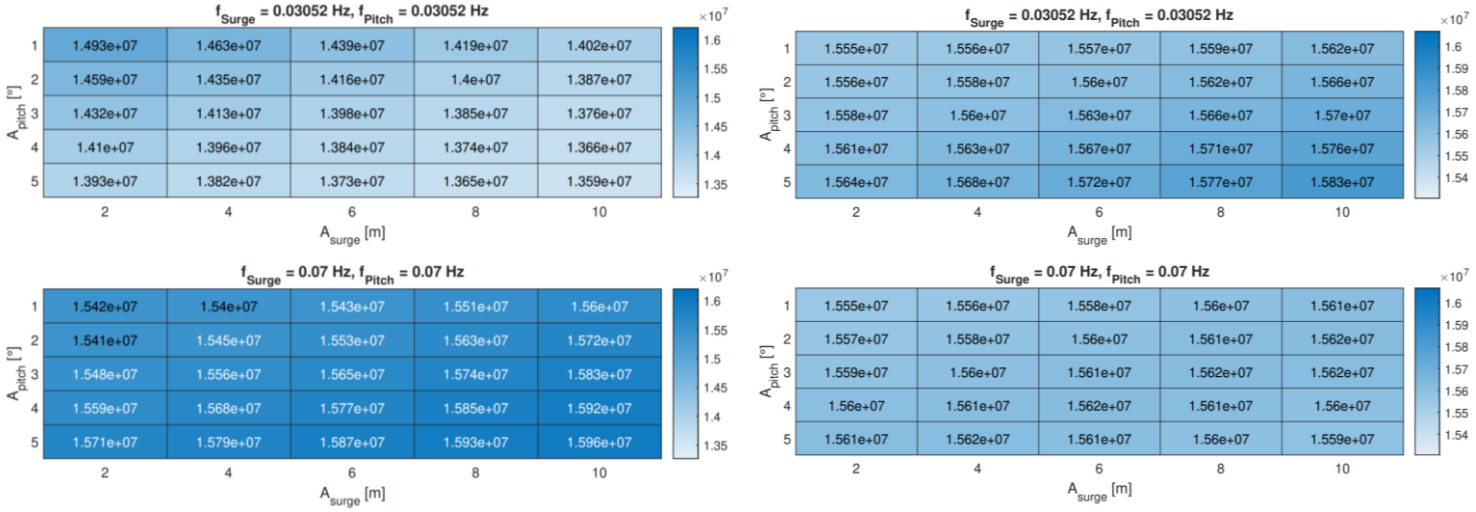

Figure 3.6 Comparison of rated and above rated operational conditions power output for varying platform pitch and surge (Ramponi, 2022).

3.2 FAST & OpenFAST Model Validation

A FAST model validation against numerous FOWT dynamic modelling codes-techniques was initially performed by Jonkman et al., 2010 during the phase IV of OC3, where a OC3 Hywind spar supported NREL 5 MW wind turbine was modelled. Specifically, ADAMS, Bladed, HAWC2, 3Dfloat, Simo, Sesam and DeepC were used during this comparative analysis. Based on the outcome conclusions, in the case where radiation damping is unsignificant, either Morison's equation (with augmented hydrostatics and wave excitation heave forces) or potential flow theory (with augmented Morison drag forces) can be used to predict the hydrodynamic loading. As for the natural frequencies, the majority of the codes (FAST included) display good agreement on the platform six DOF eigenfrequencies. The natural frequency results are included in Figure 3.7. Lack of additional linear hydrodynamic damping is directly shown in the un-damped simulation results. Overall, FAST agrees well with the different codes, however under regular waves and coupled simulations, the generated power, rotor speed (both included in Figure 3.7)

and out of plane tip deflection are all slightly underpredicted. Under irregular waves, the parametric density spectra produced by FAST mostly are in accordance with the rest of the generated outcomes.

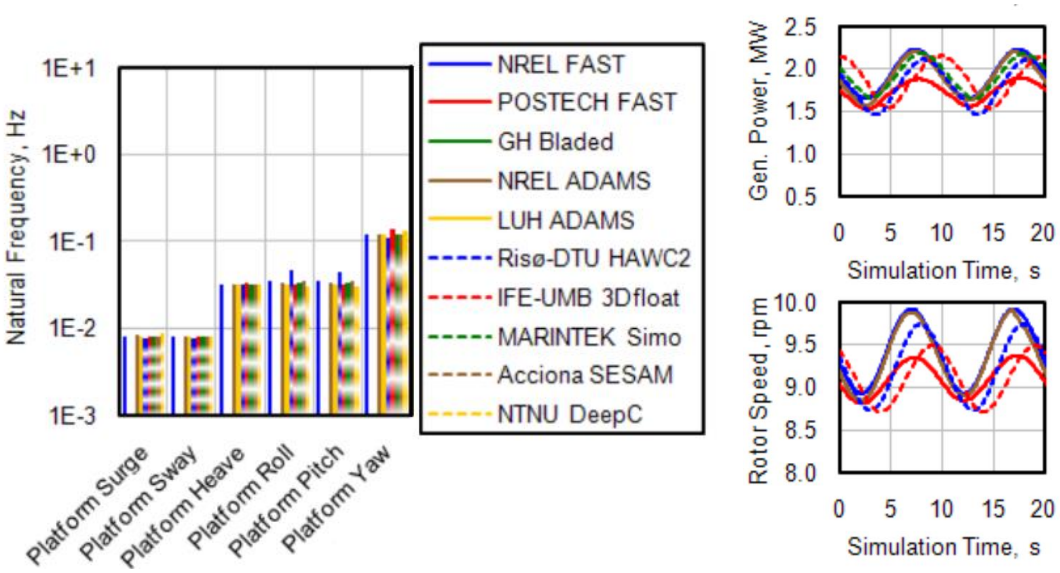

Figure 3.7 Natural frequency for platform's six DOFs (Left) and generated power, rotor speed comparisons for multiple FOWT modeling tools (Jonkman et al., 2010).

FAST's validity was also verified against the engineering modelling tools for FOWT, S4WT and SIMPACK by Duarte et al., 2013 for a spar supported FOWT. The three modelling tools produced similar results with FAST offering higher computational efficiency, overall. Specifically, for the spar motion results, FAST predicts them accurately compared to the other two software. The only exception is the heave DOF, as FAST simulates a lower mean value which is attributed to FAST also over predicting the tower base force. For both fixed and spar-floating cases, the natural frequencies calculated by all three tools appear to be in good accordance. Lastly, FAST blade tip deflection results are underpredicted again, while the blade root loads (both shear force and moment mean values) are higher.

As for the semi-sub supported FOWT configuration, Robertson et al., 2017, compared multiple wind turbine simulating codes for their ultimate and fatigue loads in a similar process to Jonkman et al., 2010. Although this project will not analyse any specific design load cases to compute these values, the general outcomes and conclusions of their work are included. In wave loading cases, FAST underpredicts both ultimate and fatigue loads while in wind cases the results became more accurate for ultimate loads. The most significant underestimation of the loads occurs during the low frequency response regions, which is connected to the resonance effect of the surge and pitch DOFs. This discrepancy might be attributed to lower level of wave excitation achieved by the modelling theory.

Progressing from code comparative validation to measured-experimental data benchmarking, the FAST model of the Statoil-Hywind FOWT demo was verified by Driscoll et al., 2016 against the Statoil's spar offshore measurements. The metocean conditions were recreated by TurbSim and FAST. The former produced wind fields based on the measured wind velocities while the latter generated statistically alike wave motions. The natural periods of platform DOFs were precisely predicted once the mooring stiffness, line lengths, tower and blade mass distributions were appropriately adjusted. Additionally, the Siemens provided power curve is predicted by the FAST model for both bottom fixed and floating conditions. As observed in Figure 3.8 a slight overestimation occurs in power region 2, slightly below the rated wind speed point. The platform motion responses were recreated with concurrence to the measurements for low and moderate sea states. The yaw DOF is not properly recreated by the FAST model. Similar is the case for roll response at low wave frequencies. The servodynamics also reproduced rotor speed and blade pitch data with good agreement to the measured ones. Lastly, blade moment effects

were also captured well by the FAST simulation in a statistical comparison, although FAST underpredicted the edge-wise moment at higher speeds and overpredicted the flap moment fluctuation.

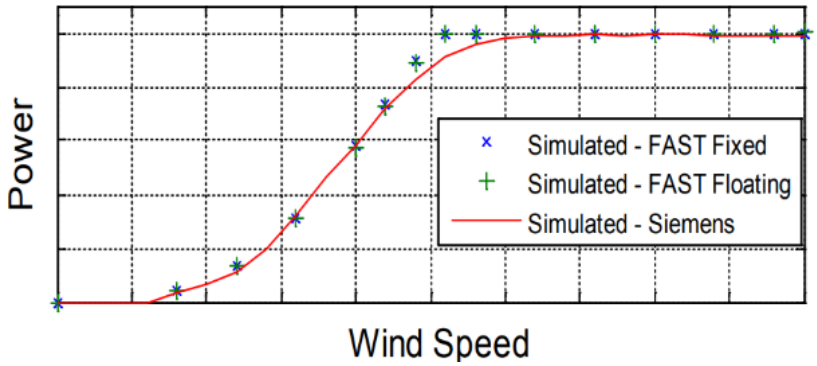

Figure 3.8 Power curve comparisons between FAST model simulations for spar-fixed and spar-floating and Siemens specified curve (Driscoll et al., 2016).

Long et al., 2018, while researching the dynamic response of a 6 MW spar FOWT, validated their BEM OpenFAST model against wind turbine measurements. Reference and simulation results are displayed in Figure 3.9, where a great agreement is observed for a still base (disabled platform motion DOFs) wind turbine's power and thrust outputs. Specifically, the maximal power and thrust measurement-simulation result differences are −2.74% and 4.54%, respectively. It is concluded that OpenFAST's fully coupled aero-hydro-servo-elastic time domain model is reliable.

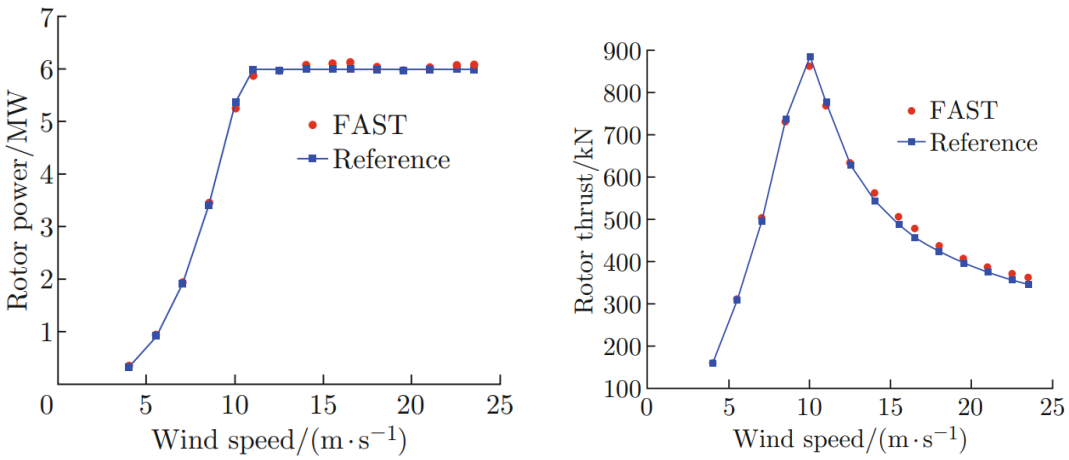

Figure 3.9 OpenFAST simulated and measured results comparison for rotor thrust and power (Long et al., 2018).

A 1/50th scale test tank model results of a 5 MW wind turbine supported by multiple different platforms, spar type included, were used to validate FAST by Robertson et al., 2013. The spar experimental apparatus is displayed in Figure 3.10. The same experimental configuration also assisted in achieving a higher level of comprehension on complex dynamic motion and performance response behaviour of FOWT structures. Firstly, in the hydrodynamics module, viscous drag is modelled only for constant diameter cylinders located at platform's centerline. Although this issue affects TLP and semi-sub platforms, spar is not affected. Secondly, the mooring lines were not dynamically modelled as FAST used to use a quasi-static mooring line model in the form of MAP++. However, currently the addition of MoorDyn module in OpenFAST allows for dynamic mooring line representation where the water and seabed effects on mooring lines are included. Therefore, this conclusion is considered obsolete (Hall, 2020). Thirdly, in order for the experimental outcomes to be properly recreated, the FAST simulation needs to include sum and difference frequency excitation as well as mean drift. These requirements are

highlighted as not including them would result in underpredicting extreme system responses. Lastly, FAST simulations precision can increase if a time signal of wave height was directly inputted instead of wave excitation modelling via wave spectrum selection.

A similar method of FAST simulation validation was completed by Coulling et al., 2013. Again, the results were compared against a 1/50th scale NREL 5 MW FOWT experimental model in a wind/wave basin but this time for a semi-sub floating platform. The experimental configuration is illustrated in Figure 3.10. In the case of pure wind loading, FAST accurately predicts the experimental outcomes (statistic-, time-series- and PSD-wise). In pure wave load cases, the linear wave energy response was also properly recreated by FAST with the mean drift and second order difference frequency effects not been incorporated in FAST by then. As for the cases of wind - wave combination, the FAST simulated data were also in a good agreement with the experimental ones. As this validation focuses on an older version of FAST for a different type of floating platform, the main takeaway is FAST's general simulation unity with the experimental outcomes.

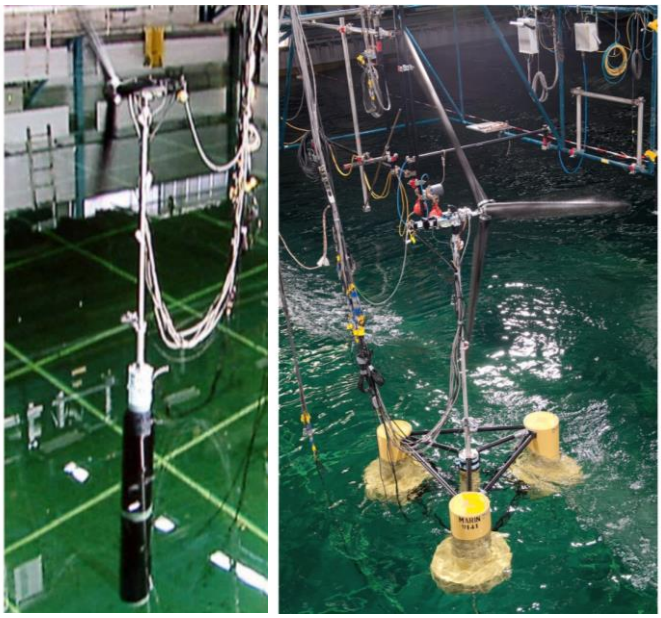

Figure 3.10 Spar type and semi-sub experimental apparatus in test tanks (Robertson et al., 2013 ; Coulling et al., 2013).

Two years later, Browning et al., 2015 validated FAST against the results of a 1/50th Froude-scaled model in tank tests, the experiments were performed for a 5 MW spar supported FOWT. Once more, the simulated natural frequencies results match the experimental measurements with a slight pitch and roll inconsistency of 8%. The free decay tests for heave and yaw decay were accurately damped in the simulations, however, this was not the case for the remaining four DOFs. Pitch and roll had added damping while surge and sway were lacking. Overall, the experiment - simulation responses compared well with differences occurring scarcely in the cases of periodic and irregular waves.

The same year, an open 1:6.5 scale sea testing of a hybrid tension-leg spar-type platform was conducted by Robertson et al. to validate the sway FOWT response and wind induced tower loads in FAST. By comparing the simulated and experimental results of Table 3.1, it is observed that tower wind loading interferes significantly with the WT system motion response under no operating conditions (which mainly happens for high wind speeds). Overall, by including tower loading in these conditions the simulation errors become insignificant. The interference effects decrease under power producing conditions as the primary wind-induced loads act on the rotor instead of the tower. They attribute FAST's main inaccuracies to lie in the model's inabilities to recreate properly the existing wave conditions and to represent the multidirectional waves behaviour. Additional errors stem from not proper usage of

metocean data in the development of the model, however these affect the specific case investigation and are not ascribed to FAST itself.

Table 3.1 Spar motion DOF mean and standard deviation values for non-operating (Left) and operating conditions (Right) (Robertson et al., 2015).

DOFs	Experiment	FAST (with Tower Load)	FAST (w/o Tower Load)	Experiment	FAST (with Tower Load)	FAST (w/o Tower Load)
Pitch (Mean)	10.73092 °	7.35102 °	5.13869 °	12.90595 °	13.95103 °	12.69992 °
Pitch (Std)	2.02462 °	2.20998 °	1.87538 °	1.05561 °	2.63459 °	2.54336 °
Surge (Mean)	2.84368 m	2.18756 m	1.52206 m	6.76051 m	4.03822 m	3.69268 m
Surge (Std)	0.52778 m	0.61528 m	0.52537 m	0.34020 m	0.72369 m	0.71435 m
Roll (Mean)	-1.86967 °	-0.12633 °	-0.10568 °	1.63395 °	-1.43630 °	-1.30943 °
Roll (Std)	2.04729 °	0.65069 °	0.63543 °	0.66471 °	0.98300 °	1.03791 °
Sway (Mean)	1.02630 m	0.04125 m	0.03307 m	0.31973 m	-0.32309 m	-0.29564 m
Sway (Std)	0.56352 m	0.18503 m	0.17650 m	0.19840 m	0.18473 m	0.19001 m

3.3 BEM – VPM in FVW / OLAF Aerodynamic Model Comparison

Sant et al., 2014 conducted research on validating the power performance of BOWT and FOWT against experimental results for BEM and Lifting Line (LL) FVW methods. While the OWT was supported by a bottom fixed platform, under steady conditions, the axial thrust, and power coefficient measurements were recreated accurately. When the OWT is supported by a TLP platform, the aerodynamic models showcased increased power fluctuations compared to reality which scaled with the surge velocity of the platform. Additionally, the fluctuations are linked through an elliptical relation with the surge displacement. For the FVW method, the wave conditions along with tip speed ratio region influence the result accuracy as for higher tip speed ratios the power deviations were more prominent compared to lower TSR values. The mean floating power coefficient deviated slightly from the bottom fixed case. The above observations were not reproduced by the BEM model, therefore proving the limitations of BEM theory in catering complex FOWT phenomena. Phenomena that become more prominent and influence the FOWT motions and system performance stronger at higher tip speed ratios. Therefore, as tip speed ratios increase, FVW methods gain a strong advantage compared to BEM. These phenomena are additionally enhanced by the platform's surge motion.

In 2016, Tran et al. conducted a CFD study into the influence of unsteady aerodynamic interference on floating turbine surge motion. The CFD results were compared to FAST's aerodynamic models, BEM and generalized dynamic wake (GDW), which can be considered an outdated version of OLAF. GDW is based on a potential flow solution to Laplace's equation and entails wake modelling in its simulation, thus increasing its accuracy level compared to BEM (Moriarty & Hansen, 2005). The unsteady aerodynamic loads affecting the rotating blades greatly alter the surge motion DOF is included in the simulation. The vortex wake development and interactions are also strongly affected by the downstream and upstream WT movement. Although these effects will not be elaborated upon further, it should be highlighted that they are fully neglected in BEM aerodynamic simulations. Additionally, compared to CFD, both BEM and GDW overpredict the unsteady power and thrust coefficients fluctuation caused by the blades' rotation effect from the tower under surge motion, as seen in Figure 3.11. Lastly, GDW generates a more precise mean power coefficient value compared to BEM, while both overestimate the mean thrust coefficient compared to CFD results.

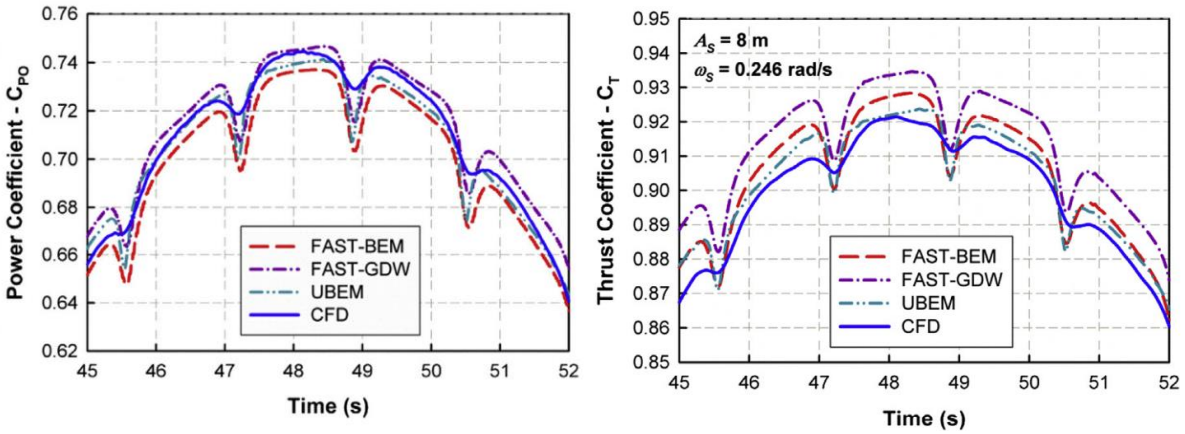

Figure 3.11 Tower interference effects on thrust (Left) and power coefficients (Right) on a FOWT model under surge motion for A_s = 8 m and ω_s = 0.246 rad/s (Tran et al., 2016).

Next, Ramos-Garcia et al., 2021 investigated the IEA 15 MW spar FOWT higher fidelity vortex methods through LL modelling to BEM in a MIRAS and HAWC2 coupled simulation. Based on their outcomes, the two aerodynamic approaches differ the most under high wind speed-regular wave conditions. Their differences scale with wave frequencies where at high ones, BEM overestimates the platform motion DOFs amplitude by more than 50% compared to LL. These outcomes can be seen in Figure 3.12, where a few BEM and LL comparative results are presented. Specifically, it is witnessed that BEM predicts higher power and thrust oscillations which can be attributed to different aerodynamic damping values. In BEM, the FOWT experiences larger platform motion oscillations, mainly in the y global coordinate direction.

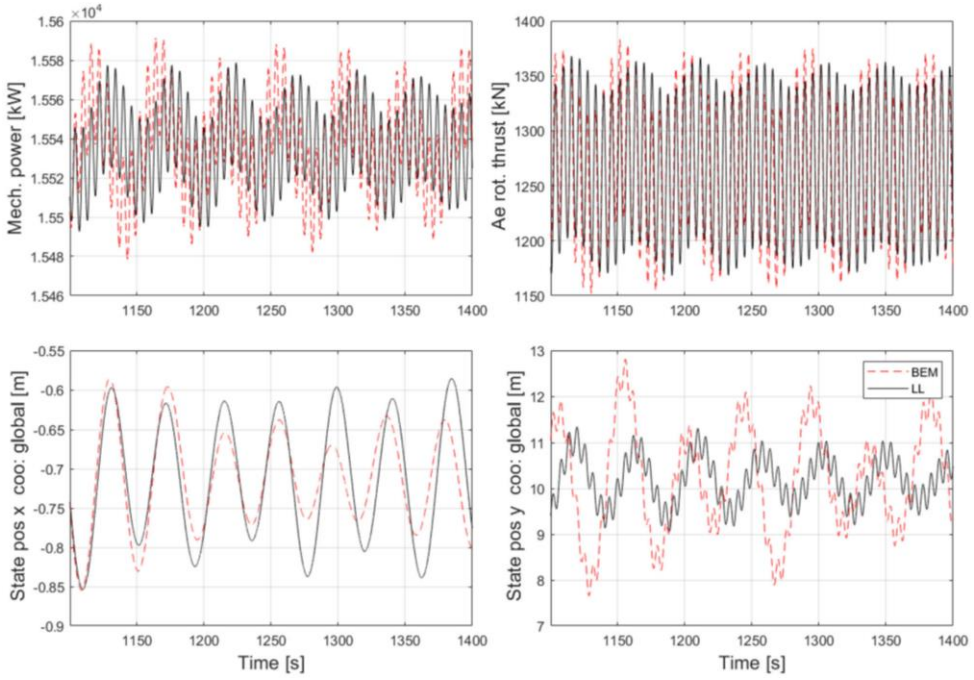

Figure 3.12 Comparison between BEM and LL methods for regular 2 m, 6 s period waves at incoming wind flow of 15 m/s (Ramos-Garcia et al., 2021).

The BEM theory was directly contrasted to the Free Vortex Wake (OLAF) method for a bottom fixed wind turbine (both the 5 MW NREL and IEA 15 MW structures) in OpenFAST by Pereira Malveiro, 2022. These two methods are additionally compared to the higher fidelity Actuator Line Method (ALM). For the bottom fixed case, the thrust coefficient results were more coherent compared to the power

coefficient ones. This is attributed to similar blade thrust calculating methods for the same airfoil data and blade elements. The aforementioned aerodynamic modelling techniques differ significantly in wind flow and upstream wake development, thus the power generated in each case differs considerably. For instance, ALM and OLAF predict greater power generation compared to BEM, which stems from BEM underpredicting the axial velocity reduction, hence less wind power is harvested. The power and thrust coefficients for the NREL 5 MW wind turbine are presented in Figure 3.13. Although OLAF is computationally more expensive compared to BEM, OLAF simulating convergence has greater credibility as it includes the developed wake and vorticity filed in it. A key difference between BEM and OLAF since BEM is complacent in modelling the blade elements in an actuator disk configuration for its simulations. Thus, between the two, OLAF's power output estimation is considered more precise at this case.

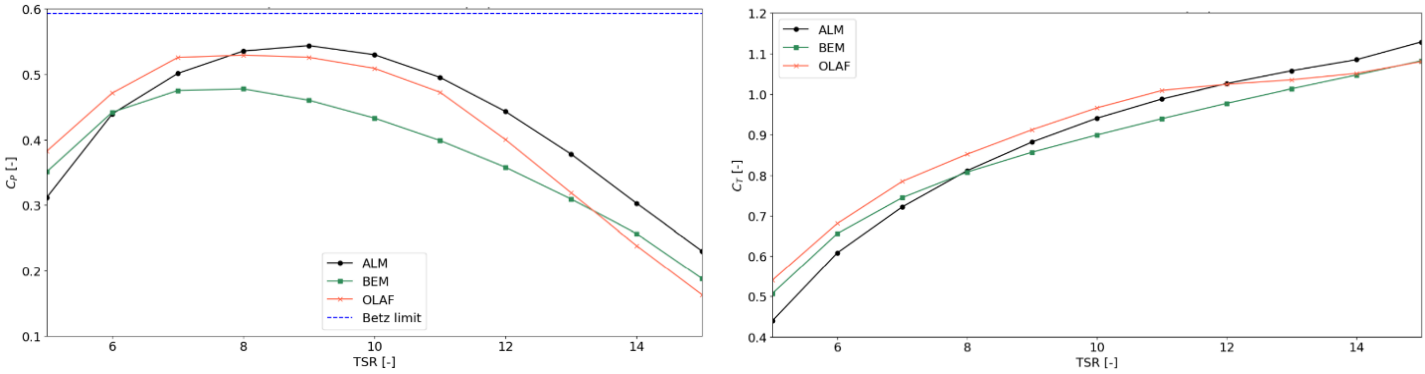

Figure 3.13 BEM, OLAF and ALM bottom fixed WT power and thrust coefficient comparison against TSR (Pereira Malveiro, 2022).

The FVW and BEM aerodynamic models were also compared by Bergua et al., 2022 during the validation research for aerodynamic loading on a FOWT rotor caused by the floating platforms large motion. OpenFAST along with other software were used to simulate BEM, dynamic BEM (DBEM), FVW and CFD models whose results were later verified against the measurements of a 1:75 scale experimental test. Under steady wind conditions (along with constant rotor speed and blade pitch), the aerodynamic thrust force is accordingly estimated by all models except for some FVW and CFD solutions that produce higher results compared to the measured data. However, the aerodynamic torque is underpredicted by the majority of the models (FAST BEM & FAST OLAF included). Under unsteady wind inflow (varying rotor speed and blade pitch), BEM, as it does not include dynamic inflow simulating capabilities, predicts lower values for thrust and torque in comparison to the other modelling approaches as seen in Figure 3.14. By combining the unsteady rotor speed with platform motion, the mean BEM load fluctuation amplitudes experience a 9% decrease compared to the higher fidelity - dynamic inflow- simulating modelling solutions (FVW included). Similarly, unsteady blade pitch with platform motion results in 18% higher BEM load fluctuation amplitudes. Concluding, although outcomes on the FOWT power performance contrasting between BEM and OLAF were not presented, an explanation behind OLAF superior results precision is provided in the form of dynamic flow inclusion. The steady BEM outcome about FAST concurs with the one asserted by Kimball et al., 2012 a decade ago. Basically, the FAST simulations precisely predict the system motion response under steady wind conditions. Once dynamic wind inflow is included, the accuracy level drops.

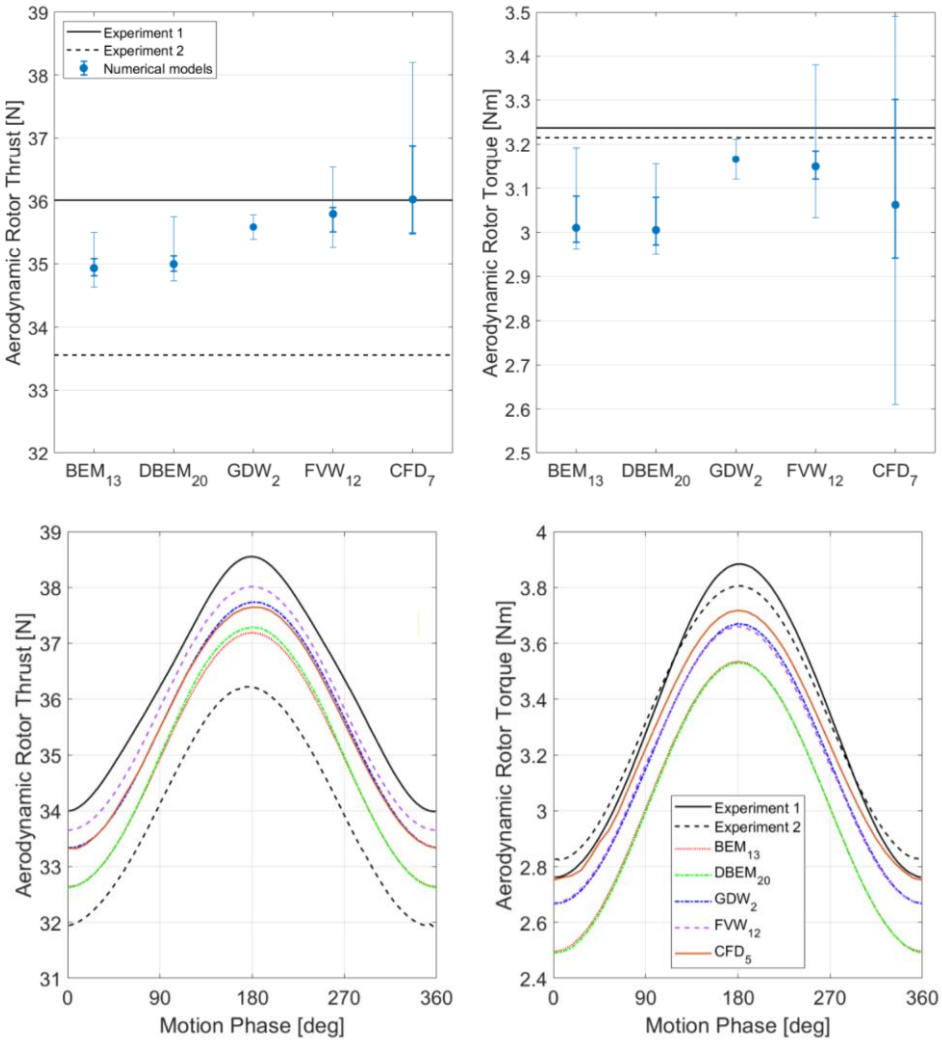

Figure 3.14 Experimental – different simulation models comparison for aerodynamic rotor thrust and torque under steady (Top) and unsteady wind conditions (Bottom) (Bergua et al., 2022).

Most recently, Wang et al., 2023 reviewed numerous aerodynamic models (BEM, FVW & CFD included) and solvers (FAST included) on simulating FOWT. A confirmed, well-established by now conclusion was reiterated, pitch and surge are crucial elements to the numerical FOWT thrust and power results. For high TSR and around the rated wind speed, the wind flow is attached and lead to aerodynamic output increase compared to a bottom fixed structure. Moreover, in high TSR regions, the aerodynamic coefficients values tend to change depending on the aerodynamic model used which is prominent in the two graphs of Figure 3.15. As the surge oscillation frequency and amplitude raises, the dynamic inflow effects become more distinguished, thus BEM simulations are in an accuracy disadvantage compared to FVW. Increasing surge frequency causes a hysteresis in flow shifts introduction to the aerodynamic model, resulting in power gains and thrust loss under surge motion at the nominal TSR region, which is captured only by FVW, not BEM. With regards to high pitch motion influence (frequency and amplitude wise), aerodynamic coefficients fluctuate by 32.8%. FOWT motion effects on power generation are additionally presented among the conclusions of their investigation. For pitch motion, backward platform motion increases the mean power generation while forward motion, the thrust and moments may increase. For surge motion, mean power experiences gains as mean thrust values experience loss.

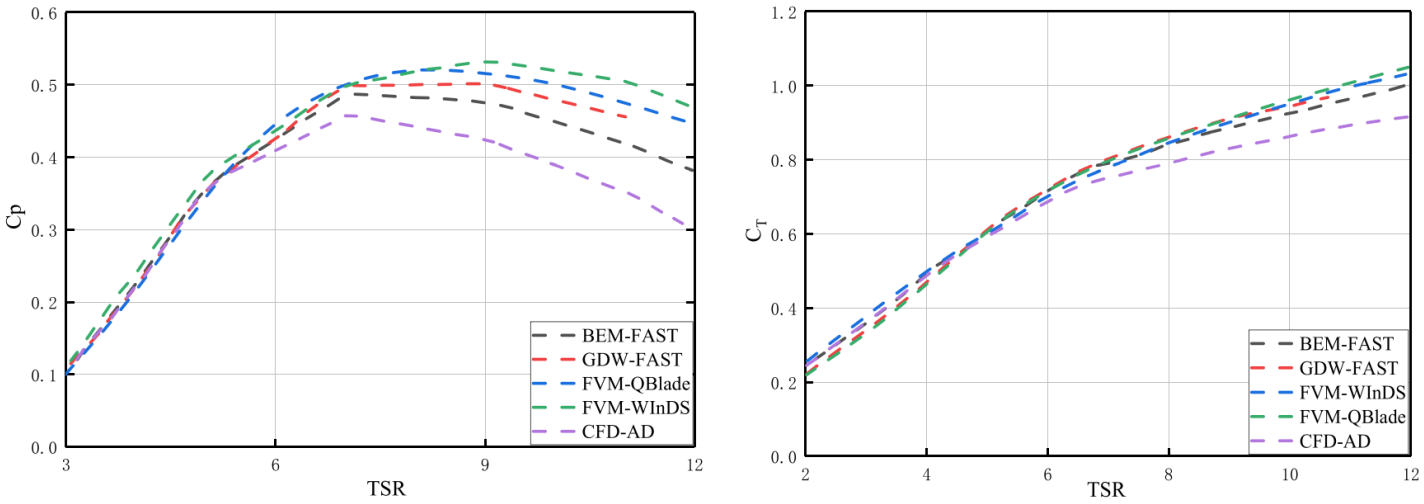

Figure 3.15 Power and thrust coefficients against TSR for different aerodynamic models (Wang et al., 2023).

Chapter 4. Model Development & Methodology

In the fourth chapter, initially, the set-up of the metocean conditions in OpenFAST is presented and then the steps followed to approximate the Hywind 6 MW wind turbine commissioned at Hywind, Scotland are discussed. Moreover, the floating spar and bottom fixed monopile foundation models developed along with the respective comparative upscaling results are analysed.

4.1 Metocean Conditions in OpenFAST

The provided Hywind measured data and OpenFAST modules have different directional definitions that need to be made compatible prior to modelling. The directional interpretations in each case were analyzed in Section 2.2.2. Moreover, they are illustrated in Figure 4.1 for completeness. In the case a 0 is placed next to a cardinal direction, that direction defines where the wind, wave or current propagates towards, whilst the arrow indicates the positive angle of 90°. It is highlighted that the Hywind wind and wave directions, although, they are measured as incoming, are converted to propagating for a less complicated methodology to be developed. Simple formulas were used to transform the measured wind, wave and current data from Hywind's perspective to OpenFAST's, as seen in Equations 4.1, 4.2 and 4.3.

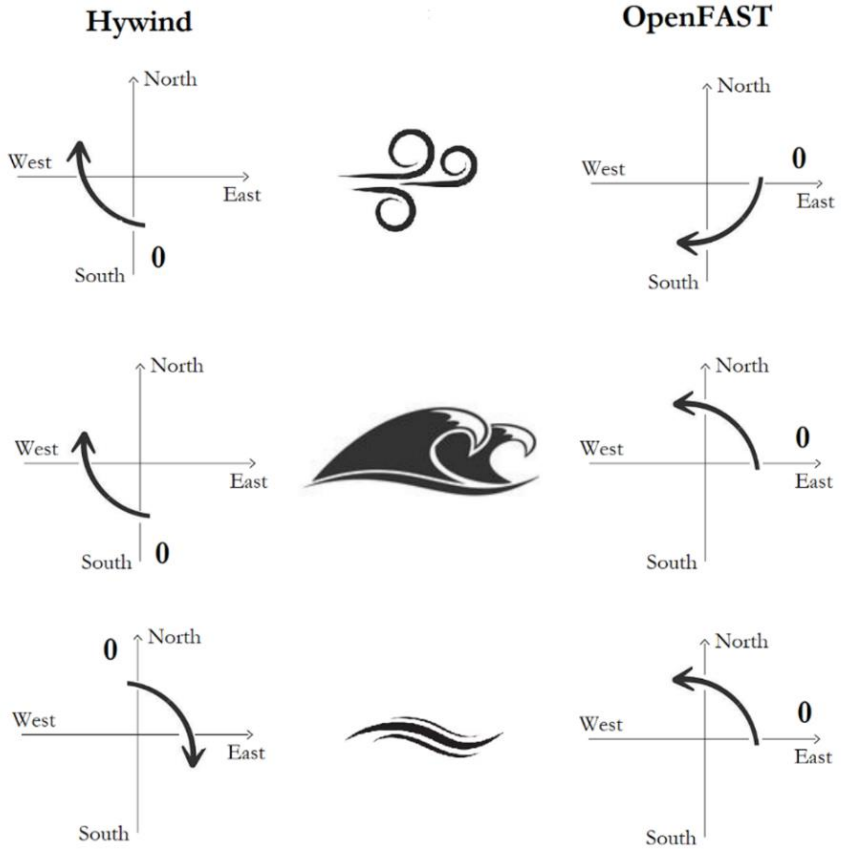

Figure 4.1 Hywind & OpenFAST directional definition for wind, wave and current.

$$\theta_{wind,OF} = \begin{cases} \theta_{wind,HW} - 270, & when\ \theta_{wind,HW} > 90 \\ \theta_{wind,HW} + 90, & when\ \theta_{wind,HW} < 90 \end{cases} \quad (4.1)$$

$$\theta_{wave,OF} = \begin{cases} 270 - \theta_{wave,HW}, & when\ \theta_{wave,HW} > 90 \\ -\theta_{wave,HW} - 90, & when\ \theta_{wave,HW} < 90 \end{cases} \quad (4.2)$$

$$\theta_{curr,OF} = \begin{cases} \theta_{curr,HW} - 270, & when\ \theta_{curr,HW} > 180 \\ 90 - \theta_{curr,HW}, & when\ \theta_{curr,HW} < 180 \end{cases} \quad (4.3)$$

In terms of wind inflow simulation, TurbSim was utilized to generate turbulent wind fields. However, it should be noted that there are slight differences observed between the resulting time series and the collected Hywind measurements. In order to highlight the deviation, Figure 4.2 illustrates specific cases from the measurements, namely Case 8 (below rated), Case 1 (above rated), and Case 4 (idling - above cut-off). It is important to clarify that the wind speed values are provided in two ways: first, through Equinor's statistical documents where mean and STD values are given, and second, through the actual measured undisturbed and corrected time series data. The input values for TurbSim are based on Equinor's statistical calculations, and throughout this report, all Hywind related generated wind fields are determined using these values. For each case, the mean reference wind speed is provided at the reference height, z_{ref}, of the hub height at 99m, as occurs from the tower base height of 13 m and added 86 m tower height.

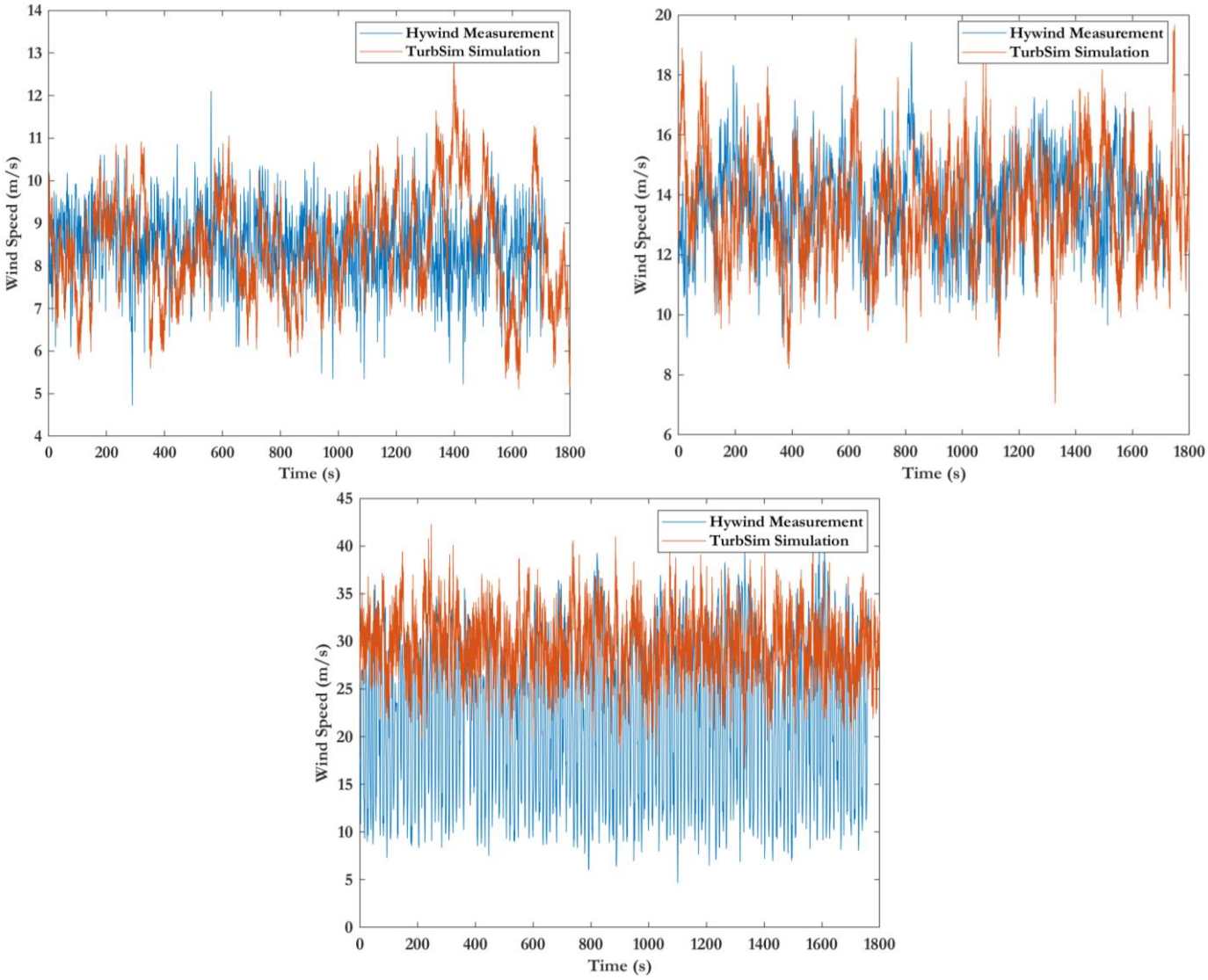

Figure 4.2 Wind Speed comparison between Hywind measured and TurbSim generated value for Case 8 (below Rated), Case 1 (above rated) and Case 4 (idling - above cut-off).

4.2 Wind Turbine Modelling

Investigation was conducted to retrieve additional data on the wind turbine, spar platform and mooring system. Unfortunately, due to wind turbine's design confidentiality, there is a severe lack of data that will have to be estimated using different techniques. Data related to the floater, mooring system, tower-blade and controller speed parameters are presented in Table 4.1, Table 4.2, Table 4.3 and Table 4.4, respectively. The values of drag and added mass Morison coefficients, C_D and C_A, are additionally included in the tables. Their values are based on literature acceptable values as seen in Equation 4.4 and OpenFAST simulation runs to adjust them accordingly and receive more precise data recreation (TU Delft, 2018).

$$C_D \in [0.6, 1.6]$$
$$C_A \in [0.5, 1.0] \quad (4.4)$$

Table 4.1 Overview of spar buoy parameters (Equinor, 2018).

Top Geometry (m)	Length: 12 Diameter: 9.45
Taper Geometry (m)	Length: 15
Bottom Geometry (m)	Length: 58 Diameter: 14.4
Draft (m)	77.6
Displacement (m³)	11754
Morison Coefficients (-)	C_D: 1.6 C_A: 0.5
Axial Morison Coefficients (-)	C_D: 1.6 C_A: 0.5

Table 4.2 Overview of controller speed parameters (Bussemakers, 2020).

Cut in Wind Speed (m/s)	4
Rated Wind Speed (m/s)	12
Cut-off Wind Speed (m/s)	25

Table 4.3 Overview of tower & blade parameters (Bussemakers, 2020).

Blade Length (m)	Apex-Root: 1.5 Root-Tip: 75.5
Blade Cone Angle (deg)	-2.5
Rotor Shaft Tilt Angle (deg)	-5
Tower Diameter (m)	Bottom: 7.5 Top: 4.85
Tower Base Height (m)	13
Tower Height (m)	86
Tower Drag (-)	0.5

Table 4.4 Overview of mooring system parameters (Equinor, 2018).

Anchor Radius (m)	640
Length (m)	Bridle: 50 Main Line: 609.7
Diameter (mm)	Bridle: 137 Main Line: 142
Wet Mass per unit Length (kg/m)	Bridle: 347 Main Line: 394
Morison Coefficients (-)	C_D: 1.6 C_A: 1.0
Axial Morison Coefficients (-)	C_D: 0.6 C_A: 0.5

4.2.1 Model Upscaling

Once the majority of the required parameters were acquired, they were utilized as inputs for the OpenFAST modules. However, it is important to note that due to limited data availability, certain inputs had to be derived from the reference NREL 5MW wind turbine model and scaled up using simple quantity scaling laws. Furthermore, several provided data could not be directly used in the modules, necessitating additional steps in the process. For instance, the blade and tower masses provided required further manipulation since the corresponding OpenFAST module inputs are based on mass per unit

length distributions. Therefore, the overall masses were determined based on a combination of acquired data and existing NREL distributions, as depicted in Figure 4.3. Moreover, the blade twist angle θ_{twist} and chord length c were scaled upon the existing model via Equation 4.5 and Equation 4.6, respectively. Lastly, blade and tower stiffnesses were proportionated based on the notion of Equation 4.7 (Zaaijer, 2021). In order for all three formulas to be valid, the same condition is required.

$$\frac{\theta_{twist,new}}{\theta_{twist,ref}} = \frac{\lambda_{ref}}{\lambda_{new}}, \qquad when \quad \frac{r}{R_{new}} = \frac{r}{R_{ref}} \tag{4.5}$$

$$\frac{c_{new}}{c_{ref}} = \frac{\lambda_{ref}^2 \cdot R_{new}}{\lambda_{new}^2 \cdot R_{old}} \tag{4.6}$$

$$\frac{S_{new}}{S_{ref}} = \left(\frac{R_{new}}{R_{ref}}\right)^3 \tag{4.7}$$

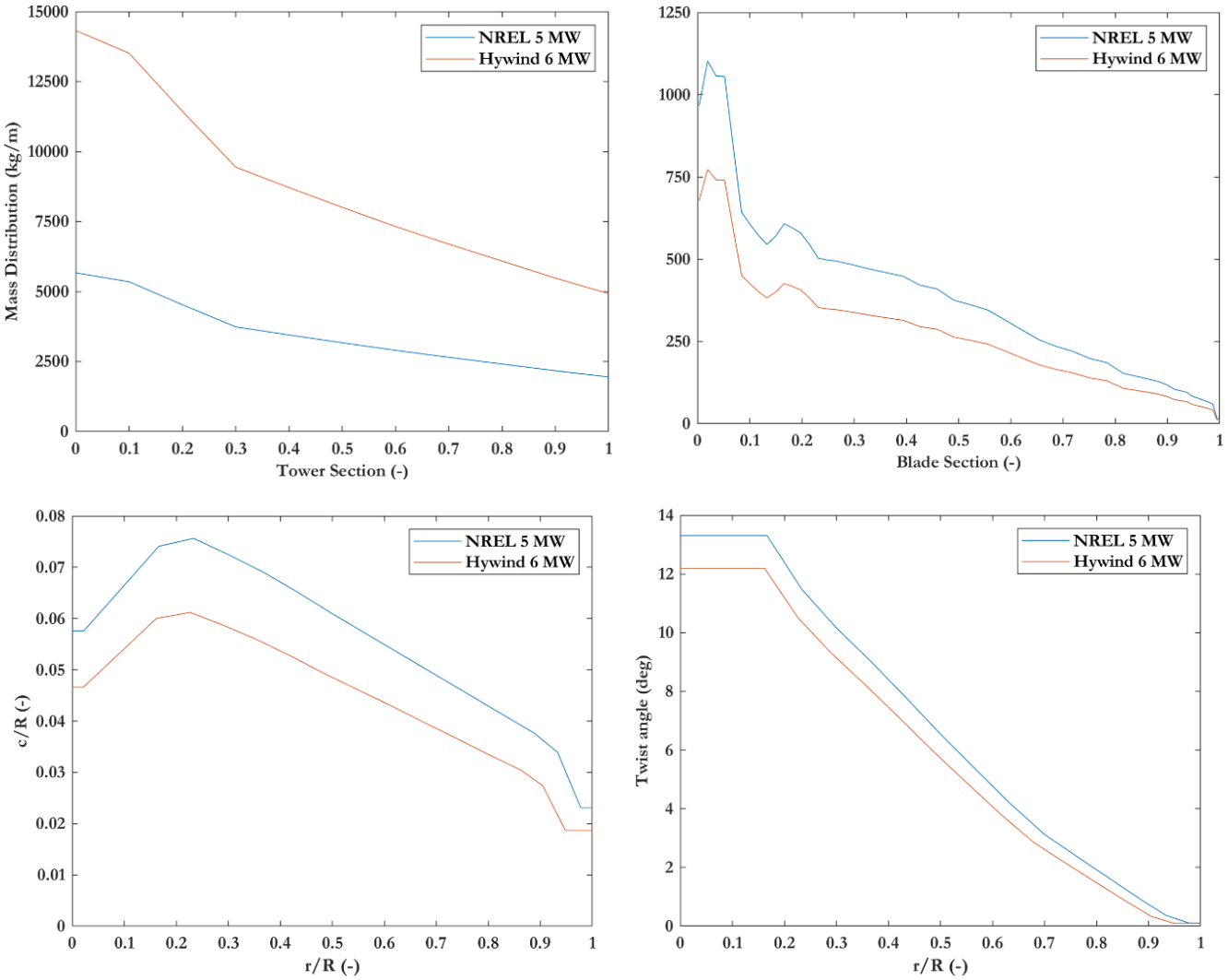

Figure 4.3 Upscaling of tower & blade mass distributions (Top), blade chord to radius and blade twist angle based on the reference NREL 5 MW data (Bottom).

The fully realised rendered wind turbine and blade models are presented in Figure 4.4 alongside the reference NREL 5 MW configuration. The ParaView 3D models presented in this study effectively demonstrate the process of upscaling and incorporating updated effects. However, a comparison between the upscaled Hywind model and the original NREL blade model reveals noticeable differences in terms of airfoil outlines and distributions. These variations were necessary in order to achieve a closer resemblance to the recreated data.

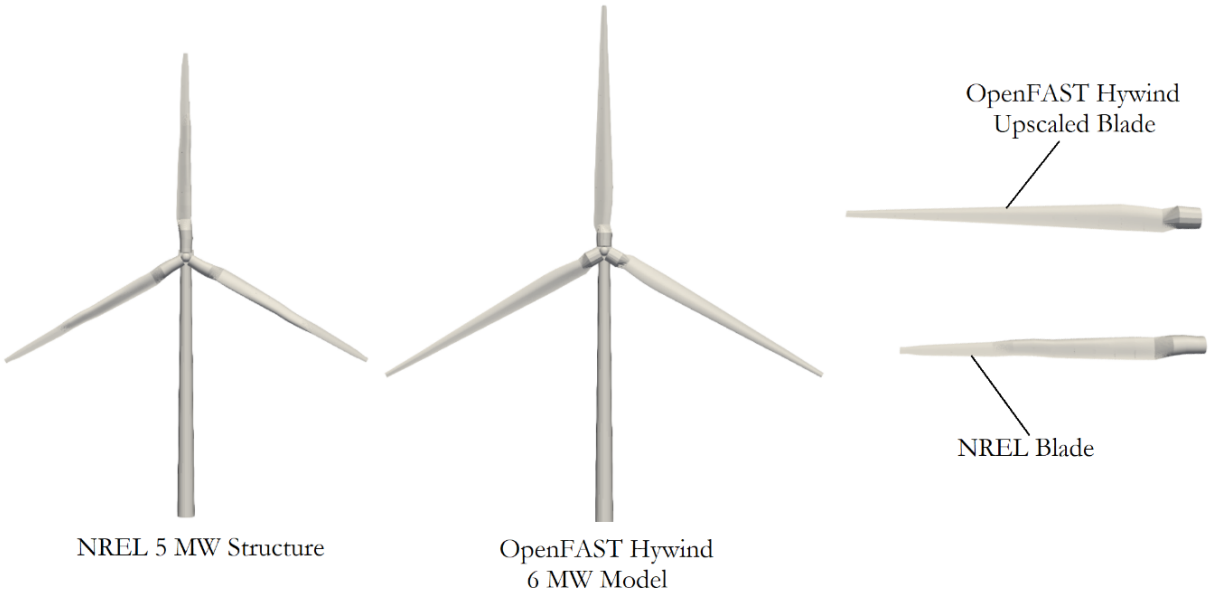

Figure 4.4 ParaView comparisons of renderred NREL & OpenFAST Hywind wind turbine structures and blades models.

4.2.2 Airfoil Distribution

The selection and incorporation of airfoil profiles and distribution for the Siemens' Hywind wind turbine have been important and challenging aspects of this project. In the initial stages of modeling, guidance from industry wind turbine modeling engineers led to an attempt to include specific blade airfoils based on certain thickness-to-chord ratios from airfoil repositories. Consequently, five airfoils were incorporated, in addition to the simple cylindrical root airfoils, with their corresponding airfoil coefficients presented in the left graph of Figure 4.5. However, it was discovered that these repository-documented airfoils exhibited lower lift and drag coefficients compared to the actual Siemens airfoils, as confirmed by industry officials. This discrepancy could be attributed to the significantly smaller Reynolds numbers during the testing of the repository airfoils. Interestingly, the 5 MW NREL-provided airfoils, which are part of the OpenFAST base model, proved to be a closer match to the real Siemens wind turbine in terms of aerodynamic coefficients (guidance from industry experts). The final selected airfoils' coefficients are presented in the right graph of Figure 4.5. While the initial airfoils were excluded from the finalized model, they are mentioned here to exemplify the intriguing evolution of the model.

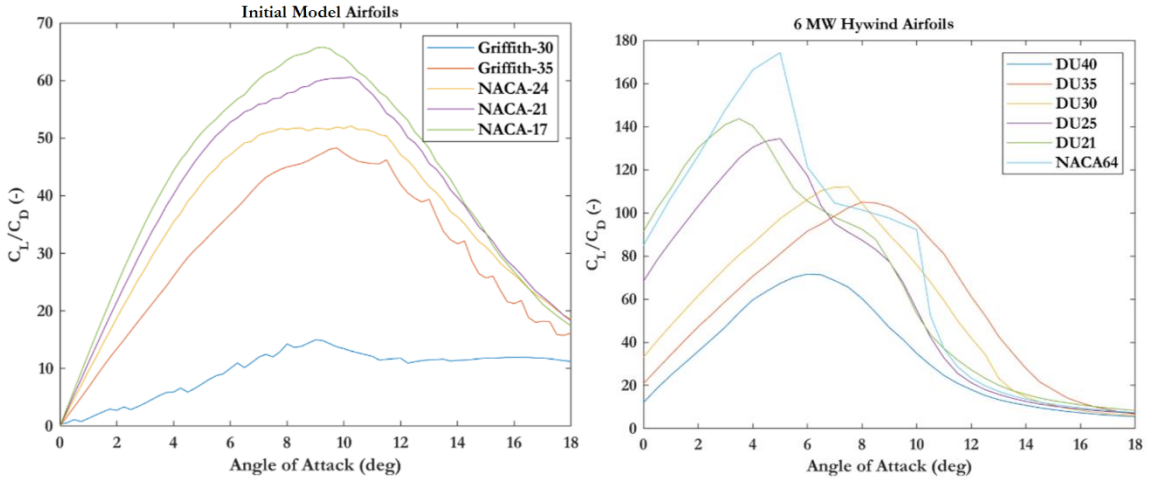

Figure 4.5 Lift over Drag coefficients of the preliminary-repository based airfoils (Left) & the final-Siemens based selected Hywind airfoils (Right).

The NREL airfoils that were ultimately chosen for inclusion in the model were accompanied by an updated blade distribution. This distribution aimed to maintain a thickness to chord ratio equal to or lower than 30 beyond the 50 m blade span threshold, as advised by industry experts. The updated airfoil distribution is showcased in Table 4.5 while the upscaled blade and airfoil profiles are illustrated in Figure 4.6.

Table 4.5 Airfoil Distribution along the blade span.

Airfoil Distribution		Blade Span (m)
1	Cylinder	8.09
2	DU 40	26.71
3	DU 35	46.14
4	DU 30	51.00
5	DU 25	55.85
6	DU 21	64.76
7	NACA 64	75.5

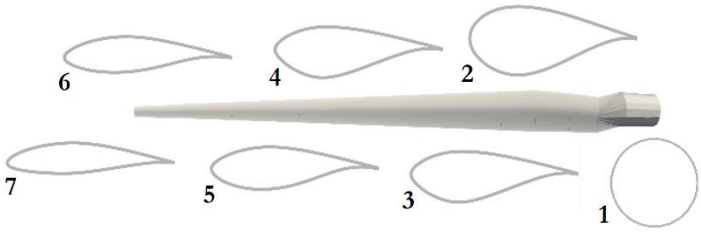

Figure 4.6 Upscaled blade & airfoil profiles.

4.2.3 Tower & Blade Mode Shapes Calculation

During the initial simulations of the updated 6 MW Hywind wind turbine model, significant disparities were observed in the blade and tower displacements. To address this issue, the secondary opensource software BModes was employed to compute the frequencies of the first 30 tower side-to-side and fore-aft, blade edgewise, and flapwise modes. After successful completion of the BModes simulations, the two dominant frequencies for each of the four displacement types were recorded, as illustrated in Figure 4.7. It should be clarified that the frequencies depicted in Figure 4.7 were selected purely based on prevailing vector displacement strength and not in any particular order of eigenfrequencies. Additionally, the normalised displacements presented in Figure 4.7 refer to components of modal displacements (Bir, 2005). Lastly, the obtained eigenmodes should be interpreted with caution due to the limited availability of data and uncertainties in the BModes inputs with regards to the Siemens SWT-6.0-154 wind turbine model.

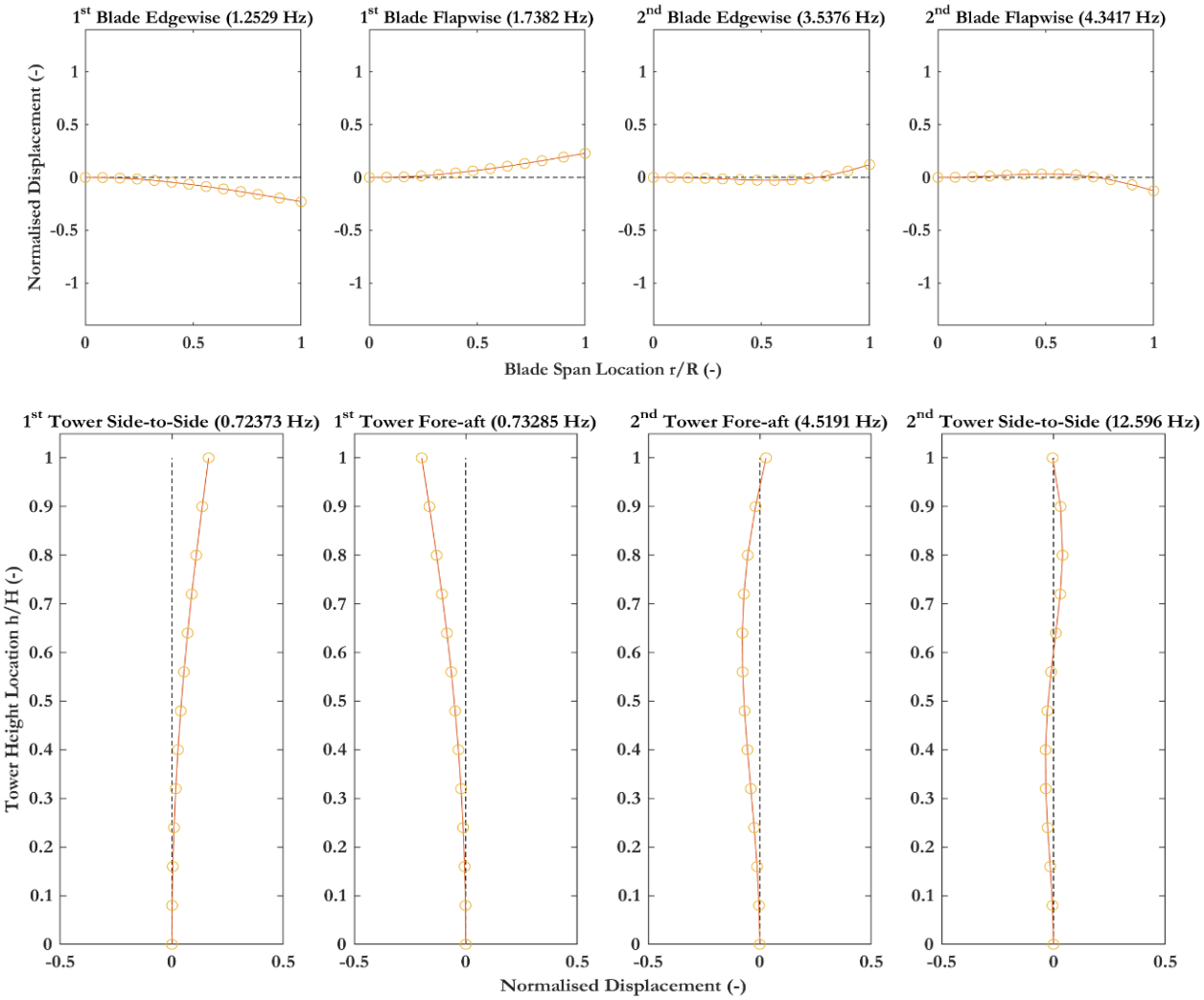

Figure 4.7 Predominant mode shapes for tower and blade structures.

Following, OpenFAST required as inputs the mode shape coefficients for the dominant frequencies per case in the form of a six-degree polynomial formula with null m_0 and m_1 coefficients, as seen in Equation 4.8. There, i ranges from 1 to 4, representing each of the potential mode shape-frequency pairs. A separation is made in Equation 4.8 between tower height location and blade span location utilising either h/H or r/R, respectively. The mode shape coefficient calculation occurred in a designated conversion file formatted in Excel to generate individually each one, per frequency and structural component.

$$Mode\ Disp_i = m_{6,i} \cdot x^6 + m_{5,i} \cdot x^5 + m_{4,i} \cdot x^4 + m_{3,i} \cdot x^3 + m_{2,i} \cdot x^2, \quad x = \frac{r}{R}\ or\ \frac{h}{H} \qquad (4.8)$$

The primary input parameters for BModes encompass structural stiffness, inertias, length distances, and masses. Among these, the structural masses of the wind turbine play a crucial role in determining the output results of BModes. The mass values used in the Hywind developed model are presented in Table 4.6. Out of the presented mass values, the tower, blade, ballasted spar platform and total dry (including both platform and wind turbine) mass values are directly retrieved (Statoil & Masdar, 2018). The remaining values are estimated based on them. It is important to note that the mass values employed in the OpenFAST simulations may slightly differ from those presented in Table 4.6, as some of them are derived from mass distributions.

Table 4.6 OpenFAST Hywind model structural mass values (Equinor, 2018; Statoil & Masdar, 2018).

Structural Member	Mass (kg)
Tower	670000
Blade	25000
Rotor	80000
Nacelle	153000
Hub	81000
Platform	10500000
Total Dry Mass	11483000

4.2.4 Controller Strategy

The NREL 5 MW reference wind turbine is typically controlled using the Induction Generator Model with Variable Rotor Resistance (IGVRR) controller, a variable-speed collective-pitch control system. The controller parameters change accordingly with the respective foundation type. Unfortunately, due to controller adjustement limitation attributed to the retrieved file type, in the developed Hywind model, the ROSCO opensource controller is used instead. For both floater and monopile supported wind turbine, the generator torque control mode in above rated conditions mode is set to TSR tracking Proportional-Integral (PI) control with constant power. Regarding the blade pitch control mode, active PI blade pitch control is utilised. Lastly, neither yaw nor flap control modes are incorporated.

Owing to confidentiality constraints, the specific details of the Siemens wind turbine controller strategy are not disclosed in this study, as it remains proprietary information. Consequently, an open-source ROSCO controller was employed, wherein a substantial portion of the input values were upscaled based on existing data from the NREL 5 MW wind turbine model. This approach allows for the replication and adaptation of certain controller parameters within the available framework. Multiple essential controller data are presented in Table 4.7. The rated TSR, λ, generator efficiency, η_{gen}, gearbox ratio, r_{gear}, values and the maximum blade pitch, $\theta_{blade,max}$ are identical to the original reference model ones. Initial tuning of the controller was conducted using Equations 4.9 - 4.13. It is important to emphasize that the upscaling Equation 4.13 is applicable in this context, as the key parameters, namely λ_{design}, $C_{p,max}$ and r_{gear} remain unchanged between the reference and upscaled models (Zaaijer & Viré, 2022).

$$\Omega_{LSS} = \frac{\lambda \cdot V_{rated}}{R} \tag{4.9}$$

$$\Omega_{HSS} = \Omega_{LSS} \cdot r_{gear} \tag{4.10}$$

$$P_{mech} = \frac{P_{el}}{\eta_{gen}} \tag{4.11}$$

$$Q_{rated} = \frac{P_{mech}}{\Omega_{HSS}} \tag{4.12}$$

$$\frac{k_{new}}{k_{ref}} = \left(\frac{R_{new}}{R_{ref}}\right)^5 \tag{4.13}$$

Where, the indeces *LSS* refers to low speed shaft (prior to the gearbox) values, *HSS* refers to high speed shaft (after the gearbox), *mech* refers to mechanical (prior to the generator), *el* to electrical (after the generator) and *k* refers to the generator torque gain constant.

Table 4.7 Rosco controller parameters.

Rated TSR (-)	7.4
Generator Efficiency (%)	0.944
Rated Mechanical Power (W)	6355932.2
Rated Generator Speed (s^{-1})	111.86
Gearbox Ratio (-)	97.0
Rated Generator Torque (Nm)	56820.0
Generator Torque Gain Constant (-)	4.9
Maximum Blade Pitch (deg)	20

Due to the project's time restrictions and unavailability of Siemens controller or power generation data, the used controller is left largely untuned against the actual Hywind turbines. Thus, the aerodynamic and performance coefficient tables (including C_p, C_t and C_q) refer to the original NREL 5 MW structure. Moreover, the controller does not receive feedback from the nacelle's velocity accumulated due to the spar platform's motion. This decision is based on the feedback floating gain necessitating the linearization of the developed OpenFAST FOWT spar model in order to be added (Lenfest et al., 2020). Then, a consequential tuning would be required to set the gain constants accordingly, a process which was circumvented also due to time constraints imposed by the project. Finally, according to Lenfest et al.'s investigation on the controller tuning effects on power generation for a semi-submersible 5 MW FOWT simulated in OpenFAST, in their corresponding cases, the addition-tuning of said feedback resulted in a similar power performance at rated wind speeds (12 m/s) and at above rated conditions (16 m/s), as seen in Figure 4.8. At rated wind speed, the power fluctuation is limited which can be ascribed to the controller's endeavor to safeguard the nacelle from sudden and violent oscillations, consequently introducing a marginal delay-hysteresis in the rotor pitch response (Lenfest et al., 2020). Despite these outcomes, further literature review is conducted and included in Section 6.2.4 to compensate for this discrepancy.

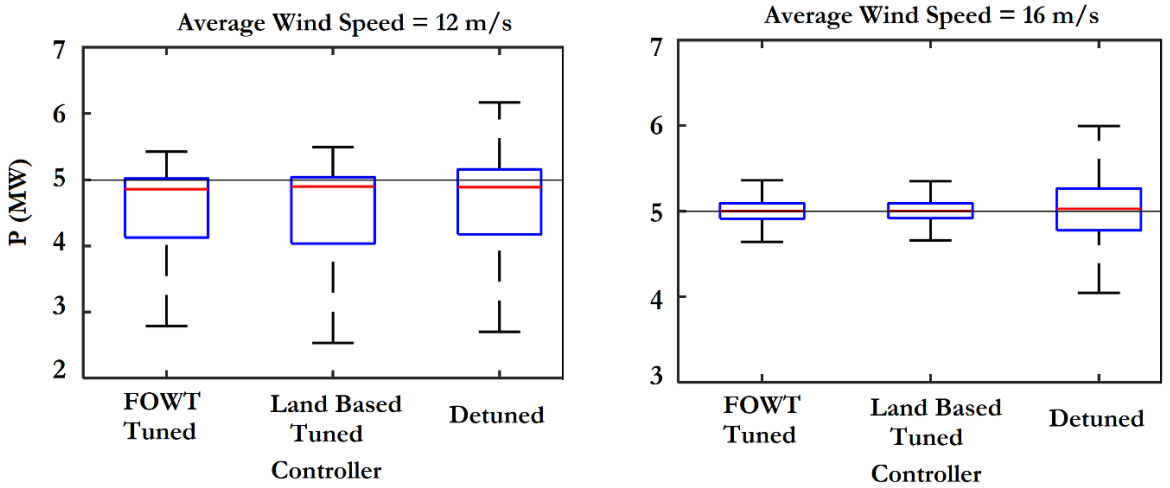

Figure 4.8 Different controller effects on generated power around the rated wind speed (12 m/s) and the above rated wind speed of 16 m/s (Lenfest et al., 2020).

With regards to the controller strategy, the list of enabled DOFs from the ElastoDyn input file are presented in Figure 4.9. Out of the included parameters, rotor-teeter is the sole DOF that is disabled throughout the entirety of the project, as the project focuses on a three bladed wind turbine. The last six parameters represent the platform lateral and rotational DOFs, which can be enabled or disabled depending on the specific circumstances and the point under investigation.

```
---------------------- DEGREES OF FREEDOM --------------------------------------
True           FlapDOF1    - First flapwise blade mode DOF (flag)
True           FlapDOF2    - Second flapwise blade mode DOF (flag)
True           EdgeDOF     - First edgewise blade mode DOF (flag)
False          TeetDOF     - Rotor-teeter DOF (flag) [unused for 3 blades]
True           DrTrDOF     - Drivetrain rotational-flexibility DOF (flag)
True           GenDOF      - Generator DOF (flag)
True           YawDOF      - Yaw DOF (flag)
True           TwFADOF1    - First fore-aft tower bending-mode DOF (flag)
True           TwFADOF2    - Second fore-aft tower bending-mode DOF (flag)
True           TwSSDOF1    - First side-to-side tower bending-mode DOF (flag)
True           TwSSDOF2    - Second side-to-side tower bending-mode DOF (flag)
True           PtfmSgDOF   - Platform horizontal surge translation DOF (flag)
True           PtfmSwDOF   - Platform horizontal sway translation DOF (flag)
True           PtfmHvDOF   - Platform vertical heave translation DOF (flag)
True           PtfmRDOF    - Platform roll tilt rotation DOF (flag)
True           PtfmPDOF    - Platform pitch tilt rotation DOF (flag)
True           PtfmYDOF    - Platform yaw rotation DOF (flag)
```

Figure 4.9 List of ElastoDyn available degrees of freedom.

Moreover, it should be emphasized that the wind turbine's controller remains consistent regardless of the foundation type. Whether it pertains to a bottom-fixed monopile or a floating spar structure, the wind turbine operates under an identical control strategy. This uniformity is further upheld as both the BOWT and FOWT cases examined in this project are subjected to identical metocean conditions.

4.2.5 Stable Wind Turbine Upscaled Results

Both the original NREL 5MW wind turbine and the updated Hywind model underwent simulation using the OpenFAST software to facilitate a comprehensive comparison of their respective outcomes. These simulations were exclusively focused on the wind turbine structure, while disregarding the presence of a floating or bottom-fixed platform. Consequently, the platform motions were deliberately disabled during the simulations. As for the chosen aerodynamic model, the BEM model was employed due to the necessity for a rapid and iterative analysis approach, allowing for swift iterations in case any inconsistencies were detected in the results. Moreover, the instantaneous results were produced by OpenFAST as the wind turbine was subjected to a non-turbulent uniformly increasing wind field. Instantaneous curves are simulated by introducing the wind turbine to a linearly increasing wind speed, ranging from 3 m/s to 25 m/s, and recording the structure's response. The objective of the validation is to support the usage of the upscaled turbine developed model along with different bottom fixed monopile and floating spar platforms to generate reliable outcomes throughout this project. The upscaled and updated Hywind wind turbine model is benchmarked against the NREL 5 MW one with regards to tower and blade modes, as seen in Figure 4.10 and generated electrical power, as presented in Figure 4.11. Additional upscaling comparison graphs pertaining to blade pitch, generator rotational speed and rotor thrust are included in Appendix B, Figure B.1, for completeness.

Upon examining the graphs of Figure 4.10, it is evident that the structural responses of the reference NREL 5 MW wind turbine and the upscaled Hywind 6 MW wind turbine exhibit a commendable level of agreement. Nevertheless, several observations can be made regarding the developed wind turbine model. Firstly, the blade displacements for both structures display fluctuating patterns around

comparable values, indicating a certain degree of similarity in their behavior. However, it is noteworthy that the tower displacements of the developed Hywind wind turbine are approximately halved when compared to the reference model. This significant reduction in tower displacement can likely be attributed to an overly stiff tower design in the developed model. Although the addition of BModes generated mode shape coefficients immensely improved the tower and blade deflections, the tower side-to-side mode showcases a slight increasing oscillation amplitude behavior after the rated point. This behavior is attributed to lack of input data for precise BModes eigenmode coefficient calculation, an operation which should be modeled with exactness, as small input errors can lead to large outcome differences (Jonkman & Butterfield, 2015). Any discrepancy due to the small displacements of the side-by-side motions are not expected to measurably affect power performance, which is the main parameter to be investigated in this project. Additionally, the blade out of plane and tower fore-aft modes experience slight oscillations around the rated wind speed point. Lastly, blade and tower displacements maximize in the region around the rated wind speed point due to the increase in aerodynamic loads and structural responses at this point (Jonkman, 2007). The developed Hywind model demonstrates a stronger manifestation of the phenomenon than the retrieved NREL model.

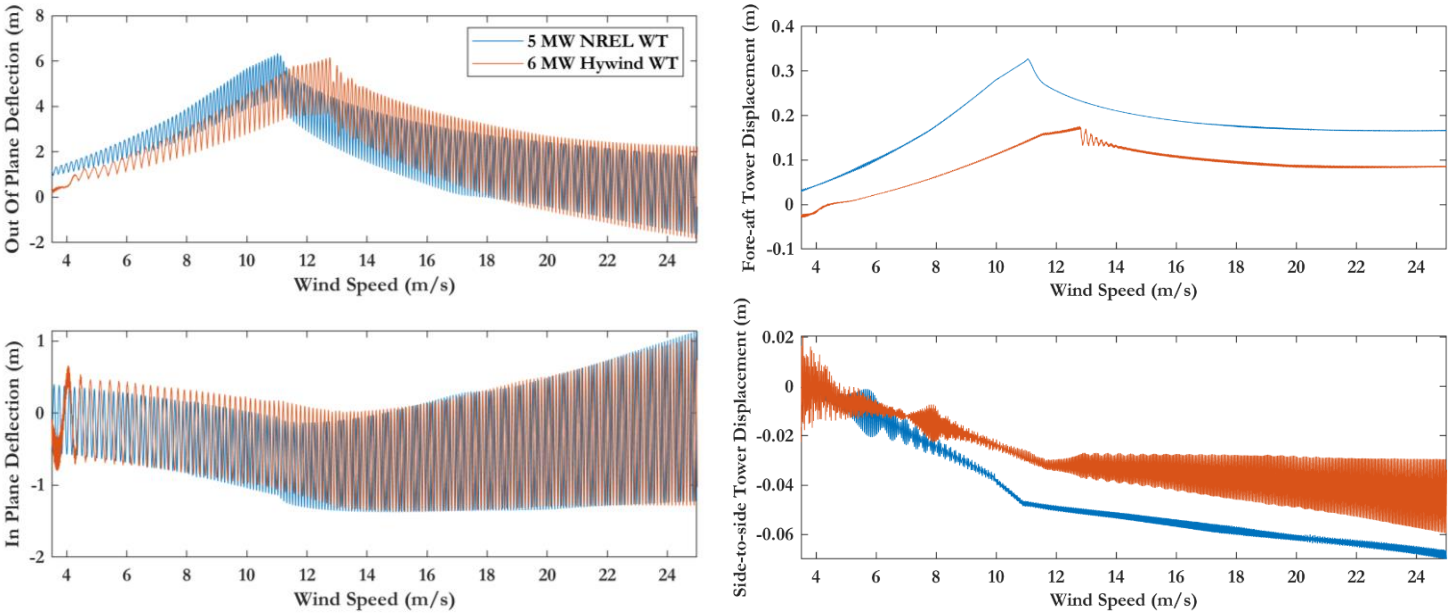

Figure 4.10 Out of plane, in plane blade & fore-aft, side-to-side tower deflections comparisons between the stable NREL 5 MW & Hywind upscaled wind turbine.

For the energy yield comparison scope of this work, Figure 4.11 showcases the wind turbine power curve upscaling from 5 to 6 MW. Through this project, this is the sole instance where an instantaneous power curve is presented instead of the industry accepted, standards based one (e.g., seen in Figure 4.13). The reason behind this power curve inclusion lies in its ability to clearly highlight the cut-in and rated wind speed points along the graph. Furthermore, the upscaling graph resembles the work of Desmond et al., where multiple upscaled power curves are depicted, including ones with rated powers of 5, 8 & 10 MW (Desmond et al., 2016). The developed model shares the same cut-in and rated wind speeds as the Hywind SWT-6.0-154 model, at 4 m/s and 12 m/s, respectively. Lastly, both the NREL and developed model's instantaneous power curves showcase a slight overestimation and fluctuation of power, respectively, around the rated power point, in the transitional 2-to-3 region, as similarly experienced by Driscoll et al., 2016 (already discussed in Section 3.2).

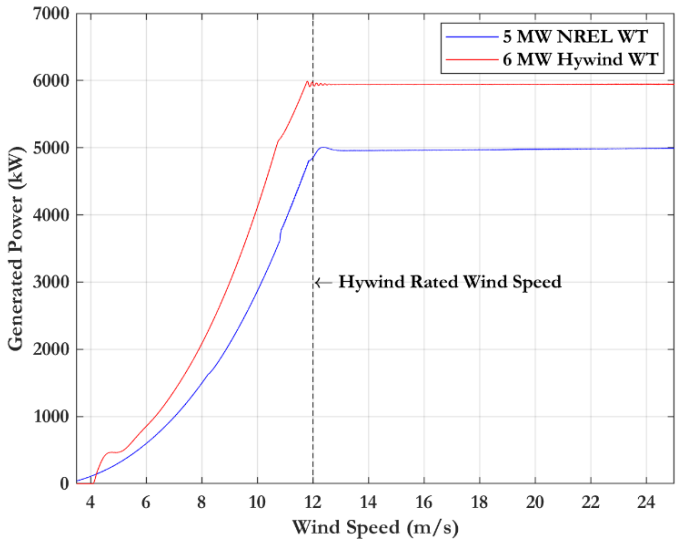

Figure 4.11 Instantaneous generated power comparison between the stable NREL 5 MW & Hywind upscaled wind turbines.

4.3 Platform Modelling

This section focuses on the development of this project's two prevalent offshore wind turbine platforms models, the spar floater and the monopile foundation. The modeling process includes the incorporation of the mooring system for the floating case. The models, additionally, are benchmarked against reference results, in order to highlight their accuracy and reliability.

4.3.1 Mooring System & Floating Spar Model

In MoorDyn, the mooring lines of the presented system are dynamically simulated. The mooring system of a Hywind Statoil spar structure is composed of six vessel points (points directly connected on the floating platform), three connection points, which link individual lines together) and three fixed points, which are secured on the seabed. The vessel points are modelled at three separate points instead of six due to their proximity. As the vessel point coordinates and line-bridle lengths are known, the connection point coordinates can be calculated, as illustrated in Figure 4.12. Based on the same logic, the fixed points coordinates are also computed. The required bridle and line material characteristics are provided in documentation and the MoorDyn input file is included in Appendix B, Figure B.2, for transparency.

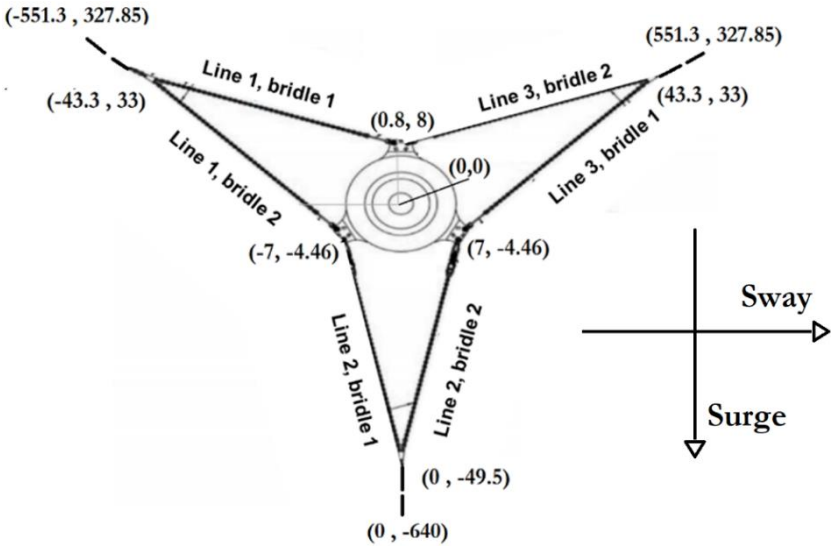

Figure 4.12 Overview of mooring line system, mooring points coordinates and lateral motion DOFs, surge and sway definition.

As the mooring line lengths influence the spar lateral displacements, surge and sway, an investigation on their effects was conducted. For the model presented, the mooring line lengths values were adjusted and the main line length was reduced by 10 m. This outcome stemmed from simulation calibration iterations aiming on optimising the model's data recreation capabilities of specific parameters. Their results were simultaneously visualised though MATLAB pipelines and the model exhibiting the highest degree of resemblance to the measurements is chosen for further development, wherein additional parameters are optimized. Similar procedure was followed for the Morison coefficients, mooring line stiffness and tower drag coefficients.

Regarding the spar floater, its model was developed in HydroDyn utilising strip theory members. An iterative approach was followed to adjust the rotor nacelle assembly mass parameters, spar inner diameter and overall mass distribution throughout the entire structure in order to achieve an accurate center of gravity for the platform spar. The provided center of gravity value at -50.03 m refers to the complete structure including substructure, tower, wind turbine and mooring system. The specific strip theory spar members along with the calculation Excel spreadsheet are included for completeness in Appendix B, Figure B.3.

Initially, a HydroDyn floating spar model was developed using Potential flow theory, however, due to time constraints and inability to access the supplementary license-locked software WAMIT, strip theory was employed as a substitute. It is highlighted that, due to this replacement, the model does not entail second order floating platform forces, drift, diffraction, or boundary layer effects. Lastly, neither second order wave kinematics nor marine growth on the submerged area of the floater are employed in the model. Similar model discrepancies such as these, are discussed in Section 5.3.

Figure 4.13 illustrates the 3D model of the created spar floater along with its mooring system and wave elevation as simulated by OpenFAST and rendered in MATLAB. Figure 4.13 additionally illustrates the developed wind turbine model as rendered in ParaView in the same scale as the floater.

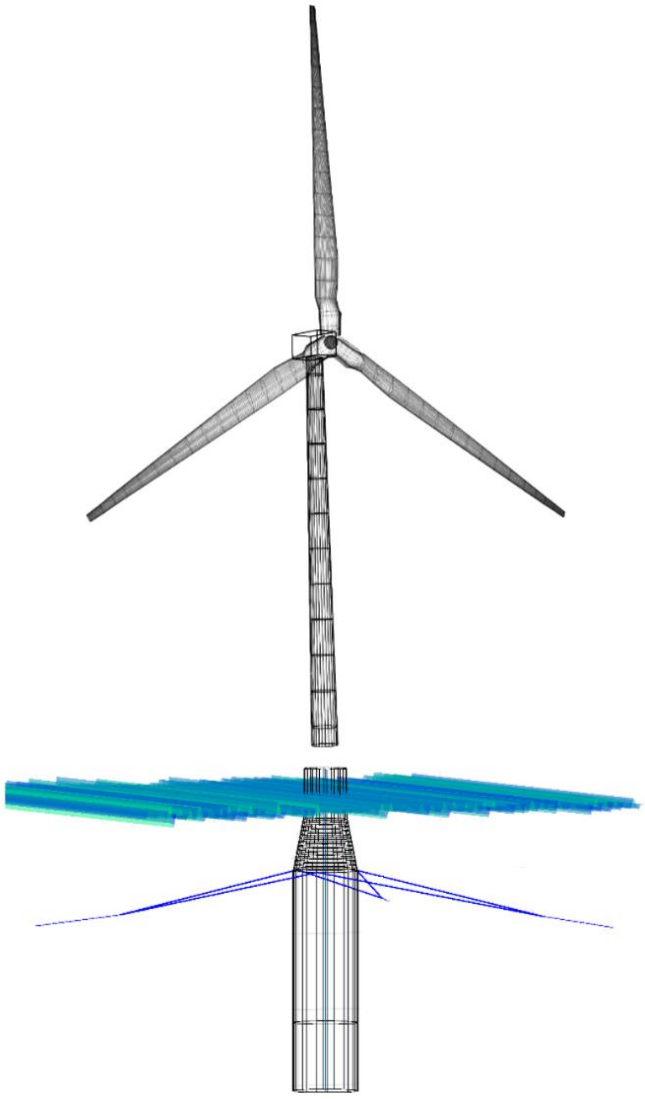

Figure 4.13 3D rendering of the Spar buoy, waves and mooring lines in MATLAB.

4.3.2 Floating Spar Wind Turbine Upscaled Results

Power curves are an essential tool for evaluating the performance of wind turbines and constitute one of the current project's main interests. The wind turbine industry typically uses the International Electrotechnical Commission (IEC) standard 61400-12 to produce power curves. The standard requires wind speed and power data to be collected at various wind speeds, typically in 0.5 m/s or 1 m/s increments, and for a minimum of 10 minutes at each wind speed. The power curve can then be

constructed by either fitting a function to the mean power data points or getting realised by separate points with additional standard deviation margins (IEC 61400-12-1, 2017).

As for the OpenFAST power curve graph generation, firstly, separate TurbSim turbulent wind fields are created as inputs in 1 m/s wind speed increments. Then, the OpenFAST simulation models run for a total of 1200 sec, out of which the initial 200 sec are discarded in order for the finalised results to be stabilised. Based on the resulted power outputs, the mean and STD margins are calculated for each wind speed ranging from 4 m/s to 25 m/s, as illustrated in Figure 4.14. For completeness reasons, six power outcomes per average wind speed fields against the simulation time are included in Appendix B, Figure B.4. In these cases, the initial 200 seconds of simulation time are not presented in the graphs, thus ranging from 0-1000 sec. In addition, the upscaled blade and tower modes as well as the spar platform motion DOFs comparison are displayed in Figure 4.15 and Figure 4.16, respectively. For aforementioned reasons, in these simulations, the aerodynamic model of BEM is employed.

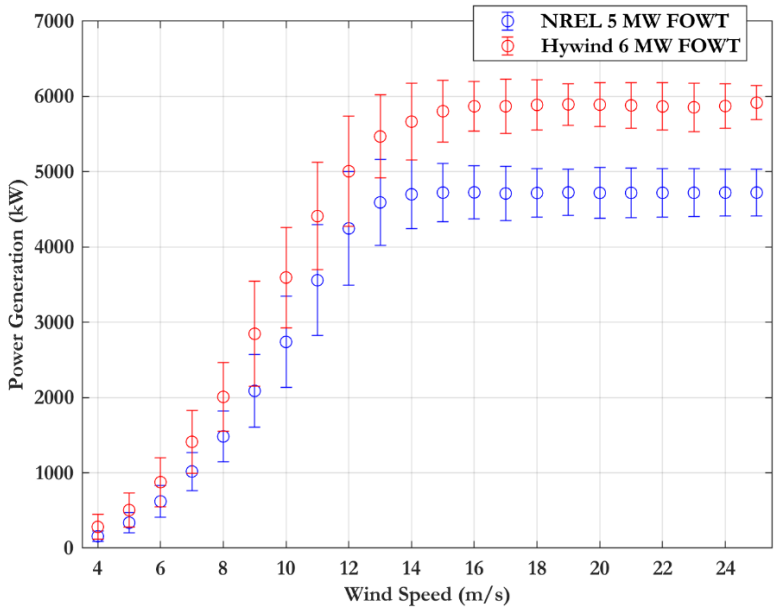

Figure 4.14 Generated power comparison between the floating spar NREL 5 MW & Hywind upscaled wind turbines.

In turbulent wind conditions, a floating offshore wind turbine can experience dynamic responses, which lead to power outputs higher than the rated one. This phenomenon is attributed to time-varying wind speeds, which causes the rotor to experience varying wind loads, leading to fluctuations in power output. In particular, the wake turbulence generated by the wind turbine can cause unsteady inflow conditions, leading to higher power production. The increased power output is caused by the fluctuating forces acting on the rotor, which can excite the natural frequencies of the turbine, causing it to oscillate and generate more power. However, these studies also show that the increase in power output is not sustainable in the long term and can lead to increased fatigue loading, which jeopardizes the structural integrity of the wind turbine (Umut et al., 2022; Jonkman, 2007).

By taking turbulence into consideration, fluctuations are introduced in the floating spar's power generation which is represented by the considerable standard deviation margins. The fluctuations are further caused by the spar's and consequential nacelle-rotor's motion, a phenomenon essentially hightlighted during Section 3.1 by multiple researchers. The motion of the platform causes variations in the blades-experienced wind speed and direction, with the angle of attack, lift and drag forces on the blades being also affected. Additionally, the motion of the nacelle can cause changes in the rotor speed and blade pitch, which further affect the power output of the turbine.

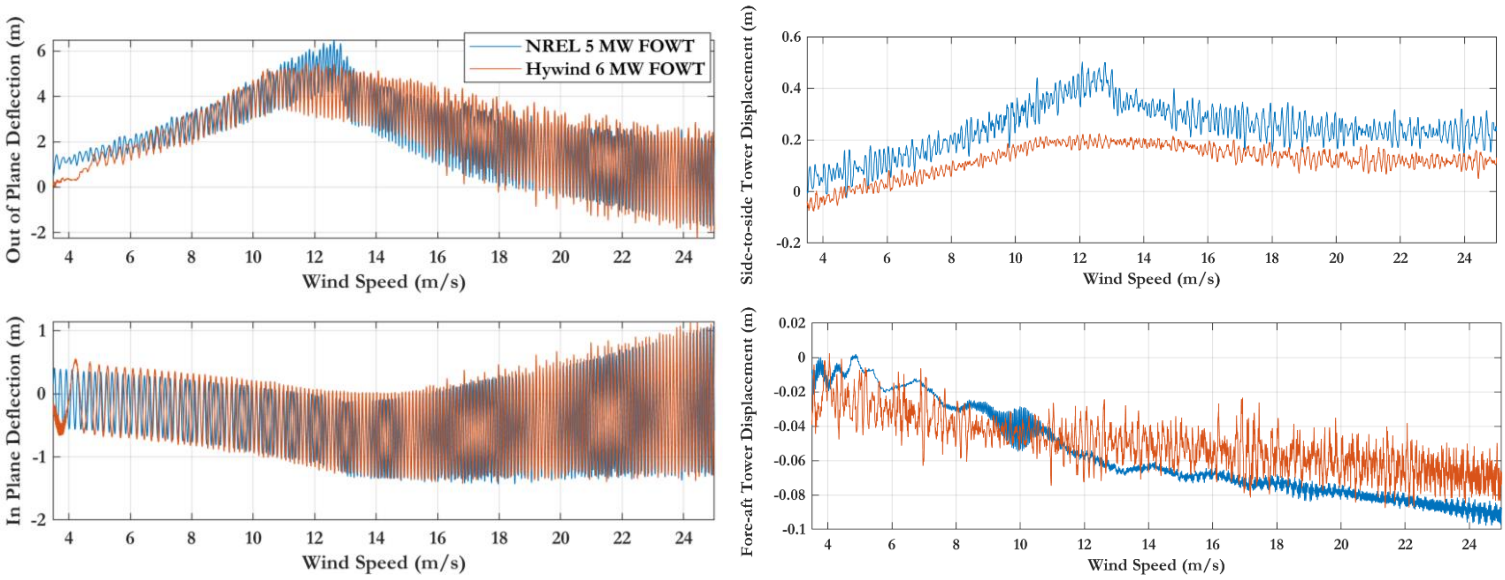

Figure 4.15 Out of plane, in plane blade & fore-aft, side-to-side tower deflections comparisons between the floating spar NREL 5 MW & Hywind upscaled wind turbine.

After comparing the stable wind turbine blade and tower modes (Figure 4.10) with the ones of the floating spar from Figure 4.15, the floater's lateral and rotational displacement effects are evident. Additonal fluctuations are exhibited in the FOWT outcomes. The significant changes attributed to the spar's addition in the model are witnessed mainly in the fore-aft tower displacement graph, where the once diverging behavior of the Hywind developed wind turbine is replaced by simple fluctuations. This can stem from eigenmode and floater movement superposition, but it is not further investigated. As the values and main phenomena of the graphs are already discussed alongside Figure 4.10, they will not be repeated.

In summary, according to the graphs of Figure 4.16, the results show a high degree of similarity in the values and time series behavior of the different spar motion DOF between the two WT models. However, the sway DOF of the platform exhibits a noticeable deviation from this trend. It is essential to accurately capture the characteristics of the mooring system as it is crucial in shaping the dynamic behavior of the platform. Specifically, one of the significant effects is the influence on the lateral displacements of the spar (Xiang et al., 2022; Hong et al., 2015). Therefore, the sway value difference is possibly attributed to different mooring line system coordination between the reference NREL and Hywind developed models. In contrast, the platform surge results of the two models are in accordance.

Furthermore, the trend of increased oscillations of the Hywind based developed model is prevalent in the graphs of Figure 4.16. The sole exception is the yaw graph, where the Hywind FOWT yaw rotational DOF is disabled in the model. This decision is supported by recent findings of Equinor which claim that the Hywind spar platforms have a roughly mean fixed yaw at 0°, without additional information on the yaw STD margins or time series measurments (Bussemakers, 2020). Further reasoning behind the yaw disabling decision is presented in Section 5.1.

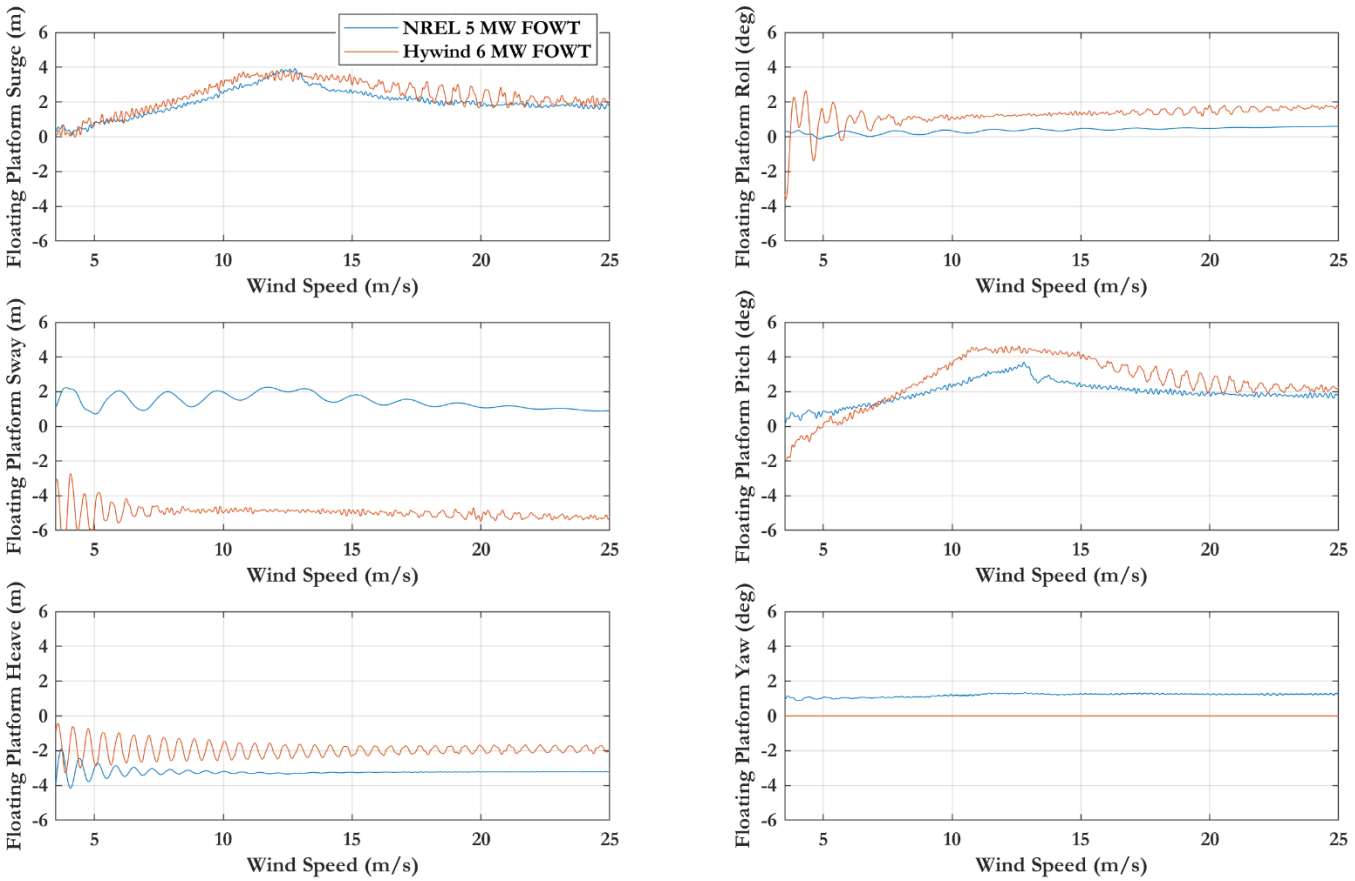

Figure 4.16 Floating spar platform motion DOF comparison between the NREL 5 MW & Hywind upscaled wind turbine model.

4.3.3 Bottom Fixed Monopile Model

The most important characteristics of the monopile structure that will replace the existing Hywind spar to support the Siemens wind turbine are presented in Table 4.8. Geometrical characteristics for the monopile, thickness t_{mon} (mm), driving length $L_{mon,driv}$ and total length $L_{mon,total}$ are guided by the experimental Equations 4.14 - 4.16, respectively (Aranya et al., 2017; Negro et al., 2018). It is clarified that no scaling laws were utilised to develop this monopile model as the outcomes. Moreover, the monopile mass, M_{mon}, is computed via the volume and density Equation 4.17. The material density, Young and shear modulus values are based on the monopile's material which is steel (Zhao et al., 2022). The monopile's uniform diameter D_{mon} is equated to the wind turbine's bottom diameter, at 7.5 m and all consequential outcomes are calculated based on that estimation. Lastly, the real water depth of the installation location was changed from 100m to 20m in order to match realistic depths of said bottom fixed wind turbine foundations.

The developed monopile foundation is modelled in Matlab and presented in Figure 4.16 along with the wave elevation and seabed planes. Both spar and monopile foundation structures are not rendered in ParaView or similar visualization software due to OpenFAST's inability to generate the required foundation and mooring system data.

$$t_{mon} = 6.35 + \frac{D_{mon}}{100} \tag{4.14}$$

$$L_{mon,driv} = 8 \cdot D_{mon} - 5 \tag{4.15}$$

$$L_{mon,total} = 14 \cdot D_{mon} - 17 \tag{4.16}$$

$$M_{mon} = \pi \cdot L_{mon,total} \cdot \left({R_{mon}}^2 - (R_{mon} - t_{mon})^2\right) \cdot \rho_{steel} \quad (4.17)$$

Table 4.8 Parameters overview of the developed monopile model (Zhao et al., 2022).

Monopile Diameter (m)	7.5
Wall Thickness (mm)	71
Driving Monopile Length (m)	55
Total Monopile Length (m)	88
Steel Density (kg/m^3)	7850
Mass Monopile (tons)	1144.7
Young Modulus (N/m^2)	210 10^9
Shear Modulus (N/m^2)	80.8 10^9

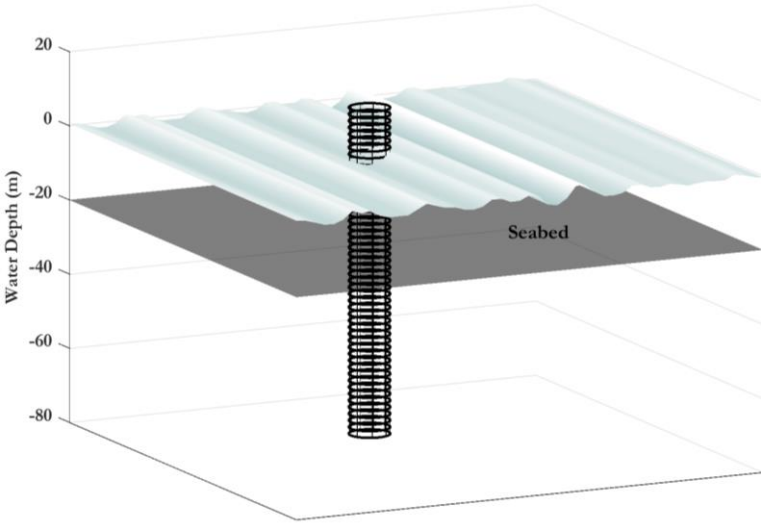

Figure 4.17 Rendered 3D model of the Monopile structure, waves and seabed in MATLAB.

The first 30 monopile eigenmodes were calculated in the SubDyn module to be benchmarked against literature eigenfrequencies of similar monopile structures, as seen in Table 4.9. In this modal analysis, the NREL 5 MW was placed on top of the developed monopile in order for the results to be comparable to the ones from literature. The predominant eigenfrequencies along with the normalised displacement-mode vectors are presented in Figure 4.18. The natural frequencies of the monopile foundation for an offshore wind turbine depend on several factors, including the soil conditions, the geometry of the foundation, and the characteristics of the wind turbine itself. A review of literature by Larsen and Hansen found that the first natural frequency of offshore wind turbine foundations typically ranges from 0.3 Hz to 1.2 Hz, depending on the factors of water depth and soil conditions (Larsen & Hansen, 2008). Jonkman et al., 2009 and Abdullahi et al., 2020 generated the first and second foundation structure fore-aft and side-to-side eigenfrequencies for the bottom fixed NREL 5 MW WT case, where a monopile structure supports the wind turbine. In their studies, a monopile model was employed consisting of a steel hollow cylindrical section with a uniform diameter of 6m, a 60mm wall thickness, and a total length of 83.15 meters. The monopile is divided into three sections, with 18.15 meters situated above the mean sea level, 30 meters submerged in seawater, and 35 meters embedded into the supporting soil (Abdullahi et al., 2020; Jonkman et al., 2009). Overall, the monopile constructed as part of this project, utilizing experimental equations, exhibits comparable geometric properties to the NREL reference monopile employed in academic investigations. Table 4.9 compares the obtained and simulated eigenfrequency outcomes of the monopiles structures discussed above.

Table 4.9 Common monopile side-to-side & fore-aft eigenfrequency values comparison (Abdullahi et al., 2020; Jonkman et al., 2009).

Eigenmode	Jonkman et al. (2009)	Abdullahi et al. (2020)	Present Study
1st Side-to-Side (Hz)	0.312	0.302	0.3156
1st Fore-aft (Hz)	0.324	0.313	0.3156
2nd Side-to-Side (Hz)	2.936	3.327	1.9363
2nd Fore-aft (Hz)	2.900	2.666	1.9363

According to the obtained findings, the three examined monopiles demonstrate comparable first eigenfrequencies in terms of side-to-side and fore-aft modes, with greater discrepancies observed in the second modes. Considering the objective of this analysis, the proximity of the first eigenfrequencies is deemed satisfactory to regard the developed OpenFAST monopile structure as reliable and draw conclusions from its results (guidance from industry experts).

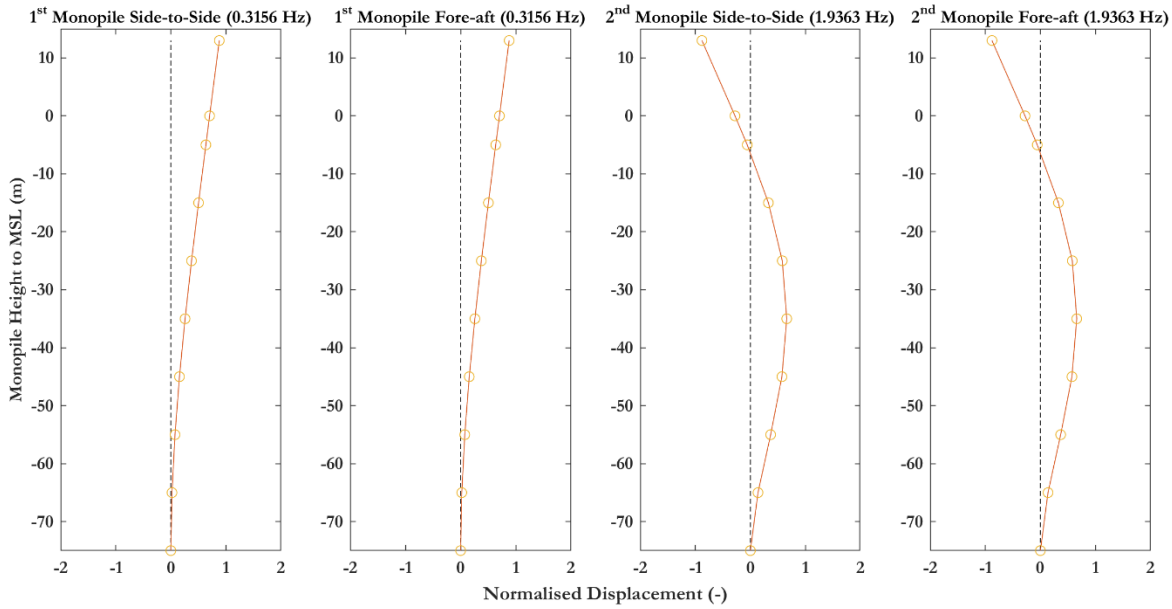

Figure 4.18 Predominant mode shapes for the monopile structure.

To clarify, guidelines for offshore wind turbine monopiles suggest that the maximum allowable lateral displacement is commonly ranging between 1% and 3% of the water depth. However, it is important to note that this is a general guideline and the actual allowable displacement may vary based on site-specific conditions and regulations (DNV GL, 2015).

4.3.4 Bottom Fixed Monopile Wind Turbine Upscaled Results

To increase the developed monopile model structural and annual energy yield validity, the mean and STD margins of the generated electrical power along with the blade-tower modes are presented in Figure 4.19 and Figure 4.20, respectively. These results are simulated with the aerodynamic model of BEM.

Similar to the FOWT mean power generation graph (Figure 4.14), where the original and upscaled curves had strong similarities, Figure 4.19's BOWT power curves exhibit a remarkable similarity when compared to each other. For this study's 6 MW BOWT, the standard deviation instantly minimises after the rated wind speed threshold of 12 m/s. is reached. In contrast, the NREL 5 MW BOWT experiences a more gradual power deviation once the aforementioned value is exceeded. It is noted that the 6 MW BOWT model encounters stronger power fluctuation prior to the rated power point, ranging from 9 m/s to 11 m/s. The observations made during the analysis of FOWT graphs regarding turbulence effects remain applicable in this context as well. However, due to the absence of amplification caused by spar movement, the instances of power exceeding the rated power value are now constrained.

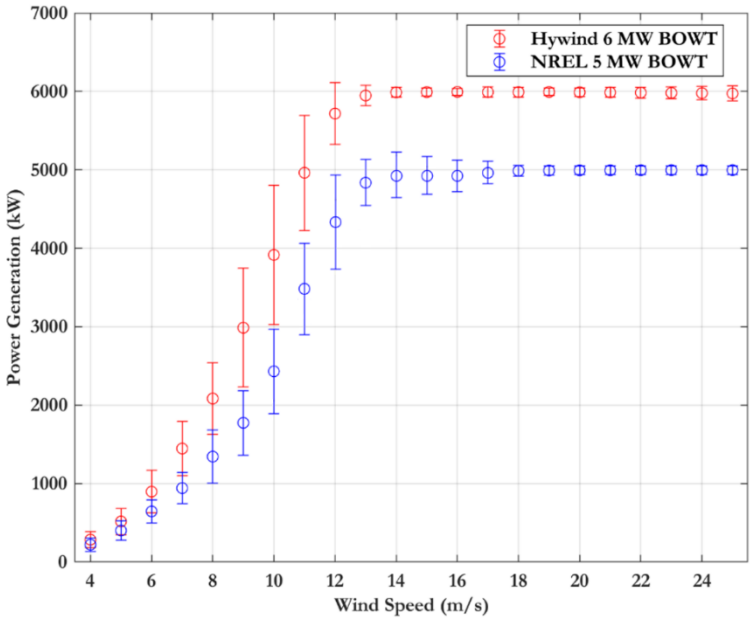

Figure 4.19 Generated power comparison between the bottom fixed monopile NREL 5 MW & Hywind upscaled wind turbines.

The out of plane, in plane blade & fore-aft, side-to-side tower deflections comparisons of Figure 4.20 are discussed. Both the blade out of plane and tower side-to-side displacements showcase a high oscillation region around the rated wind speed point. Concerning the tower fore-aft displacement, a similar situation is witnessed before the rated wind speed point. In this case, the oscillating phenomenon smoothens gradually once the rated power point is reached. Finally, the two tower mode deflection curves follow similar trends as the original NREL 5 MW curves, however their oscillating patterns greatly differ. Despite the in plane blade deflection not experiencing high fluctuations around the rated region, it displays an increasing oscillation amplitude behavior as the cut off wind speed of 25 m/s approaches.

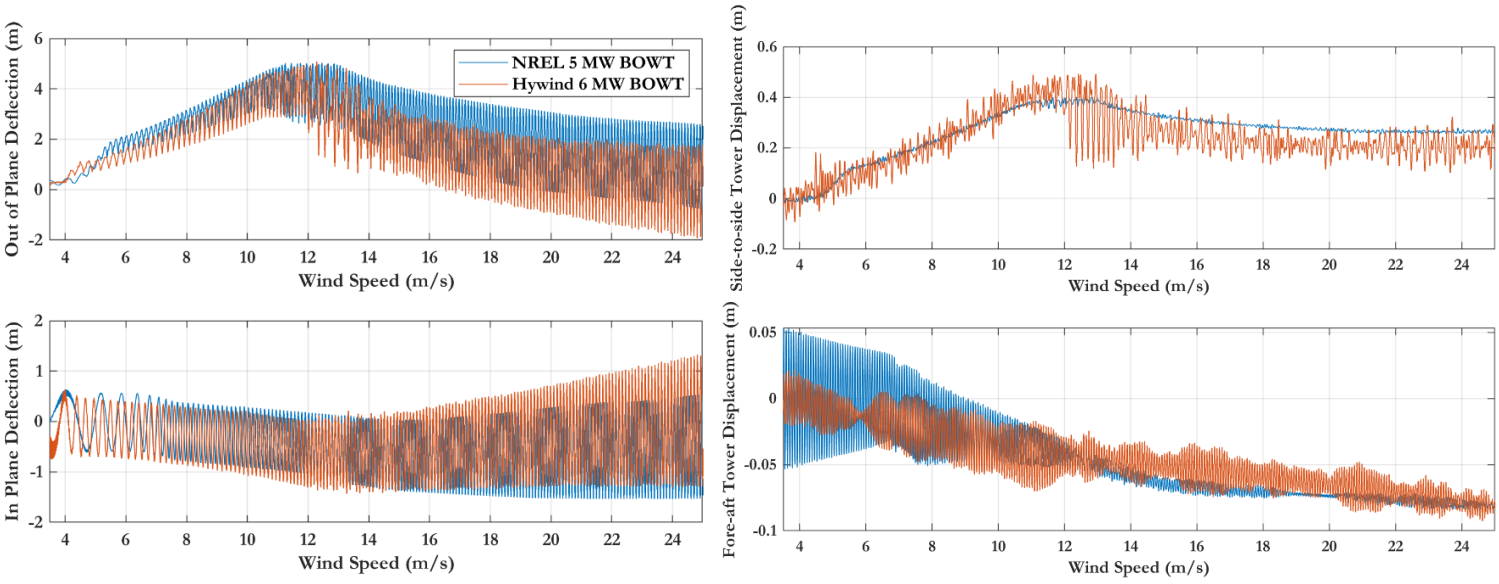

Figure 4.20 Out of plane, in plane blade & fore-aft, side-to-side tower deflections comparisons between the bottom fixed monopile NREL 5 MW & Hywind upscaled wind turbine.

Chapter 5. OpenFAST Hywind Model Benchmarking Analysis

This chapter aims to assess the degree of realism achieved by the developed OpenFAST model by comparing it to measured data from the Hywind spar. Firstly, the results of free decay tests and modal analysis are presented, which provide information on the natural frequencies deviations between the two systems. Next, the simulated OpenFAST responses are benchmarked against the Hywind spar motion measurements for three different operation cases. Finally, the discrepancies between the simulated and measured responses are investigated and discussed.

5.1 Free Decay & Eigenanalysis

The free decay simulations in OpenFAST are typically conducted as time-domain simulations of offshore floating wind turbines to obtain the natural frequencies and damping ratios of the structure. According to the OpenFAST documentation, the following changes need to be made in the input files for implementing initial conditions of free decay tests:

- ElastoDyn input file: Disable all structural DOFs except for the investigated one,
- AeroDyn & Inflow Wind input files: incoming wind speed and direction set to zero,
- HydroDyn input file: Wave kinematics and current profiles disabled,
- ServoDyn input file: Blade pitch angles set to zero.

In addition, it is necessary to specify the initial condition inputs in order to properly set up the simulation (Gao et al., 2015; Jonkman et al., 2009). In total, there were six free decay tests simulated, for each spar motion DOF respectively. The spar initial conditions for the six free decay analyses are included in Table 5.1. All the other initial conditions located in OpenFAST's ElastoDyn input file are set to 0. These conditions include tower and blade displacements, blade pitches, azimuth angles, rotor speed and nacelle-yaw angle.

In a spar floating wind turbine, the surge direction motion is coupled with the motion in the pitch direction. Similarly, the motion in the sway direction is coupled with the motion in the roll direction. The heave and yaw DOFs do not have strong coupling with other DOF motions (Xiang et al., 2022; Xu & Srinil, 2015). Thus, there are four total cases where in the free decay tests, more than one DOF is enabled, as seen in Table 5.1. Moreover, the time series and frequency domain outcomes for the six tests are presented, paired per axis, in Figure 5.1, Figure 5.2 and Figure 5.3. For completeness, the uncoupled surge-pitch and sway-roll spar motion DOF single peak frequency domain and time series graphs are included in Appendix C, Figure C.1. Lastly, the measured and simulated eigenperiods, only for the coupled results, are compared in Table 5.2.

Table 5.1 Spar platform initial free decay displacement conditions.

Spar Platform DOF	Initial DOF Displacement	DOF Coupled with
Surge (m)	5	Pitch
Sway (m)	5	Roll
Heave (m)	2	-
Roll (deg)	5	Sway
Pitch (deg)	5	Surge
Yaw (deg)	5	-

The purpose of this modal analysis is to further validate the developed model against the recorded measurements of the commissioned Hywind FOWT. Therefore, the spar rotational yaw DOF is enabled in order to assess its performance against the reported Hywind values.

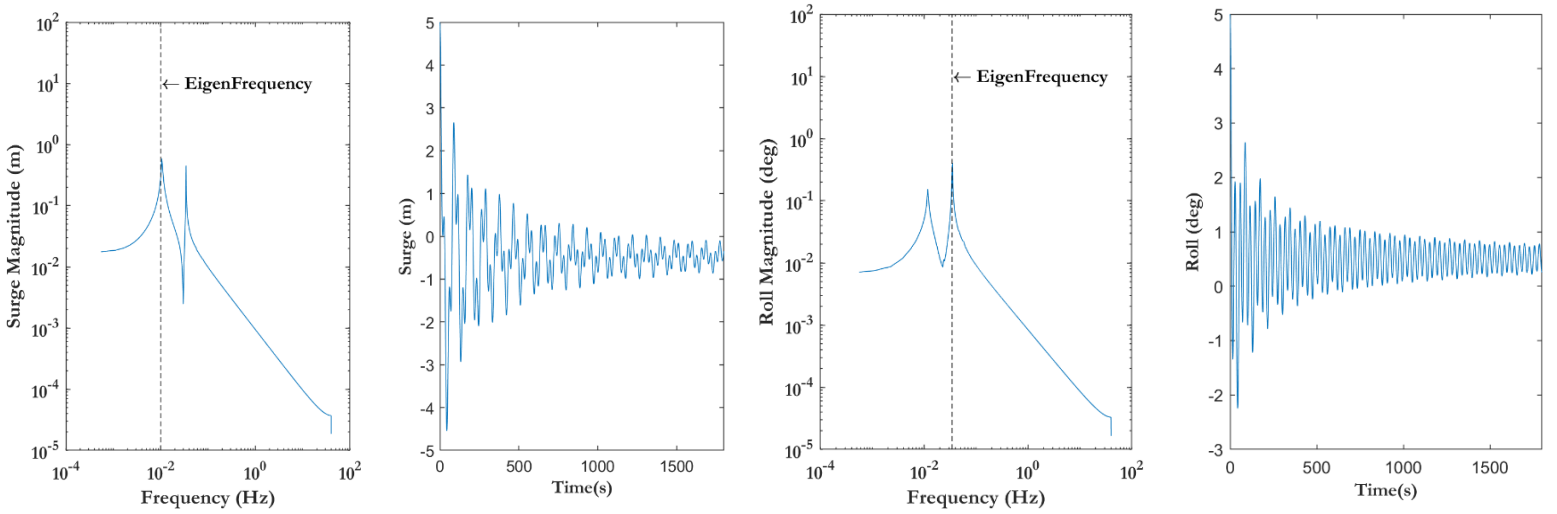

Figure 5.1 X axis spar platform motion DOFs Surge & Roll free decay time series & frequency domain graphs with eigenfrequency point.

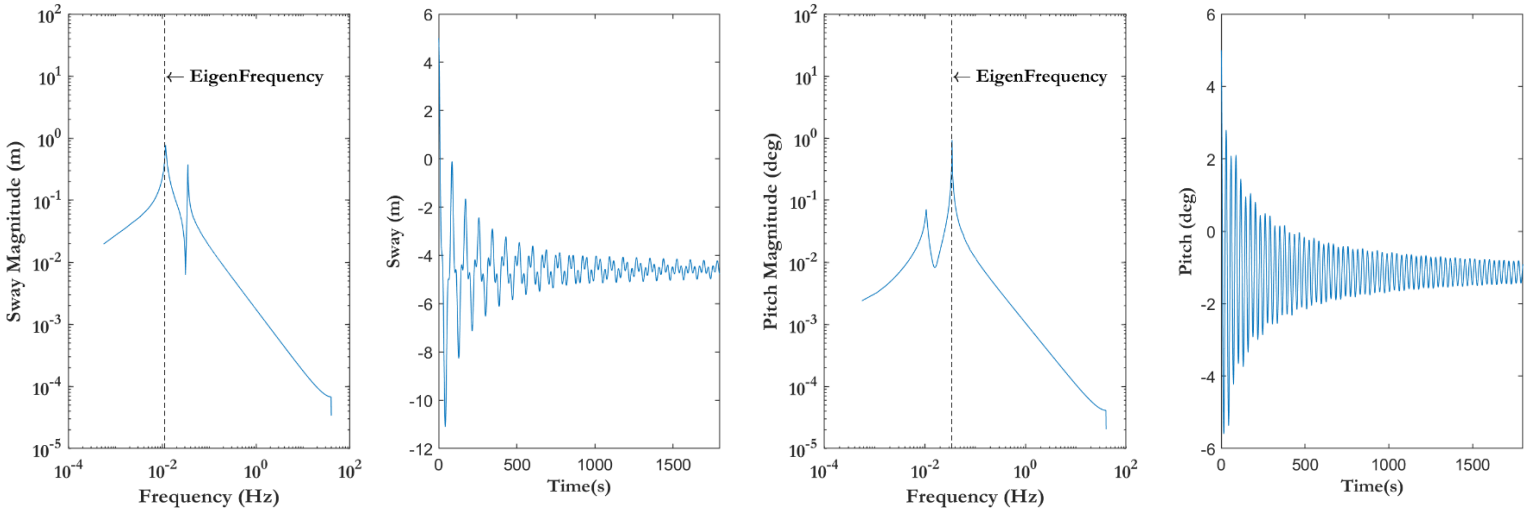

Figure 5.2 Y axis spar platform motion DOFs Sway & Pitch free decay time series & frequency domain graphs with eigenfrequency point.

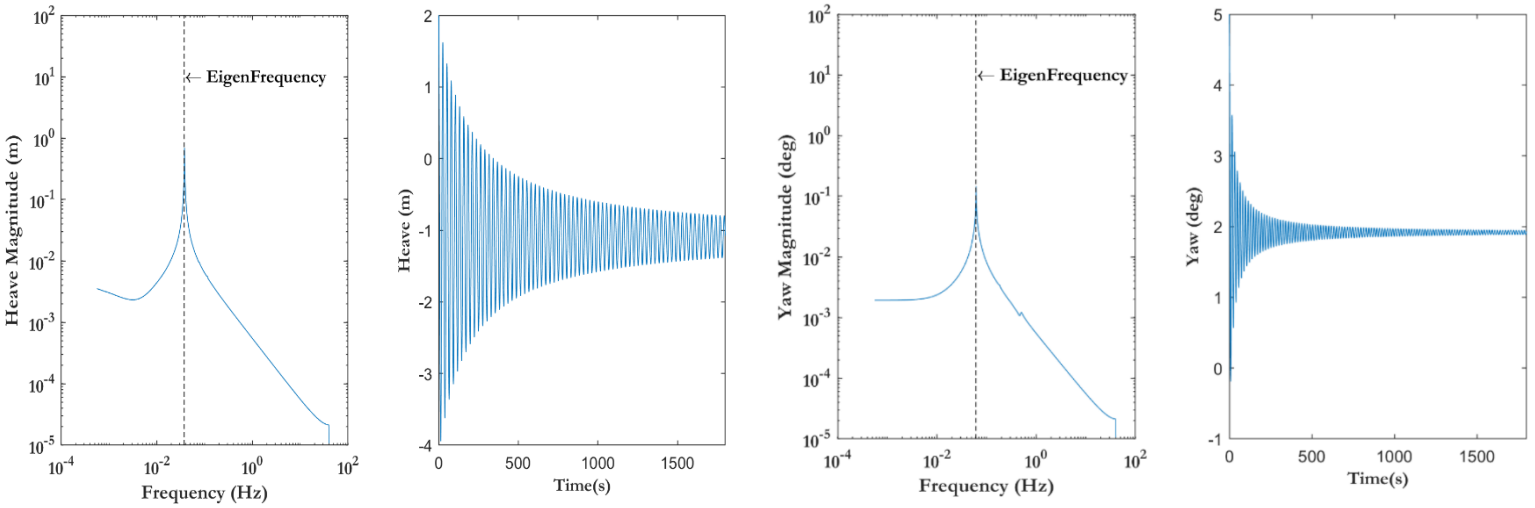

Figure 5.3 Z axis spar platform motion DOFs Heave & Yaw free decay time series & frequency domain graphs with eigenfrequency point.

The coupling effect is evident in the spar motion DOF frequency domain graphs for the surge-pitch and sway-roll pairs (Chena et al., 2019). Specifically, the graphs of Figure 5.1 and Figure 5.2 display a secondary peak, which corresponds to their coupled DOF, e.g., the minor peak of the frequency domain surge graph corresponds to the pitch eigenfrequency. This phenomenon is observed in neither the remaining (heave and yaw) DOF graphs, as they are not coupled, nor in the uncoupled surge, sway, roll and pitch graphs found in Figure C.1. Moreover, the coupling effect is also witnessed in the time-series graphs, where the damping effect exhibits significantly more variability and is noticeably less smooth in the coupled graphs of Figure 5.1 and Figure 5.2, compared to the Figure 5.3 ones. This last remark holds true for the uncoupled versions of the X and Y spar DOFs time series outcomes, as well.

The graphs obtained from the eigenanalysis tests exhibit the establishment of equilibrium after the decay of the initial displacement and oscillation. All the system DOFs ultimately return to an equilibrium position, characterized by approximately zero or insignificant displacement. The notable exception is sway, which rests at roughly 4 m. As mentioned during the discussion of Figure 4.16, this event is due to the mooring line system. Their lengths were adjusted compared to the original values provided in the Equinor documentation, in order to increase the spar motion data recreation accuracy presented in Section 5.2. Therefore, as a mooring line length recalibration was not performed to adjust the lateral spar displacement values at roughly 0 m, this sway equilibrium position is considered acceptable for the purposes of this project. Differently, the sway non-center can be attributed to the asymmetry of the Hywind mooring system, where two lines are connected on one side while only one line is present on the other side, as depicted in Figure 4.12. However, no further emphasis is given to this conjecture.

Table 5.2 Hywind measured & OpenFast model eigenperiods comparison (Equinor, 2018).

Platform Motion DOF	Hywind Eigenperiod (s)	Calculated Eigenperiod (s)	Error (%)
Surge	96	100	+4.1
Sway	96	90	-6.2
Heave	25.8	26.5	+3.8
Roll	33.7	29.5	-12.4
Pitch	33.7	29.5	-12.4
Yaw	13	16.2	+24.6

It should be highlighted that in Equinor's documentation there are no mentions on the free decay tests and eigenperiod measuring procedure, or any conventions of simulations / measurements. Given the section where it is presented in the Equinor report, this research assumes that the Hywind natural periods are simulated values, rather than derived from measurements. Hence, the discrepancy observed in the Table 5.2 eigenperiods can be attributed in part to the unknown simulation conditions. Overall, the OpenFAST simulation calculated eigenperiods closely recreate the Hywind measured ones, a remark that matches Jonkman et al., 2010 research results (Figure 3.10), where OpenFAST's eigenfrequency accurate estimation is highlighted. Specifically, both roll and pitch rotational DOF eigenfrequencies are slightly overestimated based on Jonkman's results. An observation that supports the OpenFAST model's slight eigenperiod underestimation when compared to Hywind's measurements, as eigenfrequency and eigenperiod have an inverse relationship (Jonkman et al., 2010).

Finally, despite not posing a grave discrepancy, attention should be devoted to the calculated surge and sway eigenperiods. The Hywind provided ones display the same eigenperiod value, while the OpenFAST simulated ones have a 10 s difference. This discrepancy can be ascribed to the different mooring/axis orientation configuration employed in the simulated and existing Hywind systems. Additionally, the undisclosed methodology for measuring the natural periods of Hywind further contributes to this deviation.

As expected, yaw experiences the highest error compared to the measured Hywind value. Other than model discrepancies, this error can also be attributed to Equinor's incorrect yaw measurements as established in Bussemakers' Siemens thesis project, where, specifically, the initially larger mean yaw displacement is replaced by a mean 0° yaw with unknown STD margins. In the same thesis project, the BHAWC/OrcaFlex simulated yaw eigenperiod experiences the highest error at 37% (Bussemakers, 2020).

5.2 Spar Motion Benchmarking

Out of the total eleven available Hywind cases, three different wind turbine operation – Hywind metocean condition cases are considered adequate to fully showcase the system response behavior and the overall benchmarking process. The three cases are presented and discussed in this section to assess the spar motion data recreation capabilities of the developed OpenFAST model. The cases include below rated, above rated and above cut-off wind speed conditions. Prior to each case comparison presentation, the metocean conditions of the load cases are depicted. The metocean conditions include wind velocity at hub height, significant wave height, peak wave period and current speed. The comparative analysis are presented via statistical, time series as well as power spectral density (PSD) graphs. An applied Kernel filter enhances the clarity and legibility of the PSD graphs during the data post processing procedure performed in MATLAB. These graphs display, in the form of dashed lines, the eigenfrequencies of Hywind measured spar DOFs and the peak wave frequency. Following the lateral DOF comparisons, a first order motion investigation is performed on them. A high-pass filter with a sampling frequency of 80 Hz and a cut-off frequency at 0.03 Hz is utilized on the simulated results to omit the second order motion effects. The cut-off frequency is deducted from the power spectral surge and sway graph peaks. The three distinct methods of results presentation and their respective assessment criteria are summarized in Table 5.3.

Table 5.3 OpenFAST model prediction standards per data presentation method.

Data Presentation Method	Assessment Criteria
Statistical (Mean & STD)	• Mean value numerical difference lower than 2 m/°. • STD value numerical difference lower than 2 m/°.
Time Series (to compare dynamic behavior)	Visual inspection that relatively showcase: • Agreement in 1st order lateral motion results. • Agreement in rotational motion results.
Power Spectral Density	• Peak frequency difference lower than 0.2 Hz. • No significant power amplitude disparities detected.

For completeness, the OpenFAST simulations employ both aerodynamic models discussed in Section 2.3, namely BEM and VPM-OLAF. Therefore, a brief assessment is also conducted to compare their respective abilities in approximating the Hywind measured motions. The specific OLAF input file settings selected for this analysis are presented in Appendix C, Figure C.2. The OpenFAST modelling settings are fully enabled for these simulations as presented in Figure 4.9, with the exception for yaw, due to reasons discussed in Section 5.1 and . Moreover, the heave DOF is also enabled, however, the simulated results are not included in the following discussions due to unavailability of Hywind's measured heave responses.

All eleven measurement cases that are simulated in OpenFAST are completed successfully, meaning that no diverging was observed in the spar motion simulation. This suggests that this study has developed a more stable model, compared to similar computational investigations as the one performed by Bussemakers, 2020, where only five out of eleven cases were not oscillating violently or diverging. The remaining measurement cases' statistical comparison graphs are included in Appendix C, Figure C.3, Figure C.4 and Figure C.5 for completeness purposes.

Regarding the energy yield comparison scope of this project, there are two DOFs primarily affecting the floating spar's energy yield. As established during Section 3.1, pitch and surge influence mainly the power generation of a spar FOWT (Huang & Wan, 2019). As a result, particular emphasis is given to these two DOFs, considering their significance in realistically replicating the dynamic behavior of the system.

5.2.1 Below Rated Wind Speed Operation

For this below rated wind speed – below rated turbine operation case, the statistical benchmarking of both BEM and OLAF simulated OpenFAST results against Hywind Case 8 measurements is displayed in Figure 5.5. Following, the corresponding spar motion DOF time series and filtered frequency spectra benchmarking for surge, sway, roll and pitch are presented in Figure 5.6, Figure 5.7, Figure 5.9 and Figure 5.10, respectively. Lastly, in Figure 5.8, the second order spar motion phenomena are omitted from the Hywind time series measurements for surge and sway by means of a high pass filter and only the first order motion measurements are compared to the OpenFAST BEM and OLAF simulated results. Most phenomena observed in this section are similar to other measurement cases. Therefore, results are discussed in greater detail here to minimize repetition.

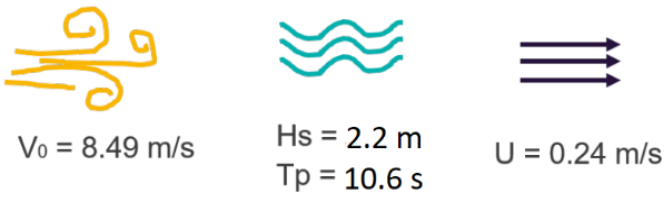

Figure 5.4 Hywind Measurement Case 8 metocean conditions.

Based on the mean and standard deviation margins of Figure 5.5, the spar motion DOFs are predicted well by OpenFAST in both BEM and OLAF aerodynamic modelling cases. Sway and pitch data are approximated better by OLAF. For surge and roll, both aerodynamic models showcase similar accuracy, with BEM's mean value being slightly closer to Hywind measurements. Finally, the measured yaw, at 0^{o} and insignificant variations, is fully represented by the disabled OpenFAST results.

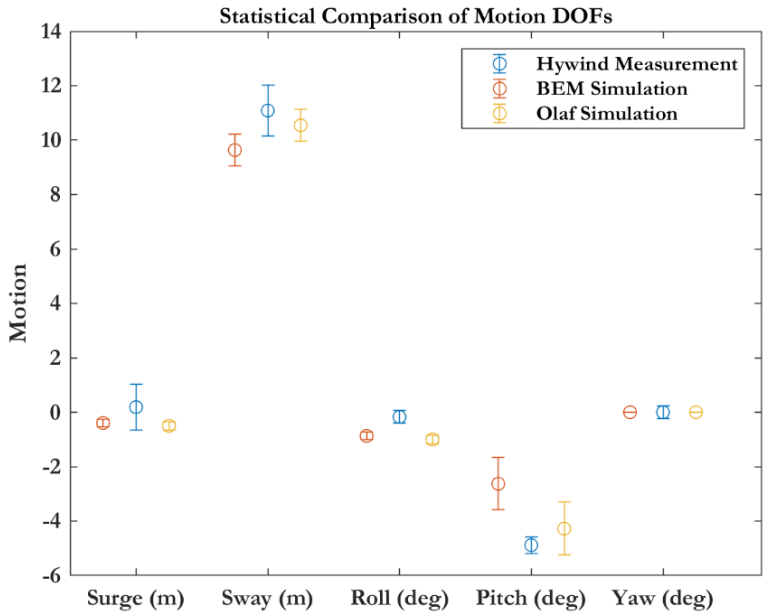

Figure 5.5 Spar platform motion DOF statistical comparison between Hywind Case 8 measurements, OpenFAST BEM & OLAF models.

With regards to surge and pitch, there are standard deviation inconsistencies observed. In the case of surge, the simulated STD is considerably lower compared to the measured one, while for pitch, the reverse holds true. Pitch's higher outcome fluctuation can be attributed to uncertain airfoil outlines and airfoil distribution as well as inaccurate mass allocation of the rotor, the nacelle and the hub . Moreover, the imprecise controller strategy implemented influences the thrust which drives the static pitch angle (Lenfest et al., 2020). The wind turbine and floater spar rotational damping coefficients may also be underestimated and thus lead to larger oscillations. Furthermore, the pitch behavior of a floating wind turbine can be significantly affected by imperfect spar center of gravity coordinates. If the center of gravity is positioned too high, it can result in a decreased stability of the turbine, resulting in larger pitch oscillations (Tran & Kim, 2015). These phenomena are evident in all FOWT operation cases, except for the idling cases, as described in sub-Section 5.2.3.

Surge, in contrast, showcases, lower oscillation amplitudes of first order motion only, as compared to the measured data which includes observable higher order drift. A possible reason is wave loads modeling inaccuracy and their interaction with the floating structure, because the current OpenFAST model does not model second order drift effects. Another reason could be the assumption of ideal hydrodynamic conditions that do not account for any real-world effects such as turbulence, wave-current interactions or the occurrences of wave groups. Additionally, the developed model entails parameters such as the spar's damping coefficients, whose values are uncertain as the existing values, although being specified by Equinor's provided documentation, they are not utilised as inputs by OpenFAST modules. Lastly, surge is affected by the mooring system damping and stiffness, which in the case of overestimation, leads to a less dynamic surge response. These outcomes are consistent in every case, with either similar surge values or slightly reduced motion.

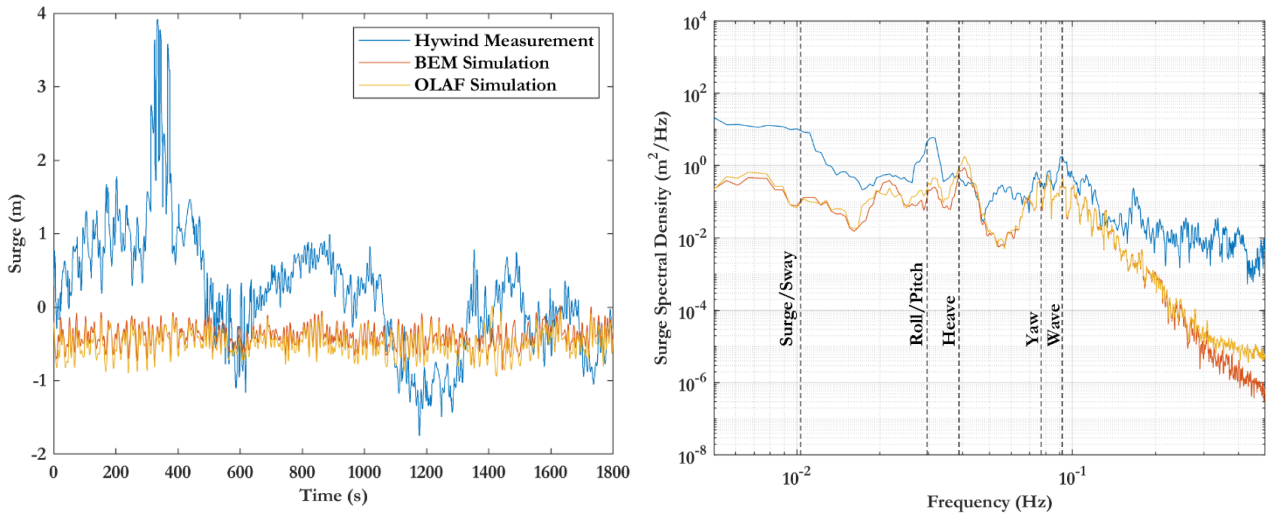

Figure 5.6 Spar platform surge time series and frequency spectra comparisons between Hywind Case 8 measurements, OpenFAST BEM & OLAF models.

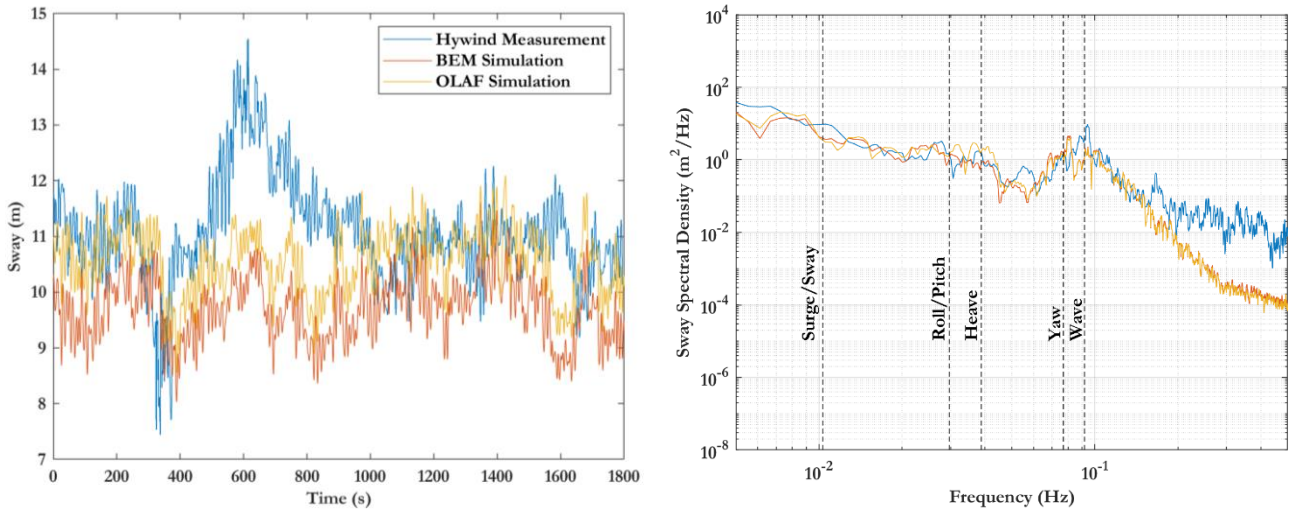

Figure 5.7 Spar platform sway time series and frequency spectra comparisons between Hywind Case 8 measurements, OpenFAST BEM & OLAF models.

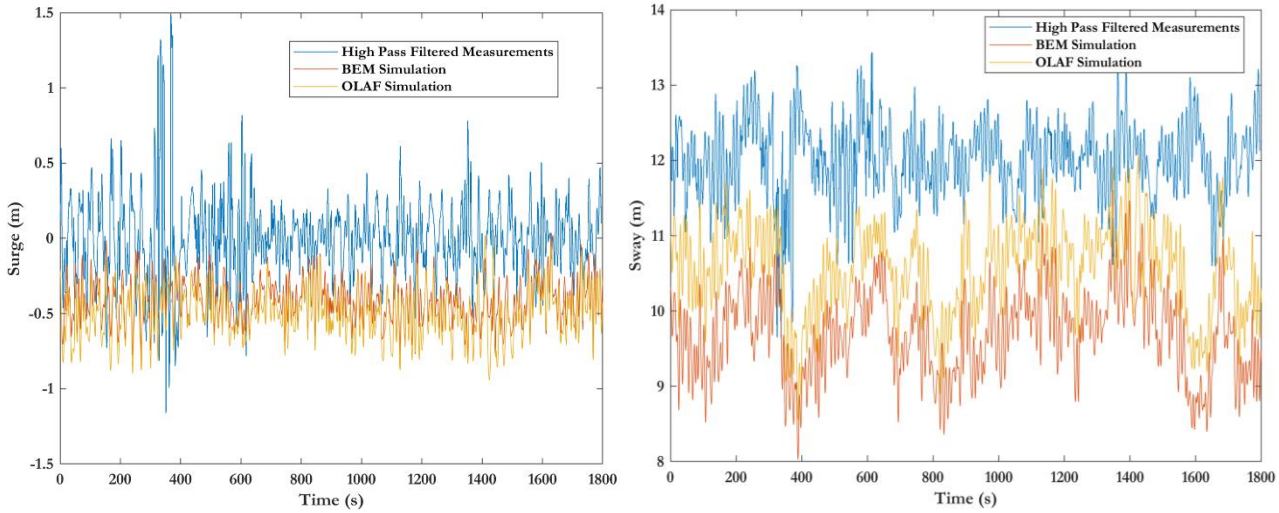

Figure 5.8 First order spar platform surge and sway time series comparisons between Hywind Case 8 measurements, OpenFAST BEM & OLAF models.

Regarding the surge time series graph of Figure 5.6, the second order drift and displacement phenomena, visible on the Hywind measurements, render the comparisons to the BEM and OLAF OpenFAST simulation results futile. This is because the latter simulations account for first order motion effects, and the generated waves do not have strong wave groups. A similar comment can be made for the sway time series graph of Figure 5.7. For that reason, the first order motion phenomena supplementary comparison of these DOFs is made in Figure 5.8. Based on them, it is evident that the OpenFAST developed model predicts well the first order lateral displacements of spar. In the case of sway, OLAF's numerical outcomes are closer to Hywind's measurements.

In frequency domain, the effects are captured greatly for both spar lateral displacements until the threshold of roughly 0.15 Hz, with the sway DOF results having a closer resemblance overall. Most of the power spectral density plots of surge, sway, roll and pitch experience a higher dividing frequency (commonly around 0.1 Hz - 0.2 Hz). At these frequencies, ordinarily, the power values are low and they do not alter significantly the outcomes. Therefore, these occuring deviations are deemed inconsequential to the overall validation.

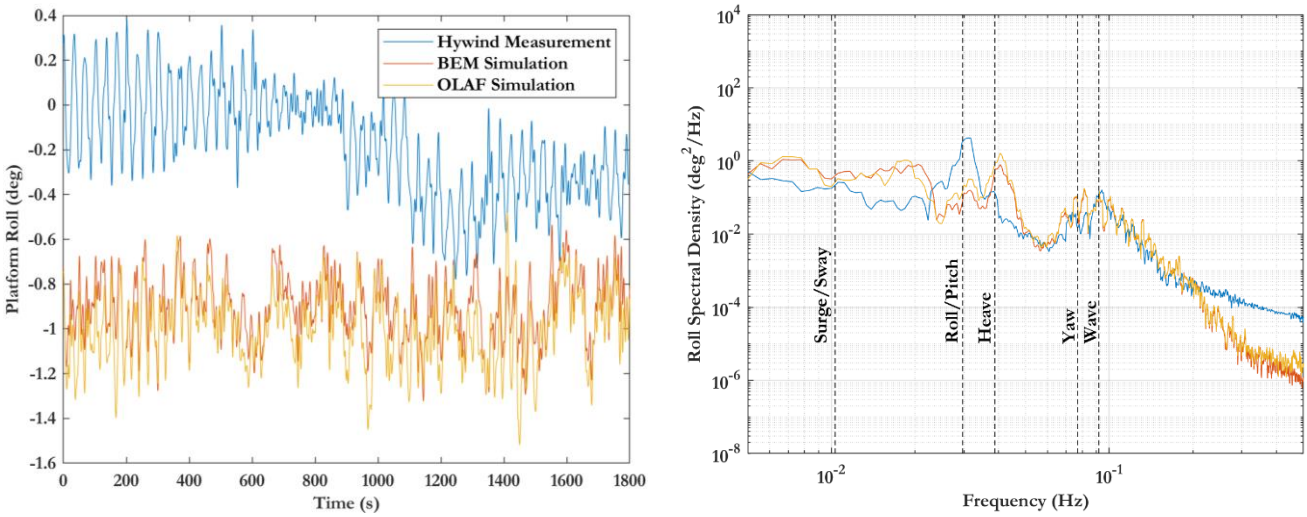

Figure 5.9 Spar platform roll time series and frequency spectra comparisons between Hywind Case 8 measurements, OpenFAST BEM & OLAF models.

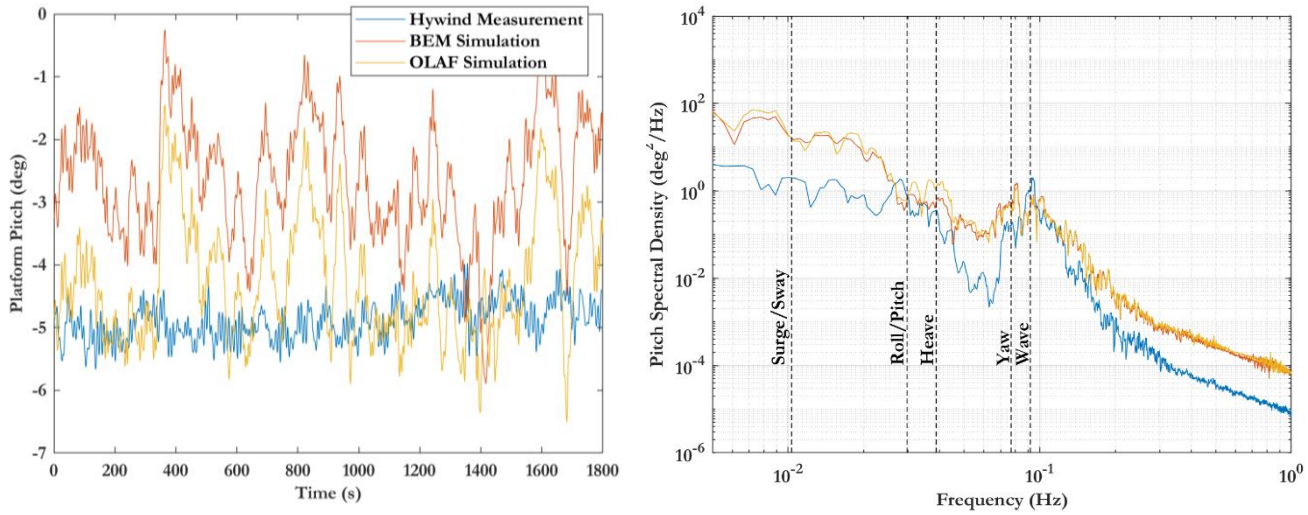

Figure 5.10 Spar platform pitch time series and frequency spectra comparisons between Hywind Case 8 measurements, OpenFAST BEM & OLAF models.

Based on the roll time series graph of Figure 5.9, it is established that, despite a slight roll equilibrium transfer from 0° to -0.4°, platform roll is recreated well to a certain extend by the developed model. Contrary to that, platform pitch for both BEM and OLAF oscillates violently compared to Hywind time series values, as seen in Figure 5.10 graph. Although OLAF appears to be closer statistically, it is seen that ultimately both aerodynamic models deviate from the measurements. The available evidence of an approximately constant spar platform pitch at -5° suggests that the platform possesses specific ballasting, mooring system and/or controller techniques that can stabilise it at a certain angle. In any scenario, these techniques are not implemented into OpenFAST and consequently, not taken into consideration during the model development. Differently, the approximately constant pitch can be the result of rotor's thrust overturning moment.

For the roll and pitch spectral densities, again, the measurements and simulated outcomes exhibit a considerable degree of agreement until the thresholds of 0.2 and 0.13 Hz, respectively. Once these frequency thresholds are exceeded, both BEM and OLAF simulated spectral densities produce underestimated results for all DOF cases, except for pitch, where the results are overestimated. Prior to the dividing frequencies of 0.15 Hz for the lateral displacements, 0.13 Hz for roll and 0.2 Hz for pitch, the eigenfrequency resonances of wave and pitch/roll are the ones that predominantly result in a power amplitude peak. In all cases and for all DOF spectral graphs, as the wave resonance occurrence is a result of the peak wave period, a value specified from Hywind measurements, the simulated and measured peaks mostly coincide with each other. In contrast, the pitch/roll peak heavily depends on the OpenFAST model's outcomes. Hence, since the respective eigenfrequencies between measured and simulated outcomes have a negligible error, the measured and simulated peaks demonstrate a relatively high degree of similarity. Lastly, in these DOF recreation cases, the aerodynamic model accuracy enhancement from BEM to OLAF is not prominent on the spectral outcomes.

Both surge and pitch spectral density graphs initially, roughly until 0.02 Hz, are not in accordance with the recorded values. In case of surge, OpenFAST either underpredicts or slightly matches the spectral energy, directly witnessed in the statistical comparison graphs as an underestimation of surge fluctuation-oscillation. Correspondingly, the OpenFAST pitch results fluctuate more, thus their spectral energy is higher prior to 0.02 Hz and post 0.2 Hz.

5.2.2 Above Rated Wind Speed Operation

For this above rated wind speed – above rated turbine operation case, the statistical benchmarking of both BEM and OLAF simulated OpenFAST results against Hywind measurements is displayed in Figure 5.12. Following, the corresponding spar motion DOF time series and filtered frequency spectra benchmarking for surge, sway, roll and pitch are presented in Figure 5.13, Figure 5.14, Figure 5.16 and Figure 5.17, respectively. Lastly, in Figure 5.15, second order spar motion is omitted from the Hywind time series measurements for surge and sway and only the first order motion measurements are compared to the OpenFAST BEM and OLAF simulated results.

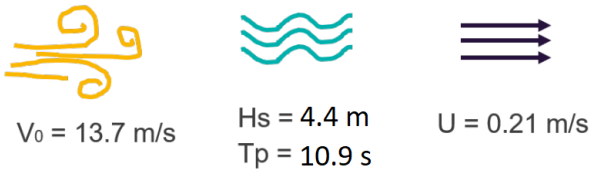

Figure 5.11 Hywind Case 1 Measurement metocean conditions.

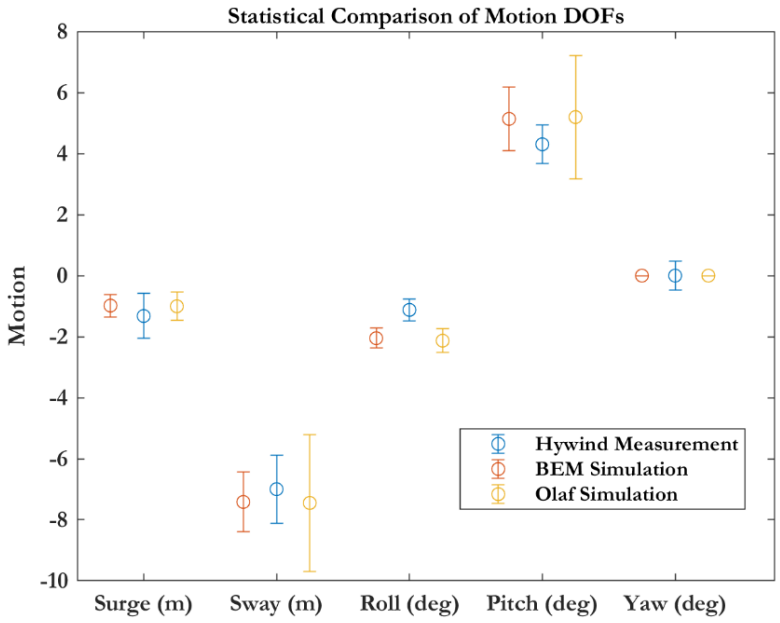

Figure 5.12 Spar platform motion DOF statistical comparison between Hywind Case 1 measurements, OpenFAST BEM & OLAF models.

Similar to the below rated operation case, the OpenFAST developed model predicts well the researched DOFs. Moreover, the comments about surge's restricted motion and pitch's amplified oscillation amplitudes are evident through the statistical comparison graph. This case also showcases highened motion fluctuations when OLAF is utilised as the aerodynamic model of choice. These effects are prevalent due to higher OLAF STD values for sway and pitch. Overall, statistically, BEM recreates the measured data more precisely only for this case. Based on the spar motion statistical comparison graphs of Appendix C, BEM and OLAF appear to predict the data with roughly similar levels of accuracy, albeit OLAF's is slightly increased. Lastly, expectedly, as stronger winds and waves surround the floating spar, the measured yaw experiences greater fluctuations. Hence, disabling yaw, now results in more significant errors, however, these errors are still considerably lower compared to the ones occuring while yaw was enabled. This last remark is valid for all Hywind measurement cases, leading to the conclusion that disbaling yaw, ultimately results in a more accurate model.

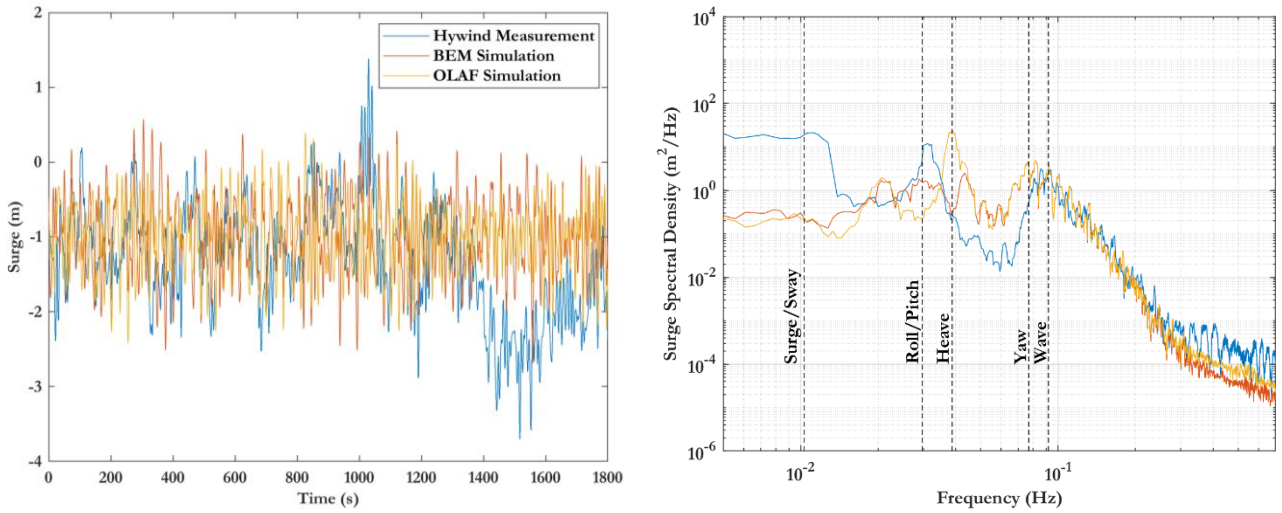

Figure 5.13 Spar platform surge time series and frequency spectra comparisons between Hywind Case 1 measurements, OpenFAST BEM & OLAF models.

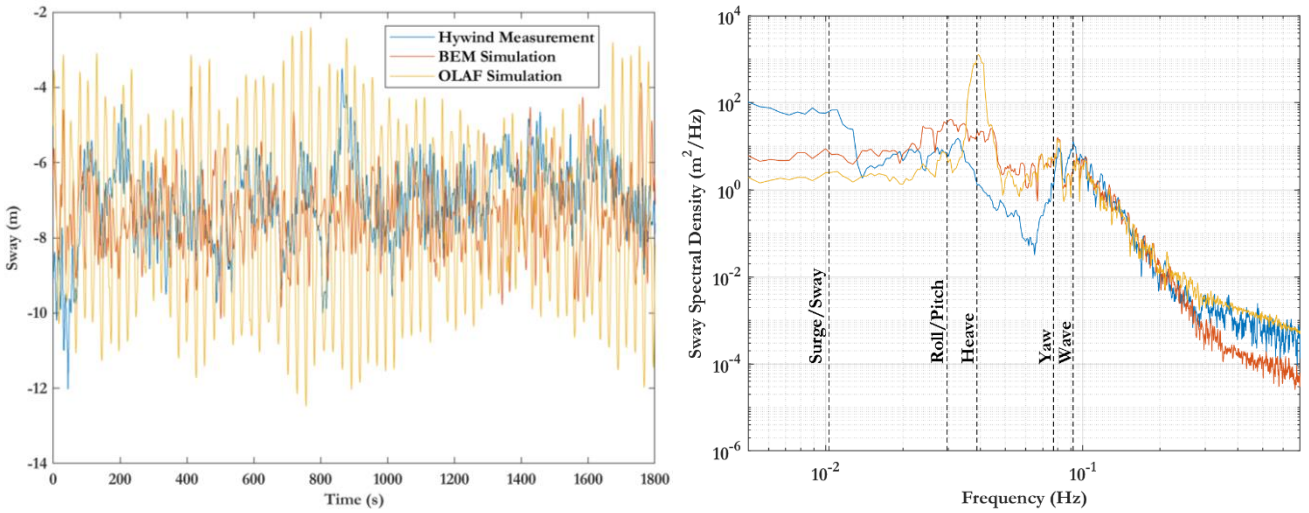

Figure 5.14 Spar platform sway time series and frequency spectra comparisons between Hywind Case 1 measurements, OpenFAST BEM & OLAF models.

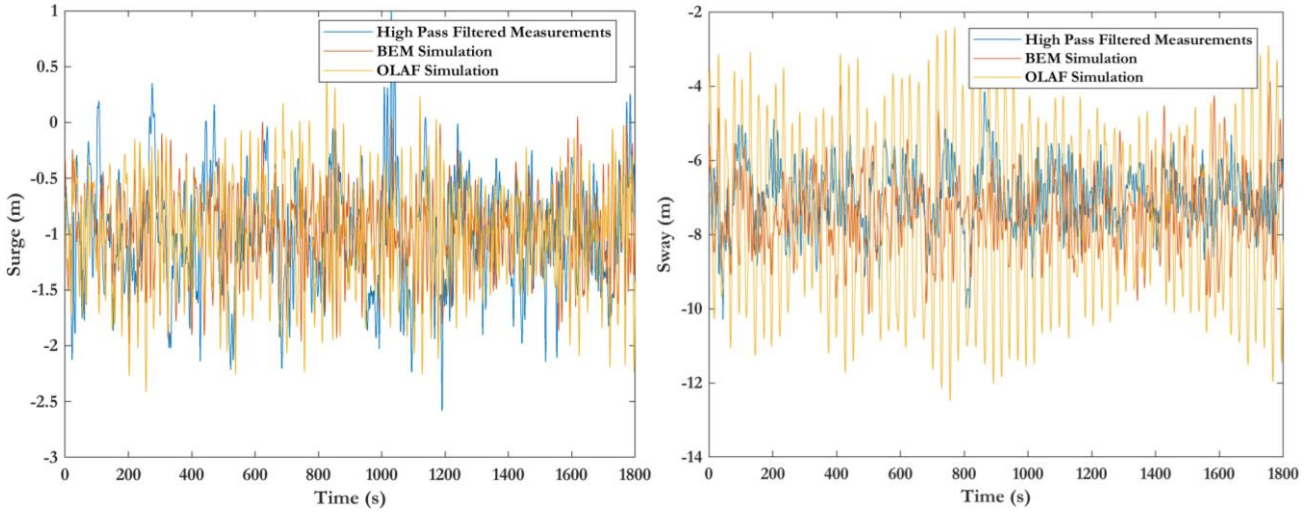

Figure 5.15 First order spar platform surge and sway time series comparisons between filtered Hywind Case 1 measurements, OpenFAST BEM & OLAF models.

Several points discussed around the statistical comparison graph are evident in the time series and spectral density plots. Time series results for surge are recreated properly by both aerodynamic models, while for sway, BEM simulation generates more comparable signals. Both lateral DOFs depict a significant underprediction, roughly two orders of magnitude, of the lower frequency power density. This lasts until the surge/sway eigenfrequency threshold is reached. This phenomenon was also observed in power spectral density graphs of surge in below rated operation cases as well as every idling case investigated DOF, albeit on a smaller scale. However, after that initial power mismatch is surpassed, the measured and simulated frequencies overlap in a significant degree.

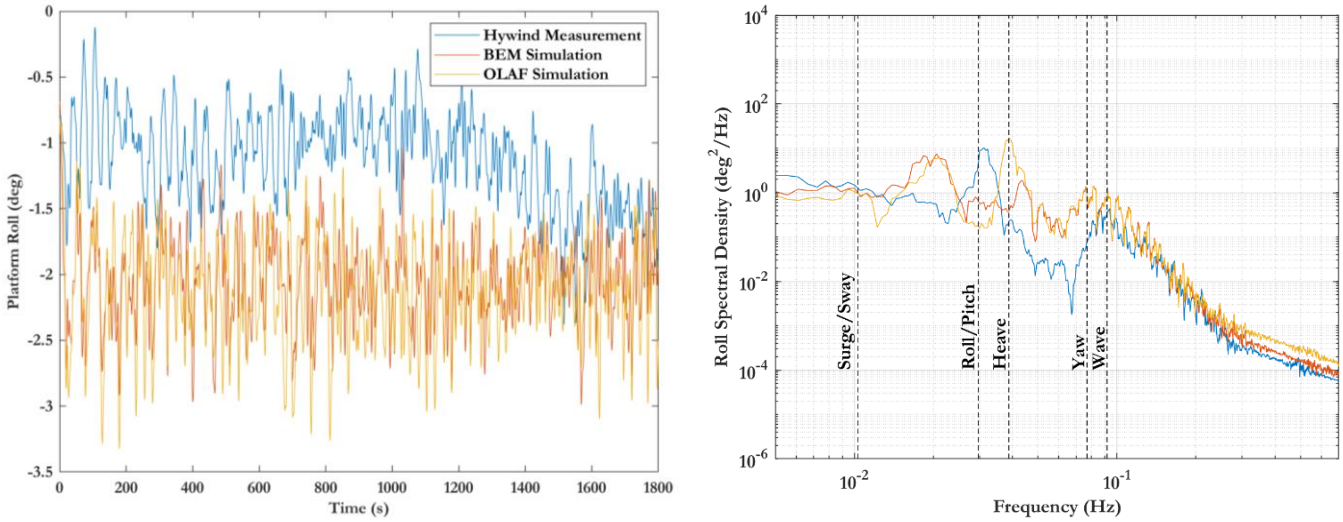

Figure 5.16 Spar platform roll time series and frequency spectra comparisons between Hywind Case 1 measurements, OpenFAST BEM & OLAF models.

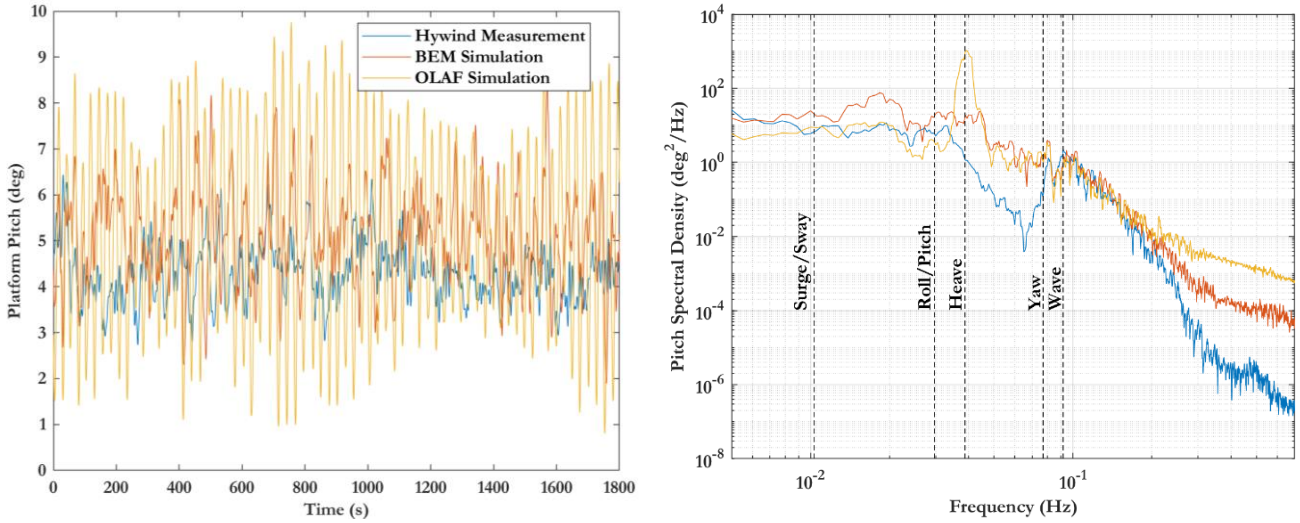

Figure 5.17 Spar platform pitch time series and frequency spectra comparisons between Hywind Case 1 measurements, OpenFAST BEM & OLAF models.

The roll rotational DOF is recreated well, albeit slightly overestimated, by both aerodynamic model simulations as seen from its time series plot. Despite power spectral peaks being overpredicted and occurring at different frequencies, the roll spectral density matches adequately the measurements. On the other hand, pitch is represented better by BEM, in both plots of Figure 5.17. The OLAF spectral density displays significant power peaks. Lastly, pitch is the sole researched DOF in this above rated operation Hywind case, where a dividing frequency is experienced, at approximately 0.2 Hz.

Energy distribution differences as the ones discussed above, can be attributed to excessive energy in the incoming wind field as generated by TurbSim. Other than the hydrodynamic damping, the aerodynamic damping can affect such responses. Aerodynamic damping of wind turbines refers to the ability of the surrounding air to resist the oscillation of a wind turbine's blades or rotor. It is affected by a plethora of factors, few of which include, blade design and stiffnesses, wind speed, air density, and turbulence intensity.

In conclusion, before analysing the no-power producing measurement cases 4 and 5, based on the discussions above along with the Appendix C spar motion DOF statistical comparison graphs, the developed Hywind based model in OpenFAST effectively forecasts the movement of the spar.

Consequently, the spar motion effects on power generation and energy yield computed results are considered reliable.

5.2.3 Above Cut-off Wind Speed Operation

For this above cut-off wind speed – idling wind turbine operation case, the statistical benchmarking of both BEM and OLAF simulated OpenFAST results against Hywind measurements is displayed in Figure 5.19. Figure 5.19 also displays the statistical motion comparison graph of the subsequent idling Hywind data that were recorded during Case 5, on the same date. The presented graphs are juxtaposed due to the discernible similarities in the phenomena they represent. Following, the corresponding spar motion DOF time series and filtered frequency spectra benchmarking for surge, sway, roll and pitch are presented in Figure 5.20, Figure 5.21, Figure 5.23 and Figure 5.24, respectively. Finally, in Figure 5.22, second order spar motion phenomena are omitted from the Hywind time series measurements for surge and sway and only the first order motion measurements are compared to the OpenFAST BEM and OLAF simulated results.

Ultimately, the idling FOWT operation is not critical for the energy yield comparative scope of the project, since during idling, the wind turbine does not produce power. They are, however, included as a means of validating the developed Hywind model regarding its realistic spar motion.

It should be mentioned that the OpenFAST modelling circumstances of these non-operational cases required changes in the Hywind based FOWT model. In ElastoDyn, all three blade pitches were set to 90° to represent a fully feathered rotor. In the same file, the generator DOF was disabled and the initial rotor speed value was set to 0 rpm.

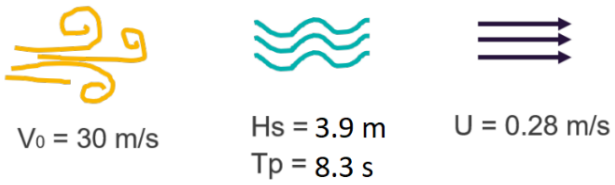

Figure 5.18 Hywind Case 4 Measurement metocean conditions.

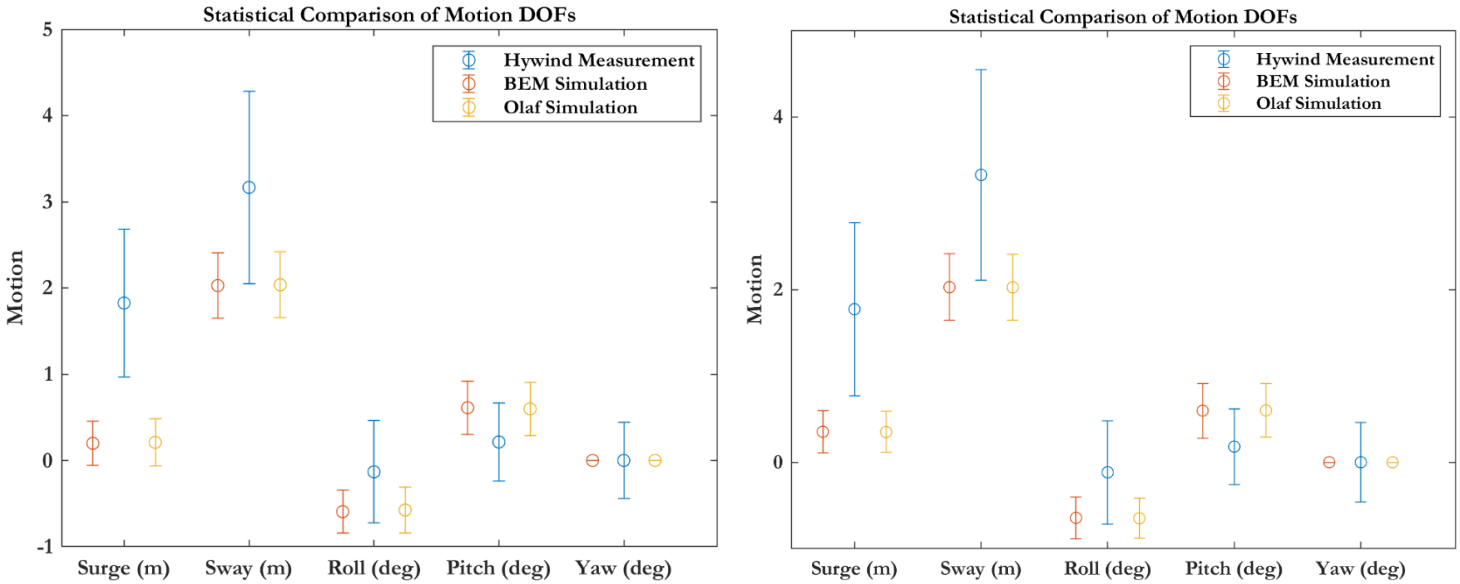

Figure 5.19 Spar platform motion DOF statistical comparison between Hywind measurements, OpenFAST BEM & OLAF models for the idling Case 4 (Left) and Case 5 (Right).

In the measurement against simulated result statistical inspection of the FOWT idling cases, most of the simulated signals' mean values are in accordance with the recorded ones with surge showcasing a stronger deviation. In addition, all simulated variations are lower than the measurements. In the case of an idling turbine, the hydrodynamic response is more apparent in the motion analysis. Previously presented cases have indicated that the OpenFAST model has increased hydrodynamic damping and the mooring system is restrictive towards lateral displacements. Thus, the surge and sway motions are limited and oscillations are overdamped. Roll is also affected by the overestimated hydrodynamic damping, while pitch STD values are comparable to the measurements for a single time. Overall, for the idling cases as well as most Hywind measured cases, rotational displacements have slightly overpredicted absolute values.

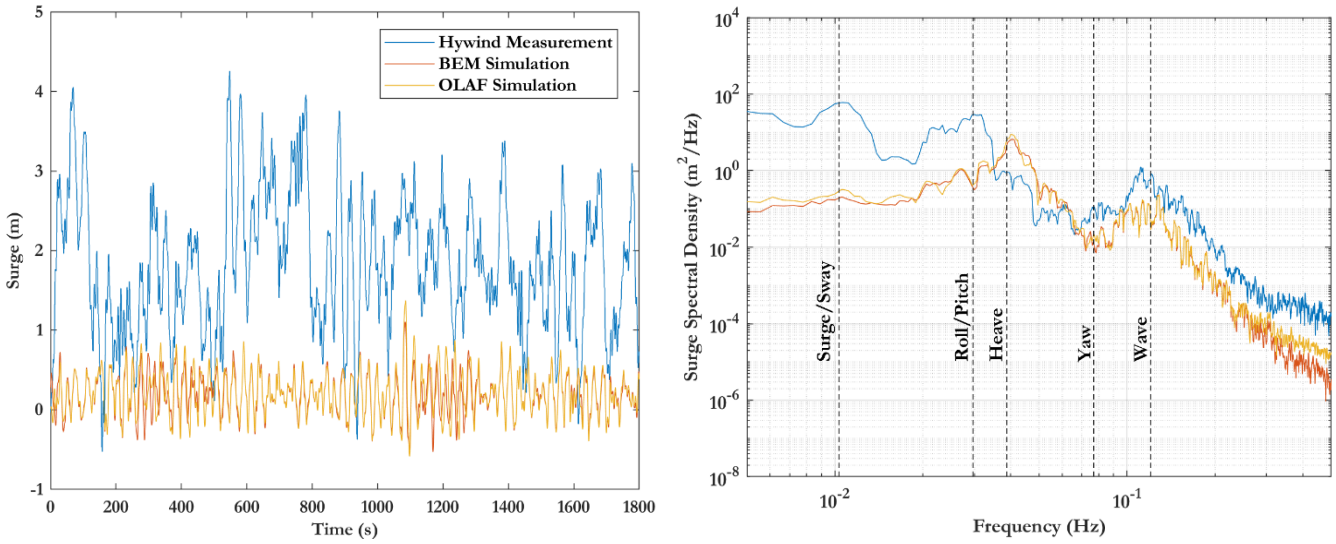

Figure 5.20 Spar platform surge time series and frequency spectra comparisons between Hywind Case 4 measurements, OpenFAST BEM & OLAF models.

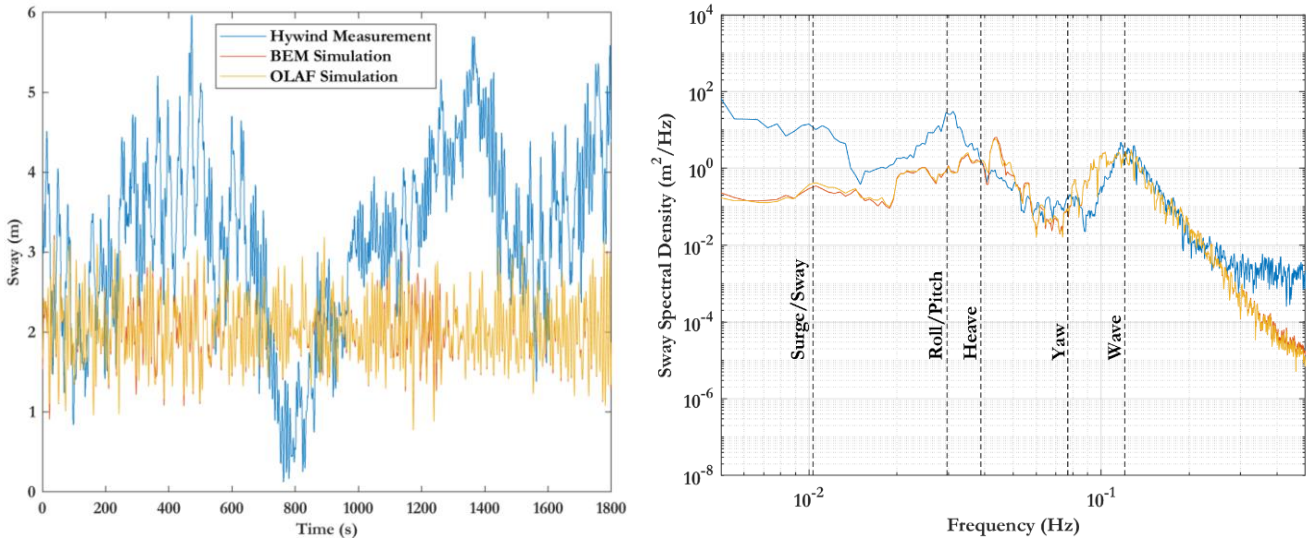

Figure 5.21 Spar platform sway time series and frequency spectra comparisons between Hywind Case 4 measurements, OpenFAST BEM & OLAF models.

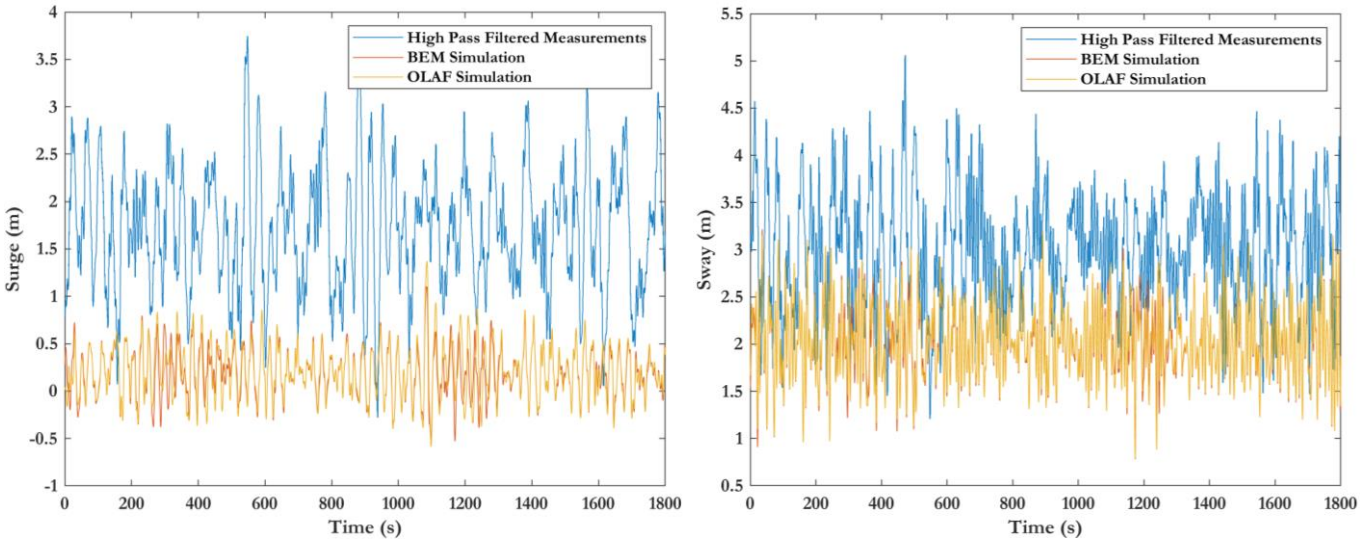

Figure 5.22 First order spar platform surge and sway time series comparisons between filtered Hywind Case 4 measurements, OpenFAST BEM & OLAF models.

The Hywind high pass filtered measurements for the idling cases oscillate more violently compared to the simulated results outcomes. Concerning the respective PSD plot comparisons, the results appear to be in accordance, mainly after the occurrence of the surge/sway eigenfrequency resonance. Most of the remarks made on previous graphs also apply here, thus they are not repeated.

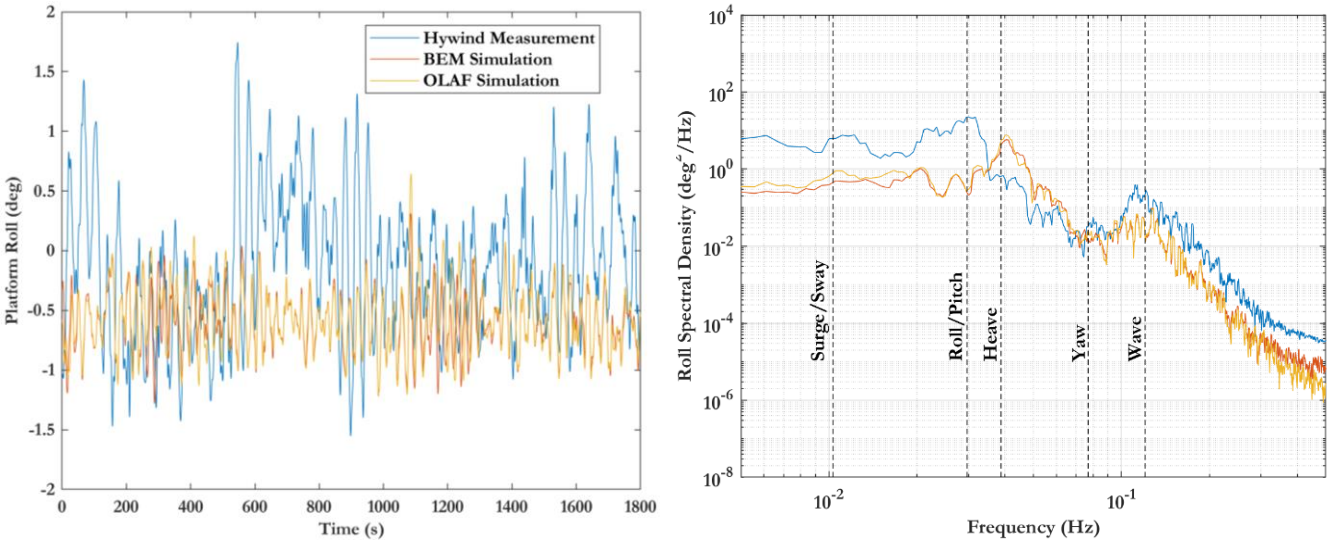

Figure 5.23 Spar platform roll time series and frequency spectra comparisons between Hywind Case 4 measurements, OpenFAST BEM & OLAF models.

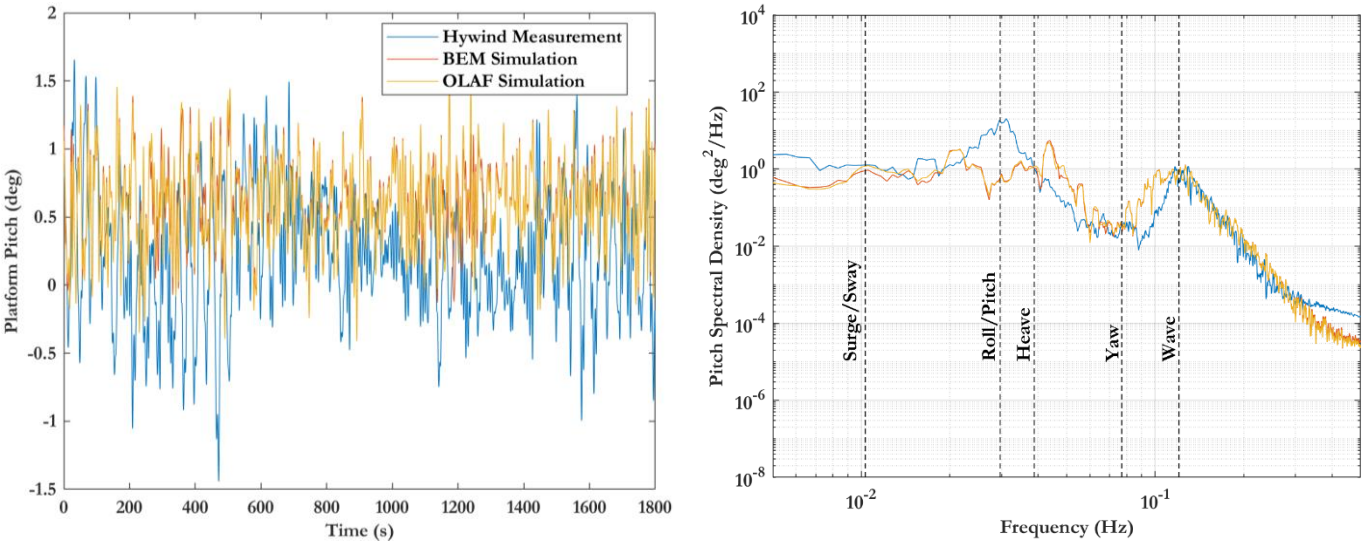

Figure 5.24 Spar platform pitch time series and frequency spectra comparisons between Hywind Case 4 measurements, OpenFAST BEM & OLAF models.

Finally, the rotational DOFs are predicted better compared to the rotational ones for this case, in both time series and spectral density schematics. This can be attributed to lack of the aerodynamic effects on the spar motion since the fully feathered rotor blades experience considerably lower aerodynamic loads. It should be mentioned that for the idling cases, both in time series and PSD plots, the BEM and OLAF simulation results showcase the greatest amount of overlap out of all operating cases that are modelled.

The aggregate results of this investigation are presented in the average and maximum summary Table C.1 in Appendix C, where the Hywind measurements for surge, sway, roll and pitch are compared to both BEM and VPM-OLAF corresponding simulated results. These difference outcomes per spar motion DOF arise by deducting the absolute statistical mean and absolute maximum Hywind measurement from the corresponding absolute OpenFAST simulated values. Therefore, a positive cell value indicates overestimation while a negative one, underestimation. The mean values are presented in the statistical comparison graphs included in this section and Appendix C, while the maximum values are presented in the time series graphs. Lastly, the underlined value per spar motion DOF comparison between the aerodynamic models highlights the higher precision one. A concluding peculiar observation concerns the mean data prediction of the lateral motion DOFs, where OLAF has a higher precision level in all Hywind measurement cases, including the idling ones, where roughly equal levels of precision are achieved.

5.3 Model Discrepancies

This work has developed a numerical model in OpenFAST that attempts to approximate the deployed Hywind spar behavior. Key assumptions were deemed necessary due to the inaccessibility of significant inputs and data at the time of conducting the research. Moreover, OpenFAST possesses inherent limitations, in the models that were employed herein, leading to modelling simplifications. These constraints contributed collectively to the differences between the developed model and the Hywind FOWT. Discrepancies that prevented an increased precision model and/or actively influence the current model are acknowledged and discussed below.

One of the greatest assumptions on the developed Hywind based OpenFAST model is regarding the high number of unknowns surrounding the Siemens wind turbine. Due to confidentiality reasons, key input parameters, which influence both structural and aerodynamical responses, are unavailable. These parameters include:

- specific airfoil profiles and distribution,
- blade and tower stiffnesses and mass distribution,
- blade chord and twist along its radius,
- tower diameter and thickness along its height,
- gearbox, generator efficiencies and shaft dimensions,
- nacelle and hub mass,
- spar platform's exact center of gravity.

Input data for stiffnesses, mass distribution, blade chord and twist angles were ultimately upscaled from the original NREL 5 MW wind turbine while the airfoil profiles selection was partially guided from industry experts. Thus, the blades are not a replica of those fitted on for Hywind. Occasionally, it was necessary to alter a parameter away from the measured value to compensate for an uncertain or possibly erroneous system response caused by an unknown input. For instance, that was the case for mooring line lengths, which, despite being presented in the Equinor documentation, were marginally revised in the OpenFAST model to enhance its outcome accuracy.

The most significant variable which affects all the FOWT dynamic responses is the controller. Throughout this project, the control strategy implemented on the Siemens SWT-6.0-154 FOWT has been an immense enigma that impacts the power generation and the spar motion, directly and indirectly, respectively. Additionally, as discussed in Sub-Section 4.2.4, due to time constraints on this work, the controller operating the FOWT does not possess specific floating-nacelle velocity feedback gains or similar techniques to counteract the spar's motion effects. It can be speculated that the SWT-6.0-154 controller employs a specific strategy tailored to the capabilities of floating platforms. Further discussion on the topic is made in Sub-Section 6.2.4, where literature review is conducted on the energy yield and power performance percentile adjustments are employed upon the developed model simulated outcomes.

Other than wind turbine discrepancies, the benchmarking results present deviations due to unidentical metocean condition representation. Firstly, dissimilarities in Hywind measured & TurbSim simulated wind fields are showcased in both time series and statistical comparison graphs. The former has been presented in Figure 4.2 while the latter is depicted in Figure 5.25. Although the recreated, turbulent wind speed time series data are not expected to identically match the Hywind measurements, they introduce small differences in the spar motion time series results. As seen in the statistical comparison graphs, the idling cases 4 and 5, experience strong deviation in their recreation attempt. This is attributed to Equinor's removal of the recorded measurements, of the instances when the blade was covering the anemometer during the idling cases. The remaining cases deliver great results in the statistical comparison scheme. Secondly, inaccurate wave and current profiles can cause deviations from reality in the dynamic response of the platform and mooring lines, which can lead to model discrepancies. HydroDyn's ability to accurately simulate these profiles is limited by factors such as numerical resolution, computational resources, and the complexity of the sea-state input. Moreover, HydroDyn's wave recreation capability is restricted further by using purely statistical wave inputs instead of user-defined wave time series measurements, which may include prevailing wave groups. It should be noted here as well that Hywind does not provide sea surface elevation time histories. Overall, the aforementioned metocean dissimilarities mainly influence the time series benchmarking results, while the statistical and PSD effects are not as obvious.

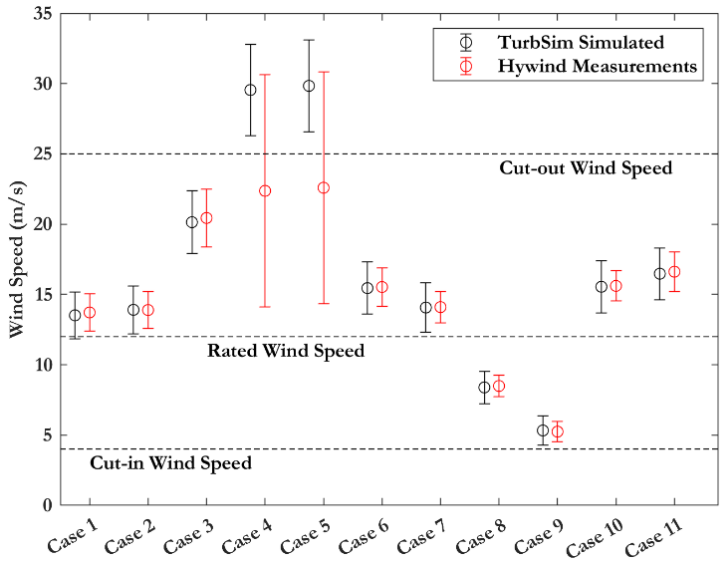

Figure 5.25 Hywind measurements & TurbSim simulated result statistical comparison for all provided cases.

For each Hywind measurement case simulation, the nacelle yaw input was equated as such that the wind turbine was perpendicular to the wind inflow. Therefore, any instances of yaw misalignment were eliminated. In reality, yaw misalignments between nacelle and incoming wind were reported, however within the scope of this work, OpenFAST could not replicate that phenomenon with the deployed controller. In combination with the disabling of spar motion yaw, the occurrences of yaw misalignment were unphysically removed from consideration. According to Shaler et al., this yaw misalignment mitigation potentially contributes to the accuracy similarity between the two aerodynamic models. Specifically, they concluded that OLAF and BEM simulation outcomes compare well even with significantly higher fidelity results with no yaw misalignment (Shaler et al., 2023).

The exclusion of potential flow theory in lieu of strip theory and not explicitly considering second order phenomena in the OpenFAST HydroDyn module leads to significant model discrepancies. The potential flow theory is essential in capturing the complex wave-body interactions which determine the hydrodynamic forces acting on the FOWT structure. Neglecting them, results in incorrect estimation of the motion and loading of the structure, leading to potential errors in the model predictions (Jonkman et al., 2015; Papillon et al., 2020). Furthermore, disregarding second order phenomena, which include drift, non-linear wave excitation, and non-linear radiation damping, that arise from the interaction between fluid and structure, also results in deviations. Drift refers to the tendency of a floating structure to move in the direction of wave propagation due to the interaction between the structure and the waves. Non-linear wave excitation is the phenomenon where the response of the structure is not proportional to the wave amplitude but depends on the square of the wave amplitude or higher powers. Non-linear radiation damping refers to the effect of wave-induced motion on the damping of the structure, which can be influenced by the non-linear behaviour of the structure in waves. Overlooking the impact of sum- and difference-frequency loads induced by second order hydrodynamics assumes that they are significantly smaller than first order effects and results in misevaluation of the system's eigenfrequencies (Bayati et al., 2014).

In addition to HydroDyn's limitations affecting the motion response of the FOWT model, MoorDyn experiences software constraints. Its constraints are primarily related to linear stiffness assumptions for mooring lines, neglecting the effects of nonlinearities and line hysteresis, which significantly impact the dynamic behaviour of FOWTs (Hall, 2020).

Compared to the real Hywind FOWT, the OpenFAST model completely neglects spar modelling details such as array cable effects and marine growth. The latter develops on the bottom of the spar as seen in Figure 5.26. Marine growth ultimately increases the drag coefficient, outer diameter and miscellaneous

mass of the platform, affecting its hydrodynamic behavior, leading to minor alterations in the response of the entire system (Shi et al., 2012).

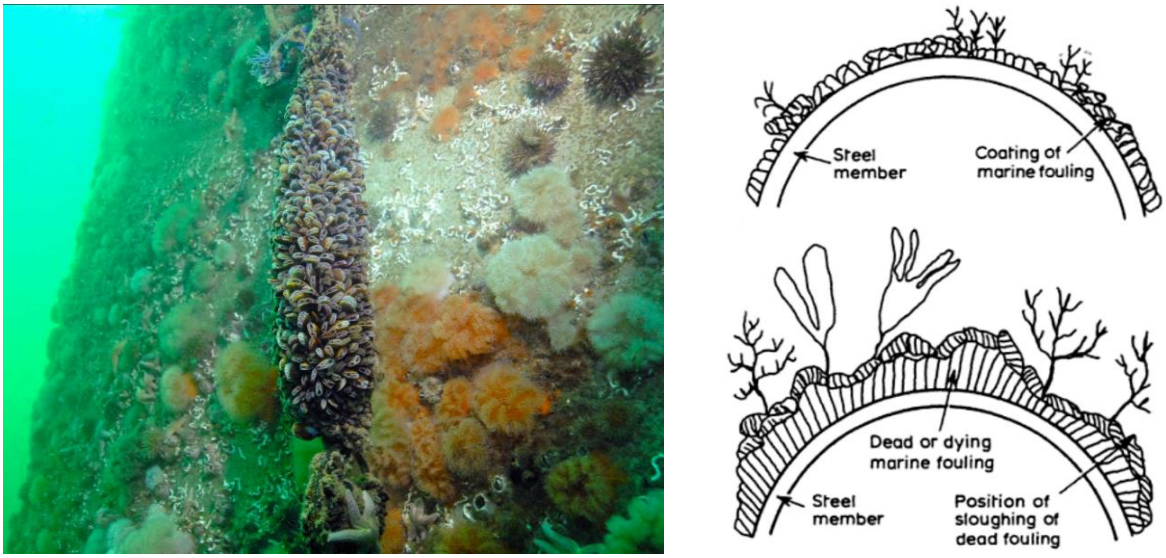

Figure 5.26 Marine growth developed on an offshore platform (Left) & explanatory schematics (Right) (Shi et al., 2012; Degraer, 2020).

Finally, Equinor's yaw measurements include inconsistencies and erroneous values (Equinor, 2018). Unfortunately, the corrected values are not retrieved but are only speculated, therefore the decision to disable the platform yaw on the developed model can result in significant discrepancies (Bussemakers, 2020). The lack of yaw leads to a fixed orientation of the spar and turbine, which is not fully representative of a realistic system. This affects the loads distribution and the response of the turbine to the wave and wind conditions, leading to inaccurate predictions of the turbine's performance.

Chapter 6. Comparison between Bottom Fixed & Floating Wind Turbine

While the foregoing chapter demonstrates the degree of realism available in the developed model alongside its shortcomings, this chapter examines the influence of metocean conditions and nacelle velocity on the power generation of the developed OpenFAST floating spar model. Following, the annual energy performances of the spar FOWT and the monopile BOWT are compared and discussed. These comparisons are simulated using both aerodynamic models, BEM and VPM-OLAF.

6.1 FOWT Motion Effects

The main difference between floating and bottom fixed structures is the ability of the floater to move more pliantly in response to the external forces, such as wind, waves, and currents, acting on them. These FOWT motion responses influence multiple parameters, including the generated power, the aerodynamic loads and the fatigue damage on the structure. Given the primary focus of this project on power generation, this section specifically examines the effects of ocean conditions and nacelle velocity on power performance.

6.1.1 Ocean Condition Effects on Spar Motion & Power Generation

As the name implies, bottom-fixed structures are securely attached to the seabed, resulting in minimal motion under oceanic conditions. This motion restrictions are primarily due to deflections along the steel structure and at the pile-soil interface. In contrast, floating structures have a certain degree of freedom to rotate and move around a defined offset. Different ocean conditions result in distinct surge, sway, heave, roll, pitch and yaw responses. As discussed thoroughly in Section 3.1, the wind turbine power performance is directly affected by the motions of a floater, with a greater emphasis on surge and pitch.

In this analysis, the developed Hywind OpenFAST FOWT model is subjected to steady wind conditions generated by InflowWind's module. A simulation was conducted for each wind speed field separately in order for the spar displacement steady state to be reached. These wind fields do not account for turbulence since this section investigates by essentially attempting to isolate the effects of hydrodynamic induced motions on power performance. That way, the resulting average and fluctuating responses can be primarily attributed to ocean hydrodynamics. BEM is the utilized aerodynamic model for this purpose due to its efficient computing prowess. The controlled ocean conditions that transpire while the varying ocean parameters are simulated, are presented in Table 6.1. It is clarified that, the current speed conditions are assumed to be homogenous at all depths to simplify this sensitivity analysis. Additionally, the incoming and propagating directions of wind, waves current are all set to 0^o, meaning that the FOWT structure is affected by these metocean conditions as seen in Figure 6.1. As a consequence of this, the wind turbine performance impact of metocean directions is not investigated during this project. The corresponding surge and pitch mean and STD values as well as time series outcomes at rated incoming wind speed for different ocean inputs are displayed in Figure 6.2 and Figure 6.3, respectively.

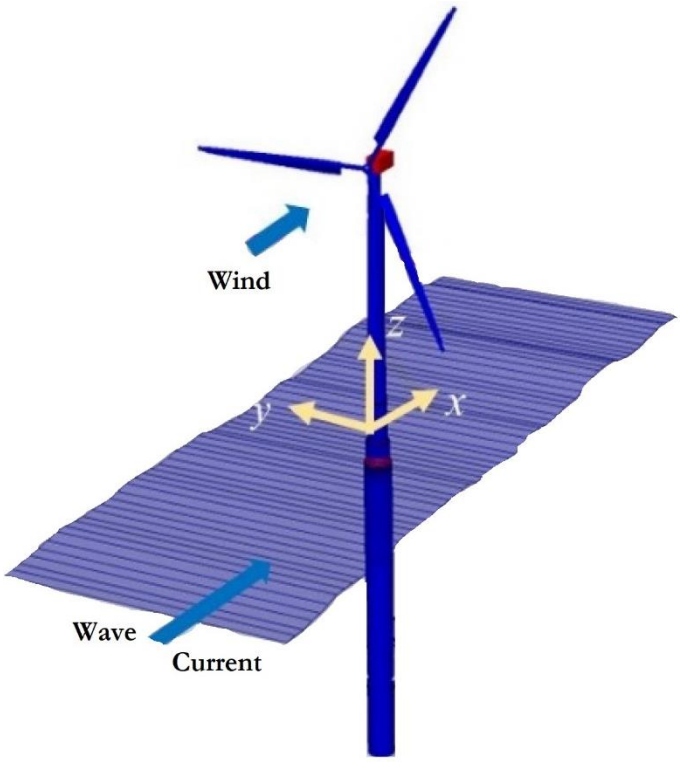

Figure 6.1 Metocean direction representation schematic (Liu & Yu, 2022).

Table 6.1 Controlled ocean conditions per varying ocean parameter.

Varying Ocean Parameter	Significant Wave Height H_s (m)	Peak Wave Period T_p (s)	Current Speed (m/s)
Current Speed	3	8	Ranging between 0.1-0.3
Wave Height & Period	Ranging between 1-8	Ranging between 4-12	**Sub-Surface:** 0.1 **Near Surface:** 0.15 **Depth Independent**: 0.2

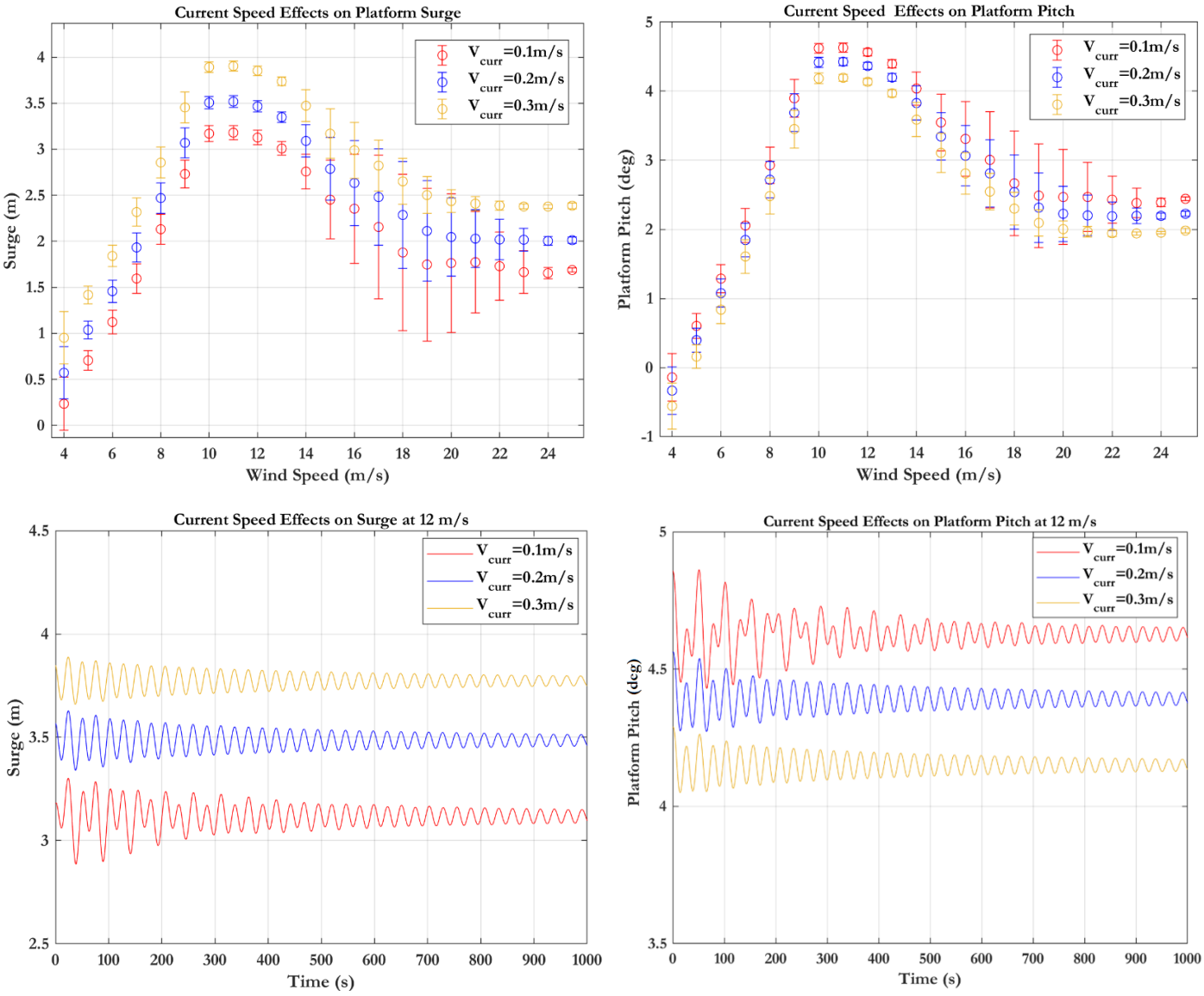

Figure 6.2 Varying current speed effects on platform surge (Left) & pitch (Right) statistical and time series outcomes.

The platform surge and pitch results of Figure 6.2 and Figure 6.3 are discussed in tandem as similar phenomena are observed in both DOFs. Surge and pitch follow an increasing trend until the wind speed of 10 m/s. The DOFs reach their maximum displacement roughly at the rated wind speed, which is attributed to the maximum wind load on the turbine blades. Consequently, the structure experiences the largest force in the horizontal direction and the greatest torque around the y axis. A significant remark is that, surge and pitch are the sole spar motion DOFs to showcase similarly increasing behavior during the partial load region. In the same region, the remaining DOFs either are stable or fluctuate as seen in Figure

4.16. Post rated wind speed, their values decrease steadily until roughly 20 m/s. Although several reasons can result in that effect, the most plausible cause is the rotor blade pitching activating after the inflow wind speed reaches the 12 m/s threshold. Thus, the aerodynamic load decreases gradually. The aforementioned phenomena are witnessed in both varying wave conditions and current speeds at similar degrees of severity.

Specifically for the current speed varying outcomes, mean surge increases linearly with greater current speeds, while, in contrast mean pitch decreases linearly. As current propagates towards the positive surge direction, the spar experiences higher hydrodynamic loads, forcing it to move laterally. The higher hydrodynamic current pressure-force results in a counteracting moment that offsets some of the wind-thrust induced moments about the FOWT structure's center of rotation. This torque counteracts the aerodynamic torque caused by the increasing wind velocities, thus the platform pitch drops. The project did not delve into the examination of a potential fringe coupling moment wherein the current directly opposes the wind direction, which could potentially induce a more substantial mean pitch offset. Regarding the STD margins, they remain relatively low until the activation of rotor blade pitching at roughly 12 m/s. Following the rated wind speed, the fluctuation increases and reaches its maximum simultaneously as the mean displacement plateaus at a local minimum. For both surge and pitch, the fluctuation amplitudes decrease linearly with increasing current velocities. All aforementioned remarks of current speed impact are evident in both statistical and time series results.

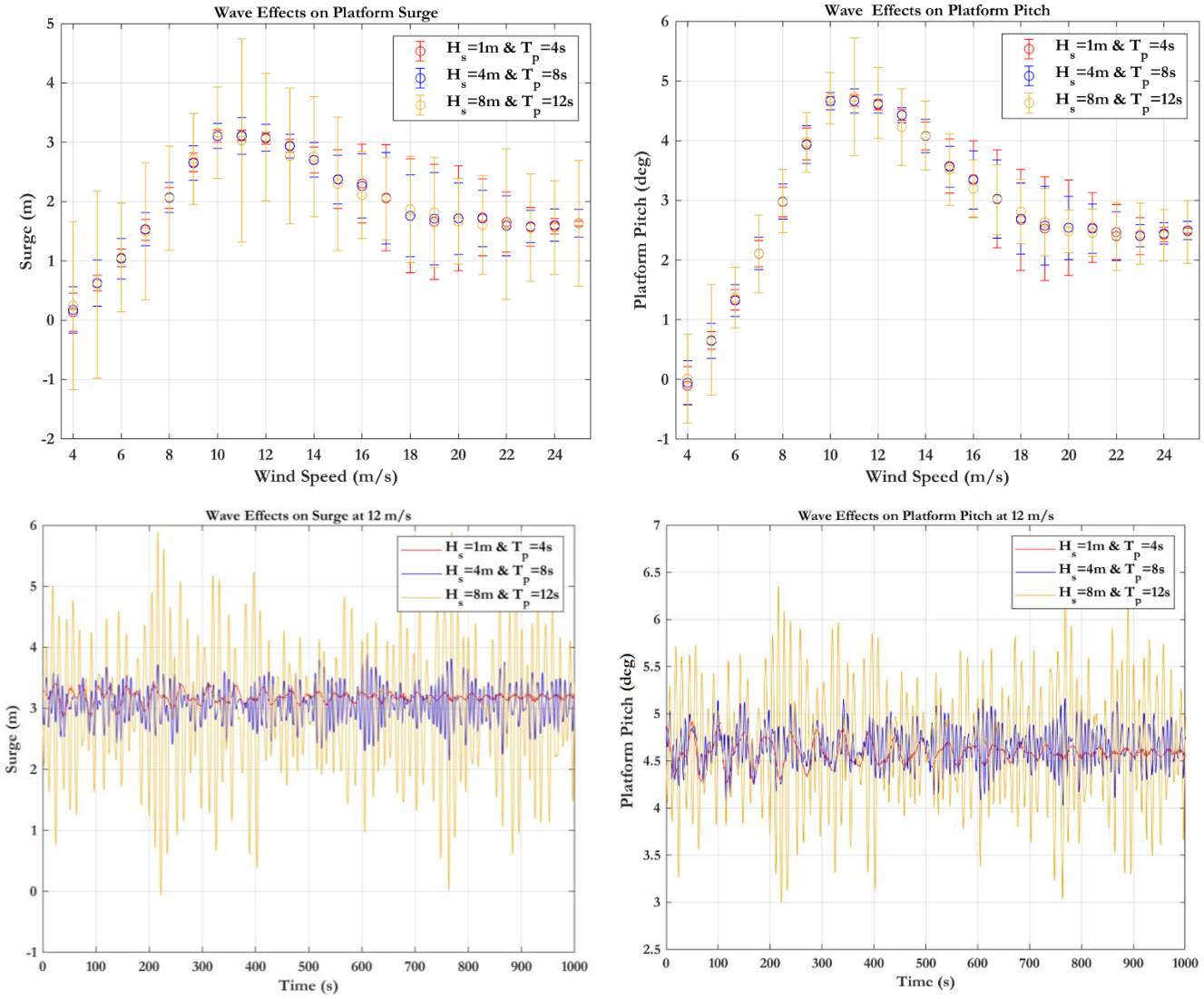

Figure 6.3 Varying wave condition effects on platform surge (Left) & pitch (Right) statistical and time series outcomes.

The varying wave conditions outcomes highlight that their impact on mean surge and pitch displacement is insignificant, while the fluctuation amplitudes are strongly affected. Both pitch's and surge's oscillation amplitudes increase strongly with wave height and peak period, albeit the oscillation amplitudes are significantly higher for surge. This phenomenon is strongly amplified around the cut-in, rated and cut-off wind speeds. Surge's and pitch's higher oscillation phenomenon at more adverse wave conditions is witnessed at all wind speeds with the exception of 18-21 m/s where the reversed incident occurs, probably due to destructive interference. As mentioned, around these wind speeds, both spar motion DOFs experience strong oscillations, regardless of the transpiring ocean conditions. Hence, the signal combination of the spar's eigenmotion and the external wave induced motions result in reduction of the overall oscillation amplitude, a phenomenon similarly evident in different WT components (Laureti & Favini, 2019). This phenomenon however, would require further investigation to be supported and solidified.

A greater outcome can be drawn when observing the steady rated wind speed time series graphs of Figure 6.2 and Figure 6.3. By subjecting the spar FOWT model to different current speeds the surge and pitch steady state equilibriums change, while the oscillation behavior is majorly the same. Conversely, varying wave conditions result in roughly the same steady state equilibrium centers for the two spar motion DOFs but their oscillation pattern and amplitudes greatly change.

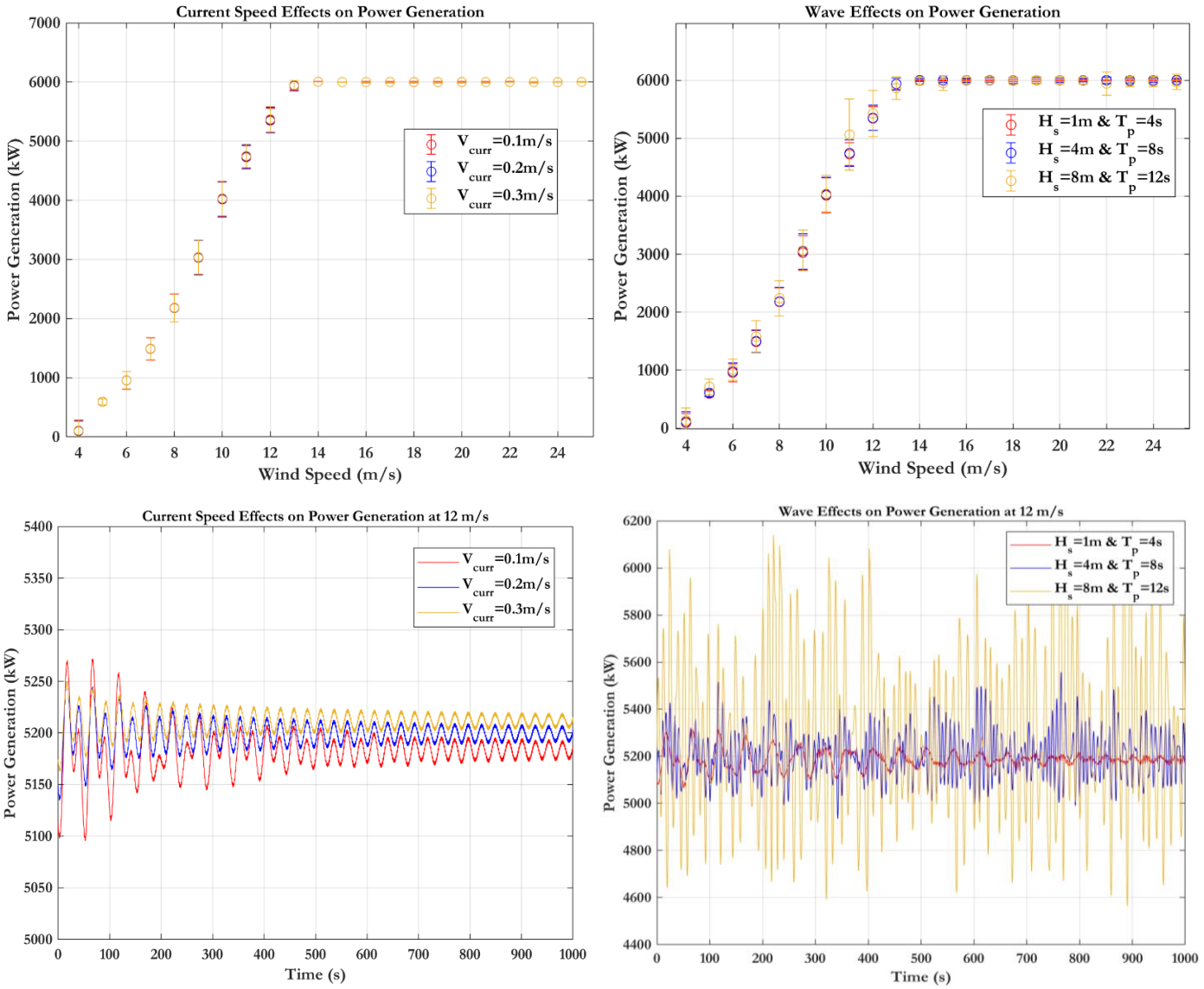

Figure 6.4 Power mean & STD margins and rated time series outcomes for non turbulent wind field on varying current speeds (Left) & varying ocean conditions (Right).

Figure 6.4 presents the ocean condition effects on the generated power mean and STD margins. It is observed that varying current speeds do not influence the FOWT power performance. This remark holds true for both mean and STD margins throughout the spectrum of operating wind velocities. Additionally, since turbulence is not incorporated in these OpenFAST simulations, after the rated power is reached belatedly at 13 m/s instead of 12 m/s, the power fluctuations disappear. Regarding the rated wind speed time series graphs, despite an initial larger power fluctuation, once the wind turbine reaches its steady state operating conditions, the respective power generations have negligible differences and the fluctuation amplitudes are approximately 20 kW.

The varying ocean condition that most strongly affects the FOWT power generation, according to the developed OpenFAST model simulations, are the waves. Compared to Lerch et al. simulation outcome, as shown in Figure 3.5, the combined wave height and peak period influence phenomenon is similar. The wave conditions' impact maximizes around the rated power point, specifically at 11 m/s. Mean power generation and power fluctuation increases with the wave height and period during partial load operation and at rated wind speeds, as seen in the time series outcomes. Similar to the current speed investigation, the wave effects diminish at full load, where the occurrence of high waves with long time periods causes sparce power fluctuations of low amplitude.

6.1.2 Nacelle Velocity Effects on Power

As the spar moves in response to wind and waves, it induces its lateral and rotational motion on the nacelle, resulting in velocity accumulation. The horizontal and rotational nacelle velocity causes the blades to experience different relative wind speeds, affecting the aerodynamic efficiency of the rotor and fluctuating the overall power generation. Additionally, this motion induces loads on the nacelle, the rotor, the drivetrain and the tower, leading to structural fatigue and damage over time (Nejad & Torsvik, 2021; Choe et al., 2021). The pitch and surge induced nacelle displacement and velocity are depicted in the schematic configuration of Figure 6.5 (Johlas et al., 2020).

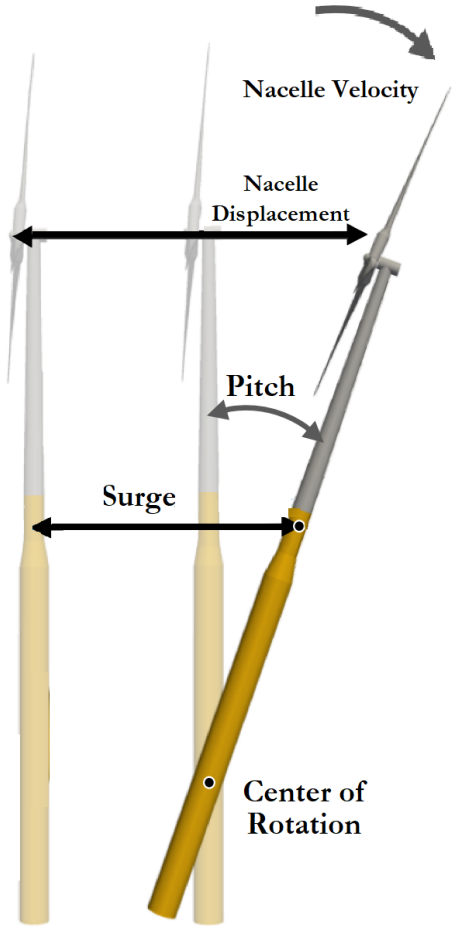

Figure 6.5 Nacelle velocity schematics based on the surge and pitch spar motions (Johlas et al., 2020).

Focusing on the nacelle velocity effects on mean power generation, simulations were conducted using the developed and validated Hywind inspired OpenFAST model. These simulations entail six different turbulent wind fields, with mean wind velocities ranging from 4 to 24 m/s in increments of 4 m/s. The aerodynamic effects were implemented using the BEM model. The transpiring ocean conditions are set to 3 m, 7 s and 0.15 m/s for H_S, T_P and depth independent current speed. The outcomes are displayed in Figure 6.6, where negative nacelle velocity indicates that it moves against the incoming wind, while positive values indicate the nacelle follows the incoming wind. It is highlighted that, the OpenFAST calculated nacelle velocity results refer solely to the x axis values, attributed to surge and pitch motions. The graphs become more comparable to one another, by being bounded within the same nacelle velocity limits of a maximum 2 m/s for the negative axis direction and a maximum 1.5 for the positive one. These higher nacelle response velocities are mainly reached in rated and above rated wind velocity fields.

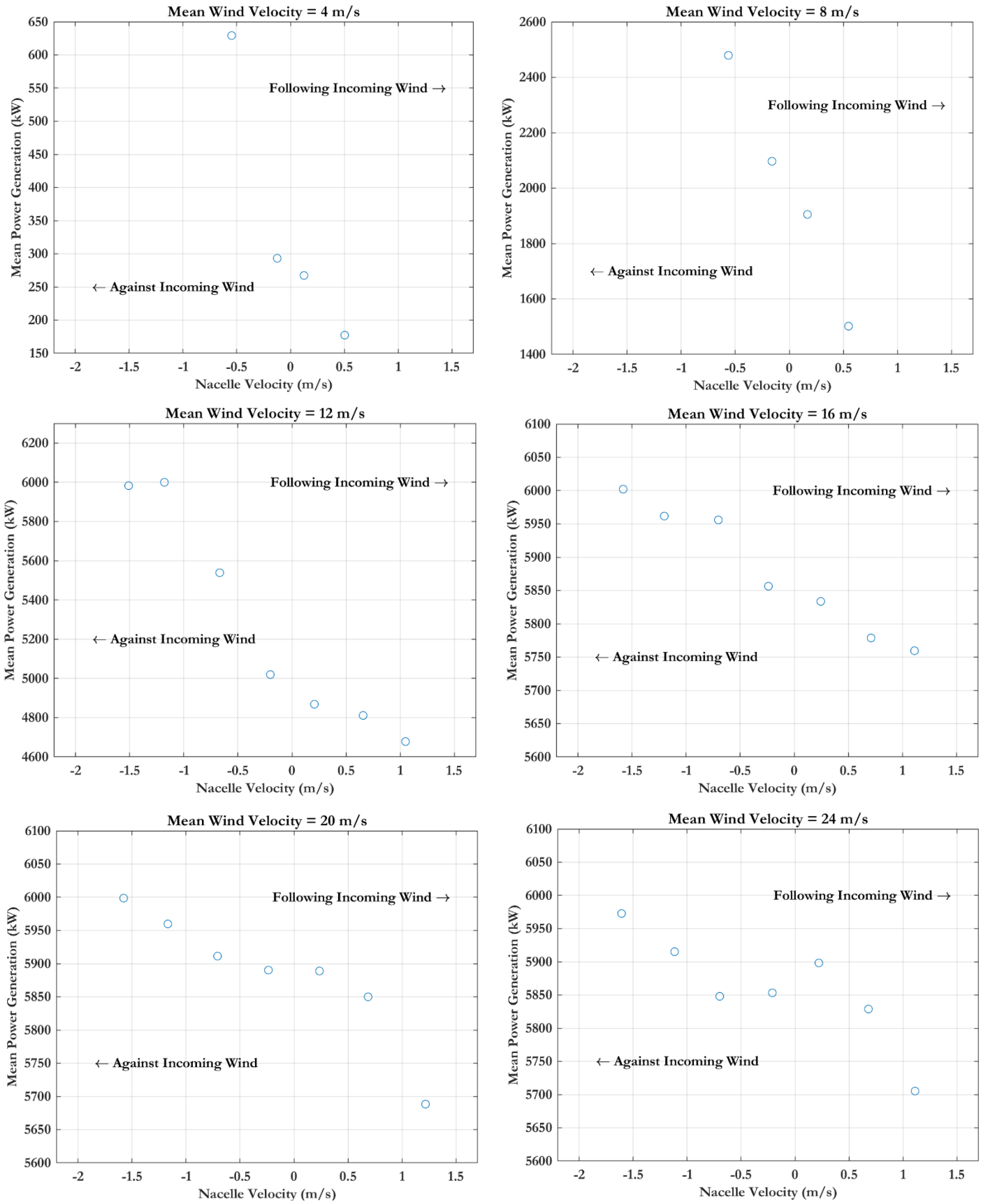

Figure 6.6 Nacelle velocity on mean power for different wind velocity fields.

Based on the Figure 6.6 outcomes, there is an overall increase in the mean generated power when the nacelle opposes the incoming wind direction, whereas the power output decreases as the top structure

aligns with the incoming wind, aggreing with the concluding observations of Dandrea, 2020. This phenomenon is mainly attributed to the varying wind speeds experienced by the rotor blades. When the nacelle opposes the wind, the rotor blades encounter relatively higher wind velocities, resulting in increased power generation. Conversely, when the top structure aligns with the wind, the rotor blades experience relatively lower wind velocities, leading to reduced power output. The aforediscussed outcomes are in accordance with Johlas et al., 2020 conclusions. The nacelle velocity impact on mean power generation subsides as the mean incoming wind velocity increases. This is attributed to the nacelle's velocity value becoming insignificant compared to wind speeds one order of magnitude greater. Therefore, the blade exprerienced relative wind does not vary considerably.

In addition, these outcomes highlight that the FOWT performance is not linearly connected to the nacelle velocity. Examples of this phenomenon are the 16 and 20 m/s mean wind velocity fields. In both instances, the relative velocity, even at the highest nacelle velocity alignment with the incoming wind at 1.5 m/s, is well above the rated wind speed. The relative experienced blade wind speed would be 14.5 m/s and 18.5 m/s, respectively. Therefore, the nacelle velocity influence does not account for such a considerable mean power drop, indicating secondary effects taking place.

Insufficient investigation notwithstanding, a plausible explanation for this phenomenon lies in the consistent variation of the blade's positioning relative to the inflow wind direction. In the realm of BEM calculations, the determination of lift and drag forces on individual blade elements relies on their angle of attack and other airfoil properties. These forces are essential in the computation of power, thrust, and torque generated by the rotor. Given the presence of oscillating nacelle motions associated with the spar floater, it is reasonable to anticipate power variations resulting from these oscillations. This arises from the blade's angle of attack experiencing "unforeseen" changes, from the controller's perspective, due to the spar floater's oscillatory movements. Potentially, a finely tuned controller with floating capabilities and capacity to compensate for angle of attack variations, has the potential to mitigate these power fluctuations presented prominently-individually after the rated power point.

Overall and as expected, the resulting power formula implemented in OpenFAST follows a more complicated structure than the one presented in sub-Section 2.1.2 (Equation 2.23), resembling more the dynamic findings of Johlas et al. (Lerch et al., 2019 ; Johlas et al., 2020).

6.2 Bottom-Fixed Monopile & Floating Spar Energy Yield Comparison

The ultimate objective of all previous discussions and analysis is the comparison between bottom fixed and floating wind turbine annual energy production (AEP) for the location of Hywind, Scotland. The FOWT and BOWT power outcomes are simulated using both aerodynamic models, BEM and OLAF. The AEP calculation procedure entails collecting hourly wind speed data and ocean statistics for Hywind, setting up the best- and worst-case conditions, conducting the individual FOWT and BOWT OpenFAST model simulations and developing the cumulative energy yield MatLab pipeline.

The Hywind, Scotland hourly wind speed time series at 100 m height were retrieved from ERA-5 by inputting the Hywind, Scotland floating wind farm coordinate margins. The hub height of the developed OpenFAST Hywind model stands at 98 m, therefore the time series data were calibrated accordingly using the power law (Equation 2.29). These annual data pertain to the year 2018, coinciding with the Equinor performed measurement's year. Figure 6.7 illustrates the probability density of the converted data, in bins of 0.5 m/s, ranging from 0 to 30 m/s.

The base Hywind ocean conditions are derived - approximated from the average retrieved Hywind case measurements, ERA-5 wave height, wave period and current speed time series for the year 2018 as well as Statoil Hywind ocean analytics (Mathiesen et al., 2014). A bounded (upper and lower bounds) approach is utilized herein to demonstrate the range of possible effects of the floater's motion as compared to a bottom fixed monopile. The upper bound is driven by an extreme 100-year return wave height, peak

wave period and current speeds. The respective H_s and T_p values are retrieved from Figure 6.6. The lower bound condition scenario represents an approximately still sea state. Thus, the spar motion will be significantly lower, approaching the monopile's relatively restricted motion. Unlike the base ocean conditions case, calmer and harsher ocean conditions do not correspond to specific Hywind measurements but are based on DNV GL regional metocean conditions as shown in Figure 6.6 (DNV GL, 2018; Mathiesen et al., 2014). Table 6.2 showcases the respective base, upper and lower bounds of the FOWT simulation ocean conditions .

It should be noted that as expected, both BEM and OLAF BOWT cases did not show noticeable variations across all their respective bounds. Hence, these additional results were not included in the graphs, as they coincide with the base case outcomes.

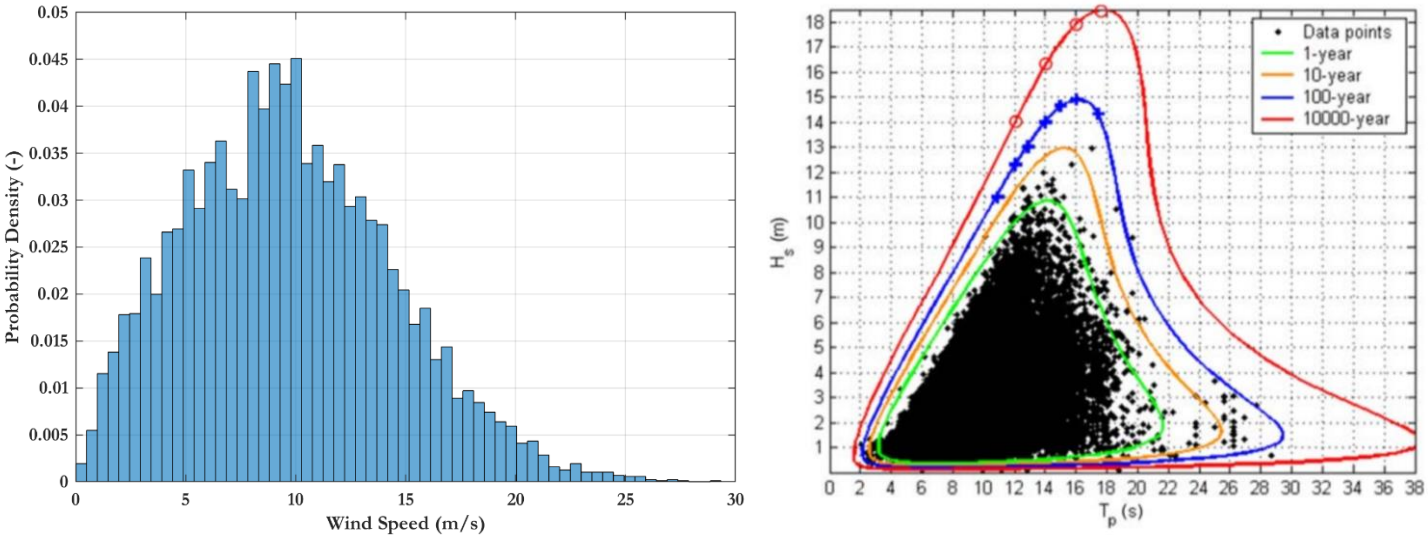

Figure 6.7 Wind speed probability density for Hywind, Scotland (Left) & extreme contours H_s-T_p for several return periods (Right) (DNV GL, 2018).

Table 6.2 OpenFAST simulation case ocean conditions (DNV GL, 2018 ; Mathiesen et al., 2014).

OpenFAST Simulation Case	Significant Wave Height H_s (m)	Peak Wave Period T_p (s)	Current Speed (m/s)
Calm - Best	0.5	2	0.05
Base	2	7	0.3
Harsh - Worst	15	16	1.28

6.2.1 BEM AEP Comparative Analysis

The mean power generation and STD values, in turbulent wind field, for BOWT and FOWT structures, as represented by monopile foundation and spar buoy, respectively, are presented in the left graph of Figure 6.8. Additionally, the mean power for monopile, base-, best- and worst-floating cases are incorporated in the right graph of Figure 6.8. These continuous lines emerge when the individual average points are connected. The aforementioned cases are not included in the mean and STD comparison graph to avoid illegible graphs. Six separate wind field power generation time series graphs are incorporated in Appendix D, Figure D.1, for transparency. To avoid redundancy and repetition, it is important to note that several observations made in the BEM comparison scenario are applicable to the

OLAF analysis as well. Consequently, further elaboration on these remarks is provided below to provide a comprehensive understanding.

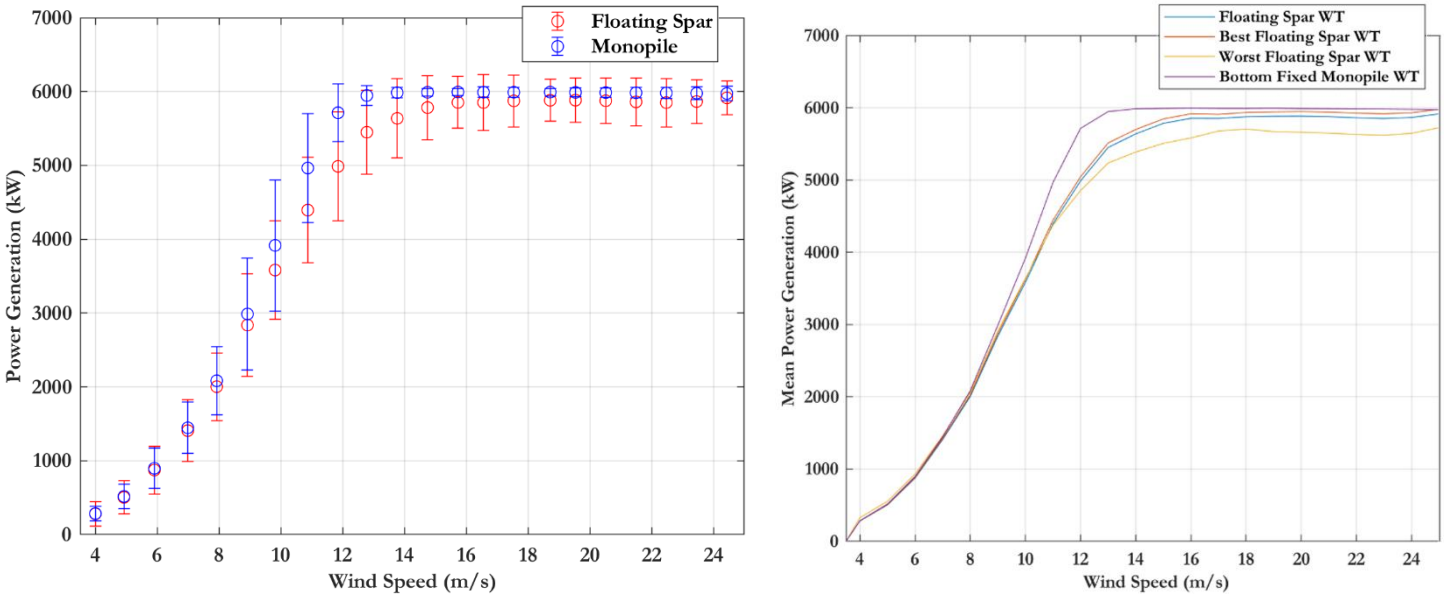

Figure 6.8 BEM power generation mean & STD margins comparison between monopile and base floating spar (Left) & mean power generation curves for the floating -base, best, worst- and bottom fixed cases (Right).

Upon comparing the per wind speed average and STD power values between the floating spar and fixed monopile configurations, noteworthy observations are drawn. The floating case displays lower mean and higher STD values. Additionally, the FOWT reaches its rated output at higher wind speeds compared to the bottom fixed one. This is attributed to the floating structure's lower hydrostatic restoring pitch moment, resulting in a mean pitch angle of approximately 4.7° during operation around the rated wind speed. This remark can be seen in the wave period graph of Figure 6.3, where ocean condition similar to the base case transpire. This average pitch angle causes a slight misalignment of the rotor plane with respect to the incoming wind, resulting in suboptimal performance and a delayed rated power generation (Wang et al., 2023). Afterwards and as the pitch angle decreases steadily, the spar's output steadily reaches the rated performance output. BOWT outperforms the FOWT mostly during the transitional 2-3 region. Furthermore, the monopile wind turbine experiences power generation fluctuations only during the partial load region due to turbulent inflow effects. Once the rated wind speed is marginally exceeded, the STD values decrease significantly and are practically negligible.

With regards to best and worst ocean conditions for floating wind turbines, it is observed that the presence of calm seas yields a marginally higher average power output compared to the baseline scenario. Conversely, during the worst-case scenario, a notable decrease in power generation is evident. This trend is valid once wind speeds exceed 10 m/s, as prior to that threshold, the worst-case scenario had exhibited superior performance. Notably, for wind speeds near the turbine's cut-in velocity, the worst-case scenario surpasses even the power output of the monopile structure, albeit slightly. This behavior could be attributed to nacelle velocity effects on power generation, since, as seen in Figure 6.6, its impact is most evident at lower wind speed fields. Therefore, while the floating spar experiences great wave heights over long periods, its top compartment accumulates velocity. Finally, contrasting to the outcomes of Figure 6.4, where ultimately the more adverse ocean conditions case outperformed the rest, Figure 6.8 outcomes highlight that by combining extremely adverse waves and current conditions, the spar FOWT's power decreases significantly.

By effectively multiplying the Hywind wind speed probabilidy density results with the mean power generation curve for all four investigated cases, Figure 6.9 is produced. This graph, practically, displays

the annual energy yield per wind speed value. The wind speed bins, in increments of 0.5 m/s, range from 4 m/s to 25 m/s, corresponding to the cut-in and cut-off wind speeds, boundaries of the wind turbine operational conditions. Phenomena analysed during the mean power generatin graph of Figure 6.8, are more prominently witnessed here.

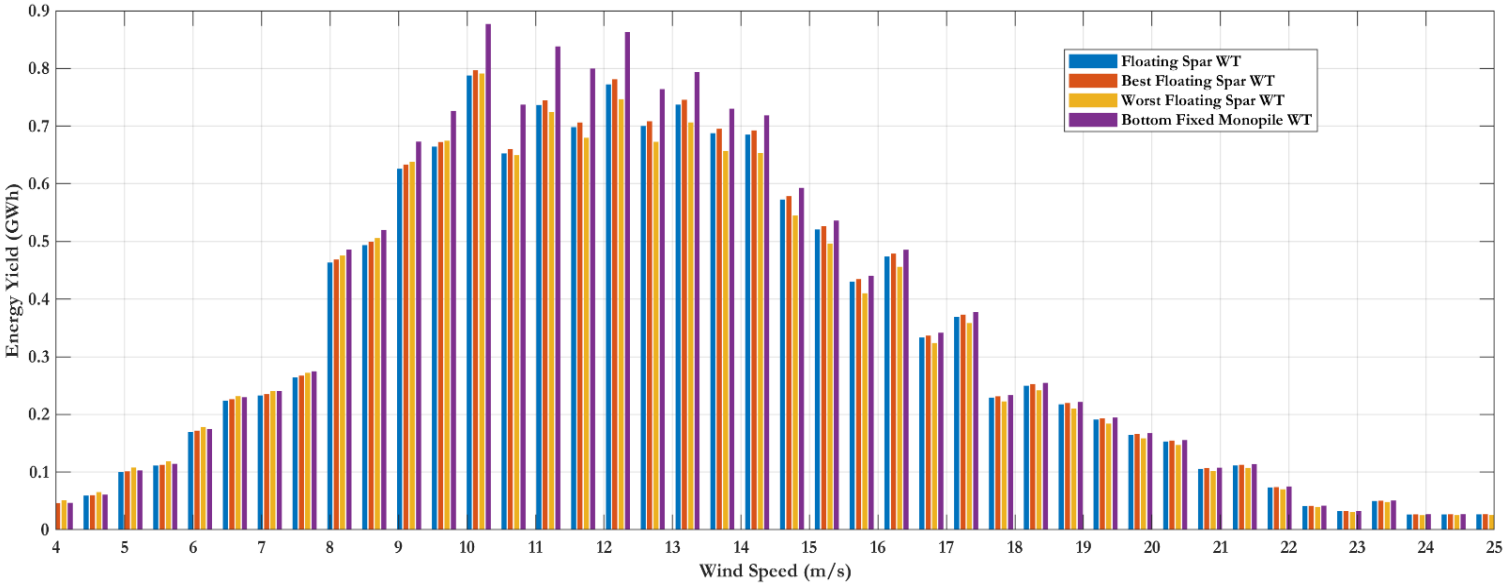

Figure 6.9 BEM energy yield comparison per wind speed bin for the floating -base, best, worst- and bottom fixed cases.

Finally, by summing the Figure 6.9 outcomes, the cumulative energy production results are calculated and presented in Figure 6.10. The base floating annual energy yield, in dashed lines, is enclosed with the best and worst AEP curves, in bold lines, ultimately generating 14.49 GWh and 14.09 GWh, respectively. The BOWT structure, ultimately, produces higher amounts of energy, at 15.30 GWh, surpassing by approximately 6.2% the base FOWT generation. The AEP outcomes are collectively analysed further during sub-Section 6.2.3.

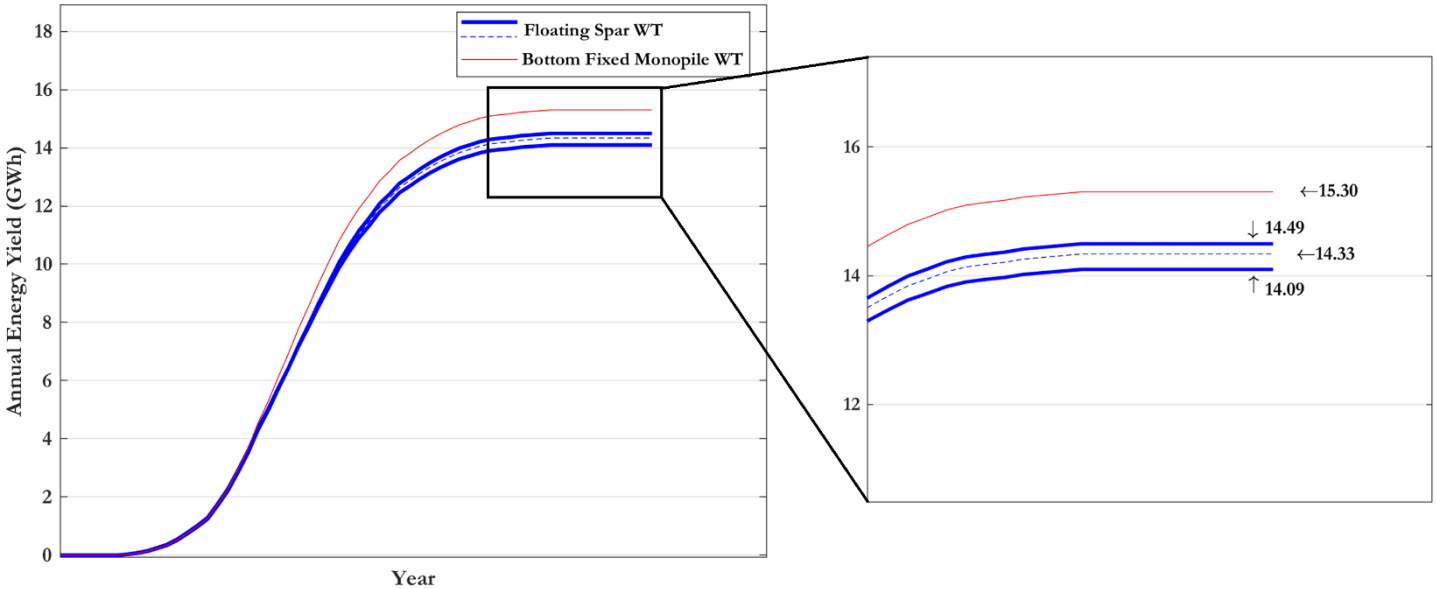

Figure 6.10 BEM AEP floating and bottom fixed cases comparisons, inlcuding floating AEP best and worst case margins.

6.2.2 OLAF AEP Comparative Analysis

According to the spar motion data recreation results of Section 5.2 and Appendix C, the two researched aerodynamic models showcase similar precision levels, especially for the significant motion DOFs of surge and pitch. Despite that, OLAF calculations entail vorticity field effects, thus increasing the realistic approach of the Hywind FOWT and BOWT OpenFAST models. The control panels and strength of vorticity are illustrated in the Paraview 3D model of the developed wind turbine as seen in Figure 6.11. The same calculating procedure followed in the BEM model analysis, is utilised for the OLAF calculation as well. The power generation, power per wind speed bins and AEP outcomes are illustrated in Figure 6.12, Figure 6.13 and Figure 6.14, respectively. Six separate wind field power generation time series graphs are incorporated in Appendix D, Figure D.2, for transparency.

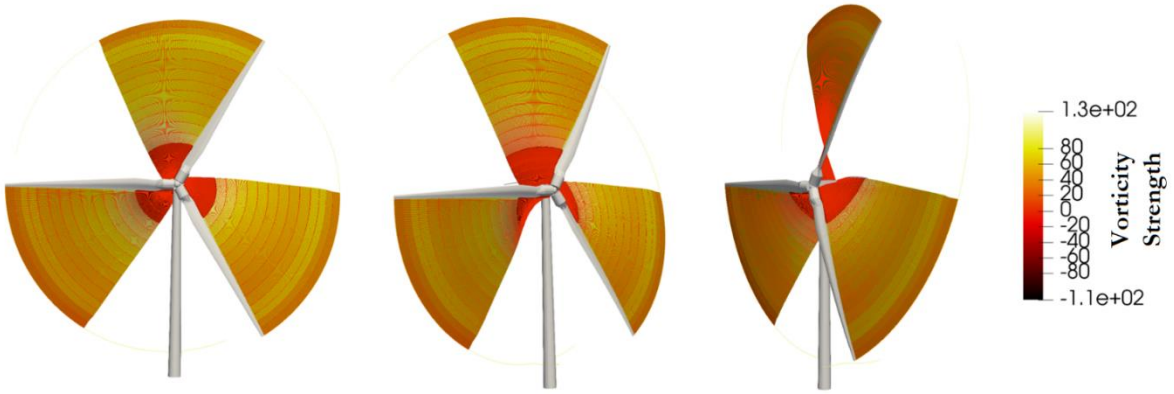

Figure 6.11 OLAF vorticity field on 3D panels rendered in Paraview.

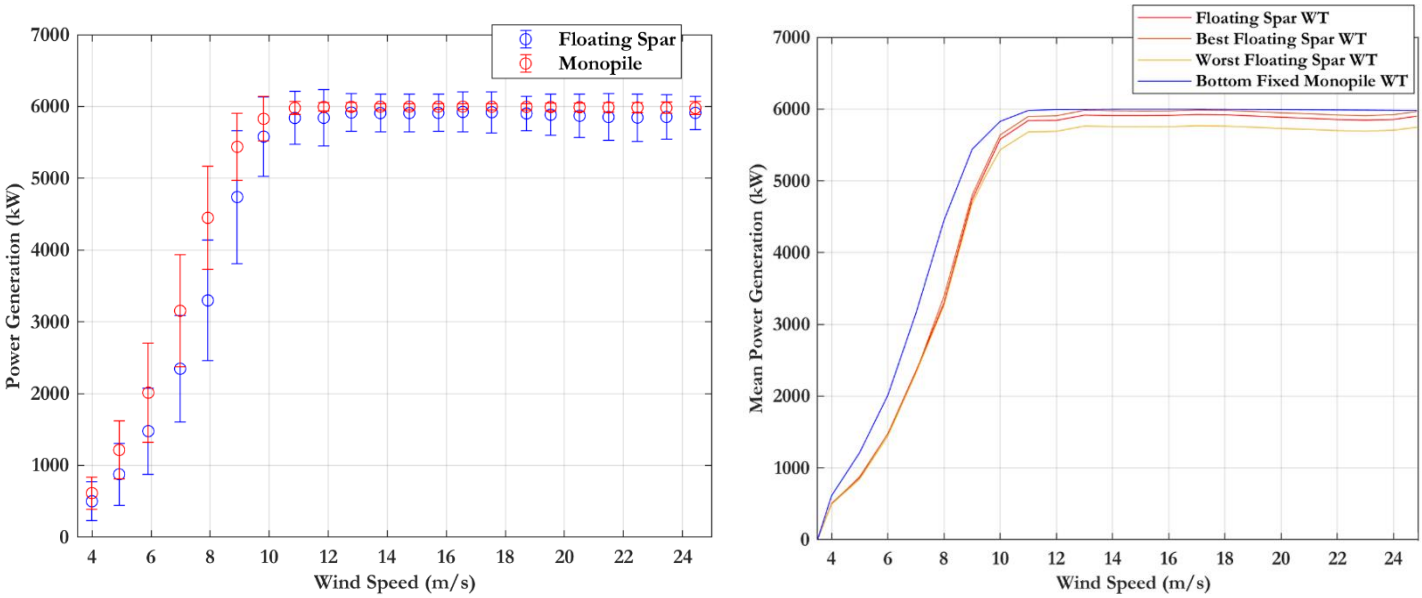

Figure 6.12 OLAF power generation mean & STD margins comparison between monopile and base floating spar (Left) & mean power generation curves for the floating -base, best, worst- and bottom fixed cases (Right).

Concerning the power production graphs of Figure 6.12, multiple BEM fixed monopile against floating spar comments are still valid, while separate remarks can be raised. A peculiar observation is the prematurely achieved rated power output of the BOWT and to a slighter extent of the FOWT case. This early attainment of the OLAF rated power, can be attributed to the unique characteristics and modeling approach of this aerodynamic model. One possible explanation for this phenomenon is the improved wake modeling capability of OLAF. It may better capture the wake effects and the interaction between the rotor and the wake, allowing for more efficient power extraction at lower wind speeds (Shaler et al., 2020). Additionally, BOWT power output is consistently higher than every FOWT case and the most

adverse FOWT case generates constantly the lowest power. For this OLAF aerodynamic model case, the BOWT 's power curve surpasses the FOWT's mostly during the partial load region, in lieu of the transitional 2-3 region, as discussed in the BEM case.

As the energy yield distribution of Figure 6.13 is partially based on the Hywind wind speed distribution, a degree of similarity between the BEM and OLAF results per wind speed was expected. As it is evident, the energy yield exceeds the 1 GWh threshold in multriple instances. Phenomena analysed during the mean power generation graph of Figure 6.12, are more prominently witnessed here.

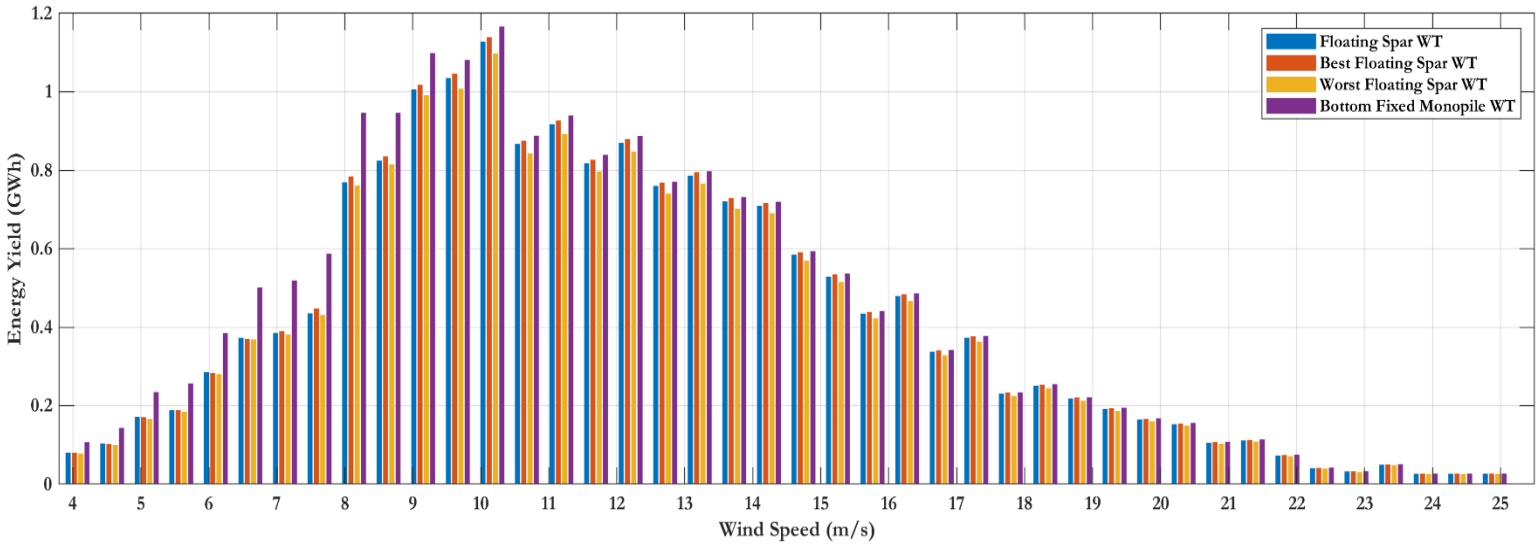

Figure 6.13 OLAF energy yield comparison per wind speed bin for the floating -base, best, worst- and monopile cases.

By accumulating the consecutive wind speed bins' energy production results, the annual yield is calculated, as shown in Figure 6.14. The base FOWT case generates 17.71 GWh, when a calm sea state results in roughly 1.5% increase compared to the base value. Conversely, the more adverse sea state production experiences a 2.25% decrease on the base case. Finally, BOWT yields an additional 7.3% of energy production, annualy, compared to the base FOWT estimation. These outcomes are discussed and compared to literature findings in the following section.

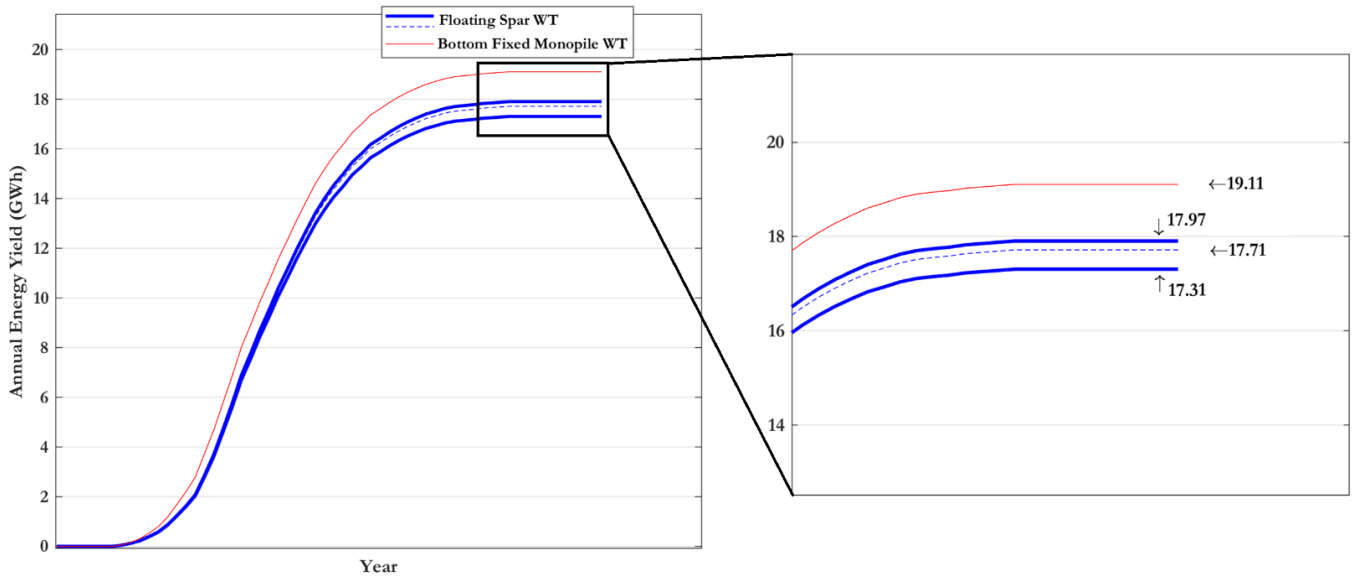

Figure 6.14 OLAF AEP floating and bottom fixed cases comparisons, including floating AEP best and worst case margins.

Overall, by constrasting the BEM and OLAF power generation results of Figure 6.8 and Figure 6.12, it is evident that all investigated cases generate higher power. This outcome was expected, as similar conclusions were discussed during literature review, where the same models were achieving higher performance outcomes when modelled with OLAF instead of BEM (Pereira Malveiro, 2022 ; Wang et al., 2023). These phenomena are greatly apparent when comparing the AEP results for monopile and floating (base case), where on average, roughly 25% increase is observed in OLAF cases compared to the corresponding BEM values. Specifically, this monopile numerical difference is substantiated by Pereira Malveiro's research findings, where for a TSR of 7, a power coefficient increase of approximately 20% was recorded when replacing BEM with OLAF.

6.2.3 AEP Result Discussion & Literature Comparisons

The AEP estimations for both developed FOWT and BOWT were compared, as presented in Table 6.3, using Equation 6.1. In cases where a positive outcome is observed, it is inferred that the energy yield of the BOWT surpasses that of the FOWT.

$$AEP_{diff} = \left(1 - \frac{AEP_{FOWT}}{AEP_{BOWT}}\right) \cdot 100\% \tag{6.1}$$

Table 6.3 Floating and Bottom-Fixed AEP difference results per simulation case.

OpenFAST Simulation Case	BEM AEP Difference (%)	OLAF AEP Difference (%)
Calm - Best	5.23	6.34
Base	6.20	7.33
Harsh - Worst	7.84	9.42

Overall, the BOWT simulation AEP estimation outperforms the FOWT by roughly 5 to 9.5% depending on the transpiring ocean conditions. The OpenFAST comparative outcomes are now objectively compared to similar literature investigations.

Firstly, in their research, Johlas et al. simulated in OpenFAST the NREL 5 MW wind turbine in offshore conditions, being structured on a monopile and on a spar buoy. The offshore wind turbines were exposed to severe irregular wave conditions and turbulent inflow wind velocities below the rated threshold. In a water depth of 200 m, the wave conditions consist of irregular, unidirectional JONSWAP waves. The waves are characterized by adverse sea states, including a significant wave height of 8 m and a peak period of 14 s. It is important to note that the wave propagation direction aligns with the hub-height wind direction. These conditions were simulated using large-eddy simulations of a neutral atmospheric boundary layer. However, specific details regarding the employed aerodynamic model have not been disclosed. Ultimately, it was estimated that the spar FOWT outperforms by 3-5.5% the BOWT as seen in the leftmost graph of Figure 6.15 (Johlas et al., 2020). It should be noted that for low inflow wind velocities and adverse ocean conditions, the BEM scenario predicts that the FOWT does surpass the monopile's AEP, as is evident in Figure 6.9 for wind speeds below 7.5 m/s.

Secondly, Wang et al., utilised a combination of two computer codes, SIMO and RIFLEX to simulate a 10 MW monopile and spar OWT. Based on their findings, it is concluded that once the studied wind turbines are subjected to wider range of wind fields, roughly a 5% difference in power performance is observed. Moreover, as depicted in the middle and rightmost graphs of Figure 6.15, BOWT showcases a higher power fluctuation prior to the rated point while around the rated wind speed, the FOWT power STD values are considerably higher. As the wind velocities progress to above rated operation, the BOWT power fluctuation is eliminated while the FOWT slightly decreases (Wang et al., 2023). These phenomena

are witnessed, for both the simulated aerodynamic models, at similar degrees in the predicted power results of the developed OpenFAST models.

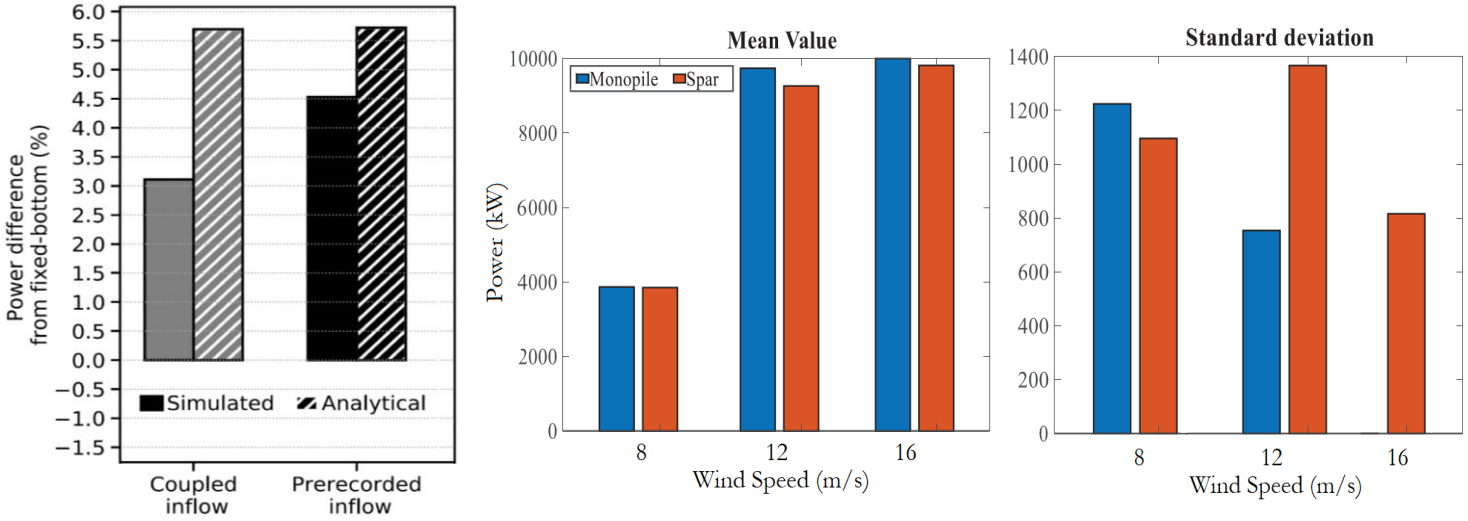

Figure 6.15 Monopile BOWT & spar FOWT power difference (Left) (Johlas et al., 2020) & power mean & STD values for different wind speeds (Right) (Wang et al., 2023).

It is essential to highlight that, although the bottom fixed structure overperforms the floating one, the floating wind turbines can be installed and commissioned in locations were the wind turbines are subjected to greater wind velocities. In this project, the monopile structure is simulated in a potentially unrealistic location. In case where the simulated location was characterized by less harsh wind and ocean conditions, such as closer to the shore where monopile structures are usually installed, then potentially the BOWT - FOWT AEP discrepancy would be lower.

6.2.4 FOWT Controller Tuning AEP Corrections-Adjustments

In addition to the already presented ROSCO floating nacelle feedback gain impact on power performance in Figure 4.8, there are more researches conducted aiming on identifying the effects of proper FOWT controller tuning on AEP. The controller tuning is performed in order to optimize the load and fatigue damages on the WT structure with regards to energy yield outcomes. Conversely to Lenfest et al., 2020 power performance outcomes where a no numerical output conclusion was drawn, (Zalkind et al., 2022; Skaare et al., 2007; Abbas et al., 2022) highlight a clear percentile difference as multiple cases of FOWT control tuning marginally affect the AEP.

Firstly, Abbas et al., compare three ROSCO control strategies for a 15 MW FOWT on the UMaine semisubmersible platform. In light of their findings, the implementation of a tuned control strategy specifically designed for FOWT, in place of a controller which lacks floating nacelle velocity feedback, such as the one developed within the scope of this project, leads to a notable 1.4% increase in AEP. Furthermore, the complete elimination of pitch saturation limitations yields an even higher AEP growth of 1.6% compared to a tuned FOWT controller's output. These improvements are directly associated with mitigating power output reductions during low wind speeds, where the absence of power-maximizing pitch saturation becomes advantageous, as well as in near-rated wind speeds, where thrust reduction effects are minimized (Abbas et al., 2022).

Secondly, in an effort to update the ROSCO controller, Zalkind et al. investigated the effects of peak shaving on the power production of a 15 MW FOWT's tuned controller. Peak shaving is conducted by minimizing the blade pitch limit, therefore enabling partial pitch saturation, in order to optimize power

at low wind speeds and reduce thrust near rated wind speeds. They concluded that for a range of peak shaving parameters, a 1% increase in AEP results in about a 5% increase in tower base damage equivalent loads, with the highest damages being recorded for the case of a spar (Zalkind et al, 2022).

Thirdly, in contrast to increasing the AEP at the expense of structural damages, Skaare et al., 2007 developed a FOWT controller on Simo-Riflex and HAWC2 focused on extending the platform life by restricting fatigue of the spar 15 MW FOWT. According to their findings, the implementation of the estimator-based control strategy for dynamic improvements incurs a decrease in the average power output, with a maximum reduction of 3.81%. Additionally, it results in increased standard deviations in both power outputs and rotor velocities (Skaare et al., 2007). The latter two AEP percentiles differences are relative to the AEP achieved by a tuned controller specifically designed for FOWTs. In conclusion, minor modifications to the controller settings, including the incorporation of floating nacelle feedback gain and blade pitch control, lead to slight adjustments in the AEP. All aforementioned control strategies along with their respective AEP increase/decrease percentiles are recapitulated in the flowchart of Figure 6.16.

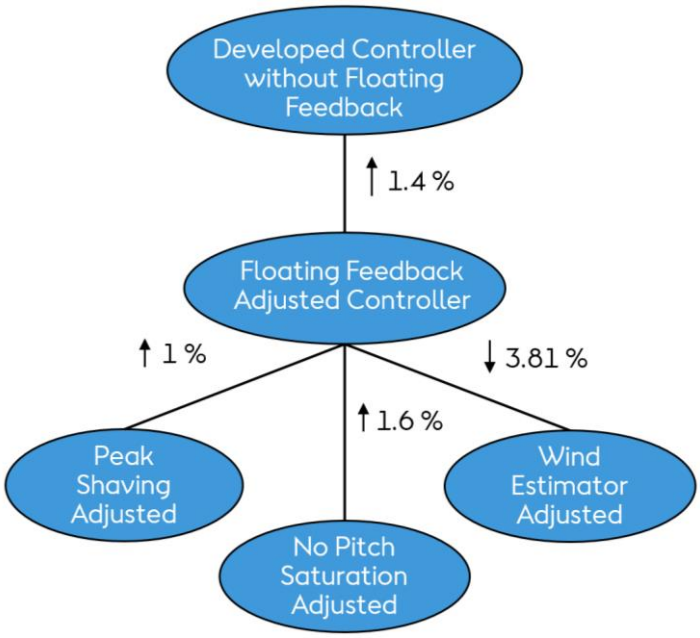

Figure 6.16 Control strategies implementation flowchart.

The developed OpenFAST models' AEP results obtained for both BOWT and FOWT are compared to the improved AEP outcomes resulting from the aforementioned control strategy changes. The first comparisons are illustrated in Figure 6.17, where separate graphs for each aerodynamic model are presented. In Figure 6.17, this project's developed controller is adjusted to entail floating nacelle velocity feedback capabilities based on the outcomes of Abbas et al. Thereafter, Figure 6.18 and Figure 6.19, for BEM and OLAF, respectively, present the AEP modifications employed, separately, by removing pitch saturation, including peak shaving and implementing the wind estimator strategy. It should be mentioned that all the presented outcomes are calculated for the base oceanic conditions. Finally, it is clarified that, although some conclusions refer to investigations performed on FOWT supported by a different floater, due to the limited literature reviews on the topic, their input is considered valid for the scope of this project.

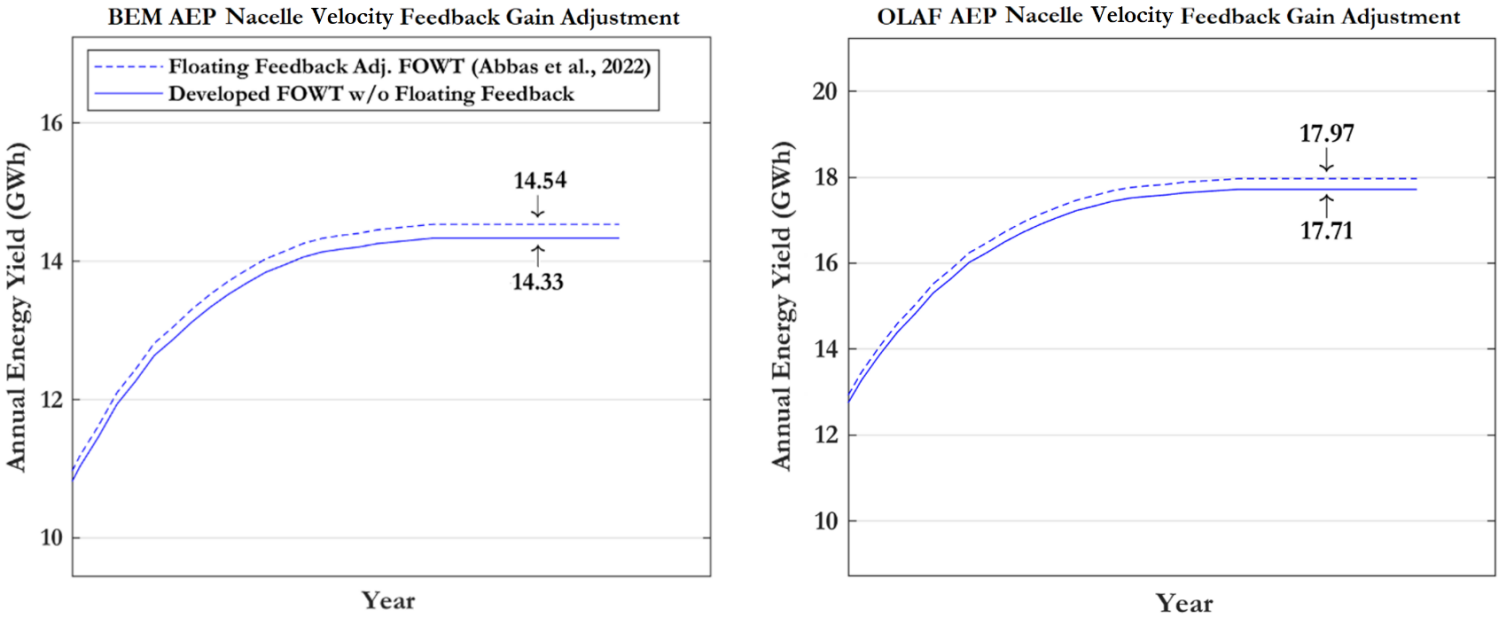

Figure 6.17 AEP results adjustment-correction for floating nacelle velocity feedback gain inclusion in the control strategy for BEM (Left) & OLAF (Right).

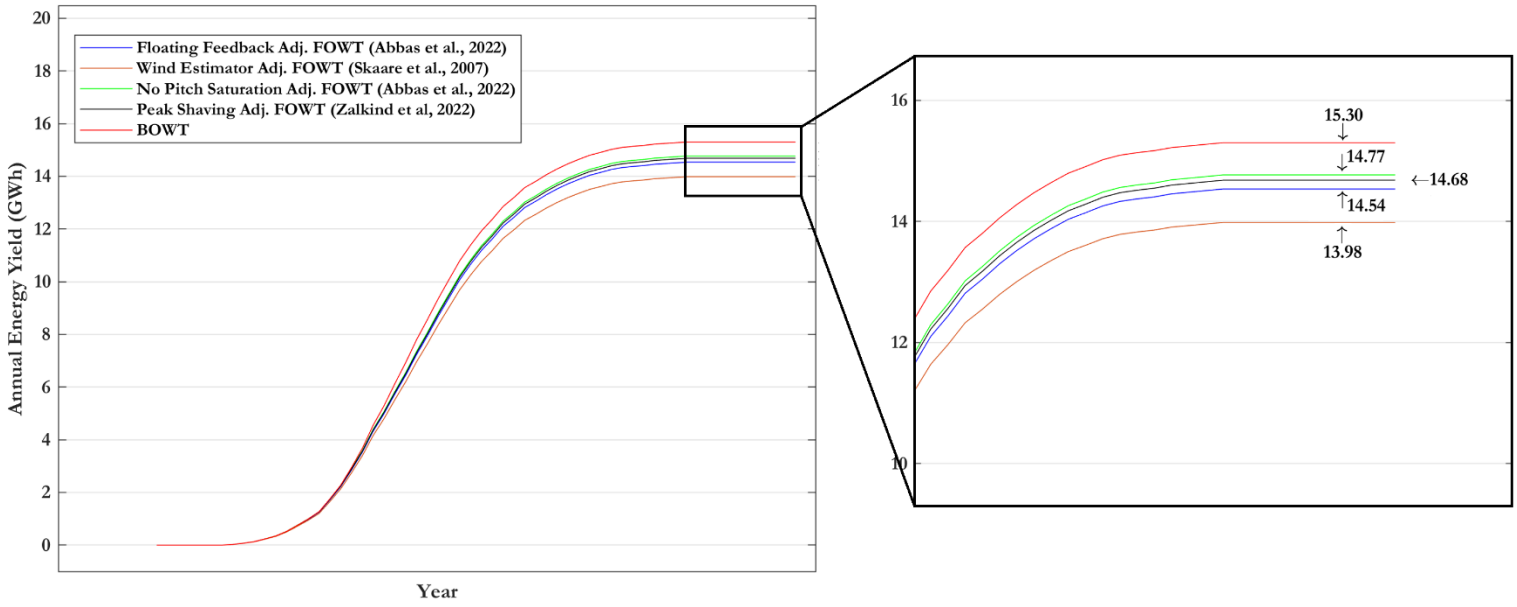

Figure 6.18 BEM AEP adjusted results comparison between four FOWT controller strategies and the developed BOWT model.

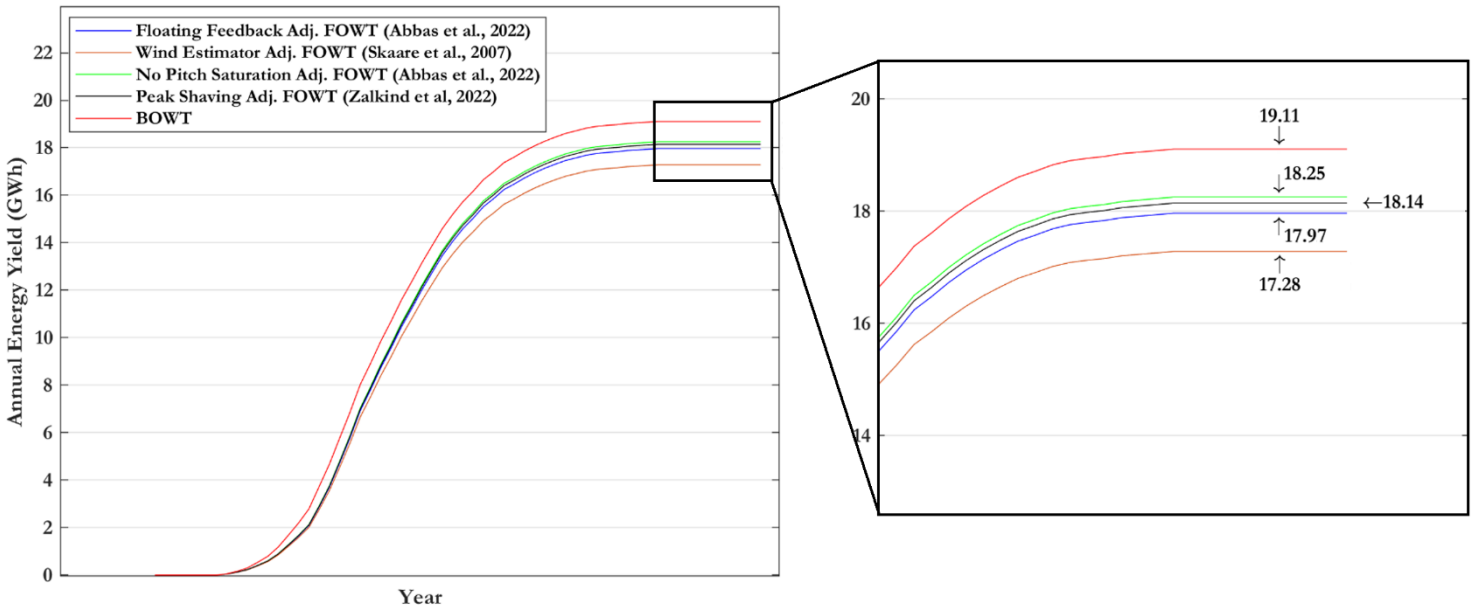

Figure 6.19 OLAF AEP adjusted results comparison between four FOWT controller strategies and the developed BOWT model.

In conclusion, the substitution of monopile BOWT structures with spar FOWT structures, incorporating suitable floating controller capabilities, leads to a reduction in annual energy yield of 4.96% under BEM simulation. Furthermore, when the VPM-OLAF model is utilized, the AEP experiences a decrease of 5.90%. These variations, including the AEP comparisons between FOWT and BOWT under different control strategies, as computed using Equation 6.1, are summarized in Figure 6.20 for both aerodynamic models. When employing BEM, the projected decrease in wind turbine AEP output, resulting from the utilization of a spar floater instead of a bottom-fixed monopile foundation, ranges from 3.46% (when the controller is optimized for maximum power extraction) to 8.62% (when the controller is optimized for maximum structural longevity). Conversely, when using VPM-OLAF, the estimated wind turbine AEP output for a spar floater compared to a monopile substructure ranges from 4.50% to 9.58% under similar conditions as mentioned previously.

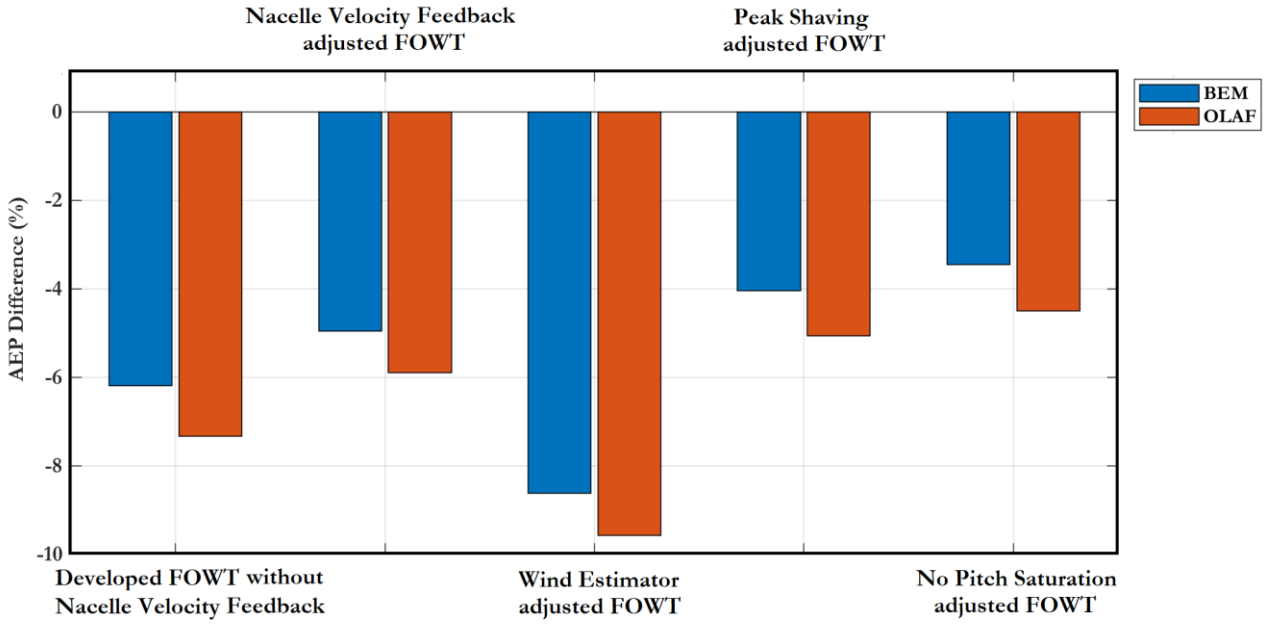

Figure 6.20 Replacement of BOWT by FOWT impact on AEP for five controller strategies as simulated with the aerodynamic models BEM and OLAF.

Chapter 7. Conclusions

The concluding chapter of this project presents the key findings derived from the analysis and observations made throughout the research. They are systematically summarized by addressing the research objective and answering the research questions posed earlier in Chapter 1. Subsequently, the outcomes are thoroughly discussed, alongside recommendations for potential future improvements.

7.1 Answers to the Research Objective & Questions

An aero-hydro-elasto-servo coupled model, referenced on the deployed Hywind Scotland spar FOWT, was developed using the opensource software OpenFAST. For said site, metocean statistics and measured spar motions were provided by Equinor. The developed model's spar motion was benchmarked as a sanity check of its realism, via means of modal analysis, statistical, time series and frequency response comparisons against the full-scale measured data. Both aerodynamic BEM and OLAF models were used for the simulation. Once the developed spar FOWT was reasonably benchmarked, a similar monopile BOWT model was developed in OpenFAST using the same controller as the FOWT. Thereafter, the spar motion effects on FOWT power generation were investigated. Finally, comparative analyses on annual energy production differences between monopile BOWT and spar FOWT for different sea state conditions and different spar FOWT control strategies were conducted.

In the paragraphs that follow, the primary conclusion to this research objective is first addressed. Subsequently, enlightenment to each research question are reported in the sequential order that they were introduced in this report.

The following primary research objective was established for this project:

Investigation of power performance differences between monopile BOWT and spar FOWT for the two aerodynamic models employed, BEM and VPM-OLAF.

As discussed in Section 6.2, the performance of the monopile BOWT structure marginally surpasses that of the spar FOWT structure, irrespective of the prevailing sea state conditions. This holds true for both the BEM and OLAF aerodynamic models, although the AEP difference between the two foundations decreases when simulating aerodynamic phenomena using the BEM model. Specifically, when comparing the energy yield of the BOWT to the FOWT, the deviation ranges from 5.23% to 7.84% for BEM, while for VPM-OLAF, the difference ranges between 6.34% to 9.42%. This AEP difference steadily increases as ocean conditions progress from calm, nearly still sea states to more challenging conditions. Furthermore, when OLAF is employed instead of BEM, the estimated AEP results for both BOWT and FOWT increase by approximately 25% across all ocean state scenarios.

For base oceanic conditions [H_s = 2m, T_p = 7s & V_{curr} = 0.3 m/s], when this study adjusts the computed AEP for nacelle velocity feedback using an adjustment factor based on (Abbas et al., 2022), replacing the monopile BOWT structures with spar FOWT structures leads to a reduction in annual energy yield of 4.96% under BEM simulation. When the VPM-OLAF model is utilized, the AEP experiences a decrease of 5.90%. Additional FOWT employed controllers, optimized towards maximizing either power performance or structural life integrity, lead to an estimated AEP decrease from the use of a spar floater instead of a monopile foundation which ranges from 3.46% to 8.62%, respectively, for BEM. Conversely, when utilizing the VPM-OLAF model, the estimated AEP reduction for a spar floater compared to a monopile substructure ranges from 4.50% to 9.58% under similar conditions as mentioned earlier.

Finally, the BOWT and FOWT mean power curves showcase differences depending on the aerodynamic model used. For BEM, the monopile WT outperforms the spar one mostly during the transitional 2-3 region of the power curve. Moreover, at low incoming wind speeds, the FOWT experiencing adverse ocean conditions slightly surpasses the BOWT in power generation. This is potentially attributed to nacelle velocity induced an increase in the rotor blade relative/experienced wind speed. In OLAF's case,

the BOWT outperforms the FOWT for the entirety of partial load operation. For both cases, the monopile WT experiences power fluctuation only during the partial load region, while the floating spar WT's power fluctuates throughout. The former phenomenon is mainly attributed to turbulent wind fields, whereas the latter is influenced by both turbulence and the motion of the spar.

1) *How can the Hywind FOWT be modelled in OpenFAST and what assumptions are made with regards to unknown-uncertain parameters e.g., controller and airfoil distribution?*

The developed Hywind OpenFAST model is comprised of the mooring system, the spar floater, and the wind turbine structure. The mooring lines are simulated using MoorDyn, while the spar floater is modeled in HydroDyn using strip theory. Detailed documentation containing essential data for these components facilitated the model construction process with minimal assumptions. However, confidentiality constraints surrounding the structural, geometric, and mass data of the Siemens-supplied wind turbine structure for Hywind, Scotland required upscaling based on the NREL 5 MW wind turbine and the limited available information sparsely provided. The selection of airfoil profiles and blade distribution relied on internal steering. The wind turbine's controller was treated as proprietary as even obtaining the rated wind speed value proved challenging. The developed FOWT model employed a control strategy based on the ROSCO opensource controller. Through multiple calibration tests, its performance was optimized through an iterative process. It is important to note that the developed controller is not properly tuned for floating conditions, however additional research was conducted to incorporate the discrepancies by adjusting the AEP outcomes of the project.

2) *Where do the developed Hywind OpenFAST model discrepancies stem from?*

The Hywind OpenFAST model that has been developed entails certain discrepancies that have an impact on the dynamic responses of the floating offshore wind turbine (FOWT), thereby affecting the accuracy of the generated data. Based on the analysis conducted in Section 5.3, these model discrepancies are summarized below. Firstly, due to data limitations and restrictions, uncertain wind turbine geometric and structural data are used as inputs in OpenFAST modules. A significant unknown variable is the control strategy operating on the actual Hywind FOWT. Secondly, the simulation of metocean conditions also introduces discrepancies in the model. This is either due to measurement uncertainties, in the case of wind field recreation, or OpenFAST module computational limitations, in the case of HydroDyn's predicted wave and current behavior. Thirdly, in addition to HydroDyn's limitations, OpenFAST's dynamic mooring line simulation module, MoorDyn, also experiences software constraints. Finally, modelling abridgments implemented in the developed model lead to less accurate and more unrealistic outcomes. These simplifications include neglecting array cables, marine mass on the submerged spar, second order hydrodynamic phenomena, nacelle yaw misalignments as well as disabling the spar motion DOF of yaw. The last simplification is potentially decided based on incorrectly measured time series yaw data.

3) *How do the spar's motion degrees of freedom influence the power generation?*

The main concern regarding the use of spar FOWT compared to BOWT is the motion of floaters, which affects the generated power outcomes. Structural loading is beyond the scope of this project. Based on the literature research conducted and the findings of this project, among the six DOFs associated with spar motion, surge and pitch are the ones connected to power generation. An increased pitch angle results in a slight misalignment of the rotor plane with the incoming wind, leading to suboptimal performance and a delayed attainment of rated power generation. Furthermore, the lateral velocity of surge and the rotational velocity of pitch accumulate on the nacelle, causing the rotor blades to experience varying relative wind velocities depending on the nacelle's velocity and its direction. The average power generation increases when the nacelle counteracts the incoming wind flow, whereas it decreases when the nacelle aligns with the wind direction. This effect diminish in significance as the inflow wind speeds

increase. Apart from any discrepancies in control strategies, these two factors primarily contribute to the relatively lower power performance of FOWT compared to BOWT.

4) *How do the ocean conditions affect the spar motion and the power production of the FOWT?*

The motion response of the spar is directly influenced by the prevailing oceanic conditions, which include current speeds and wave effects. The findings of this study reveal that the two essential spar motion DOFs, surge and pitch, are primarily affected by both varying conditions to different extents. Specifically, increasing the current velocities results in a linear increase on both the mean offset and oscillatory behavior of these DOFs. Subjecting the FOWT to more adverse wave conditions, strongly increases the fluctuation amplitudes of surge and pitch. Overall, it was observed that current speeds affect the surge and pitch steady state equilibrium centers, while wave conditions significantly affect the oscillation dynamics. Among these two investigated ocean parameters, power generation is influenced mainly by wave conditions as different current speeds have a minute effect on the output's mean and the STD margins (noticeable through time series results). There could be a fringe coupling moment where the current is directly opposite to wind direction which triggers even larger mean pitch offset but this was not investigated in this project. Mean power generation increases slightly and power fluctuation increases strongly with the wave height and period during partial load operation. For power generation, the fluctuating behavior diminishes at full load, where the occurrence of high waves with long time periods causes sparce power fluctuations of low amplitude.

5) *Which of the two aerodynamic OpenFAST models, BEM and VPM-OLAF, produces higher precision results?*

In the comprehensive simulation of all eleven Hywind measured cases using the developed OpenFAST models, specific observations can be made. As discussed in Section 5.2 and based on the mean summary Table C.1, both the BEM and VPM-OLAF aerodynamic models demonstrate comparable accuracy in recreating spar motion data. Notably, Case 1 and Case 8 deviate from this trend, with each case favoring a different aerodynamic model. In Case 1, which involves above-rated operation, the BEM model demonstrates more accurate prediction of spar motion. Conversely, in Case 8, which involves below-rated operation, the OLAF model yields more precise results. Moreover, OLAF's predicted outcomes have increased oscillation amplitudes compared to the ones produced using BEM. Regarding the idling cases, both models have approximately the same degree of accuracy. Lastly, regarding the two aerodynamic model accuracy per spar motion DOF, OLAF predicts better the results of lateral motion, while the rotational DOFs are predicted sufficiently by both.

7.2 Recommendations for Future Improvements

The research setup's full potential has not been fully realized, as evident from the identified model discrepancies. There are several key areas of the developed spar model that can be further improved. This section highlights such potential future works.

To enhance the reliability of the measured data, it is recommended to obtain more feature-complete measurements. This can be achieved by measuring additional FOWT parameters and collecting longer timeseries data windows with larger date range coverage to minimize statistical uncertainty and improve understanding of the spar's motion characteristics. Furthermore, detailed time series measurements of wave conditions would significantly improve the model, specifically by eliminating the influence of turbine motion on wind statistics, such as in the idling operation measurement cases. By gaining access to validated measured data, the prevailing uncertainty surrounding the disabled spar motion DOF of yaw can be effectively addressed. Although the influence of spar yaw on FOWT power performance and energy yield may not be deemed critical, enabling it during the simulation process will significantly enhance the reliability of the updated model.

In general, obtaining more comprehensive and precise information about the existing system would invariably lead to a superior model. Addressing the key discrepancies in the developed model involves focusing on the wind turbine rotor geometry characteristics and the control strategy employed in the actual Hywind floating wind turbines. Additionally, the currently used OpenFAST Hywind model ROSCO controller is not explicitly tuned for floating, due to time constraints. Once majority of these crucial data are made accessible, it will be possible to update the Hywind OpenFAST coupled model accordingly. The latter could involve capturing detailed aspects of the mooring system, such as precise anchor positions, water depths, or catenary chain profiles.

Furthermore, it is important to integrate the neglected modelling components that were excluded from the developed model of this project, primarily due to limitations in software accessibility and time constraints. Specifically, during the development of the spar model, an initial attempt was made to construct a potential flow theory model. However, this endeavor was abandoned due added complexity and the need to use third party commercial hydrodynamics software. As a result, the alternative approach of strip theory was adopted for constructing the spar model, albeit at the expense of disregarding second order hydrodynamic phenomena. The use of OpenFAST's strip theory also neglected frequency dependent radiation-diffraction effects. An opportunity exists to conduct a comparison between the performance of a potential-flow theory-based model, using the same turbine and mooring system, to assess the accuracy of the predicted spar motion effects by both models. Such a comparison would provide a comprehensive assessment of the agreement between the model's power performance and energy yield predictions.

Finally, the monopile could be made more realistic by fine tuning its section diameters and wall thickness (along conical sections) in accordance with actual monopile designs. The monopile utilized herein is a simplified system with acceptable modal characteristics that served its purpose as a rigid bottom fixed foundation for comparison against the developed spar model.

References

Abbas J., Zalkind D., Pao L., Wright A., "A reference open-source controller for fixed and floating offshore wind turbines", Wind Energy Science: 7, 2022, pp. 53–73.

Abdullahi A., Wang Y., Bhattacharya S., "Comparative Modal Analysis of Monopile and Jacket Supported Offshore Wind Turbines including Soil-Structure Interaction", International Journal of Structural Stability and Dynamics, 2020.

Aranya L., Bhattacharyab S., Macdonalda J., Hogana S.J., "Design of monopiles for offshore wind turbines in 10 steps", Soil Dynamics and Earthquake Engineering 92, 2017, pp. 126–152.

Arapogianni A., Genachte A., Ochagavia R. M., Vergara J. P., "Deep water: The next step for offshore wind energy", European Wind Energy Association, 2013.

Bashetty S., Ozcelik S., "Review on Dynamics of Offshore Floating Wind Turbine Platforms", Energies 14: 6026, 2021.

Bayati I., Jonkman J., Robertson A., Platt A., "The Effects of Second-Order Hydrodynamics on a Semisubmersible Floating Offshore Wind Turbine", National Renewable Energy Laboratory, 2014.

Bergua R., Robertson A., Jonkman J., Branlard E., "OC6 Project Phase III: Validation of the Aerodynamic Loading on a Wind Turbine Rotor Undergoing Large Motion Caused by a Floating Support Structure", European Academy of Wind Energy, Wind Energy Science Discussions, 2022.

Bianchi F. D., De Battista H., Mantz R. J., "Wind Turbine Control Systems Principles, Modelling and Gain Scheduling Design", Springer, 2007.

Bir G., "User's Guide to BModes (Software for Computing Rotating Beam Coupled Modes)", National Renewable Energy Laboratory NREL, 2005.

Browning J.R., Jonkman J., Robertson A., Goupe A.J., "Calibration and validation of a spar-type floating offshore wind turbine model using the FAST dynamic simulation tool", Journal of Physics: Conference Series 555 012015, 2014.

Bussemakers P. J. M., "Validation of aero-hydro-servo-elastic load and motion simulations in BHawC/OrcaFlex for the Hywind Scotland floating offshore wind farm", NTNU & Delft University of Technology Master Thesis, 2020.

Chena J., Hub Z., Liua G., Wan D., "Coupled Aero-Hydro-Servo-Elastic Methods for Floating Wind Turbines", Collaborative Innovation Center for Advanced Ship and Deep-Sea Exploration, 2019.

Choe D., Kim H., Kim M., "Sequence-based modeling of deep learning with LSTM and GRU networks for structural damage detection of floating offshore wind turbine blades", Renewable Energy 174, 2021, pp. 218-235.

Coulling A.J., Goupee A.J., Robertson A. N., Jonkman J. M., Dagher H. J., "Validation of a FAST semi-submersible floating wind turbine numerical model with DeepCwind test data", Journal of renewable and sustainable energy 5 023116, 2013.

Dandrea J., "Study of the Motions and Nacelle Accelerations of the Windcrete Floating Offshore Wind Turbine According to the IEC 64100-3 Procedure", Master Thesis Escola T`ecnica Superior d'Enginyeria Industrial de Barcelona, 2020.

Desmond C., Murphy J., Blonk L., Haans W., "Description of an 8 MW reference wind turbine", The Science of Making Torque from Wind, Journal of Physics: Conference Series 753, 2016.

DHI, "Decode offshore wind engineering challenges at every stage", DHIGroup, 2021, Retrieved on 16/01/2023 from https://blog.dhigroup.com/2021/10/19/decode-offshore-wind-engineering-challenges-at-every-stage/

Dinh V. N., McKeogh E., "Offshore Wind Energy: Technology Opportunities and Challenges", Proceedings of the 1st Vietnam Symposium on Advances in Offshore Engineering, 2018, pp. 3-22.

DNV GL, "Guidelines for Offshore Structural Reliability, Technical report 7-1, Part 2: Load and Resistance Factors Design.", 2015.

DNV GL, "Metocean Characterization Recommended Practices for U.S. Offshore Wind Energy", 2018.

Degraer S., Carey D., Coolen J., Hutchison Z., "Offshore Wind Farm Artificial Reefs Affect Ecosystem Structure and Functioning", Oceanography Vol. 33, 2020.

Driscoll F., Jonkman J., Robertson A., Sirnivas S., Skaare F., Nielsen F. G., "Validation of a FAST Model of the Statoil-Hywind Demo Floating Wind Turbine", Energy Procedia 94, 13th Deep Sea Offshore Wind R&D Conference, 2016, pp. 3 – 19.

Duarte T., Tomas D., Matha D., Sarmento A., Schuon F., "Verification of engineering modelling tools for floating offshore wind turbines", Proceedings of the ASME 2013 32nd International Conference on Ocean, Offshore and Arctic Engineering, 2013.

Equinor, "Hywind Scotland Data Description", ORE Catapult and Equinor ASA, 2018.

Ezio S., Claudio C., "Exploitation of wind as an energy source to meet the world's electricity demand," Journal of Wind Engineering and Industrial Aerodynamics, 1998, pp. 74–76.

Farrugia R., Sant T., Micallef D., "A study on the aerodynamics of a floating wind turbine rotor", Renewable Energy 86, 2016, pp. 770-784.

Gao Z., Yu H., Moan T. "Dynamic response analysis of a spar-type floating wind turbine under free decay motion", Renewable Energy: 80, 2015, pp. 301-311.

Hall M., "MoorDyn V2: New Capabilities in Mooring System Components and Load Cases", Presented at the ASME 39th International Conference on Ocean; Offshore and Arctic Engineering, National Renewable Energy Laboratory, 2020.

Hall M., "MoorDyn User's Guide", 2015, Retrieved on 26/2/2023 from http://www.matt-hall.ca/files/MoorDyn%20Users%20Guide%202015-12-15.pdf

Hong S., Lee I., Hyeon Park S., Lee C., Chun H., Lim H. C., "An experimental study of the effect of mooring systems on the dynamics of a SPAR buoy-type floating offshore wind turbine", International Journal of Naval Architecture and Ocean Engineering, 2015.

Huang Y., Wan D., "Investigation of Interference Effects Between Wind Turbine and Spar-Type Floating Platform Under Combined Wind-Wave Excitation", Sustainability 12 246, 2019.

IEC 61400-12-1, "Wind energy generation systems – Part 12-1: Power performance measurements of electricity producing wind turbines" Edition 2.0 2017-03, International Electrotechnical Commission, 2017.

International Energy Agency (IEA), "Net Zero by 2050: A Roadmap for the Global Energy Sector", Global Wind Energy Council (GWEC), 2021.

Jacobson M. Z., Delucchi M. A., Bauer Z. A. F., Wang J., Weiner E., Yachanin A. S., "100% Clean and Renewable Wind, Water, and Sunlight All-Sector Energy Roadmaps for 139 Countries of the World", Joule 1, 2017, pp. 108–121.

Johlas H. M., Martínez-Tossas L. A., Churchfield M. J., Lackner M. A., Schmidt D. P., "Floating platform effects on power generation in spar and semisubmersible wind turbines", Wind Energy 24, 2020, pp. 901–916.

Jonkman J.M., "Dynamics Modelling and Loads Analysis of an Offshore Floating Wind Turbine", National Renewable Energy Laboratory Technical Report, 2007.

Jonkman J., "FAST: An Open-Source Platform for Wind Turbine Multi-Physics Engineering Modeling", NAWEA 2017 Symposium, National Renewable Energy Laboratory, 2017.

Jonkman J.M., Buhl Jr M.L., "FAST User's Guide", National Renewable Energy Laboratory, 2005a.

Jonkman J.M., Buhl Jr M.L., "TurbSim User's Guide", National Renewable Energy Laboratory, 2005b.

Jonkman J., Butterfield S., Musial W., Scott G., "Definition of a 5-MW Reference Wind Turbine for Offshore System Development", National Renewable Energy Laboratory Technical Report NREL, 2009.

Jonkman J., Butterfield S., "Verification of FAST v8 by Comparison with Test Data from the OC3 and OC4 Wind Turbine Rotor Blades", Conference: 33rd Wind Energy Symposium, 2015.

Jonkman J., Musial W., "Offshore Code Comparison Collaboration (OC3) for IEA Task 23 Offshore Wind Technology and Deployment", National Renewable Energy Laboratory, 2010.

Jonkman J.M., Robertson A.N., Hayman G.J., "HydroDyn User's Guide and Theory Manual", National Renewable Energy Laboratory, 2015.

Journée J.M.J., Massie W.W., "Offshore Hydromechanics: First Edition", Delft University of Technology, 2021.

Karimirad M., Moan T. "Effect of Aerodynamic and Hydrodynamic Damping on Dynamic Response of a Spar Type Floating Wind Turbine", NTNU, 2010.

Kimball R.W., Goupee A.J., Coulling A.J., Dagher H.J., "Model Test Comparisons of TLP, Spar-buoy and Semi-submersible Floating Offshore Wind Turbine Systems," Proc. 2012 SNAME Annual Meeting and Expo, 2012.

Koulouri A., Moccia J., Wilkes J., "Saving water with wind energy", European Wind Energy Association (EWEA), 2014.

Larsen T.J., Hansen A.M., "How to design concrete structures using Eurocode 2: Some practical tips." Proceedings of the Danish Structural Concrete Association No. 56, 2008.

Laureti M., Favini B.,"Pressure Oscillations in Aft-Finocyl SRMs", SciTech, 2019.

Lee H., Lee D., "Effects of platform motions on aerodynamic performance and unsteady wake evolution of a floating offshore wind turbine", Renewable Energy 143, 2019, pp. 9-23.

Lee J., Zhao F., Backwell B., Clarke E., Williams R., "Global Wind Report 2022", Global Wind Energy Council (GWEC), 2022.

Lenfest E., Goupee A. J., Wright A., Abbas N., "Tuning of Nacelle Feedback Gains for Floating Wind Turbine Controllers using a Two-DOF Model", Presented at the ASME 2020 39th International Conference on Ocean: Offshore and Arctic Engineering, 2020.

Lerch M., De-Prada-Gil M., Molins C., "The influence of different wind and wave conditions on the energy yield and downtime of a Spar-buoy floating wind turbine", Renewable Energy 136, 2019, pp. 1-14.

Li X., Zhu C., Fan Z., Chen X., Tan J., "Effects of the yaw error and the wind-wave misalignment on the dynamic characteristics of the floating offshore wind turbine", Ocean Engineering 199 106960, 2020.

Liu B, Yu J., "Dynamic Response of SPAR-Type Floating Offshore Wind Turbine under Wave Group Scenarios", Energies: 15(13):4870, 2022.

Long M., Yanping H., Tao Z., Yongsheng Z., Yadong L., "Research on Dynamic Response Characteristics of 6 MW Spar-Type Floating Offshore Wind Turbine", J. Shanghai Jiao Tong Univ. (Sci.) 23(4), 2018, pp. 505-514.

Lyu G., Zhang H., Li J., "Effects of incident wind/wave directions on dynamic response of a SPAR-type floating offshore wind turbine system", Acta Mechanica Sinica 35(5), 2019, pp. 954–963.

Martini M., Guanche R., Armesto J. A., Losada I. J., "MetOcean conditions influence over floating wind turbine energy production", Proceedings of the ASME 2015 34th International Conference on Ocean, Offshore and Arctic Engineering, 2015.

Matha D., Cruz J., Masciola M., Bachynski E., Atechson M., Goupee A., Gueydon S., Robertson A., "Floating Offshore Wind Energy: The Next Generation of Wind Energy", Springer, 2016, pp. 133-240.

Mathiesen M., Meyer A., Kvingedal B., "Hywind Buchan Deep Metocean Design Basis", Statoil, 2014.

Moriarty P.J., Hansen A.C., "AeroDyn Theory Manual", National Renewable Energy Laboratory, 2005.

Mutlu S. B., Fredsøe J., "Hydrodynamics around cylindrical structures.", World Scientific, 2006.

National Renewable Energy Laboratory, "4. User Documentation", 2021, Retrieved on 13/2/2023 from https://openfast.readthedocs.io/en/dev/source/user/

National Renewable Energy Laboratory, "4.2.8.2. HydroDyn Input Files", 2021, Retrieved on 13/2/2023 from https://openfast.readthedocs.io/en/dev/source/user/hydrodyn/input_files.html

National Renewable Energy Laboratory (NREL), "OpenFAST", 2021, Retrieved on 2/2/2023 from https://www.nrel.gov/wind/nwtc/openfast.html

Negro V., Gutiérrez J., Esteban M., Alberdi P., Imaz M., Serraclara J., "Monopiles in offshore wind: Preliminary estimate of main dimensions", Universidad Politécnica de Madrid, 2018.

Nejad A., Torsvik J., "Drivetrains on floating offshore wind turbines: lessons learned over the last 10 years", Forsch Ingenieurwes - Springer, 2021.

Papillon L., Costello R., Ringwood J., "Boundary element and integral methods in potential flow theory: a review with a focus on wave energy applications", Journal of Ocean Engineering and Marine Energy 6, 2020, pp. 303-337.

Pereira Malveiro C., "Aerodynamics of a 15-MW and a 5-MW Reference Wind Turbine Using Varying Fidelity Tools", Delft University of Technology Master Thesis, 2022.

Platt A., Jonkman B., Jonkman J., "InflowWind User's Guide", National Wind Technology Center, 2016.

Ramos-García N., Kontos S., Pegalajar-Jurado A., González Horcas S., Bredmose H., "Investigation of the floating IEA Wind 15 MW RWT using vortex methods Part I: Flow regimes and wake recovery", Wind Energy 25, 2022, pp. 468–504.

Ramponi R., "Investigation of the effect of prescribed coupled motions in the power production of a Floating Offshore Wind Turbine", Politecnico di Milano Master Thesis, 2022.

Rinker J., Gaertner E., Zahle F., Skrzypi´nski W., Abbas N., Bredmose H., Barter G., Dykes K., "Comparison of loads from HAWC2 and OpenFAST for the IEA Wind 15 MW Reference Wind Turbine", Journal of Physics: Conference Series 1618 052052, 2020.

Robertson A., Jonkman J. M., Masciola M. D., Molta P., "Summary of Conclusions and Recommendations Drawn from the DeepCWind Scaled Floating Offshore Wind System Test Campaign", National Renewable Energy Laboratory, 2013.

Robertson A., Koh J. H., Jonkman J., Driscoll R., Yin Kwee E., "Validation of SWAY Wind Turbine Response in FAST, with a Focus on the Influence of Tower Wind Loads", National Renewable Energy Laboratory, 2015.

Robertson A., Wendt F., Jonkman J. M., "OC5 Project Phase II: Validation of Global Loads of the DeepCwind Floating Semisubmersible Wind Turbine", Energy Procedia 137, 14th Deep Sea Offshore Wind R&D Conference, 2017, pp. 38–57.

Sant T., Bonnici D., Farrugia R., Micallef D., "Measurements and modelling of the power performance of a model floating wind turbine under controlled conditions", Wind Energy 18, 2014 pp. 811–834.

Selås S. M., "Hywind Scotland", Equinor, 2018, Retrieved on 28/2/2023 from https://www.equinor.com/energy/hywind-scotland

Shaler K., Anderson B., Martínez-Tossas L., Branlard E., Johnson N., "Comparison of free vortex wake and blade element momentum results against large-eddy simulation results for highly flexible turbines under challenging inflow conditions", Wind Energy Science 8, 2023, pp. 383–399.

Shaler K., Branlard E., Platt A., "OLAF User's Guide and Theory Manual", National Renewable Energy Laboratory, 2020.

Shaler K., Branlard E., Platt A., Jonkman J., "Preliminary Introduction of a Free Vortex Wake Method into OpenFAST", Journal of Physics: Conference Series 1452, 2020.

Shi W., Park H., Baek J., Kim C., "Study on the Marine Growth Effect on the Dynamic Response of Offshore Wind Turbines", International Journal of Precision Engineering and Manufacturing Vol. 13, 2012, pp. 1167-1176.

Sivaselvan M. V., "Numerical Simulation of the Influence of Platform Pitch Motion on Power Generation Steadiness in Floating Offshore Wind Turbines", Environmental Science and Sustainable Development, 2017.

Skaare B., Hanson T., Nielsen F., "Importance of Control Strategies on Fatigue Life of Floating Wind Turbines.", Proceedings of the 26th International Conference on Offshore Mechanics and Arctic Engineering, 2007.

Statoil, "Hywind Scotland Pilot Park Environmental Statement", 2015, Retrieved on 28/2/2023 from https://marine.gov.scot/datafiles/lot/hywind/Environmental_Statement/Environmental_Statement.pdf

Statoil, Masdar, "Hywind Scotland: The world's first commercial floating wind farm", 2018.

Thibierge A., "Validation of a vortex panel method for aerodynamics and aero-elasticity of Wind Turbine", KTH Master Thesis, 2020.

Tran T., Kim D., "A CFD study into the influence of unsteady aerodynamic interference on wind turbine surge motion", Renewable Energy 90, 2016, pp. 204-228.

Tran T., Kim D., "The platform pitching motion of floating offshore wind turbine: A preliminary unsteady aerodynamic analysis", Journal of Wind Engineering and Industrial Aerodynamics 142, 2015, pp. 65-81.

TU Delft, "Chapter12: Wave forces on slender cylinders", Lecture Slides, 2019, Retrieved on 15/02/2023 from https://ocw.tudelft.nl/wp-content/uploads/Part_4.pdf

Tumewu Y, Petrone C., Sivaselvan M. V., "Numerical Simulation of the Influence of Platform Pitch Motion on Power Generation Steadiness in Floating Offshore Wind Turbines", Environmental Science and Sustainable Development, 2017.

Umut O., Dexing L., Raphael A., Choisnet T., Cheng P., "Power curve measurement of a floating offshore wind turbine with a nacelle-based lidar", The Science of Making Torque from Wind, Journal of Physics: Conference Series 2265, 2022.

UN75 (United Nations), "The Climate Crisis- A Race We Can Win", 2019, Retrieved on 14/01/2023 from https://www.un.org/en/un75/climate-crisis-race-we-can-win

United Nations, "Paris Agreement", 2015, Retrieved on 16/01/2023 from https://unfccc.int/sites/default/files/english_paris_agreement.pdf

US Department of Energy, "Wind Energy Benefits", WINDExchange, 2015, pp. 1-2.

Viré A., "How to float a wind turbine", Rev Environ Sci Biotechnol 11, 2012, pp. 223–226.

Wang X., Cai C., Cai S., Wang T., Wang Z., Song J., Rong J., Li Q., "A review of aerodynamic and wake characteristics of floating offshore wind turbines", Renewable and Sustainable Energy Reviews 175 113144, 2023.

Wang S., Xing Y., Karuvathil A., Gaidai O., "A comparison study of power performance and extreme load effects of large 10-MW offshore wind turbines", IET Renewable Power Generation, 2023, pp. 1-20.

Wen B., Tian X., Dong X., Peng Z., Zhang W., "Influences of surge motion on the power and thrust characteristics of an offshore floating wind turbine", Energy 141, 2017, pp. 2054-2068.

Wen B., Tian X., Dong X., Peng Z., Zhang W., Wei K., "The power performance of an offshore floating wind turbine in platform pitching motion", Energy 154, 2018, pp. 508-521.

World Health Organization (WHO), "Air Pollution", 2014, Retrieved on 14/01/2023 from http://www.who.int/mediacentre/news/releases/2014/air-pollution/en/

Xiang G., Xiang X., Yu X., "Dynamic Response of a SPAR-Type Floating Wind Turbine Foundation with Taut Mooring System", Journal of Marine Science and Engineering 10, 2022.

Xu X., Srinil N., "Dynamic response analysis of spar-type floating wind turbines and mooring lines with uncoupled VS coupled models", Proceedings of the ASME 2015 34th International Conference on Ocean, Offshore and Arctic Engineering, 2015.

Yu M., Hu Z., Xiao L., "Wind-wave induced dynamic response analysis for motions and mooring loads of a spar-type offshore floating wind turbine" J Hydrodyn. Ser. B 26, 2015, pp. 865–874.

Zaaijer M., "Wind Turbine Design System design and scaling", TU Delft Lecture Slides, 2021.

Zaaijer M., Viré A., "Introduction to wind turbines: physics and technology", 2022.

Zalkind D., Abbas N., Jasa J., Wright A., Fleming P., "Floating wind turbine control optimization", The Science of Making Torque from Wind, 2022.

Zhao X., Cai L., Ji X., Zeng W., Liu J., "Mechanical Properties of Polyethylene Fiber Reinforced Ultra High-Performance Concrete (UHPC)", Materials 15: 8734, 2022.

Appendix A

Case	Date	Hs	Tp	Wind	Current	Wave-dir	Wind-dir	Curr-dir
8	2018-03-26 23:30	2.2	10.6	8.5	0.24	14	172	16
3	2018-01-14 15:40	4.2	8.7	20.4	0.32	165	174	24
9	2018-04-14 00:40	2.1	10.5	5.2	0.32	107	171	195
6	2018-02-13 01:20	2.1	6.5	15.5	0.27	201	174	187
7	2018-02-24 04:50	2.5	7.3	14.1	0.17	164	161	150
2	2018-01-09 09:40	3.2	9.3	13.9	0.09	131	146	303
1	2018-01-06 08:00	4.4	10.9	13.7	0.21	17	11	19
11	2018-07-29 04:00	3.0	7.9	16.6	0.33	161	179	44
10	2018-05-02 04:00	2.3	6.5	15.6	0.12	185	175	233
4	2018-01-24 11:30	3.9	8.3	30.0	0.27	174	212	27
5	2018-01-24 11:40	3.9	8.3	30.3	0.30	175	213	37

Case no.	Date	Mean wind [m/s]	Std. [m/s]	Wind direction
8	26.03.2018 23:30	8.49	0.75	172
3	14.01.2018 15:40	20.44	2.07	174
9	14.04.2018 00:40	5.24	0.74	171
6	13.02.2018 01:20	15.53	1.36	174
7	24.02.2018 04:50	14.1	1.12	161
2	09.01.2018 09:40	13.89	1.3	146
1	06.01.2018 08:00	13.72	1.33	11
11	29.07.2018 04:00	16.62	1.41	179
10	02.05.2018 04:00	15.61	1.07	175
4	24.01.2018 11:30	29.96	3.47	212
5	24.01.2018 11:40	30.35	3.41	213

		Hs [m]			Tp [s]			Wave direction [deg]		
Case no.	Date	Total	Wind sea	Swell	Total	Wind sea	Swell	Total	Wind sea	Swell
8	26.03.2018 23:30	2.23	0.94	2.03	10.6	7.95	10.6	14	313	14
3	14.01.2018 15:40	4.21	2.93	3.02	8.7	8	8.7	165	168	163
9	14.04.2018 00:40	2.07	1.48	1.44	10.5	8	10.5	107	111	103
6	13.02.2018 01:20	2.13	2.09	0.4	6.5	6.5	14.6	201	201	61
7	24.02.2018 04:50	2.51	2.45	0.52	7.3	7.3	8.3	164	164	174
2	09.01.2018 09:40	3.25	2.32	2.29	9.3	7.55	9.3	131	134	127
1	06.01.2018 08:00	4.41	2.42	3.68	10.9	7.7	10.9	17	19	16
11	29.07.2018 04:00	3.02	2.74	1.27	7.85	7.85	8.3	161	163	148
10	02.05.2018 04:00	2.28	2.26	0.3	6.5	6.5	8.3	185	185	170
4	24.01.2018 11:30	3.87	3.06	2.36	8.3	8	8.3	174	184	160
5	24.01.2018 11:40	3.85	3.07	2.32	8.3	8	8.3	175	186	157

		Current direction [deg]				Current speed [m/s]			
Case no.	Date	-3.72m	-11.72m	-31.72m	-67.72m	-3.72m	-11.72m	-31.72m	-67.72m
8	26.03.2018 23:30	11	174	16	16	0.25	0.27	0.24	0.21
3	14.01.2018 15:40	22	17	57	26	0.28	0.37	0.21	0.43
9	14.04.2018 00:40	187	196	194	211	0.37	0.38	0.33	0.21
6	13.02.2018 01:20	188	185	186	203	0.31	0.23	0.28	0.25
7	24.02.2018 04:50	140	143	157	187	0.19	0.17	0.19	0.13
2	09.01.2018 09:40	311	324	296	52	0.11	0.14	0.08	0.06
1	06.01.2018 08:00	19	32	17	18	0.23	0.21	0.22	0.19
11	29.07.2018 04:00	47	41	34	79	0.2	0.26	0.27	0.58
10	02.05.2018 04:00	224	241	242	32	0.12	0.12	0.14	0.09
4	24.01.2018 11:30	28	27	18	33	0.31	0.22	0.28	0.28
5	24.01.2018 11:40	38	36	29	47	0.34	0.27	0.28	0.33

Figure A.1 Hywind Scotland measured metocean data (including current, wave and wind parameters) for the eleven separate date cases (Equinor, 2018).

Appendix B

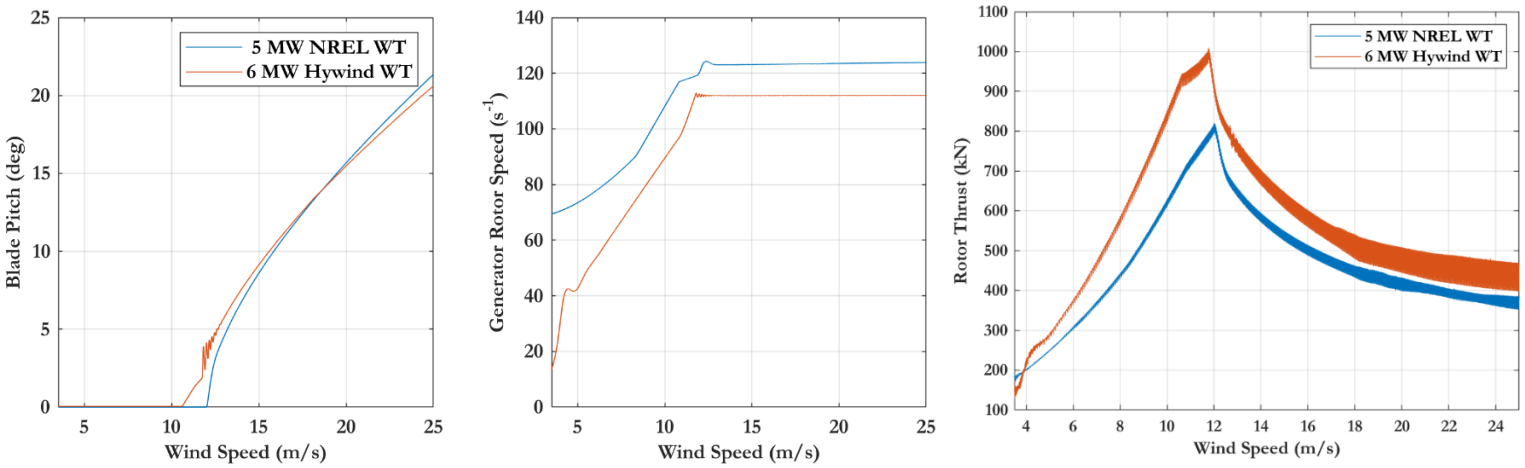

Figure B.1 Instantaneous blade pitch, generator rotor speed and rotor thrust comparison between the stable NREL 5 MW & Hywind upscaled wind turbines.

```
---------------------- MoorDyn Input File ------------------------------------
Mooring system for OC3-Hywind
FALSE     Echo      - echo the input file data (flag)
---------------------- LINE TYPES --------------------------------------------
Name      Diam     MassDen      EA      BA/-zeta   EI     Cd      Ca      CdAx    CaAx
(-)        (m)      (kg/m)      (N)      (N-s/-)    (-)    (-)     (-)     (-)     (-)
Bridle     0.132    348      800000000    -0.8      0.0    1.6     1.0     0.1     0.0
MainLine   0.147    432      500000000    -0.8      0.0    1.6     1.0     0.1     0.0
---------------------- POINTS ------------------------------
ID     Attachment  X      Y       Z       M      V     CdA   CA
(-)      (-)      (m)    (m)     (m)     (kg)  (m^3) (m^2)  (-)
1     fixed    -551.3   327.85   -100.0    0      0      0     0
2     Vessel    0.8      8        -19.6    0      0      0     0
3     Vessel   -6.0     -3.86     -19.6    0      0      0     0
4    connect   -43.3     33       -30      0      0      0     0
5     fixed     0       -650     -100.0    0      0      0     0
6     Vessel   -6.0     -4.46     -19.6    0      0      0     0
7     Vessel    6.0     -4.46     -19.6    0      0      0     0
8    connect    0       -49.5     -30      0      0      0     0
9     fixed     551.3    327.85   -100.0    0      0      0     0
10    Vessel    6.0     -4.46     -19.6    0      0      0     0
11    Vessel    0.8      8        -19.6    0      0      0     0
12    connect   43.3     33       -30      0      0      0     0
---------------------- LINES -------------------------------------
ID      LineType    AttachA    AttachB   UnstrLen   NumSegs    Outputs
(-)       (-)         (-)        (-)       (m)        (-)       (-)
1       Bridle       4          2         50         1          p
2       Bridle       4          3         50         1          p
3       MainLine     1          4         595.7      1          p
4       Bridle       8          6         50         1          p
5       Bridle       8          7         50         1          p
6       MainLine     5          8         595.7      1          p
7       Bridle       12         10        50         1          p
8       Bridle       12         11        50         1          p
9       MainLine     9          12        595.7      1          p
---------------------- SOLVER OPTIONS ----------------------------------------
0.0125    dtM       - time step to use in mooring integration (s)
3.0e6     kbot      - bottom stiffness (Pa/m)
3.0e5     cbot      - bottom damping (Pa-s/m)
1.0       dtIC      - time interval for analyzing convergence during IC gen (s)
150       TmaxIC    - max time for ic gen (s)
4.0       CdScaleIC - factor by which to scale drag coefficients during dynamic relaxation (-)
0.001     threshIC  - threshold for IC convergence (-)
```

Figure B.2 OpenFAST MoorDyn input file used in floating cases.

Members Height (m)	Diameter(m)	Thickness (m)	Length (m)	Volume (m3)	Mass (kg)	CoG contributions	CoG Output (Should be 0)
-77.6	14.4	0.474175					674.4698687
-59.6	14.4	0.474175	18	373.2172765	2892433.89	-52063810.07	
-19.6	14.4	0.33	40	829.3717255	6427630.87	0	
-19	14.07	0.215	0.6	8.7476004	67793.9031	2711756.124	
-18	13.74	0.215	1	9.3535105	72489.7064	2943082.079	
-17	13.41	0.215	1	9.1307275	70763.1381	2943746.546	**Steel Density (kg/m3)**
-16	13.08	0.215	1	8.9079445	69036.5699	2940957.877	7750
-15	12.75	0.215	1	8.6851615	67310.0016	2934716.071	
-14	12.42	0.215	1	8.4623785	65583.4334	2925021.129	**Total Mass(Tonnes)**
-13	12.09	0.215	1	8.2395955	63856.8651	2911873.05	10538.65327
-12	11.76	0.215	1	8.0168125	62130.2969	2895271.834	
-11	11.43	0.215	1	7.7940295	60403.7286	2875217.483	
-10	11.1	0.215	1	7.5712465	58677.1604	2851709.994	
-9	10.77	0.215	1	7.3484635	56950.5921	2824749.369	
-8	10.44	0.215	1	7.1256805	55224.0239	2794335.608	
-7	10.11	0.215	1	6.9028975	53497.4556	2760468.71	
-6	9.78	0.215	1	6.6801145	51770.8874	2723148.676	
-4.6	9.45	0.1	1.4	9.0402641	70062.0468	3755325.707	
7.4	9.45	0.1	12	35.2308	273038.7	15017128.5	

Structure Compartements	Mass (kg)	Cog Separate
Hub	81000	98
Tower	670000	51.5
Nacelle	153000	98
Blade	25000	98
Platform	10504000	-59.6
Total	11483000	-50.03

Figure B.3 Spar Center of gravity value iterative calculation Excel spreadsheet.

Table B.1 Spar floater HydroDyn members' parameters.

Member Depth rel. to MSL (m)	Member Diameter (m)	Member Thickness (m)
-77.6	14.40	0.474175
-59.6	14.40	0.474175
-19.6	14.40	0.33
-19.0	14.07	0.215
-18.0	13.74	0.215
-17.0	13.41	0.215
-16.0	13.08	0.215
-15.0	12.75	0.215
-14.0	12.42	0.215
-13.0	12.09	0.215
-12.0	11.76	0.215
-11.0	11.43	0.215
-10.0	11.10	0.215
-9.0	10.77	0.215
-8.0	10.44	0.215
-7.0	10.11	0.215
-6.0	9.780	0.215
-4.6	9.450	0.1
7.4	9.450	0.1

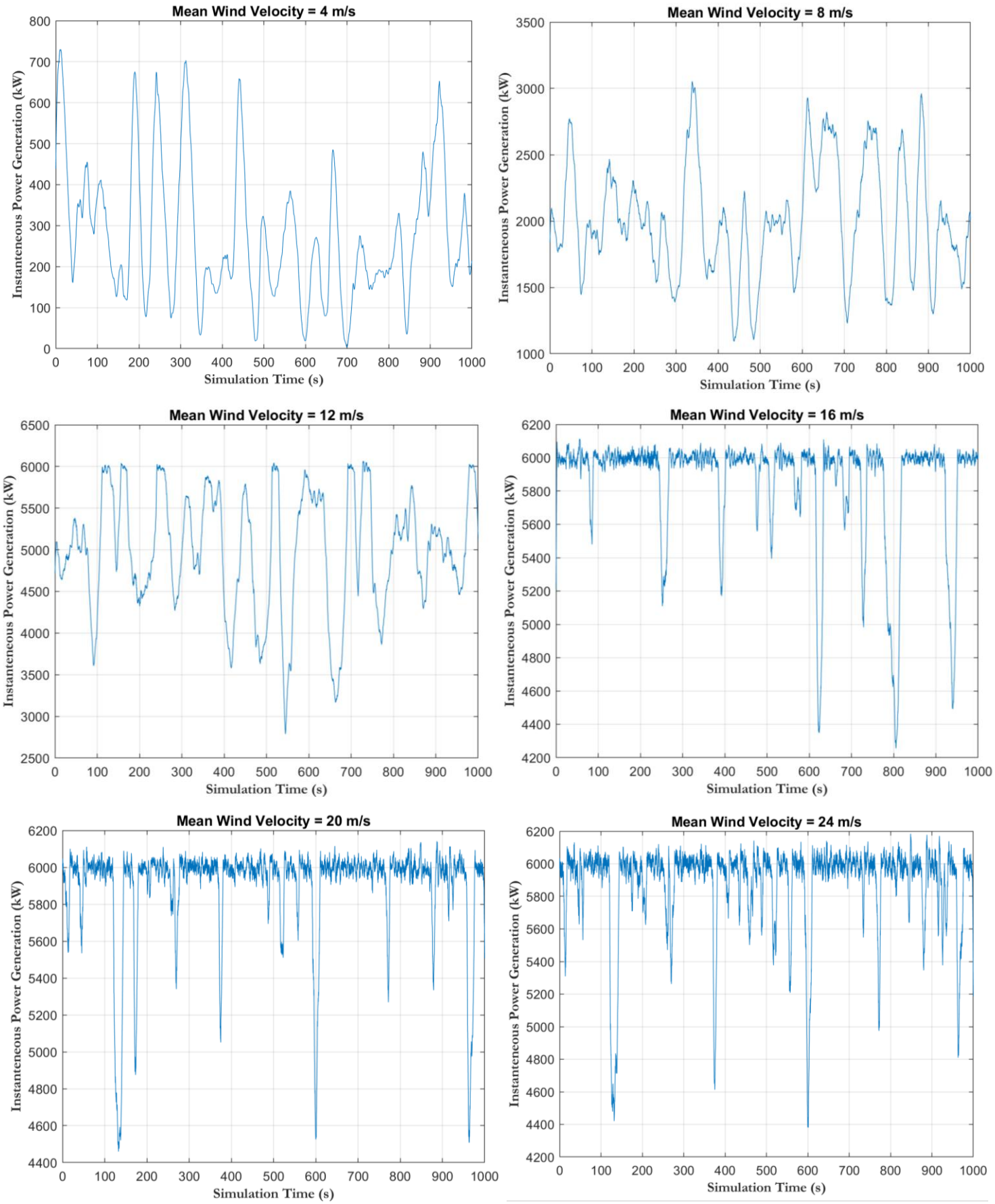

Figure B.4 Instanteneous power generation against simulation time of the developed spar FOWT 6 MW for six different wind velocity fields using the BEM aerodynaic model.

Appendix C

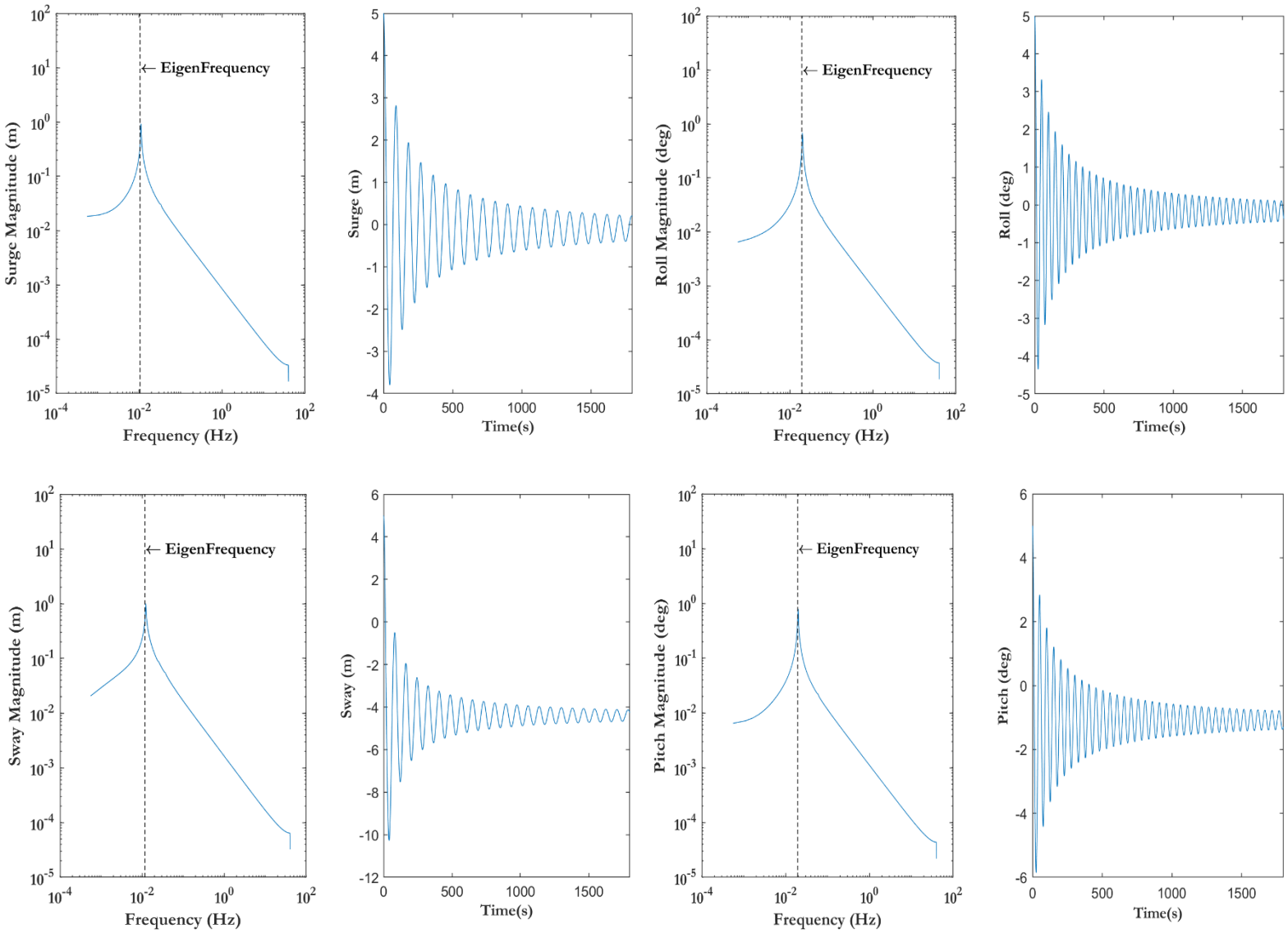

Figure C.1 Uncoupled X and Y axis spar platform motion DOFs free decay time series & frequency domain graphs with eigenfrequency point.

```
---------------------------- FREE WAKE INPUT FILE -----------------------------------------------
Free wake input file for the BAR turbine
---------------------------- GENERAL OPTIONS ----------------------------------------------------
5 IntMethod          Integration method {1: RK4, 5: Forward Euler 1st order, default: 5} (switch)
0.0125  DTfvw              Time interval for wake propagation. {default: dtaero} (s)
0.0     FreeWakeStart      Time when wake is free. (-) value = always free. {default: 0.0} (s)
0.0     FullCircStart      Time at which full circulation is reached. {default: 0.0} (s)
---------------------------- CIRCULATION SPECIFICATIONS -----------------------------------------
1       CircSolvingMethod  Circulation solving method {1: Cl-Based, 2: No-Flow Through, 3: Prescribed, default: 1 }(switch)
default CircSolvConvCrit   Convergence criteria {default: 0.001} [only if CircSolvingMethod=1] (-)
default CircSolvRelaxation Relaxation factor {default: 0.1} [only if CircSolvingMethod=1] (-)
default CircSolvMaxIter    Maximum number of iterations for circulation solving {default: 30} (-)
"unused" PrescribedCircFile File containing prescribed circulation [only if CircSolvingMethod=3] (quoted string)
================================================================================================
---------------------------- WAKE OPTIONS -------------------------------------------------------
------------------ WAKE EXTENT AND DISCRETIZATION ----------------------------------------------
80      nNWPanel           Number of near-wake panels (-)
100      WakeLength         Total wake distance (D)
50       FreeWakeLength     Wake length that is free (D) {default: WakeLength}
False   FWShedVorticity    Include shed vorticity in the far wake {default: False}
------------------ WAKE REGULARIZATIONS AND DIFFUSION -------------------------------------------
0       DiffusionMethod    Diffusion method to account for viscous effects {0: None, 1: Core Spreading, "default": 0}
3       RegDeterMethod     Method to determine the regularization parameters {0:  Manual, 1: Optimized, 2: Chord, 3: Span, default: 0 }
default RegFunction        Viscous diffusion function {0: None, 1: Rankine, 2: LambOseen, 3: Vatistas, 4: Denominator, "default": 3} (switch)
1       WakeRegMethod      Wake regularization method {1: Constant, 2: Stretching, 3: Age, default: 1} (switch)
3.00    WakeRegFactor      Wake regularization factor (m or -)
2.00    WingRegFactor      Wing regularization factor (m or -)
1000    CoreSpreadEddyVisc Eddy viscosity in core spreading methods, typical values 1-1000
------------------ WAKE TREATMENT OPTIONS -------------------------------------------------------
True    TwrShadowOnWake    Include tower flow disturbance effects on wake convection {default:false} [only if TwrPotent or TwrShadow]
0       ShearModel         Shear Model {0: No treatment, 1: Mirrored vorticity, default: 0}
------------------ SPEEDUP OPTIONS --------------------------------------------------------------
2       VelocityMethod     Method to determine the velocity {1:Biot-Savart Segment, 2:Particle tree, 3:Segment tree, default: 1}
1.5     TreeBranchFactor   Branch radius fraction above which a multipole calculation is used {default: 2.0} [only if VelocityMethod=2]
1       PartPerSegment     Number of particles per segment [only if VelocityMethod=2]
```

Figure C.2 OpenFAST OLAF input file used in both flaoting and bottom fixed cases.

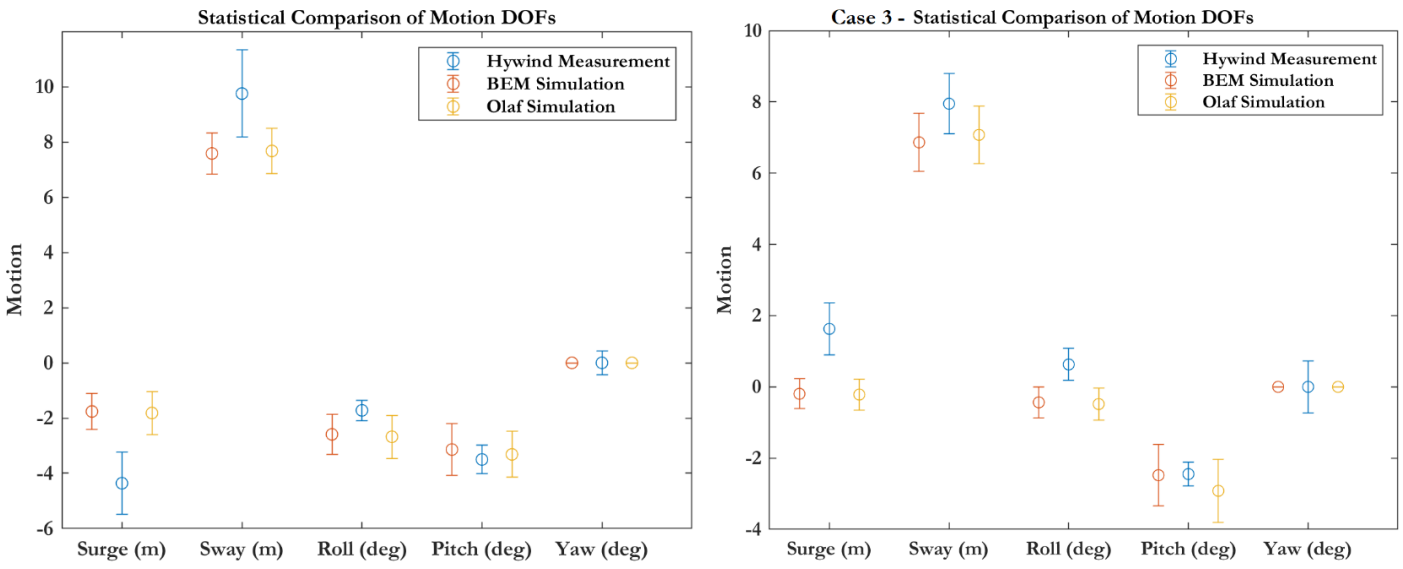

Figure C.3 Spar platform motion DOF statistical comparison between Hywind measurements, OpenFAST BEM & OLAF models for Case 2 (January 9th - Left) & Case 3 (January 14th - Right).

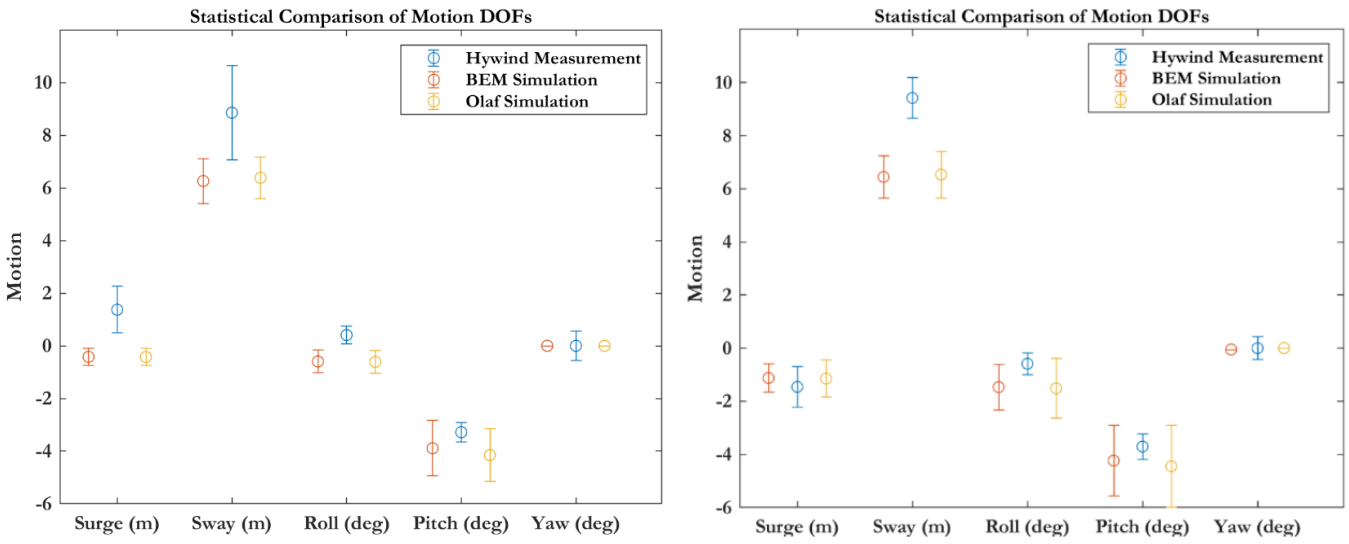

Figure C.4 Spar platform motion DOF statistical comparison between Hywind measurements, OpenFAST BEM & OLAF models for Case 6 (February 13th - Left) & Case 7 (February 24th - Right).

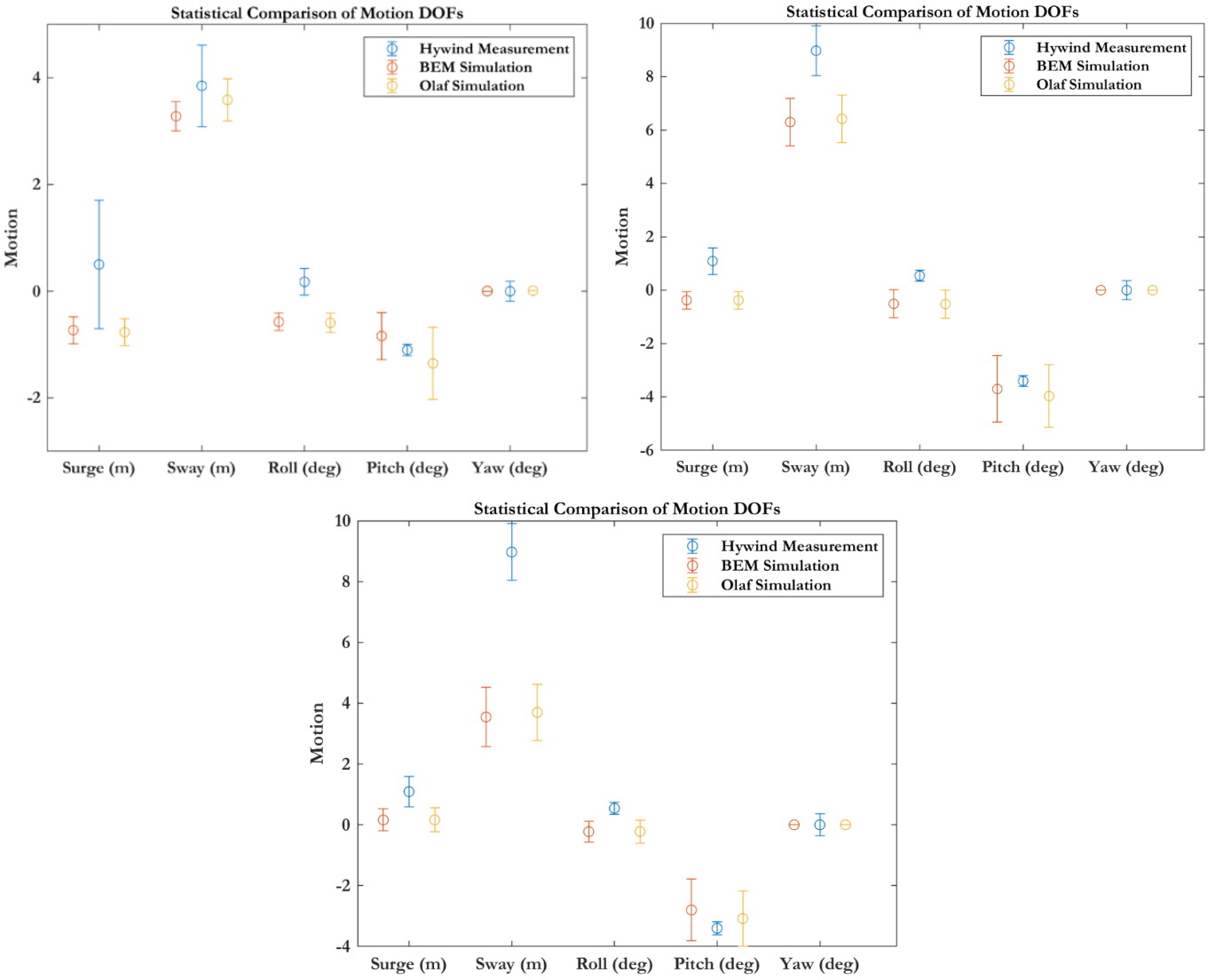

Figure C.5 Spar platform motion DOF statistical comparison between Hywind measurements, OpenFAST BEM & OLAF models for Case 9 (April 14th - Left), Case 10 (May 2nd – Right) & for Case 11 (July 29th - Bottom).

Table C.1 Hywind measured data numerical difference compared to absolute mean (Above) & maximum (Bottom) BEM and OLAF spar motion DOF simulated results.

Hywind Case	BEM Surge Diff. (m)	OLAF Surge Diff. (m)	BEM Sway Diff. (m)	OLAF Sway Diff. (m)	BEM Roll Diff. (°)	OLAF Roll Diff. (°)	BEM Pitch Diff. (°)	OLAF Pitch Diff. (°)
1 Above Rated	-0.29	-0.32	0.42	0.45	0.93	1.01	0.83	0.89
2 Above Rated	-2.60	-2.54	-2.14	-2.02	0.87	0.95	-0.36	-0.19
3 Above Rated	-1.43	-1.41	-1.04	-0.92	-0.55	-0.61	0.03	0.47
4 Idling	-1.51	-1.54	-1.13	-1.11	0.46	0.46	0.38	0.39
5 Idling	-1.45	-1.42	-1.34	-1.30	0.53	0.55	0.42	0.42
6 Above Rated	-1.21	-1.17	-2.52	-2.34	-0.34	-0.40	0.64	0.82
7 Above Rated	-0.37	-0.06	-3.65	-3.56	0.88	0.92	0.53	0.74
8 Below Rated	0.41	0.39	-1.16	-0.52	0.81	0.79	-2.21	-0.61
9 Below Rated	0.21	0.28	-0.72	-0.47	-0.40	-0.43	-0.26	0.25
10 Above Rated	-0.72	-0.71	-2.77	-2.71	-0.03	-0.02	0.30	0.42
11 Above Rated	-1.61	-1.58	-5.07	-4.98	-0.58	-0.57	-0.18	-0.10

Hywind Case	BEM Surge Diff. (m)	OLAF Surge Diff. (m)	BEM Sway Diff. (m)	OLAF Sway Diff. (m)	BEM Roll Diff. (°)	OLAF Roll Diff. (°)	BEM Pitch Diff. (°)	OLAF Pitch Diff. (°)
1 Above Rated	-1.24	-1.22	-1.17	0.19	0.56	0.79	3.14	3.62
2 Above Rated	-0.84	-0.89	-2.50	-2.96	-0.18	-0.39	-1.49	-1.36
3 Above Rated	-2.95	-2.91	-3.04	-3.92	-1.36	-1.28	-1.35	-1.35
4 Idling	-3.15	-2.95	-2.83	-2.80	-1.36	-1.16	-0.09	-0.09
5 Idling	-2.97	-2.92	-3.34	-3.30	-1.31	-1.21	0.23	0.22
6 Above Rated	-3.32	-3.32	-4.72	-4.64	-0.87	-0.80	-1.18	0.81
7 Above Rated	-0.38	-0.06	-4.37	-4.16	0.26	0.60	-1.62	-1.79
8 Below Rated	-3.58	-3.60	-3.36	-2.82	0.60	0.75	-0.44	1.62
9 Below Rated	-3.41	-3.42	-1.72	-1.47	-0.86	-0.82	-0.54	0.43
10 Above Rated	-1.96	-1.88	-3.29	-3.21	-0.20	-0.20	-2.69	-2.10
11 Above Rated	-2.26	-2.11	-7.11	-7.37	-1.10	-0.94	-1.77	-1.18

Appendix D

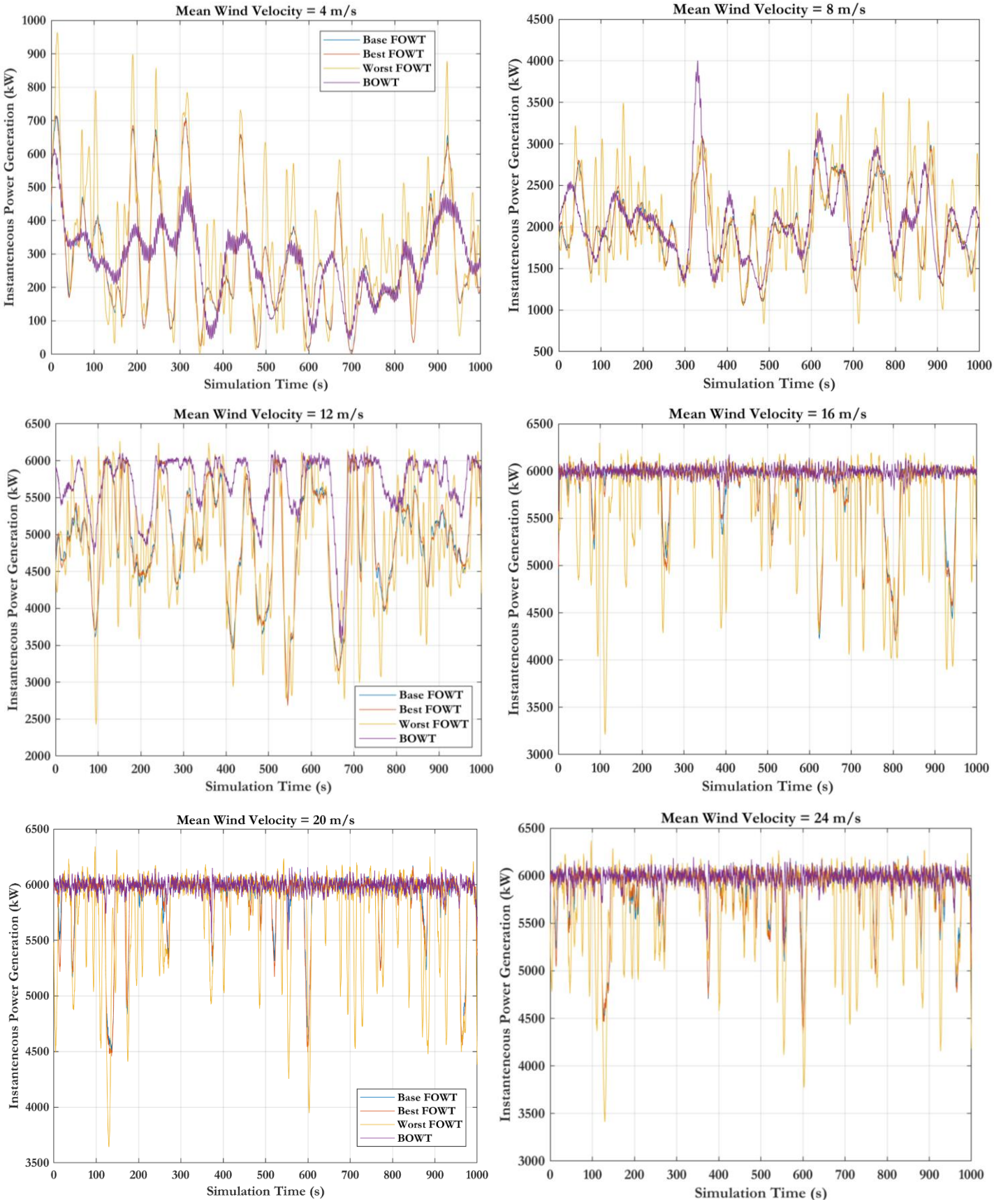

Figure D.1 BEM instanteneous power generation of Base FOWT, Best FOWT, Worst FOWT and BOWT against simulation time for six different wind velocity fields.

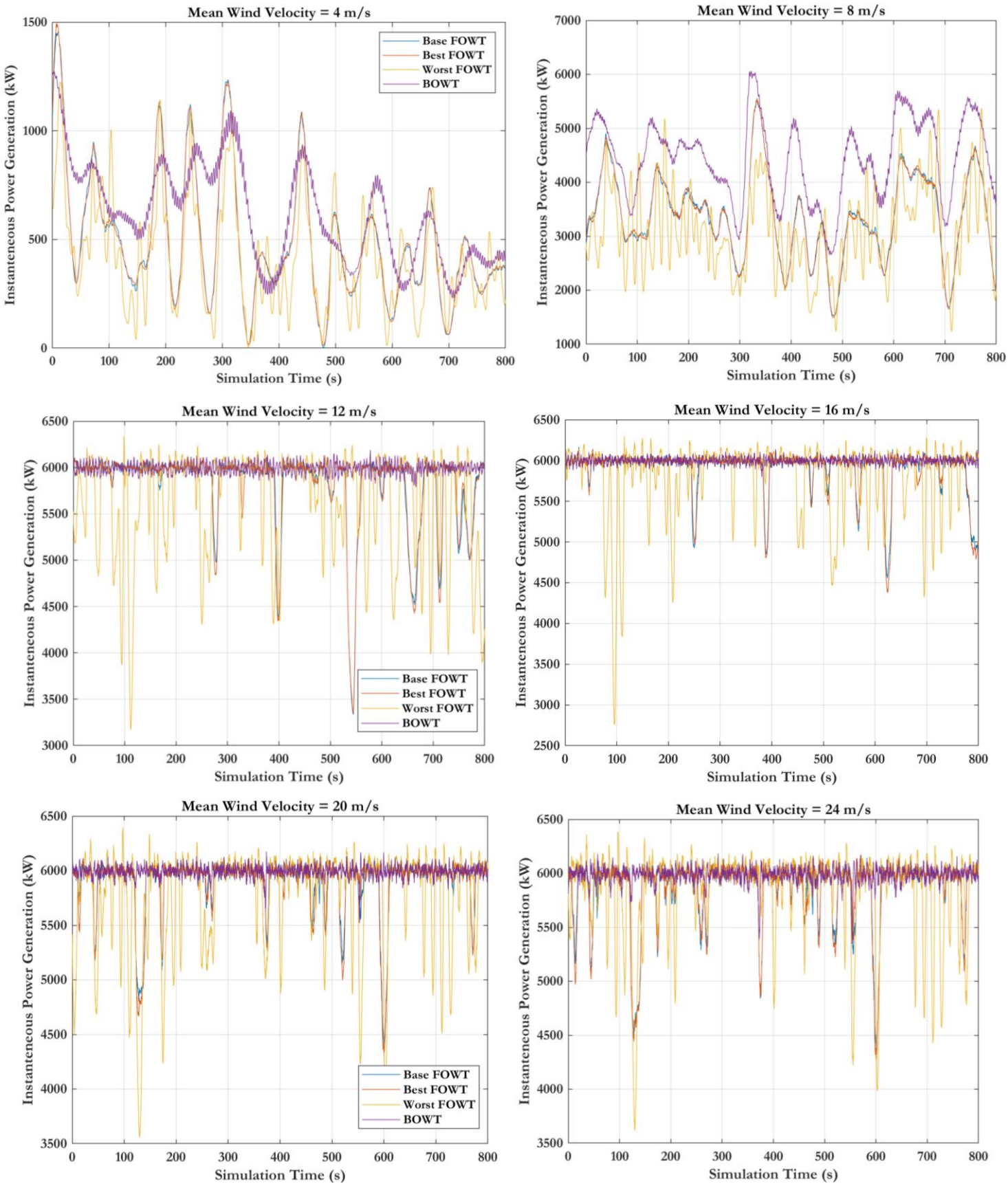

Figure D.2 OLAF instanteneous power generation of Base FOWT, Best FOWT, Worst FOWT and BOWT against simulation time for six different wind velocity fields.

[This page is left intentionally blank]

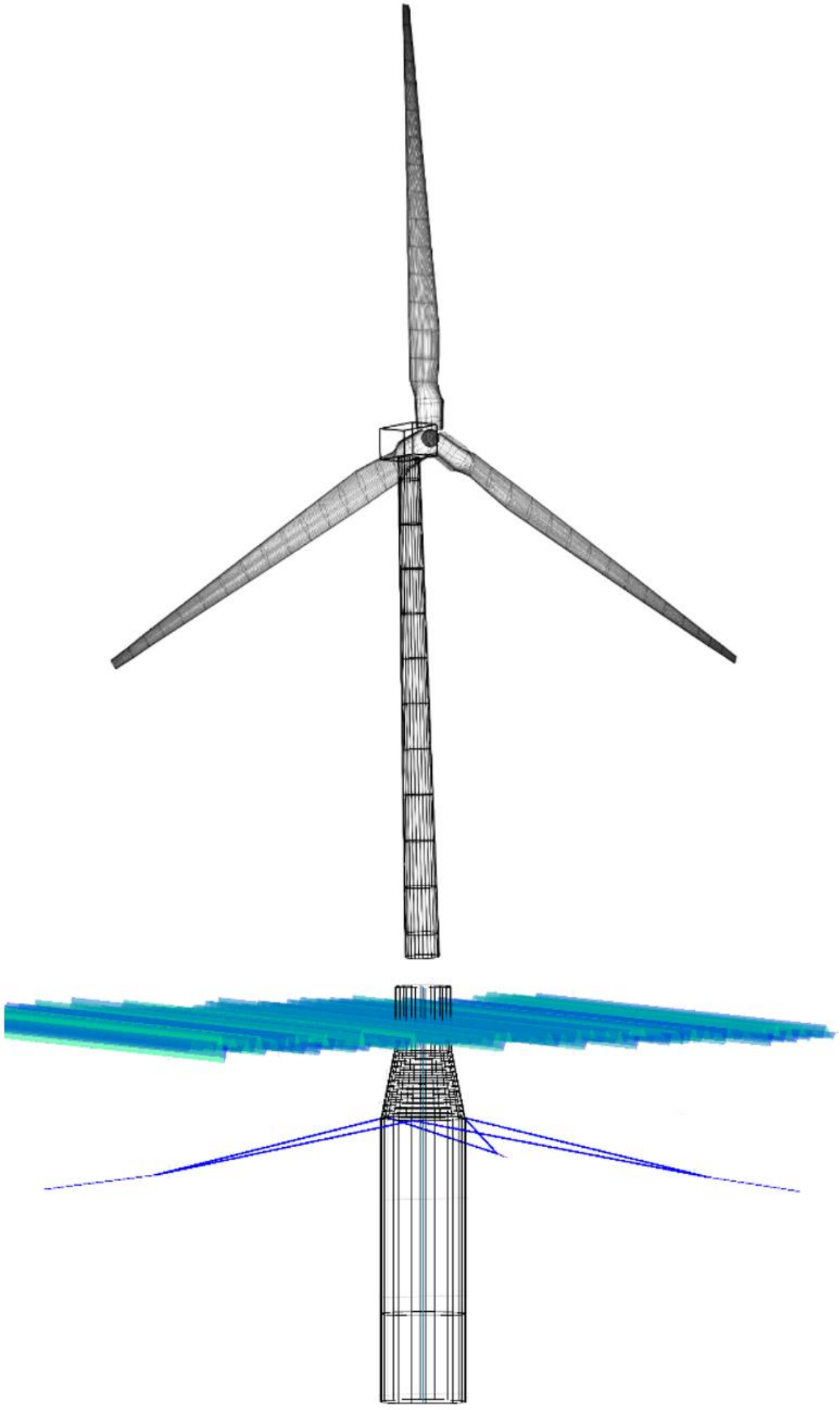

[END]